

Annual Report 2005

Institute of Nuclear
and Hadron Physics



Forschungszentrum
Rossendorf

Wissenschaftlich-Technische Berichte

FZR-442

2006

Annual Report 2005

Institute of Nuclear and Hadron Physics

Editors:

W. Enghardt, K. Fahmy, E. Grosse, B. Kämpfer,
C. Schneidereit, A. Wagner, R. Wünsch



**Forschungszentrum
Rossendorf**

Wissenschaftlich-Technische Berichte

FZR-442

2006

Annual Report 2005

Institute of Nuclear and Hadron Physics

Editors:

W. Enhardt, K. Fahmy, E. Grosse, B. Kämpfer,
C. Schneidereit, A. Wagner, R. Wünsch



**Forschungszentrum
Rossendorf**

Cover Picture:

The Brewster-angle-microscopic image of a DNA film of $\approx 1 \mu\text{m}$ thickness on ZnSe is shown. The central area of $40 \mu\text{m}$ diameter was exposed to IR-FEL macropulses at a wavelength of $9 \mu\text{m}$ that is absorbed by the chemical groups of the DNA backbone. Structural transitions induced by the picosecond micropulses at a repetition rate of 13 MHz accumulate during the $400 \mu\text{s}$ long macropulse causing an almost linear increase in reflectivity. After the macropulse, the relaxation of the DNA structure proceeds on a ms time scale. Both phases carry information on the kinetics of the fundamental process of base pair opening and closing, respectively, involved in the vital functions of gene expression and DNA replication.

Explanation of special symbols:

The letters given in parentheses in the following text and used as superscripts in the titles of the scientific contributions do express our grateful acknowledgement to the funding, sponsoring or grants provided by several institutions.

Research projects were funded by the Federal Ministry of Education and Research BMBF (B), by the Saxon Ministry of Education and Arts SMWK (S), by the German Research Foundation DFG (D), by the German Academic Exchange Service DAAD (A), by the European Commission (E), by the GSI Darmstadt (G), by the FZ Jülich (J), and by the special program HSP III (H) or were sponsored within Scientific agreements with eastern European countries (W).

All rights reserved.

Typeset using T_EX©

Contents

Page

<i>Preface</i>	1
Structure of Matter: Subatomic Physics	3
Hadrons in the Early Universe Prior to Nucleosynthesis M. Bluhm, B. Kämpfer	5
Primordial Nucleosynthesis: Impact of the Reaction $pn \leftrightarrow D\gamma$ W. Wustmann, B. Kämpfer	6
Test Measurement of the Photodisintegration of the Deuteron R. Beyer, E. Grosse, A.R. Junghans, J. Klug, G. Rusev, A. Wagner	7
Photodisintegration of the p- Nucleus ^{92}Mo M. Erhard, E. Grosse, A.R. Junghans, J. Klug, K. Kosev, C. Nair et al.	8
Determination of the Total Dipole Strength in ^{98}Mo and ^{100}Mo G. Rusev, R. Schwengner, M. Erhard, S. Frauendorf, E. Grosse, A.R. Junghans et al.	9
Systematics of Magnetic Dipole Strength in the Stable Even-Mass Mo Isotopes G. Rusev, R. Schwengner, F. Dönau, M. Erhard, S. Frauendorf et al.	10
Statistical Properties of Observed Narrow Resonances in Photon-Scattering Experiments on ^{92}Mo, ^{98}Mo and ^{100}Mo G. Rusev, R. Schwengner, M. Erhard, E. Grosse et al.	11
A Monte Carlo Code for γ-Ray Cascade Simulations in Photon-Induced Reactions G. Rusev, E. Grosse, A.R. Junghans, R. Schwengner, A. Wagner	12
Photon Scattering from the $N = 50$ Nuclei ^{89}Y and ^{90}Zr up to the Neutron-Separation Energies R. Schwengner, N. Benouaret, G. Rusev, E. Grosse et al.	13
First In-Beam MCP Detector Test Measurements K. Kosev, N. Nankov, M. Friedrich, A. Hartmann et al.	14
Energy Distribution of Secondary Electrons by Swift Heavy Ions in Thin Foils N. Nankov, M. Friedrich, A. Hartmann, A.R. Junghans et al.	15
Reconstructing the Secondary Electron Velocity Distribution Using the TOF Method K. Kosev, N. Nankov, M. Friedrich, A. Hartmann et al.	16
Limits of the Time Resolution of the Time-of-Flight Spectrometer for Fission Fragments and Exotic Nuclei N. Nankov, M. Friedrich, A. Hartmann, A.R. Junghans et al.	17
e^+e^- Measurements with HADES F. Dohrmann, E. Grosse, B. Kämpfer, K. Kananki, R. Kotte et al.	18

Dielectron Production in Heavy-Ion Collisions at Relativistic Energies	
H.W. Barz, M. Zétényi, B. Kämpfer, Gy. Wolf	19
Isospin Effects in Virtual Bremsstrahlung	
L.P. Kaptari, B. Kämpfer	20
The $\omega - \pi\gamma^*$ Transition Form Factor	
L.P. Kaptari, B. Kämpfer	21
Evidence for In-Medium Changes of Four-Quark Condensates for ω Mesons	
R. Thomas, S. Zschocke, B. Kämpfer	22
$\omega - \phi$ Production Near Threshold and the OZI Rule	
L.P. Kaptari, B. Kämpfer	23
Study of Λ Production in C + C Reactions at 2 AGeV with the HADES Spectrometer	
K. Kanaki, F. Dohrmann, E. Grosse, B. Kämpfer, R. Kotte et al.	24
Investigation of K^+ Meson Production in C + C Reactions at 2 AGeV with HADES	
A. Sadovsky, R. Kotte, F. Dohrmann, E. Grosse, B. Kämpfer et al.	25
Inclusive K^\pm Production in Proton-Nucleus Collisions near Threshold	
W. Scheinast, F. Dohrmann, L. Naumann, E. Grosse et al.	26
Effect of K^* Exchange on Azimuthal Asymmetry for Pentaquark Production in pp Collisions	
H.W. Barz, M. Zétényi	27
Coherent Photo-Excitation of Θ^+	
A.I. Titov, B. Kämpfer, S. Date, Y. Ohashi	28
Chemical Freeze-Out in Relativistic Heavy Ion Collisions	
J. Cleymans, B. Kämpfer, N. Xu, S.M. Wheaton, M. Kaneta	29
Critical End Point Effects on the QCD Equation of State	
M. Bluhm, B. Kämpfer	30
Baryon Number Fluctuations for $N_f = 2$ QCD in a Quasi-Particle Model	
M. Bluhm, B. Kämpfer, R. Schulze	31
Imaging the Proton Emission Source in Central Al + Al Collisions at 1.9 A·GeV	
R. Kotte for the FOPI Collab.	32
Particle Production in Antiproton-Proton Interactions	
R. Kliemt, K.T. Brinkmann, H. Müller, R. Jäkel	33
Algebraic Approach to Bare Nucleon Matrix Elements	
S. Zschocke, B. Kämpfer, G. Plunien	34
Impact of Nucleon Mass Shift on the Freeze-Out Process	
S. Zschocke, L. Csernai, E. Molnar, J. Manninen, A. Nyiri	35
Effect of Four-Quark Condensates on In-Medium Nucleon Self-Energies	
R. Thomas, S. Zschocke, B. Kämpfer	36
Implications of Modified Gluon Bremsstrahlung in Charm Stopping	
H. Schade, R. Thomas, B. Kämpfer, G. Barnaföldi	37
Neutron Beam Characteristics, Collimator Design and Detector Simulations for ELBE-nToF	
J. Klug, E. Altstadt, C. Beckert, R. Beyer, H. Freiesleben et al.	38

Development of Neutron-Time-of-Flight Detectors for the Investigation of Astrophysically Relevant (γ,n) Reactions	
R. Beyer, E. Grosse, A. Hartmann, K. Heidel, L. Hutsch et al.	40
Absolute Efficiency Calibration of HPGe Detectors for Photoactivation Experiments	
C. Nair, A.R. Junghans, M. Erhard, E. Grosse, K.D. Schilling et al.	41
Pneumatic Delivery System for Photoactivation Experiments at the Bremsstrahlung Facility at ELBE	
K.D. Schilling, A. Wagner, J. Claußner, M. Sobiella et al.	42
Liquid Nitrogen Filling Control System for Cryogenic Detectors at ELBE	
J. Steiner, A. Wagner, U. Wolf	43
Investigation of the HADES Alignment Quality by Improved Trigger Simulations	
J. Wüstenfeld	44
Studies of a Separator Dipole Magnet for Tagging Experiments for Photon-Induced Transmutation at ELBE	
F. Dohrmann, A. Sytcheva, E. Grosse	45
Testing the Performance of Timing RPC Detectors at ELBE	
R. Kotte, L. Naumann, F. Dohrmann, D. Stach	46
A Straw Tube Based Transition Radiation Tracker for the CBM Experiment at FAIR	
L. Naumann, J. Marzec, V. Peshekhonov, D. Seliverstov et al.	47
Study of the Reaction $pp \rightarrow pp\omega$	
R. Schleichert, S. Trousov, et al. for the ANKE Collaboration	48

Life Sciences:

Biostructures and Radiation

49

FEL-Light-Induced Changes in DNA Observed by Dynamic Brewster Angle Microscopy	
M. Sczepsan, G. Furlinski, D. Wohlfarth, W. Seidel, K. Fahmy	51
Structure and pH-Sensitivity of the Transmembrane Segment 3 of Rhodopsin	
S. Madathil, G. Furlinski, K. Fahmy	52
Photothermal Beam Deflection Spectroscopy on Uranyl Compounds at the Free Electron Laser Facility FELBE	
H. Foerstendorf, K. Heim, W. Seidel, G. Bernhard	53
Selection of FELBE Radiation Pulses Using a Laser-Activated Plasma Switch	
S. Friebel, S. Winnerl, W. Seidel, H. Schneider, M. Helm	54
Single Shot Infrared Ellipsometry with a Free Electron Laser	
M. Gensch, J.S. Lee, W. Seidel et al.	55
The Optical Beamline to the High Magnetic Field Laboratory (HLD)	
R. Wünsch, T. Herrmannsdörfer	56
Mode Conversion in the Partial Waveguide of FEL2	
R. Wünsch, C.A.J. van der Geer	57
Analysis of MLEM and OSEM Reconstruction Algorithms for Different Geometries of PET Scanners	
G. Shakirin, P. Crespo, W. Enghardt	58

First Experiments on In-Beam PET at Hard Photon Beams	
D. Möckel, J. Pawelke, M. Sommer, E. Will, W. Enghardt	59
Experimental Setup of a PET-Scanner for Educational Purposes	
T. Würschig, W. Enghardt	60
Washout studies performed via in-beam PET	
F. Fiedler, M. Sellesk, W. Enghardt	61
Optimum Detector Arrangements for In-Beam PET with Direct Time-of-Flight	
P. Crespo, F. Fiedler, J. Pawelke, G. Shakirin, W. Enghardt	62
Very Low Activity PET Measurements with LSO-Based Positron Tomographs	
P. Crespo, N. Abolmaali, R. Bergmann, E. Will, W. Enghardt	63
Systematic Measurement of Channeling Radiation Yields for Diamond	
W. Wagner, B. Azadegan, J. Pawelke	64
Peak Shape Analysis of Channeling Radiation Spectra	
B. Azadegan, J. Pawelke, W. Wagner	65
Planar Channeling Radiation from 17-34 MeV Electrons in Quartz	
B. Azadegan, W. Wagner, J. Pawelke, L.Sh. Grigoryan	66
Radiation Background Measurement at the ELBE Channeling X-Ray Beam Line	
J. Pawelke, B. Naumann, W. Wagner	67
Optimization of FISH for the Determination of RBE of Soft X-Rays for the Human Mammary Epithelial Cell Line 184A1	
A. Lehnert, E. Lessmann, J. Oswald, J. Pawelke	68
Dosimetric Validation of the Electron Photon Transport Code AMOS	
U. Reichelt, J. Henniger, W. Enghardt	69
Basic Evaluation of the Influence of Tungsten in Cells at Photon Irradiation	
U. Reichelt, W. Enghardt, J. Pawelke	70
Index	71
Publications, Proceedings, Poster, Talks, Teaching Activities, Awards, Calls, Theses, Patents and Workshops	73
Publications	75
Proceedings and Reports	93
Posters at Conferences	96
Talks at Conferences and other Institutes	97
Talks of Visitors	102
Lectures	105
Calls, Awards and Theses	106
Patents and Meetings organized by the IHK	108
Personnel	109
Departments of the IKH	111
Personnel of the IKH	112
Guest Scientists	113

Preface

The *Forschungszentrum Rossendorf (FZR)* at Dresden is a multidisciplinary research center within the *Wissenschafts-Gemeinschaft G. W. Leibniz (WGL)*, one of the German agencies for extra-university research. The center is active in investigations on the structure of matter as well as in the life sciences and in environmental research. The **Institute of Nuclear and Hadron Physics (IKH)** within the FZR avails for its research the coupling of radiation to matter in subatomic dimensions as well as to tissue, to cells, and to their components. Its research in the field of **Subatomic Physics** is part of the FZR-program **Structure of Matter** and its investigations concerning the interaction of **Biostructures and Radiation** contribute to the *Life Science* program of the FZR. In this field the IKH exploits possibilities for transfer and introduction of experimental and theoretical techniques from particle and nuclear physics to projects in radiobiology and biophysics. Much of this kind of interdisciplinary transfer is connected to the Radiation Source *ELBE* at the FZR. With its superconducting accelerator for relativistic electrons this large installation provides photons in the wide wavelength range from fm to mm - i.e. *bremsstrahlung* for the investigation of photonuclear processes, hard X-rays for radiobiological and other studies and infrared light for research on the structural dynamics of biomolecules. The investigation of radiation-induced processes not only dominates the projects in nuclear astrophysics as pursued at *ELBE*, it also is a central theme of the experimental and theoretical research performed by the IKH in close connection to the heavy ion synchrotron *SIS* and the upcoming *FAIR* facility at Darmstadt. *ELBE* also will deliver compact bunches of secondary neutrons and fission fragments; both offer new possibilities in laboratory studies related to the cosmic breeding of the chemical elements thus complementing the astrophysics-motivated studies with *bremsstrahlung* photons.

Several contributions to this Scientific Report describe the progress made in the production of the different kinds of secondary radiation at *ELBE*, the experimental equipment to be installed for their use and the attempts to optimize the experimental conditions with respect to resolution, luminosity and background conditions. Its main aim, however, is to present the research projects of the Institute by several articles each. The experimental conditions at *ELBE* proved to be very favorable for photon-induced processes in the excitation energy range characteristic of the environments relevant to the cosmic element production. This holds for the time shortly after the Big Bang when first nuclei are formed and it is especially so for hot scenarios inside heavy stars accompanying the formation of higher-*Z* elements. As here photodisintegration the "p-process" becomes important, several investigations on electromagnetic dipole strength distributions in various nuclei near $Z=40$ and $N=50$ were performed. Using the photo-activation technique interesting results were obtained for some nuclides with presently unexplained discrepancies to abundance predictions. Photon - or electron - induced fission is of special use as the source of neutron-rich nuclei whose properties are of importance for the detailed understanding of the stellar production of heavy elements. In this field neutron beams in the MeV-range available soon at *ELBE* will play a role as well as in research dedicated to the nuclear physics foundations of transmutation processes proposed in connection with future generations of nuclear power plants.

Hadron physics at the IKH - the other research activity in subatomic physics - studies the strong (nuclear) interaction within the hadronic medium and especially in high density phases of hadronic matter. Experiments observing the consequences of increasing hadron density and

theoretical concepts based thereon are an important ingredient for the understanding of the Big Bang and later high density cosmic scenarios. The IKH is heavily involved in research performed at the high energy heavy-ion accelerators at GSI-FAIR and especially within the international HADES-CBM project. Theoretical studies mainly refer to these experiments but they also touch even higher energies where a phase transition to a quark gluon plasma occurs.

In its second part this Report describes the research in the life sciences, partly performed using nuclear technology. In the past IKH contributed considerably to the field of tumor-conform radiotherapy by employing positron emission tomography. The successful operation of a PET scanner simultaneously to the irradiation of tumors with heavy ion beams considerably improved the reliability and reproducibility of the radiation therapy with fast ions. This in-situ PET as developed at the IKH has been shown to also allow the control of irradiations performed with protons and it may even be used with photons, as shown by first numerical studies. Beams from ELBE have been developed for another interesting field: Quasi-monochromatic X-rays of easily variable energy as produced in electron channeling have been investigated systematically and a strong suppression of the unwanted background continuum was achieved. Thus, a probe for the study of the elementary processes causing radiation-induced cell damage and for other investigations is available now.

Following the conceptual design studies for the free electron laser (FEL) at ELBE including detailed calculations on magnetic undulators for the infrared (IR) and THz regime the biophysics department of the Institute has concentrated on the use of IR radiation in the study of biomolecular dynamics under non-destructive and native-like conditions. Fundamental aspects of the structure and conformational changes of pharmacologically relevant receptor proteins and of DNA play a key role in these investigations up to now performed with IR from other, less favorable sources. Novel approaches using FEL pump and visible probe beams have been established to study the motion of the DNA backbone. A representative result is depicted on the front cover of this Report: Obtained with a thin DNA film it demonstrates the powerful combination of spatial resolution with the time-resolved detection of IR pulse-induced changes of optical properties of DNA.

The interaction between the different fields of research at IKH has led to considerable synergy effects with respect to hardware for performing the experimental investigations as well as in the field of computer simulations needed for their analysis. In these areas the transfer of information and expertise from the large international particle and nuclear physics community to the life sciences has been farther promoted by the IKH. Thus the Institute's various areas of research from laboratory studies on cosmic processes to the interaction of radiation with biostructures have common grounds.

The scientific activities of the institute have benefited from various support. We gratefully acknowledge the close and fruitful collaboration with the Technical University (TU) Dresden and with GSI Darmstadt. These contacts and those to many other scientific institutions in Germany and abroad are of vital importance for the Institute. Specific projects were subsidized by the Federal Ministry for Education and Research (BMBF), the Saxon Ministry for Science and Art (SMWK), FAIR/GSI Darmstadt and Forschungszentrum Jülich. We express our gratitude to them as well as to the Deutsche Forschungsgemeinschaft (DFG) and to the European Union (EU) for the support of several research projects initiated by the Institute.



Structure of Matter:

Nuclear and Hadron Physics

Research in **nuclear physics** at the Forschungszentrum Rossendorf focused on the synthesis of the chemical elements in cosmic processes. Experimental beam time at the superconducting linear accelerator ELBE was devoted to the investigation of interactions of photons with nuclei up to or beyond particle separation energies. Such interactions govern the redistribution of isotopic abundances in cosmic scenarios with high temperatures as a characteristic for the production of many heavy nuclides.

Systematic studies of the electromagnetic response in the region of medium-mass nuclei were performed both experimentally and theoretically. Results of experiments done at ELBE and at the Dynamitron accelerator in Stuttgart, in combination to theoretical developments achieved at the IKH, resulted in publications on the structure of shape isomers and on the distribution of magnetic dipole strength up to the particle separation energies. The study of electromagnetic dipole strength in $^{92,98,100}\text{Mo}$ up to threshold was completed by analyzing the resolved strength in about 300 identified transitions per nucleus and by investigating the unresolved continuum strength on the basis of random matrix formalisms. The methods developed allow for the first time to study the evolution of electromagnetic strength across the particle separation energy which is of crucial importance for astrophysical nuclear network calculations.

Since no contemporary model of explosive nucleosynthesis is able to describe the abundance of the neutron-deficient Mo and Ru isotopes we continued the investigation of disintegration reactions using bremsstrahlung photons at ELBE and Coulomb-dissociation experiments with radioactive beams at GSI. At ELBE, several photo-disintegration reactions on Mo isotopes have been studied by activation measurements over a wide energy range and compared to theoretically predicted cross sections yielding constraints for current and future astrophysical models. In order to access short-lived activities in photo-disintegration reactions a pneumatic delivery system for fast sample transports is being installed.

First experimental tests of time-of-flight detection of neutrons from photo-disintegration of the deuteron showed the capability of the ELBE facility for studies of big-bang nucleosynthesis reactions.

The set-up of a new time-of-flight facility for neutron-induced reactions has progressed with Monte-Carlo simulations, construction, and tests of various components. The collaborative effort between the IKH, the Institute for Safety Research of FZR and the Institute for Nuclear and Particle Physics of TU Dresden led to the design of an effective production facility for pulsed neutron beams to be used for astrophysical and nuclear transmutation experiments.

Hadron physics at the IKH concerns the structure of matter under conditions occurring in the cosmos, i.e. high density and temperature. The research focuses on studies of compressed nuclear matter and on in-medium properties of its constituents. With the complex detector system HADES – comprising 6 very large tracking detectors delivered by the FZR detector laboratory and installed at the heavy-ion synchrotron SIS of GSI Darmstadt – the behavior of vector mesons via their e^+e^- decay channels was investigated in a first series of experiments. The dielectron production is a clean and sensitive probe for changes of meson properties in the nuclear environment. In $C + C$ collisions, studied at 1 and 2 AGeV, some collisional compression occurs, whereas the study of elementary hadron reactions like $p + p$ is aimed at determining "free" η and ω meson production cross sections and form factors.

Similarly to the strangeness production, whose intensive study by the IKH has produced very interesting information on the self-energy of strange hadrons in a hadronic medium and on its

density dependence, the dilepton studies are expected to also have significant impact on nuclear astrophysics and cosmology (i.e. Big Bang) related aspects. In both fields the experimental investigations are intimately connected to theoretical studies performed within the Institute as well as with visitors and theory groups at other places. The theoretical research is mainly done by studying in-medium hadron modifications on the basis of QCD sum rules or effective hadron models, or by adapting the transport model to dielectron processes. Perspective work is devoted to the theory of special probes of very dense nuclear matter.

This is anticipating the starting Compressed Baryonic Matter (CBM) project at the future Facility of Anti-protons and Ion Research (FAIR) in Darmstadt. IKH has joined the CBM project to bring forward the developments needed for the integration of HADES into the upcoming FAIR installations. The development and construction of state-of-the-art detectors as well as their tests at ELBE will be an important aim in the coming years. Here restive plate chambers (RPC's) have been selected to become a major contribution of IKH to FAIR-CBM as well as to FAIR-R³B, an experimental installation for the study of nuclear processes of astrophysical interest.

The regular seminar talks from both the nuclear and the hadron physics departments evidences the close connection of the scientific methods and goals in both fields. The seminar talks are a basic part of the institute's scientific culture, especially intended for the education of diploma and PhD students.

The research in **nuclear physics** has profited from collaborating with groups in the following institutions:

TU Dresden, Inst. for Safety Research of FZR, TU Darmstadt, GSI Darmstadt, Univ. Stuttgart, Univ. Köln, INRNE Sofia (Bulgaria), Univ. of Sofia (Bulgaria), Charles Univ. Prague (Czech Republic), JINR Dubna (Russia), Univ. of Notre Dame (USA), Univ. of Washington at Seattle (USA).

The **hadron physics** results described in this report were obtained in the following international collaborations:

HADES: Univ. Frankfurt, TU München, Univ. Giessen, GSI Darmstadt, FZR, Institute of Physics Bratislava (Slovakia), LNS Catania (Italy), LPC and Univ. Blaise Pascal Clermont (France), Jagellonian Univ. Cracow (Poland), JINR Dubna (Russia), Univ. degli Studi di Milano (Italy), ITEP Moscow (Russia), INR Moscow (Russia), MEPhI Moscow (Russia), Univ. of Cyprus (Cyprus), Institute de Physique Nucleaire d'Orsay (France), Nuclear Physics Institute Rez (Czech Republic), Univ. of Santiago de Compostela (Spain), Univ. of Valencia (Spain).

KaoS: TU Darmstadt, Univ. Frankfurt, Univ. Marburg, GSI Darmstadt, Jagellonian Univ. Cracow (Poland).

We still benefit from previous contributions to other hadron experiments like FOPI, COSY-TOF and COSY-ANKE, which are continuously delivering interesting results; some data mentioned in this report stem from these.

Hadrons in the Early Universe Prior to Nucleosynthesis

M. BLUHM, B. KÄMPFER

The evolution of matter in a homogeneous and isotropic world model is governed by Friedmann's equations

$$\dot{e} = -3\mathcal{C}(e+p)\sqrt{e}, \quad (1)$$

$$\dot{R} = \mathcal{C}R\sqrt{e}, \quad (2)$$

where e denotes the energy density, p is the pressure, R stands for the scale factor, and the dynamical scale is determined by $\mathcal{C} = \frac{1}{M_{Pl}}\sqrt{\frac{8\pi}{3}}$ with M_{Pl} being the Planck mass. These equations are to be supplemented by the conservation of baryon charge, $R^3 n_B = const$, and entropy conservation, $R^3 s = const$. Here, n_B is the baryon density and s the entropy density. To integrate this system of coupled equations one needs an equation of state, say in the form $p(T, \mu_B)$, i.e. the pressure as a function of temperature T and chemical potential μ_B . From $e + p - Ts = \mu_B n_B$, $s = \partial p / \partial T$ and $n_B = \partial p / \partial \mu_B$ all needed quantities follow.

Lattice QCD calculations have proven that a resonance gas model with many excited hadron states is presumably appropriate for the equation of state of strongly interacting matter. A sizeable part of strong interactions is thereby encoded in the resonances. The equation of state must be supplemented by the photon, neutrino, electron and muon components.

Given the observed tiny asymmetry of baryons to antibaryons, as described by the ratio of baryons and photons, $\eta = n_B/n_\gamma \approx 6 \times 10^{-10}$, one can follow the evolution of the energy densities of various components. In Fig. 1, the energy densities of nucleons, kaons, pions and the total of photons, neutrinos, electrons and muons as well are exhibited. Remarkable is the abrupt change of the scaled nucleon energy density in the temperature interval 40-30 MeV. (We follow the time arrow, i.e. the temperature drops with elapsing time). This is the stage where the previously tiny baryon-anti-baryon asymmetry is changed rapidly in a clear dominance of baryons, due to cooling; the anti-baryons (which follow the baryons down to 40 MeV and then continue to drop) are annihilated away and just the surplus of baryons survives, constituting the present hard core of visible matter in the universe. At this stage, the chemical potential strongly increases, driven by baryon conservation, from about 1 eV (after cosmic confinement) towards 1 GeV (prior to nucleosynthesis) [1]. The scaled nucleon energy density afterwards slowly increases (relative to the scaled energy density of relativistic matter residing in γ , e^\pm and ν 's). After a long time interval (far outside the scale displayed

here) the nucleon energy density meets the energy density of relativistic matter – this is the stage where the universe changes from a radiation dominated era to a matter dominated era.

As second interesting point we emphasize the strong and unexpectedly long-lasting dominance of pions over nucleons which ceases just prior to nucleosynthesis below 1 MeV. The value of η determines the position of the crossing of pion and nucleon energy densities. Within the presently accepted range of values of η it appears unlikely that the pion component could influence the nucleosynthesis [2].

As the temperature in the expanding and cooling universe drops below the mass of a certain particle species, its respective number and energy densities become exponentially suppressed. This is schematically shown in Fig. 1 for the relativistic matter component: We have taken out pions or muons in the energy density when the temperature falls below m_π or m_μ to highlight such an effect. (Due to entropy conservation, the dropping of temperature would stall for a moment in such a schematic description; this is often considered as "flash" emerging from an annihilating subcomponent, e.g. from $\mu^+ - \mu^-$ annihilation.) Actually, both the energy density (and correspondingly the temperature, too) drops gradually, as shown for the pion component separately.

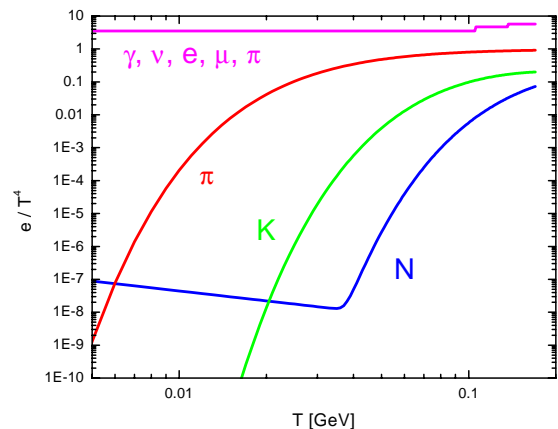


Fig. 1 Energy densities scaled by T^4 as a function of temperature. π : pions, K : kaons, N : nucleons (without anti-nucleons), relativistic matter includes photons (γ), electrons and positrons (e^\pm), all three neutrino species (ν), muons (μ) and pions, the latter both ones only up to temperatures corresponding to the respective rest masses. For $\eta = 10^{-10}$.

[1] B. Kämpfer, M. Bluhm, J. Phys. G 31 (2005) S1141

[2] M. Bluhm, B. Kämpfer, G. Soff, J. Phys. G 31 (2005) S1151

Primordial Nucleosynthesis: Impact of the Reaction $pn \leftrightarrow D\gamma$

W. WUSTMANN,¹ B. KÄMPFER

The recently released WMAP data constrain the present day ratio $\eta = n_B/n_\gamma$ to a narrow interval around 6×10^{-10} thus relating the baryon density n_B and photon density n_γ . Since η is an important cosmological parameter which is thought to be conserved during the evolution of the universe it represents a link to early stages after the Big Bang. During the primordial nucleosynthesis (hereafter called Big Bang Nucleosynthesis and abbreviated by BBN) the light elements ^2H (=D), ^3He , ^4He , and ^7Li have been synthesized and their abundances are fairly precisely measured. It turns out that the calculated BBN results depend also on η . A sensible test of the cosmological concordance model is, therefore, accomplished by an agreement of η inferred from a comparison of BBN data and calculations and WMAP data. This links cosmic stages at $1 - 10^3$ sec (BBN) with 300000 years (microwave decoupling, quantified, e.g., by WMAP measurements) and present day observations at a world age of 13 billion years. Tensions would signal a lacking understanding of either microscopic particle and nuclear processes or of the macroscopic evolutionary Friedmann model (general relativity) or give some hints to "new physics" beyond the standard model of particle physics, like extra dimensions, a zoo of new (not yet observed) particles, time variation of natural "constants" etc.

It is tempting to reconsider the impact of various nuclear reactions on the BBN results before checking the compatibility of η_{BBN} and η_{WMAP} . It turns out that the data base for the reaction $pn \leftrightarrow D\gamma$ is particularly poor. In Fig. 1, the R factor $R = N_A \sqrt{\frac{2T_{cms}}{\mu_{np}}} \sigma(T_{cms})$ is exhibited (N_A is Avogadro's number, μ_{np} stands for the reduced mass; the cross sections $\sigma^{pn \rightarrow D\gamma}$ and $\sigma^{\gamma D \rightarrow pn}$ are related by $\sigma^{np \rightarrow D\gamma}(s) = \frac{3}{2} \frac{\lambda(s, 0, m_D^2)}{\lambda(s, m_n^2, m_p^2)} \sigma^{\gamma D \rightarrow np}(s)$, where λ is the kinematical triangle function and s denotes the invariant mass of the $2 \leftrightarrow 2$ reactions obeying the relations $T_{cms} = \sqrt{s} - m_n - m_p$, $s = m_D(m_D + 2E_\gamma)$ with $m_{D,p,n}$ denoting the masses of deuteron, proton and neutron, respectively).

We have studied the impact of these cross sections on the abundance of the mentioned light primordial elements by employing a publicly available nuclear reaction net work. In doing so we constructed a sensitivity function by (i) reducing the standard SKM parametrization [3] of $\sigma^{pn \rightarrow D\gamma}$ by 30% in a narrow interval of T_{cms} , (ii) calculating the reaction rate with a fifth-order polynomial refit, and (iii) running the BBN code with this modified rate. Results are exhibited in Fig. 2. The strongest sensitivity to a modified reaction cross section is found in the interval

$T_{cms} = 20 - 200$ keV. Only the ^7Li abundance is sensitive to a possible change of the cross section which could be caused by new and precise measurements with high statistical significance.

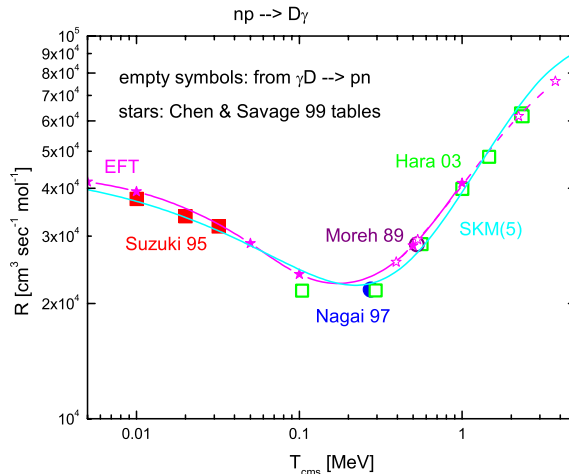


Fig. 1 The astrophysical R factor as a function of the kinetic energy T_{cms} in the pn center of mass system. Data from [1] (error bars suppressed), solid and dashed curves with stars: EFT (2-loop effective field theory [2]), gray curve: SKM fifth-order polynomial parametrization [3].

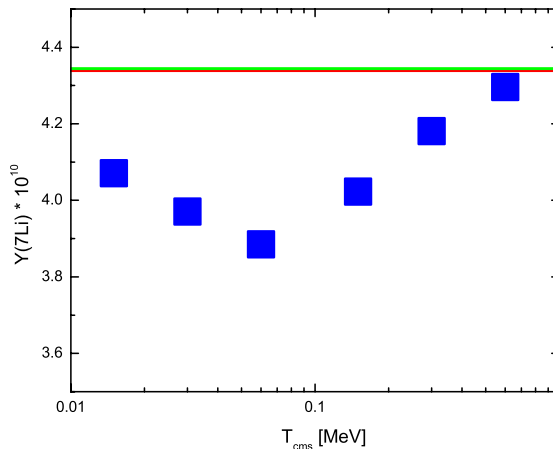


Fig. 2 Sensitivity function (squares) for the scaled ^7Li abundance as a function of T_{cms} . The horizontal lines are for EFT and SKM(5). Calculations are done for $\eta = 6 \times 10^{-10}$.

- [1] R. Moreh, T.J. Kennett, W.V. Prestwich, Phys. Rev. C 39 (1989) 1247; T.S. Suzuki et al. Astrophys. J. Lett. 439 (1995) L59; Y. Nagai et al., Phys. Rev. C 56 (1997) 3173; K.Y. Hara et al., Phys. Rev. D 68 (2003) 072001
- [2] J.W. Chen, M.J. Savage, Phys. Rev. C 60 (1999) 065205
- [3] M.S. Smith, L.H. Kawano, R.A. Malaney, Astrophys. J. Supp. 85 (1993) 219

¹TU Dresden, Institut für Theoretische Physik

Test Measurement of the Photodisintegration of the Deuteron

R. BEYER,¹ E. GROSSE,² A.R. JUNGHANS, J. KLUG, G. RUSEV, R. SCHWENGER, A. WAGNER

The photodisintegration of the deuteron, $d(\gamma,n)p$, or its inverse reaction $n(p,\gamma)d$ is one key reaction in the network of the Big Bang nucleosynthesis [1]. It is the first step in the buildup of complex nuclei. There are several theoretical investigations dealing with this reaction and a wealth of experimental data exists, see Fig. 1.

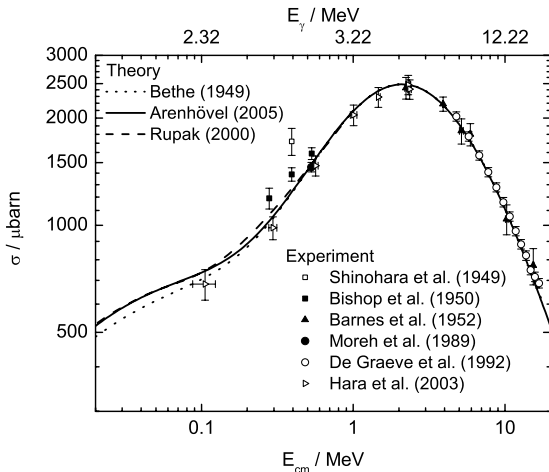


Fig. 1 Theoretical and experimental data on the $d(\gamma,n)p$ cross section. All references can be found in [2].

In the astrophysically relevant energy range from 30 to 130 keV [1], the theoretical calculations as well as the experimental data differ significantly. Especially in this energy region there exists only one experimental data point showing a need of more and precise measurements at this energies. Development of adequate neutron detectors is in progress [3] and test measurements have been done at the bremsstrahlung facility at the ELBE accelerator [4].

Targets of 5 g deuterated polyethylene (CD_2) and of 5 g polyethylene (CH_2) were irradiated by bremsstrahlung photons about 6 hours each. At the same time a target of 5 g ^{11}B was irradiated to determine the photon flux.

The electron beam of 5.5 MeV kinetic energy was employed to reduce the beam-induced neutron background, by staying below the neutron separation energy of every surrounding material. The reduction of the pulse repetition rate to 1.6 MHz caused a reduction of the average beam current to $90 \mu A$ but prevented overlapping time-of-flight spectra from adjacent beam pulses.

To determine the photon flux, the scattered photons from ^{11}B were measured with a HPGe detector. From the count rate in the ^{11}B transitions in the photon-energy spectrum one can calculate the incoming pho-

ton flux Φ_γ using

$$\Phi_\gamma(E_\gamma) = \frac{A_{Peak}}{\varepsilon_\gamma \cdot T_{live} \cdot I_S \cdot N_B \cdot W} \quad (1)$$

Here A_{Peak} is the number of counts in the ^{11}B transition, ε_γ is the efficiency of the HPGe detector, T_{live} is the dead-time-corrected measurement time, I_S is the integrated cross section, N_B the number of ^{11}B nuclei, and W is the angular correlation coefficient. The CH_2 time-of-flight spectrum was normalized to the CD_2 spectrum, using the respective photon fluxes, and subtracted as background from the CD_2 spectrum. From the resulting spectrum one can determine the differential $d(\gamma,n)p$ cross section $\frac{d\sigma}{d\Omega}$ via

$$\frac{d\sigma}{d\Omega}(E_{cm}) = \frac{\dot{N}_n(E_{cm})}{\Phi_\gamma(E_{cm}) \cdot \varepsilon_n \cdot N_D \cdot \Omega} \quad (2)$$

Here $\dot{N}_n(E_{cm})$ is the neutron count rate, $\Phi_\gamma(E_{cm})$ is the incoming bremsstrahlung spectrum, ε_n is the neutron detection efficiency, N_D is the number of target nuclei and Ω is the solid angle of the detector.

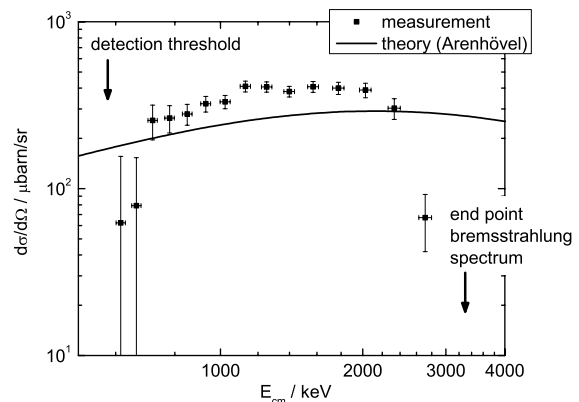


Fig. 2 Differential cross section of $d(\gamma,n)p$ (symbols).

The result is shown in Fig. 2, where the error bars represent the statistic uncertainties only. The systematic uncertainty is in the order of 100% and is mainly caused by the bad signal-to-background ratio, the uncertainty of the absolute normalization of the photon flux, the uncertainty in the end point energy of the bremsstrahlung spectrum, and the uncertainty of the neutron detectors efficiencies. Investigations to minimize these uncertainties are in progress.

- [1] S. Burles, K.M. Nollet, Phys. Rev. Lett. 82 (1999) 4176
- [2] R. Beyer, Diplomarbeit (2005)
- [3] R. Beyer et al., this report, p. 40
- [4] R. Schwengner, R. Beyer et al., NIM A 555 (2005) 211

¹also Friedrich-Schiller-Universität Jena

²also TU Dresden

Photodisintegration of the p -Nucleus ^{92}Mo

M. ERHARD, E. GROSSE,¹ A.R. JUNGHANS, J. KLUG, K. KOSEV, C. NAIR, N. NANKOV, G. RUSEV, K.D. SCHILLING, R. SCHWENGER, A. WAGNER

35 neutron deficient stable isotopes between Se and Hg are shielded from the rapid neutron-capture process by stable isobars and bypassed by the slow neutron-capture process. They are called p -(process) nuclei and they are believed to be produced in chains of photodisintegration reactions on heavy seed nuclei in a supernova explosion [1]. In many network calculations of the p -process nucleosynthesis, Mo and Ru isotopes are produced with lower abundance than determined experimentally. Therefore we tested the photodisintegration rates of ^{92}Mo to improve the nuclear physics input to the network calculations [3].

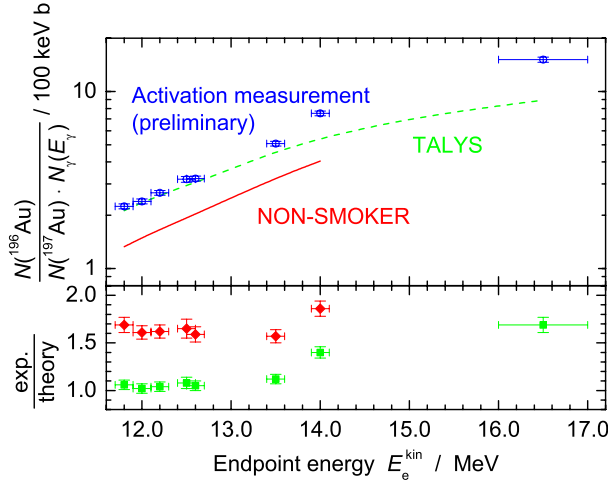


Fig. 1 Preliminary results for the activation yield of the $^{197}\text{Au}(\gamma, n)^{196}\text{Au}$ reaction with Au targets irradiated at the NRF target site. The experimental yield is normalized to the number of ^{197}Au atoms and to the absolute photon flux. The data are compared to yield integrals computed with the cross sections from TALYS [4] (dashed line) and NON-SMOKER [5] (full line) using the same absolute photon flux.

Photoactivation is a two-step experiment which is split up into the activation and the decay measurement. The targets are activated with bremsstrahlung at ELBE at the nuclear-resonance-fluorescence (NRF) measurement site and in the electron beam dump, respectively. The former is used to determine the absolute photon flux in a NRF measurement with transitions from an enriched ^{11}B target, the latter has a 50 to 100 times higher photon flux and serves to activate the p -process target (e.g. $^{\text{nat}}\text{Mo}$) [2]. At both irradiation sites, the photodisintegration of gold ($^{197}\text{Au}(\gamma, n)^{196}\text{Au}$) is used as calibration reaction to quantify the photon flux in the beam dump. The γ -rays following the β -decay of the activated targets were measured with high-purity-germanium detectors (HPGe, 100, 90, or 60 % efficiency relative to

$3'' \times 3''$ NaI) situated in a lead castle to shield it from background radiation. From the full-energy-peak of prominent transitions the yield integral was derived in dependence of the electron beam energy. Fig. 1 shows a comparison with the integral of photon flux times disintegration cross section, as taken from model calculations. Yield integrals calculated with the photodisintegration cross sections using the TALYS and the NON-SMOKER code, are represented by the dashed and full lines respectively.

To compare theory and experiment (Fig. 2), the measured reaction yield integrals of the $^{\text{nat}}\text{Mo}$ target were normalized with the relative yield integral of the $^{197}\text{Au}(\gamma, n)$ reaction. The effect of different target masses is taken into account. The similarity of the relative data shown in Fig. 2 as compared to the NON-SMOKER data suggest already that the predicted underproduction of Mo/Ru isotopes might not be due to wrong photodisintegration rates. Absolute cross section data currently under analysis will allow to draw a firm conclusion.

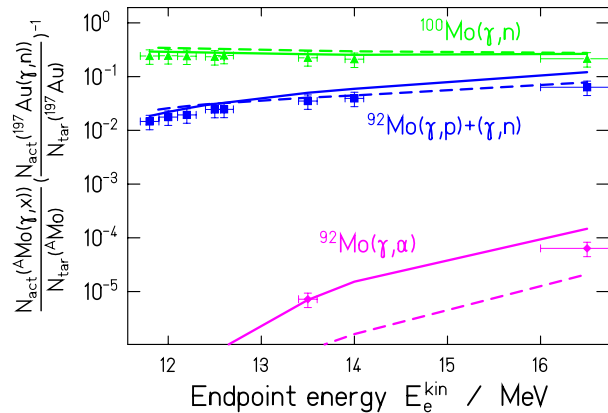


Fig. 2 Measured activation yields for different Mo isotopes as a function of the bremsstrahlung endpoint energy. The data are normalized to the activation yield of $^{197}\text{Au}(\gamma, n)$ irradiated simultaneously. The symbols denote the experimental yields of $^{100}\text{Mo}(\gamma, n)$ (triangles), $^{92}\text{Mo}(\gamma, p/n)$ (squares), and $^{92}\text{Mo}(\gamma, \alpha)$ (diamonds). (Dashed) lines show results from TALYS [4] (NON-SMOKER [5]) calculations.

- [1] M. Arnould and S. Goriely, Phys. Rep. 384 (2003) 11
- [2] M. Erhard, E. Grosse et al., IKH Annual Report 2004, FZR-423 (2005) 13
- [3] M. Erhard, A.R. Junghans et al., nucl-ex/0512026v1
- [4] A.J. Koning, S. Hillaire, and M.C. Duijvestin, AIP Conference proceedings 769 (2005) 177
- [5] T. Rauscher and F.-K. Thielemann, At. Data and Nucl. Data Tables 88 (2004) 1

¹also TU Dresden

Determination of the Total Dipole Strength in ^{98}Mo and ^{100}Mo ^D

G. RUSEV, R. SCHWENGNER, M. ERHARD, S. FRAUENDORF,¹ E. GROSSE,² A.R. JUNGHANS, K. KOSEV, N. NANKOV, K.D. SCHILLING, A. WAGNER

The response of nuclei to dipole radiation is of importance for the test of nuclear models and is relevant for the nucleosynthesis in hot or explosive scenarios.

We performed photon-scattering experiments on ^{98}Mo and ^{100}Mo with bremsstrahlung [1] at the ELBE accelerator. The electron-beam energy was selected to be $E_e^{\text{kin}} = 13.2\text{MeV}$, above the neutron separation energy of the two isotopes. As was discussed in Ref. [2] the measured spectra do not contain information for all narrow resonances as prominent peaks, many of them are so weak that they are only observed as a continuum. In order to obtain an estimate of the total strength we performed GEANT 3 simulations to determine the spectrum of photons non-resonantly scattered from the target. A comparison between the simulated non-resonant background and the measured spectra is shown in Fig. 1. The measured spectra are corrected for detector response and efficiency, they are also corrected for the (n,γ) intensity from the surrounding materials, which is less than 1% from the resonant γ -rays from the target.

The residuum spectrum from the subtraction of measured and simulated background contains the intensity of ground state transitions as well as branching transitions. We used a code for γ -ray cascade simulations [3] to determine a spectrum of cascade transitions with 100 keV energy bins. Performing such simulations for the whole level schemes of ^{98}Mo and ^{100}Mo enable us to correct the residuum spectrum in Fig. 1 for branching and feeding transitions. The corrected spectrum contains the intensities of the transitions to the ground state which are proportional to the cross section for elastic scattering $\sigma_{\gamma\gamma}^0$. The relation $\sigma_{\gamma}^{\text{abs}} = \sigma_{\gamma\gamma}^0/B_0$ [4] was used to calculate the absorption cross section $\sigma_{\gamma}^{\text{abs}}$, where an average branching ratio B_0 was obtained from the output of the γ -ray cascade simulations. The determined photon absorption cross sections are compared in Fig. 2 with the results from (γ,n) experiments on ^{98}Mo and ^{100}Mo [5]. Apparently the data match properly.

The method presented here allows for the determination of the total strength from photon-scattering experiments and the extension of the available data for the photo absorption cross section from (γ,n) reactions to energies below the neutron separation energy.

- [1] R. Schwengner, R. Beyer et al., Nucl. Instr. Meth. A 555 (2005) 211
- [2] G. Rusev, R. Schwengner et al., this report, p. 11
- [3] G. Rusev, E. Grosse et al., this report, p. 12
- [4] F. Metzger, Prog. in Nucl. Phys. 7 (1959) 54
- [5] H. Beil, R. Bergère et al., Nucl. Phys. A227 (1974) 427

¹also University of Notre Dame, USA

²also TU Dresden

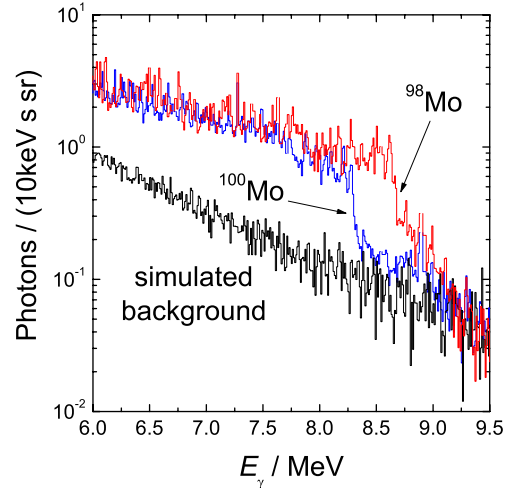


Fig. 1 Comparison between the measured spectra from ^{98}Mo and ^{100}Mo and non-resonant background simulated with GEANT 3.

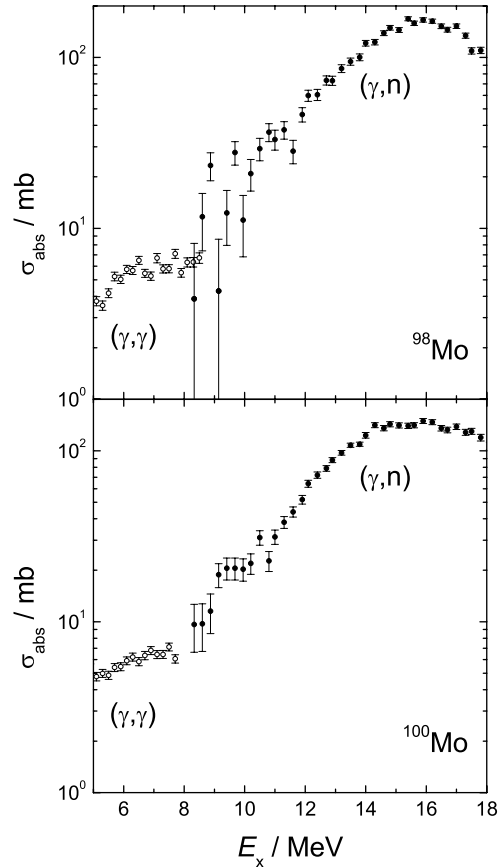


Fig. 2 Comparison of the absorption cross section determined from our photon-scattering experiments (open circles) with results from (γ,n) experiments on ^{98}Mo and ^{100}Mo [5] (filled circles).

Systematics of Magnetic Dipole Strength in the Stable Even-Mass Mo Isotopes^D

G. RUSEV, R. SCHWENGNER, F. DÖNAU, M. ERHARD, S. FRAUENDORF,¹ E. GROSSE,² A.R. JUNGHANS, L. KÄUBLER, K. KOSEV, L. KOSTOV,³ S. MALLION, K.D. SCHILLING, A. WAGNER, H. VON GARREL,⁴ U. KNEISSL,⁴ C. KOHSTALL,⁴ M. KREUTZ,⁴ H. H. PITZ,⁴ M. SCHECK,⁴ F. STEDILE,⁴ P. VON BRENTANO,⁵ J. JOLIE,⁵ A. LINNEMANN,⁵ N. PIETRALLA,⁶ V. WERNER⁷

The origin and strength of magnetic-dipole ($M1$) radiation in nuclei has been the subject of various experimental and theoretical investigations. Generally, large $M1$ strength is generated by spin-flip transitions or by a recoupling of the spins in few-particle multiplets. In nearly spherical nuclei, 1^+ states with large $B(M1, 0^+ \rightarrow 1^+)$ values were described as two-phonon states with mixed proton-neutron symmetry [1]. In deformed nuclei, an isovector mode representing rotational oscillations of protons against neutrons was predicted [2] and observed [3] as a group of 1^+ states with energies around 3 MeV.

The isotopic chain of stable even molybdenum isotopes offers the possibility to study the behavior of $M1$ strength simultaneously with increasing neutron number and the onset of deformation. We have studied the nuclides ^{92}Mo , ^{98}Mo and ^{100}Mo in photon-scattering experiments. The nuclide ^{92}Mo was investigated using the bremsstrahlung facility at the ELBE accelerator [4] at an electron energy of 6 MeV. The nuclides ^{98}Mo and ^{100}Mo were studied at the Dynamitron accelerator of the University of Stuttgart at various energies up to 3.8 MeV [5]. Transition strengths were deduced from intensities of ground-state and branching transitions. The cumulative $M1$ strengths of the even Mo isotopes from ^{92}Mo to ^{100}Mo up to an excitation energy of 4 MeV are shown in Fig. 1. The data included for ^{94}Mo and ^{96}Mo were taken from Refs. [6] and [7], respectively. Positive parity was assumed for all $J = 1$ states found up to 4 MeV in ^{98}Mo and ^{100}Mo .

The experimental $M1$ strengths have been compared with predictions of quasiparticle-random-phase-approximation (QRPA) calculations in a Nilsson-like deformed basis [8]. The hamiltonian used for the description of 1^+ states includes the Nilsson mean-field plus monopole pairing at the particular deformation and interaction terms composed of the isoscalar and isovector parts of the total angular momentum operator and the spin operator. The results of the calculations are compared with the experimental values in Fig. 1. The calculated total strengths up to 4 MeV are somewhat below the experimental values, but the increase of the total strength and its fragmentation with increasing neutron number is in agreement with the

experiment. This tendency is caused by the increasing deformation. The large strength observed in ^{94}Mo is mainly caused by a two-phonon state which cannot be treated in the present QRPA calculations.

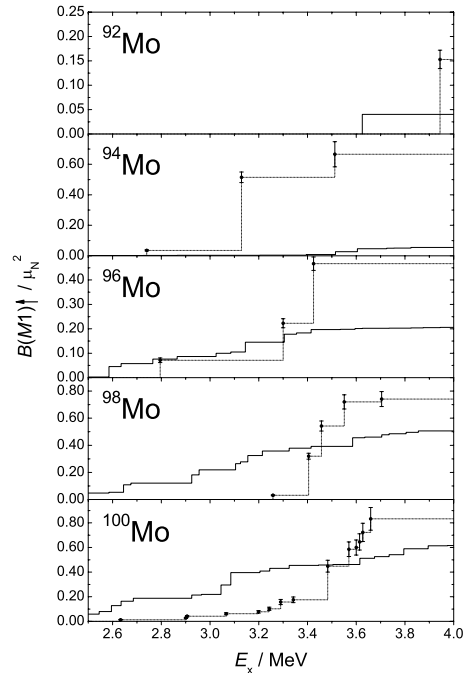


Fig. 1 Cumulative $M1$ -strengths in stable even-mass Mo isotopes. Experimental values are given as circles with dotted lines. The results of the QRPA calculations are shown as solid lines.

- [1] N. Pietralla, C. Fransen et al., Phys. Rev. Lett. 83 (1999) 1303
- [2] N. Lo Iudice and F. Palumbo, Phys. Rev. Lett. 41 (1978) 1532
- [3] A. Richter, Prog. Part. Nucl. Phys. 34 (1995) 261
- [4] R. Schwengner, R. Beyer et al., Nucl. Instr. Meth. A 555 (2005) 211
- [5] G. Rusev, R. Schwengner et al., Phys. Rev. Lett. 95 (2005) 062501
- [6] C. Fransen, N. Pietralla et al., Phys. Rev. C 67 (2003) 024307
- [7] C. Fransen, N. Pietralla et al., Phys. Rev. C 70 (2004) 044317
- [8] F. Döna, Phys. Rev. Lett. 94 (2005) 092503

¹also University of Notre Dame, USA

²also TU Dresden

³INRNE Sofia, Bulgaria

⁴Institut für Strahlenphysik, Universität Stuttgart, 70569 Stuttgart, Germany

⁵Institut für Kernphysik, Universität Köln, 50937 Köln, Germany

⁶Nuclear Structure Laboratory, Dept. of Physics & Astronomy, SUNY, Stony Brook, NY 11794-3800, USA

⁷Wright Nuclear Structure Laboratory, Yale University, New Haven, CT 06520-8124, USA

Statistical Properties of Observed Narrow Resonances in Photon-Scattering Experiments on ^{92}Mo , ^{98}Mo and $^{100}\text{Mo}^{\text{D}}$

G. RUSEV, R. SCHWENGER, M. ERHARD, S. FRAUENDORF,¹ E. GROSSE,² A.R. JUNGHANS, K. KOSEV, K.D. SCHILLING, A. WAGNER

The random matrix treatment of the nucleus as a system of interacting fermions predicts distributions of the level spacings and of the level widths. The level spacings distribution is a measure for the fluctuations of the level distances around a uniform (equidistant) level scheme. This distribution has two extremes of no level repulsion - the Poisson distribution and of strong repulsion - the Wigner one. The level widths show fluctuations around an average value Γ as well. If the amplitudes of the transition matrix elements are assumed to form Gaussian ensemble, then the width distribution is well described by a χ^2 distribution with zero degree of freedom, known as Porter-Thomas distribution [1].

These distributions are evident of thermal neutron-scattering experiments right at the neutron separation energy and by results of β -decay spectroscopy in the range close to the ground state. The photon-scattering experiments performed with continuum bremsstrahlung allow a simultaneous excitation of all levels with spin $J = 1$ and they are a good tool to investigate the statistical properties of the nuclear levels in the intermediate excitation range. The analysis suffers from unresolved branchings which appear at the low energy part of the spectrum and the insufficient resolution to resolve all resonances at high energy close to the neutron threshold.

We performed photon-scattering experiments on ^{92}Mo , ^{98}Mo and ^{100}Mo with bremsstrahlung with an end-point energy of 13.2 MeV, well above the neutron separation energy of all investigated isotopes. In the analysis of the statistical properties of the isolated resonances we selected a range from $E_\gamma = 4$ MeV to the neutron threshold in order to remove most of the branching transitions. The resonances were collected in groups of 50 transitions according to their energy. An average spacing and average width was determined for each group and a histogram was created. The histograms of the individual groups were averaged, and are presented in Figs. 1 and 2.

To obtain an estimate of the possible corrections necessary to account for the incorrect interpretation of non-ground-state transition energies as level energies and for not observed transitions we have performed respective Monte Carlo simulations [2] of level sequences describing a Wigner or a Poisson case. Only a small distortion is caused, when the transition energies resulting from these simulations are treated as level energies. In any case, our Mo data do closely resemble Wigner and Porter-Thomas distributions indicating a quantum chaotic behavior as predicted for Gaussian orthogonal ensemble.

- [1] C.E. Porter, R.G. Thomas, Phys. Rev. 104 (1956) 483
 [2] G. Rusev, E. Grosse et al., this report, p. 12

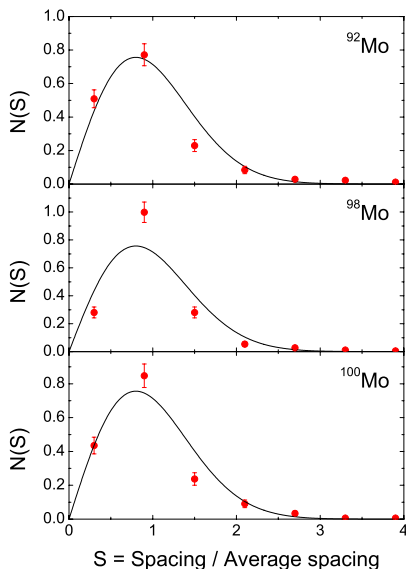


Fig. 1 Nearest neighbor level distributions of isolated narrow resonances above 4 MeV. The drawn lines represent a Wigner distribution.

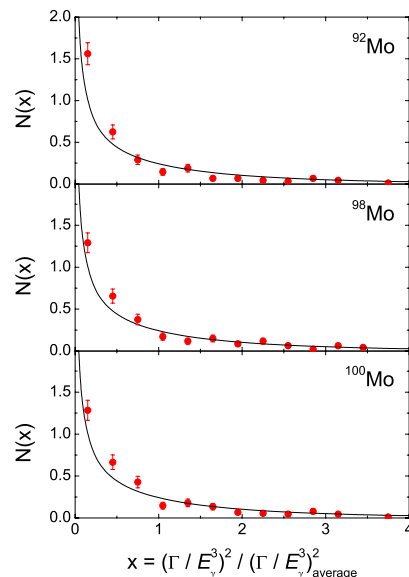


Fig. 2 Distribution of the transition widths of isolated narrow resonances above 4 MeV, all reduced by the phase space factor E_γ^3 . The drawn lines depict the Porter-Thomas distribution.

¹also University of Notre Dame, USA

²also TU Dresden

A Monte Carlo Code for γ -Ray Cascade Simulations in Photon-Induced Reactions^D

G. RUSEV, E. GROSSE,¹ A. R. JUNGHANS, R. SCHWENGER, A. WAGNER

Photon-induced reactions are considered to pass through a compound nucleus with a cross section proportional to the product of the excitation width Γ_0 and the decay width Γ_f . Once excited by the absorption of a real photon, the level can decay by emission of a γ -ray or a particle. The total absorption cross section becomes a superposition of the cross sections of all possible channels of the reaction: $\sigma \sim \sum \sigma_f$, $\sigma_f \sim \Gamma_0 \Gamma_f / \Gamma$, $\Gamma = \sum \Gamma_f$. The probability for de-excitation of a given level by a γ -ray transition to the ground state, to an intermediate state, or by emission of a particle may be comparable. A Monte Carlo program for the simulation of γ -ray cascades was developed as a tool in the analysis of photon-scattering and photo-dissociation experiments.

The program is based on the nuclear statistical model. A level scheme of a nucleus is created according to the back-shifted Fermi gas model, containing levels with spin $J = 0, 1$ and $2 \hbar$. The level density parameter and the back-shift energy are taken from a recent systematics [1]. The level density of states with $J = 1$ is shown in Fig. 1 (a). The Wigner distribution, presented in Fig. 1 (b) is used for the fluctuations of level spacings. A priori known strength functions for $E1$, $M1$ and $E2$ transitions are used to calculate the aver-

age widths of the levels. For the case of molybdenum isotopes, a Lorentzian fit of $\sigma_{\gamma,n}$ data [2] is used for the $E1$ strength function, the $M1$ and $E2$ ones are taken from a global parameterization from the reference input parameter library RIPL-2 [3]. The widths of the individual levels are assigned according to the Porter-Thomas distribution [4] and the average strength functions. Since it is impossible to store the information of all partial decay widths we use the pseudo-random-generator method [5].

In Fig. 1 we present the distributions discussed above compared with results of the simulations for 1000 nuclear realizations. The results of the program are used in the analysis of the photon-scattering experiments at ELBE accelerator to estimate the feeding and branching transitions not observed as prominent peaks in the measured spectra.

- [1] T. von Egidy and D. Bucurescu, Phys. Rev. C83 (2004) 044311
- [2] H. Beil, R. Bergère et al., Nucl. Phys. A227 (1974) 427
- [3] <http://www-nds.iaea/RIPL-2/>
- [4] C.E. Porter and R.G. Thomas, Phys. Rev. 104 (1956) 483
- [5] F. Becvar, Nucl. Instr. Meth. A417 (1998) 434

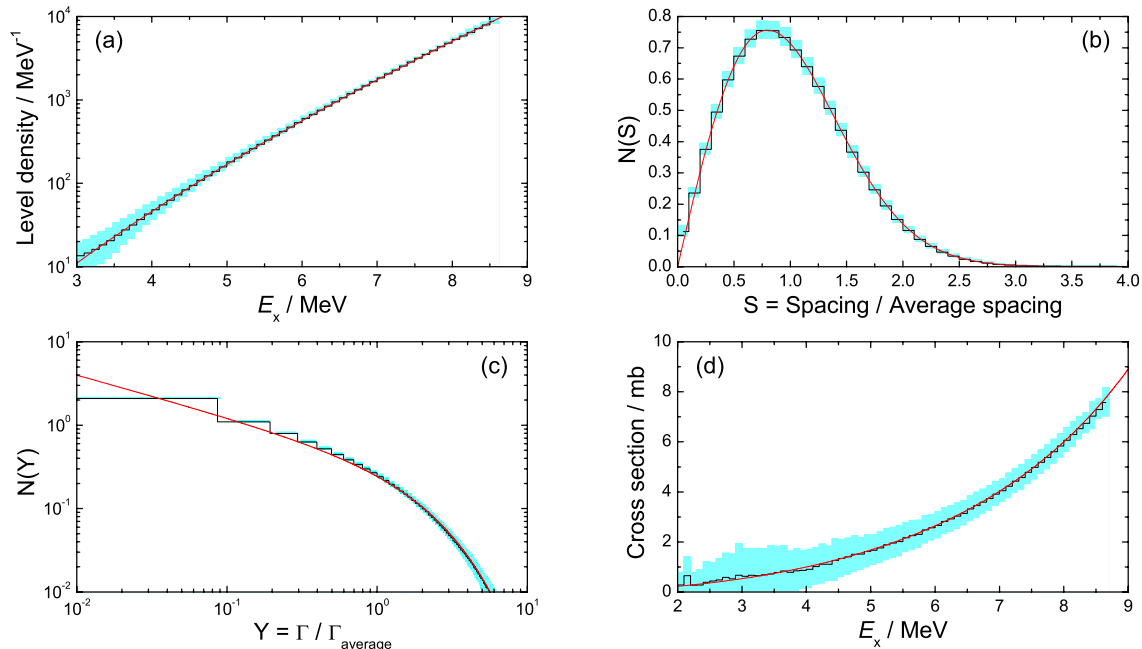


Fig. 1 Comparisons between the distributions included in the program (solid lines) and the mean values of the results of the simulations (histograms) for (a) the level density, (b) the spacings distribution, (c) the widths distribution and (d) the absorption cross section. Hatched areas show the 1σ -variation of the mean values due to fluctuations in the level spacings and widths.

¹also TU Dresden

Photon Scattering from the $N = 50$ Nuclei ^{89}Y and ^{90}Zr up to the Neutron-Separation Energies^D

R. SCHWENGMER, N. BENOURET,¹ G. RUSEV, R. BEYER, M. ERHARD, E. GROSSE,² A.R. JUNGHANS, L. KOSTOV,³
J. KLUG, C. NAIR, K.D. SCHILING, A. WAGNER

The origin and behavior of the dipole strength close to the neutron-separation energies of nuclei is a challenge to the theoretical description of many-body systems and has important implications for astrophysical problems. For example, it influences reaction rates in specific processes of the nucleosynthesis [1]. In order to study the influence of proton number Z and neutron number N , of shell closures and deformation on the dipole-strength distribution we have performed photon-scattering experiments on even-even stable molybdenum isotopes [2, 3, 4] and started to study the chain of stable $N = 50$ nuclei with an experiment on ^{88}Sr [5].

We have continued this study with experiments on the odd-even nucleus ^{89}Y and the even-even ^{90}Zr using the photon-scattering facility at the ELBE accelerator [6]. The experiment on ^{89}Y was carried out with bremsstrahlung produced by an electron beam hitting a niobium radiator of $7\ \mu\text{m}$ thickness. The kinetic energy of the electrons was $13.2\ \text{MeV}$ and the average electron current was $580\ \mu\text{A}$. A $10\ \text{cm}$ thick aluminum absorber was placed behind the radiator in order to reduce the low-energy part of the bremsstrahlung spectrum. The target consisted of $3303.16\ \text{mg}$ of ^{89}Y , combined with $339.5\ \text{mg}$ of ^{11}B used for the calibration of the photon flux. The measuring time was $97\ \text{h}$. The nuclide ^{90}Zr was studied at two different electron energies of 9.0 and $12.8\ \text{MeV}$ during irradiations of 61 and $62\ \text{h}$, respectively. In the experiment at $E_e^{\text{kin}} = 9.0\ \text{MeV}$, a niobium radiator of $4.3\ \mu\text{m}$ thickness was used while at $E_e^{\text{kin}} = 12.8\ \text{MeV}$ the radiator thickness was $7\ \mu\text{m}$. The average current was about $520\ \mu\text{A}$ in the two experiments. The target consisted of $4054.2\ \text{mg}$ $^{90}\text{ZrO}_2$ enriched to 97.7% combined with $339.5\ \text{mg}$ of ^{11}B . Gamma rays were measured with four high-purity germanium detectors of 100% efficiency relative to a $3'' \times 3''$ NaI detector. All detectors were surrounded by escape-suppression shields of bismuth germanate scintillation detectors. Two detectors were placed at 90° relative to the photon-beam direction while the other two were positioned at 127° to deduce angular distributions of the γ rays. Spectra of photons scattered from ^{89}Y at $E_e^{\text{kin}} = 13.2\ \text{MeV}$ and from ^{90}Zr at $E_e^{\text{kin}} = 12.8\ \text{MeV}$ are shown in Fig. 1 and Fig. 2, respectively.

About $200\ \gamma$ transitions were observed in ^{89}Y and ^{90}Zr in the energy range from $5\ \text{MeV}$ to the neutron-separation energies at 11.5 and $12.0\ \text{MeV}$, respectively. The analysis of the γ -ray spectra is in progress. The

dipole-strength distribution to be deduced from the γ -ray intensities will be compared with the dipole-strength distributions of the $N = 50$ isotones ^{88}Sr [5] and ^{92}Mo [3] in order to evaluate the behavior of the $E1$ strength below the giant dipole resonance with changing ratio N/Z in comparison with theoretical predictions.

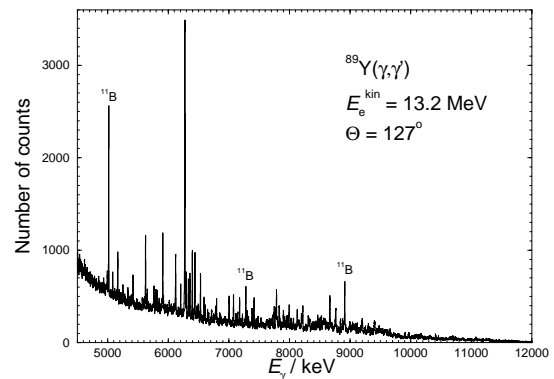


Fig. 1 Part of a spectrum of photons scattered from ^{89}Y at $E_e^{\text{kin}} = 13.2\ \text{MeV}$. The label ^{11}B marks transitions of the calibration standard combined with the target.

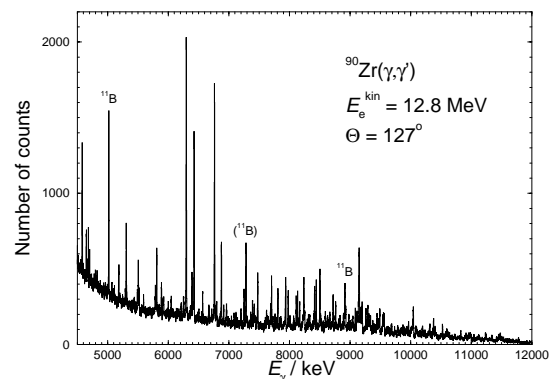


Fig. 2 Part of a spectrum of photons scattered from ^{90}Zr at $E_e^{\text{kin}} = 12.8\ \text{MeV}$. Transitions of the calibration standard are labelled ^{11}B .

- [1] S. Goriely, Phys. Lett. B 436 (1998) 10
- [2] G. Rusev, R. Schwengner et al., Phys. Rev. Lett. 95 (2005) 062501
- [3] G. Rusev, R. Schwengner et al., IKH Annual Report 2003, FZR-401 (2004) 7
- [4] G. Rusev, R. Schwengner et al., this report, p. 11
- [5] R. Schwengner, G. Rusev et al., IKH Annual Report 2004, FZR-423 (2005) 6
- [6] R. Schwengner, R. Beyer et al., Nucl. Instr. Meth. A 555 (2005) 211

¹Permanent address: Université des Sciences et de la Technologie Alger, Algeria

²also TU Dresden

³INRNE Sofia, Bulgaria

First In-Beam MCP Detector Test Measurements^G

K. KOSEV, N. NANKOV,¹ E. GROSSE,² M. FRIEDRICH,³ A. HARTMANN, K. HEIDEL, A.R. JUNGHANS, K.D. SCHILLING, M. SOBIELLA, A. WAGNER

In order to detect fission fragments produced by the high-intensity photon beam from the bremsstrahlung at ELBE, a double time-of-flight spectrometer is constructed. To gain a deeper knowledge of the properties of this spectrometer, extensive experimental investigations have been carried out at the 5 MeV FZR TANDDEM accelerator.

A detector setup consisting of two equal sets of microchannel plate detectors (MCP) with foils, accelerating grids and electrostatic mirrors has been built as depicted in Fig.1. A ³⁵Cl beam passed through an aperture of 500 μm such that the beam current could be reduced to less than 1 pA. A beam monitor Si detector positioned in front of the spectrometer provided us with information about the quality of the beam as demonstrated in Fig.2. The beam particles knocked secondary electrons (SE) out subsequently from the 2 μm and the 5 μm metallised mylar foils. Their thickness was optimized to meet the requirements of low energy and angular spread. The electrons were then accelerated by an electrostatic field of more than 10 kV/cm and afterwards deflected by 90° by an electrostatic mirror before they hit a stack of MCPs with a 2D-position-sensitive delay-line anode[1]. For time reference, which enabled us to obtain the TOF between the two foils positioned at a distance of 27 cm, signals from the back side of the MCP stack were derived (see Fig. 3).

The detector setup was operated inside a vacuum chamber at about 1x10⁻⁷ mbar.

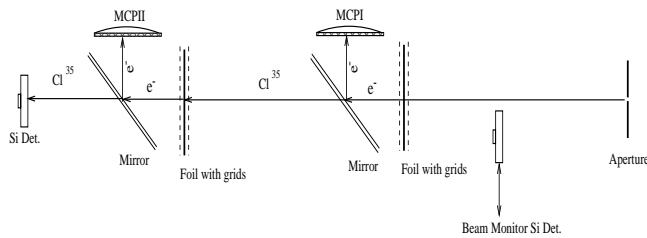


Fig. 1 Experimental setup. The heavy ion beam enters the setup from the right.

A dedicated electronics setup was implemented for these measurements. To process the signals from the MCP, we used inhouse made Constant-Fraction-Discriminators based on the ARC technique with adjustable thresholds down to 3 mV. The time sequence of the signals was measured by a CAEN V775 Time-to-Digital-Converter mod-

ule and recorded by MBS DAQ [2]. Data analysis of the collected data was done by APE [3].

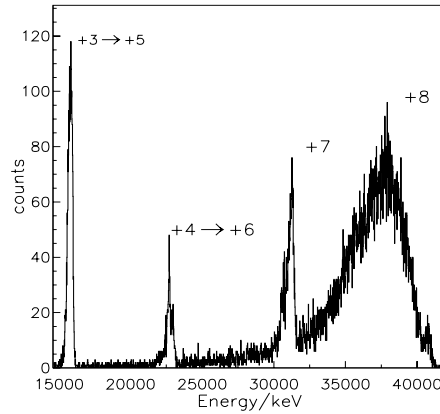


Fig. 2 Energy spectrum of a cocktail ³⁵Cl beam obtained with a 60 μm silicon detector. Several energy peaks correspond to different charge states. Arrows depict charge exchange processes inside the accelerator.

As demonstrated in Fig.3, the energy distribution, corresponding to the different charge states is reflected in the TOF spectrum. It is also obvious that the beam quality reasonably affects the time resolution.

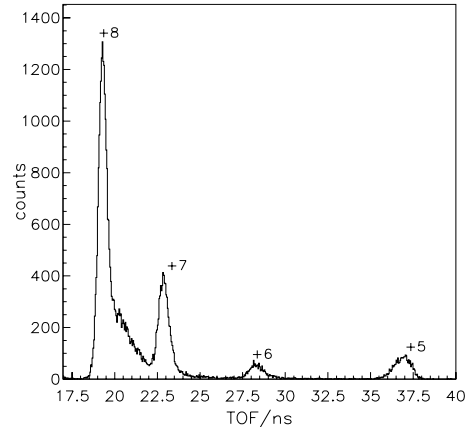


Fig. 3 Obtained TOF spectrum for a foil-foil distance of 27cm.

- [1] K.Kosev et al., IKH Annual Report 2004, FZR-423 (2005) 24
- [2] MBS DAQ, <http://www-w2k.gsi.de/daq>
- [3] APE, <http://www-aix.gsi.de/computing/ape.htm>

¹also INRNE, Sofia, Bulgaria

²also TU Dresden

³FZ Rossendorf, FWI

Energy Distribution of Secondary Electrons by Swift Heavy Ions in Thin Foils^G

N. NANKOV,¹ M. FRIEDRICH,² A. HARTMANN, A.R. JUNGHANS, K. KOSEV, K.D. SCHILLING, A. WAGNER

For the experimental studies of exotic neutron-rich nuclei, produced via bremsstrahlung induced photo-fission, two-dimensional, position-sensitive time-of-flight (TOF) spectrometer has been developed [1]. The energy and the angular distribution of the secondary electrons (SEs) seems to be one of the basic factors limiting the time and the position resolution. For the experimental study of this phenomenon two independent methods were applied. The time-of-flight method is discussed in a separated report [2]. The other method utilizes the transparent properties of the electrostatic mirror. One can show theoretically that the electrostatic mirror will reflect the SEs only if the following condition is satisfied:

$$\frac{\Delta V}{\Delta V_f} \geq 0.5, \quad (1)$$

where ΔV_f and ΔV are the foil acceleration potential between the foil and the grid and the mirror deflection potential. At higher accelerating voltages the mirror will become transparent for the SEs. Indeed such effect was experimentally observed with a good agreement with the above equ. (1). The slope of the efficiency drop in this transparent mode reflects the SEs energy distribution. The efficiency as a function of the accelerating voltage has an error function behavior. Since the standard deviation of this function is the standard deviation of the SEs energy distribution. Because the efficiency drop follows stepless the saturation part of the efficiency curve one can conclude that the slope of the drop is caused only by the energy distribution of the SEs.

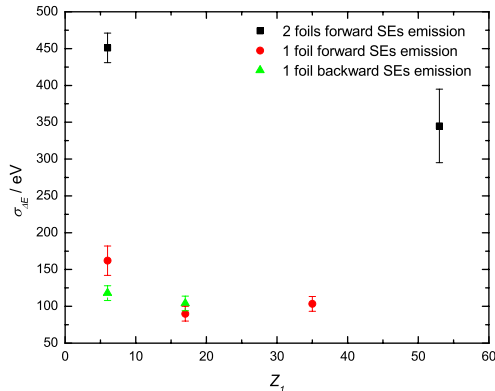


Fig. 1 Widths of the SEs energy distribution for ions with a different atomic number (Z_1), different foil thicknesses and different types of SEs emission (forward and backward).

Using this method the SEs energy distribution for several ion-energy combinations has been measured and

evaluated. Additional measurements with different geometries have been conducted in order to investigate the effect of the foil thickness as well as the difference between forward and backward emitted SEs. The results are shown in Fig. 1. From the ascending slope of the efficiency curve one can derive the transversal SEs energy distribution and hence their angular distribution. Since the longitudinal spread in the SEs energies does not lead to any changes in the efficiency curve at low accelerating voltages the observed slope can be explained only by the transversal momentum spread of the SEs, knocked out from the foil by the ions. With the increasing accelerating voltage this initial transversal energy spread is fully compensated and at some point the efficiency does not change any more. This transition has been also observed as a decrease of the beam spot on the position sensitive anode of the detector. Knowing the transversal energy spread and the longitudinal energy one can determine the angular spread of the SEs. The experimental results are shown in Fig. 2. Measurements with different ions have been made to determine the influence of the foil thickness and the type of the emission (forward and backward).

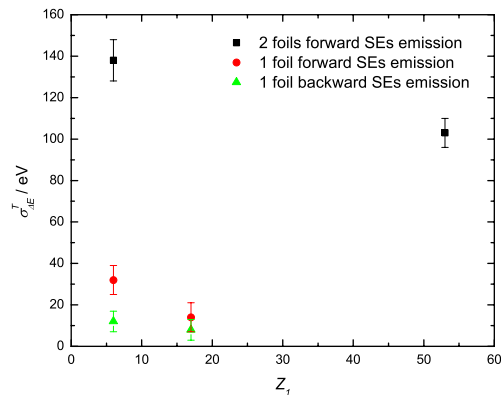


Fig. 2 Widths of the transversal SEs energy distribution for different projectile types, different foil thicknesses and different type of SEs emission (forward or backward).

According to the TOF measurements of the SEs energy distribution the mean SEs energy is in order of 1000 eV for ³⁵Cl ions at 40 MeV. Recalculation to the angular spread gives a value of $\pm 7(3)$ degree.

- [1] N. Nankov, E. Grosse et al., Proc. 3rd Int. Workshop on Nucl. Fission and Fission-Product Spec., Chateau de Cadarache, 2005, p. 357
 [2] K. Kosev, N. Nankov et al., this report, p. 16

¹also INRNE, Sofia, Bulgaria

²FZ Rossendorf, FWI

Reconstructing the Secondary Electron Velocity Distribution Using the TOF Method ^G

K. KOSEV, N. NANKOV,¹ E. GROSSE,² M. FRIEDRICH,³ A. HARTMANN, K. HEIDEL, A.R. JUNGHANS, K.D. SCHILLING, M. SOBIELLA, A. WAGNER

The high-intensity photon beam at ELBE will be used to produce exotic neutron-rich nuclei via bremsstrahlung induced photo-fission. The neutron-rich fragments will then be identified via precise mass and charge determination, using a high resolution double-arm time-of-flight (TOF) spectrometer (see Ref. [1]).

The method is based on the detection of secondary electrons (SE), knocked out from thin aluminised mylar (PE) foils, when the heavy particles are passing through. The SE are then accelerated by an electrostatic field and deflected by 90° by an electrostatic mirror before they impinge on a stack of micro-channel plate (MCP) detectors with a 2D delay-line position-sensitive anode. The energy and the velocity distribution of those SE is an important issue for the TOF spectrometer. A detector setup consisting of two sets of MCP detectors with foils, accelerating grids and electrostatic mirrors is represented in Fig. 1. It was positioned inside a vacuum chamber at 1×10^{-7} mbar.

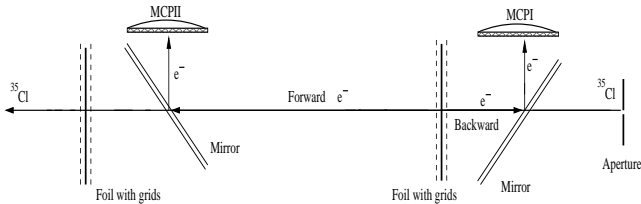


Fig. 1 Experimental setup. The heavy ion beam enters the setup from the right.

A 40 MeV ³⁵Cl beam was let through a cylindrical aperture with diameter of 500 μm. The beam particles knocked SE out from the first 2 μm PE foil both in backward and forward direction. The backward accelerated electrons were deflected and produced signals in the first MCP. The forward ones met the second mirror after travelling a distance of approximately 20 cm, which reflected them in the direction of the second MCP stack. For time reference which enabled us to obtain the SE TOF and convert it to velocity (see Fig. 2), signals from the back side of the MCP detectors were taken. The sequence of the signals arrival times was processed by a CAEN V775 Time-to-Digital Converter module and recorded by MBS DAQ

[2]. The experimental data were analyzed by APE [3].

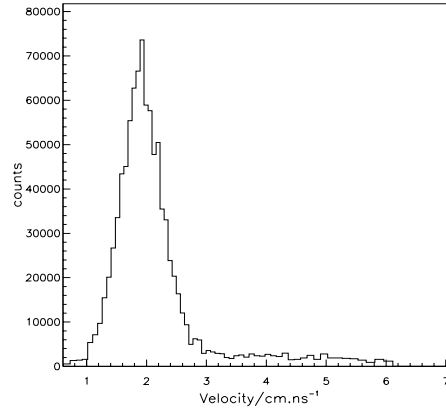


Fig. 2 Velocity spectrum of secondary electrons emitted by an 40 MeV ³⁵Cl beam impinging onto a 2 μm PE foil.

Fig.3 shows the derived SE energy spectrum.

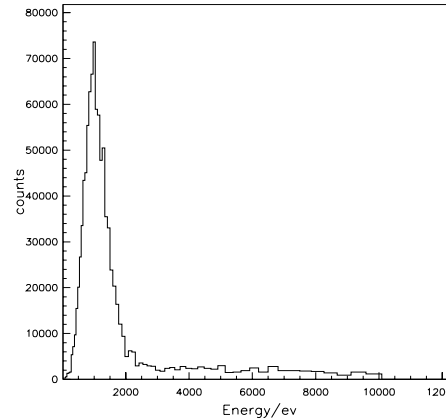


Fig. 3 Energy spectrum of the SE obtained after subtraction of the acceleration potential. One sees a prominent peak centered at around 900 eV with sigma of 300 eV. We estimate that the actual sigma value could be 15-20 % less due to uncertainties of the electron flight paths.

- [1] H. Sharma, A. Wagner, E. Grosse, IKH Annual Report 2002, FZR-372 (2003) 36
- [2] MBS DAQ:<http://www-w2k.gsi.de/daq>
- [3] APE:<http://www-aix.gsi.de/computing/apc.htm>

¹also INRNE, Sofia, Bulgaria

²also TU Dresden

³FZ Rossendorf, FWI

Limits of the Time Resolution of the Time-of-Flight Spectrometer for Fission Fragments and Exotic Nuclei^G

N. NANKOV,¹ M. FRIEDRICH,² A. HARTMANN, A.R. JUNGHANS, K. KOSEV, K.D. SCHILLING, A. WAGNER

The time resolution of the time-of-flight (TOF) spectrometer for fission fragments and exotic nuclei (See ref. [1]) has been extensively tested on the beam of the 5 MeV TANDEM at FZ-Rossendorf. Different geometry configurations with different distances between the two micro-channel plates (MCP) detectors has been used in order to find the optimum conditions for the time resolution and the efficiency. Additionally different ion-energy combinations have been used. For a linear TOF spectrometer the TOF resolving power $T/\Delta T$ is simply related to the energy width of the ion beam $E/\Delta E$ after the first detector in the following way if we assume a perfect detector with a zero timing:

$$\frac{T}{\Delta T} = 2 \frac{E}{\Delta E}. \quad (1)$$

The relation does not depend on the ion flight path length, meaning that theoretically two different long systems should have the same resolving power even the TOF peaks have different widths. Any deviation from this rule should point out to limitations of the detector timing. The test has been done with a ³⁵C beam at 40 MeV with two different flight path lengths of 102 and 270 mm. The energy of the ions has been measured with a Si-detector with a 150 keV (FWHM) energy resolution. The voltages of the MCP detector have been optimized to achieve the best possible timing. The results are presented in Fig. 1. The actual resolving power has been derived unfolding the contribution of the ion initial energy spread and the energy straggling inside the foil from the measured values. The larger error bars for the long system account for the slightly different ion flight paths due to the small angular straggling inside the first mylar foil.

The results from the simulation show good agreement with those calculated empirically according to equ. 1. The measured resolving power differs for the long and the short systems. This fact points out that a MCP detectors time resolution limit has been achieved at

the moment. Possible reasons include the initial beam energy spread which was measured to be more than a 2% as well as the energy loss straggling inside the foils.

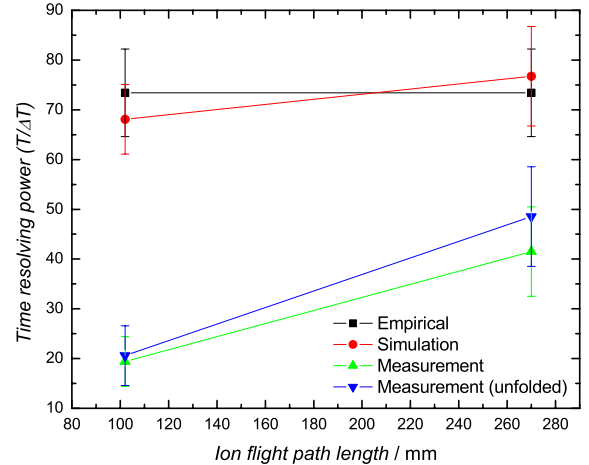


Fig. 1 Time resolving power as a function of the ion flight path. The straight lines are only guide for the eye.

Both those effects lead also to broadening of the secondary electrons (SEs) energy distribution. In fact it can reach up to 10%. Calculations using the isochronous condition found in ref. [2] have shown that if the detector would not be operated in a zero timing modus the 10% SEs energy width will limit its time resolution to 210ps which accounts for 23% of the measured time resolution drop in the short system.

- [1] N. Nankov, E. Grosse et al., Proc. 3rd Int. Workshop on Nucl. Fission and Fission-Product Spec., Chateau de Cadarache, 2005
- [2] N. Nankov, K. Kosev et al., IKH Annual Report 2004, FZR-423 (2005) 25

¹also INRNE, Sofia, Bulgaria

²FZ Rossendorf, FWI

e^+e^- Measurements with HADES^{B,G}

F. DOHRMANN, E. GROSSE,¹ B. KÄMPFER, K. KANAKI, R. KOTTE, L. NAUMANN, A. SADOVSKY, J. WÜSTENFELD
AND THE HADES COLLABORATION

In 2005, the HADES collaboration concentrated on completing the first analysis of experimental proposals S200 and S262 focused on di-electron production in nucleus-nucleus and nucleon-nucleon collisions. The sampled data cover the reactions C + C at 2.0 AGeV (November 2002), C + C at 1.0 AGeV (August 2004), p + p at 2.2 (2.0) GeV (September 2003, February 2004). A new data set on Ca + Ca at 2 (1.8) AGeV was taken in October 2005 [1]. In November-December 2005 the test of a RPC equipped module in the TOFINO region ($18^\circ - 44^\circ$) has been performed. The complete coverage of the TOFINO region with RPC is a prerequisite for a new series of experiments for studying high multiplicity reactions like Au + Au. Here we report on the status of the di-electron analysis.

Fig. 1 exhibits the invariant mass distribution of e^+e^- pairs measured in C + C collisions at 2 AGeV. The various e^+e^- sources as implemented in the simulation software are displayed as indication for the yields expected without medium effects; they also visualize the resolution of the detector (which was not yet completely equipped with all tracking devices when these data were taken). A detailed interpretation with advanced transport model calculations will be given separately [2, 3]. The necessary filter software is now provided to accomplish such a comparison of data and theory. The data sample is rich enough to bin the invariant mass spectrum for several transverse momentum intervals thus delivering additional information on the conditions under which the di-electrons were created.

The raw invariant mass distribution of e^+e^- pairs recorded in the reaction C + C at 1 AGeV is based on 840×10^6 first-level trigger events. It will be compared with the data taken at 2 AGeV.

The aim of the p + p experiment is to calibrate the spectrometer by measuring well known reactions like $pp \rightarrow pp$, and in particular $pp \rightarrow pp\eta$ with subsequent decays $\eta \rightarrow \pi^+\pi^-\pi^0$ and $\eta \rightarrow e^+e^-\gamma$ using the missing mass technique. As an example, Fig. 2 exhibits the missing mass distribution of pp . By comparing this distribution to the known η mass one can deduce the mass resolution of the spectrometer to be 2-4%. The set-up for this measurement was the same as used for studying the above described reaction C + C at 2 AGeV. Two out of six sectors were equipped with all four tracking planes. Substantial improvement is expected for the scheduled run p(3.5 GeV) + p, where all sectors are envisaged to be completely equipped. Moreover, at this energy investigations of the ω meson production mechanism are feasible. Such studies are necessary for understanding the in-medium production

of vector mesons in heavy-ion collisions.

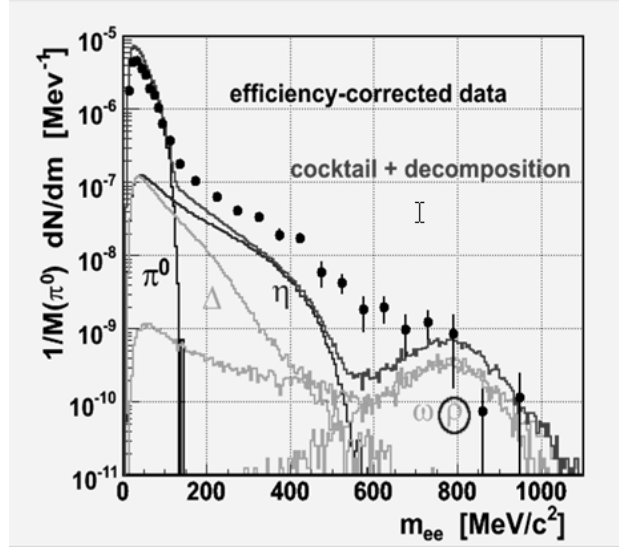


Fig. 1 Invariant mass distribution of di-electrons in C + C collisions at 2 AGeV [2]. The simulations are based on the PLUTO generator with thermal di-electron emission with two temperature parameters of 60 and 89 MeV.

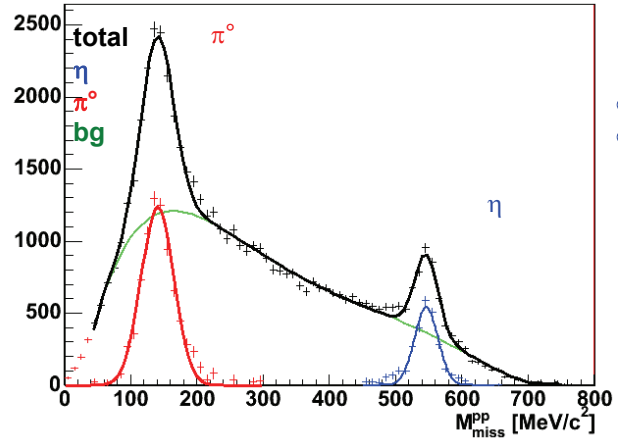


Fig. 2 Proton-proton missing mass distribution for $\eta \rightarrow e^+e^-\gamma$ events (defined by two proton tracks, one electron track and one positron track) measured in pp reactions at 2 GeV kinetic beam energy. The π^0 peak (left) and η peak (right) were fitted by Gaussians, separately shown after background subtraction.

- [1] P. Salapura et al. (HADES), Nucl. Phys. A 749 (2005) 150c
- [2] R. Holzmann et al. (HADES), Nucl. Phys. A (2006) in print
- [3] H.W. Barz, M. Zeteny, IKH Annual Report 2005

¹also TU Dresden

At present large effort is being taken to observe modification of particles which are imbedded in nuclear matter. Measurements of the dielectron spectrum of vector mesons are a proper tool. Recent data [1] for C + C collisions at 2 A·GeV are now made available by the HADES collaboration at GSI. At the same time new methods have been developed to describe the evolution of particle properties during a heavy-ion collision.

The starting point of these approaches are the Kadanoff-Baym equations which describe the time evolution of the Green functions as a function of the self-energies. The Wigner transform of the Green function $iS^<(x, y)$ can be interpreted as a generalized phase-space density suggesting a test particle ansatz

$$iS^<(x, p) = \sum_i \delta(\mathbf{x} - \mathbf{x}_i) \delta(\mathbf{p} - \mathbf{p}_i) \delta(p^0 - p_i^0)$$

which is appropriate for numerically solving the Kadanoff-Baym equations. In contrast to the standard BUU (Boltzmann-Ühling-Uhlenbeck) approach the phase space distribution contains a mass distribution usually given by the spectral function of the particles in a stationary state. The equations of motion for the three spatial coordinates $\mathbf{x}_i(t)$ and the four components of the momentum $p_i(t)$ of the test particles i can be found in [2,3].

Here we apply this off-shell transport model to calculate the dielectron production for the reaction carbon on carbon. We have included the effect of a mass shift and the collisional broadening into the self-energies of the ρ and ω vector mesons. The self-energies control the mass distribution and the life time of the produced vector mesons. We assume that these additional quantities are a linear function of the matter density. Most of the vector mesons are created via the decay of resonance states of the nucleon. Furthermore vector mesons are also created in pion annihilation processes like $\pi\pi \rightarrow \rho$ and $\pi\rho \rightarrow \omega$.

The aim of the study is to analyze the direct decay of the vector mesons into dielectrons. However most of the dielectrons come from Dalitz decays of excited particles (e.g. of π^0 , η , ω , nucleonic resonances) and the bremsstrahlung during the hadron-hadron collisions. All these processes are taken into account in the calculations.

In Fig. 1 we show the invariant dielectron mass spectrum for the C + C collision at 2 A·GeV in comparison with recent HADES data. The calculations demonstrate the effect of the self-energies. The dashed curve was obtained using the vacuum self-energy for the ρ

and ω mesons while the solid curve shows the effects of the collisional broadening and the mass shifts of 200 MeV and 50 MeV of the vector mesons.

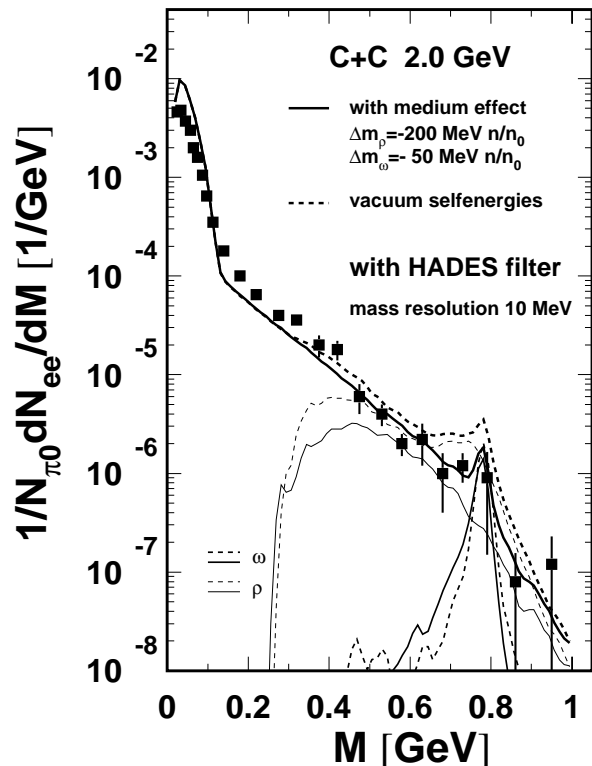


Fig. 1 Dielectron invariant mass spectrum calculated with vacuum properties (dashed lines) and in-medium properties (full lines) of the ρ and ω mesons in comparison with HADES data [1]. The calculations are folded with a mass resolution of 10 MeV.

The influence of the mass shift is hardly seen for both types of mesons. The mass shift of the ρ meson is covered by its large width while the effect for the ω meson is small because of the small size of the C + C system in which the mesons are produced at about half normal nuclear matter density only and most of them decay outside the reaction zone and they recover their vacuum mass before their decay.

- [1] R. Holzmann (for HADES collaboration), Nucl. Phys. A (2006) in print
- [2] W. Cassing and S. Juchem, Nucl. Phys. A 672 (2000) 417
- [3] S. Leupold, Nucl. Phys. A 672 (2000) 475

¹KFKI Budapest, Hungary

Isospin Effects in Virtual Bremsstrahlung^B

L.P. KAPTARI,¹ B. KÄMPFER

The HADES collaboration plans a systematical investigation of elementary hadronic reactions which are of relevance for disentangling the various contributions to di-electron spectra in heavy-ion collisions. One important continuum contribution is the virtual bremsstrahlung in pp and pn reactions. In particular, the reaction $Dp \rightarrow e^+e^-p_{sp}pn$ allows to tag the sub-reaction $np \rightarrow e^+e^-np$ with the deuteron's (D) remnant p_{sp} detected in the very forward direction. The reaction $pp \rightarrow e^+e^-pp$ is directly accessible in experiments with proton beam and liquid hydrogen target. To provide a theoretical base line we have calculated the virtual bremsstrahlung processes according to the diagrams depicted in Fig. 1 within an effective baryon-meson theory ensuring gauge invariance and Ward-Takahashi identity when using effective vertices, internal radiation and seagull diagram and proper spin-3/2 propagators as well.

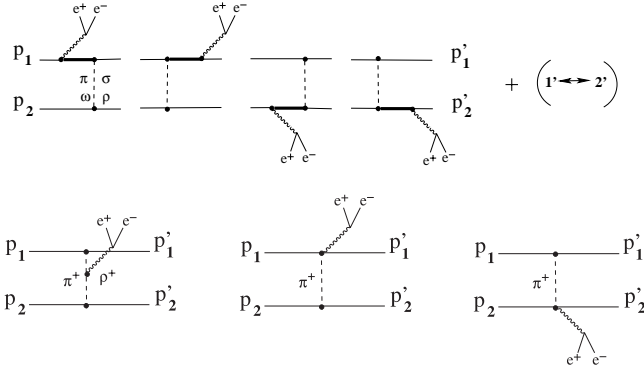


Fig. 1 Born diagrams for virtual bremsstrahlung. Upper row: pure bremsstrahlung diagrams. The fat line may be a nucleon or a Δ . Lower row: internal radiation diagram (left) and seagull diagrams. The dashed line may be a π^+ or ρ^+ .

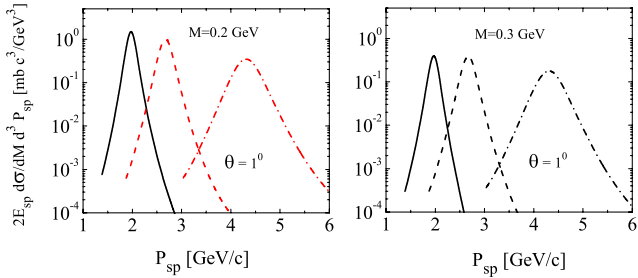


Fig. 2 Dependence of the differential cross section $2E_{sp} \frac{d\sigma}{dM d^3 p_{sp}}$ for the reaction $Dp \rightarrow p_{sp} np e^+e^-$ on the spectator momentum at two values of the invariant mass M of the lepton pair. The solid, dashed and dot-dashed lines correspond to beam energies $T_{kin} = 1.25, 1.90$ and 3.50 AGeV. The spectator proton is assumed to be detected at $\theta = 1^\circ$ in the laboratory frame.

Intermediate ρ and ω excitations are included in effective form factors exploiting vector meson dominance. Results are exhibited in Figs. 2 and 3 for the reaction $Dp \rightarrow e^+e^-p_{sp}pn$. For further details see [1]. Isospin effects are quantified in Fig. 4; they are determined to a large extent by the seagull terms.

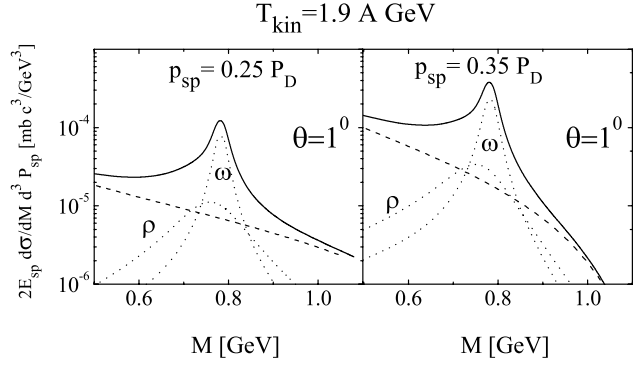


Fig. 3 Effects of sub-threshold vector meson production in the reaction $Dp \rightarrow p_{sp} pn e^+e^-$ at low values of the spectator momentum as indicated. Dashed lines depict the smooth background contribution from pure bremsstrahlung processes, dotted lines are separate contributions from ρ and ω mesons, and solid lines are for the total cross section including all interferences.

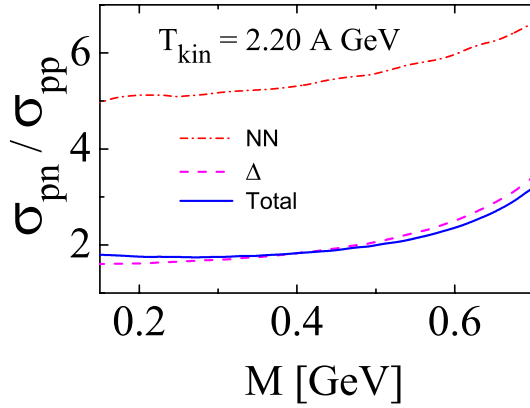


Fig. 4 The ratio $\sigma(pn \rightarrow pnc^+e^-)$ to $\sigma(pp \rightarrow ppc^+e^-)$ as a function of the invariant mass at $T_{kin} = 2.2$ GeV. The dot-dashed and dashed curves exhibit results with only nucleon and Δ contributions, respectively. The ratio of the total cross sections is denoted by the solid line.

[1] L.P. Kaptari, B. Kämpfer, Nucl. Phys. A 764 (2006) 338

¹Bogolyubov Laboratory of Theoretical Physics, JINR Dubna, 141980, Russia

The $\omega - \pi\gamma^*$ Transition Form Factor ^{B,G}

L.P. KAPTARI,¹ B. KÄMPFER

Form factors encode information on the internal structure of composite systems. Hadrons, as ensembles of quarks and gluons, require non-trivial form factors. For instance, the Dalitz decay $\omega \rightarrow \pi e^+ e^-$, belonging to the scheme $V \rightarrow P\gamma^*$, where V and P stand for vector mesons and pseudo-scalar mesons and γ^* denotes a virtual photon decaying into a di-electron $\gamma^* \rightarrow e^+ e^-$, is described by a transition form factor $F_{\omega\pi\gamma^*}(s_{\gamma^*})$ related to the ratio of matrix elements $\langle \omega | \pi^0 \gamma^* \rangle / \langle \omega | \pi^0 \gamma \rangle$ with normalization $F_{\omega\pi\gamma^*}(0) = 1$.

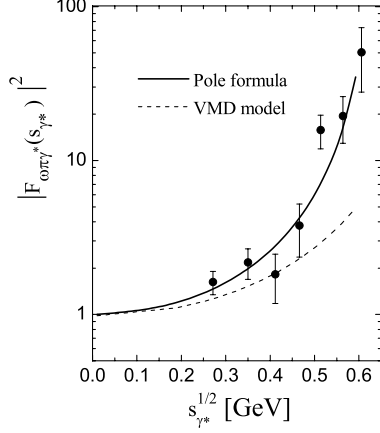


Fig. 1 $\omega - \pi\gamma^*$ transition form factor data extracted from L. G. Landsberg, *Phys. Rep.* 128 (1985) 301. Shown are our calculations for the reaction $pp \rightarrow pp\pi^0 e^+ e^-$ at kinetic beam energy of 2.2 GeV with either a VDM model (dashed curve) or a pole parametrization (solid curve).

The data base for the transition form factor $F_{\omega\pi\gamma^*}$ is quite poor as evidenced in Fig.1. The vector meson dominance (VDM) model fails in describing the data.

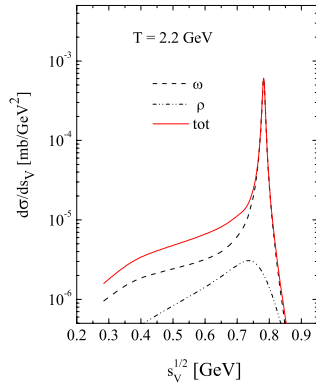


Fig. 3 Cross section $d\sigma/ds_V$ (left, $s_V \equiv s_{\pi\gamma^*} = s_{\pi^0 e^+ e^-}$) and double differential cross section $d\sigma/ds_V ds_{\gamma^*}$ (right, with detector resolution) for the reaction $pp \rightarrow pp\pi^0 e^+ e^-$ at kinetic beam energy of 2.2 GeV.

In this situation a new dedicated measurement with high precision is appropriate.

In the reaction $pp \rightarrow pp\pi^0 e^+ e^-$, the produced particles $\pi^0 e^+ e^-$ may emerge from either an ω or a ρ , and a smooth background contribution of non-resonant intermediate processes is conceivable too. In particular, the $\rho - \omega$ interference [1] may disturb the extraction of the wanted ω transition form factor. To clarify this issue we have calculated [2] the cross section within an effective nucleon-meson theory based on the diagrams in Fig.2. The resulting cross section is displayed in Fig.3 (l.h.s.). Due to the small branching ratio for $\rho^0 \rightarrow \pi^0 \gamma$ the ρ contribution is sub-leading, but still modifies the ω peak by an interference. The transition form factor can be extracted from the double differential cross section $d\sigma/ds_V ds_{\gamma^*}$ (see Fig.3, r.h.s.) via

$$|F_{\omega\pi\gamma^*}|^2 = \frac{s_{\gamma^*}^* \lambda^{3/2}(s_V, s_{min}, m_{\pi}^2) d\sigma/ds_V ds_{\gamma^*}}{s_{min} \lambda^{3/2}(s_V, s_{\gamma^*}, m_{\pi}^2) d\sigma/ds_V ds_{min}} \quad (1)$$

in a narrow interval around ω pole mass and with appropriate normalization at $s_{min} = s_{\gamma^*} \rightarrow 0$. The originally employed form factor is recovered within 0.5% accuracy, despite of interference effects. This gives some confidence that an improved measurement of the ω transition form factor with the present set-up of HADES is feasible in pp reactions.

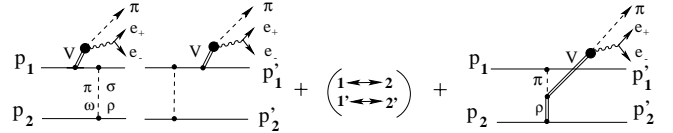
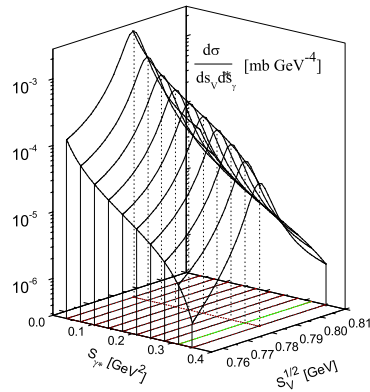


Fig. 2 Set of evaluated tree-level diagrams. $V = \omega, \rho$, and the fat dot denotes the $\omega - \pi\gamma^*$ transition form factor.



[1] A.I. Titov, B. Kämpfer, *Eur. Phys. J. A* 12 (2001) 217 [2] L.P. Kaptari, B. Kämpfer, to be published

¹Bogolyubov Laboratory of Theoretical Physics, JINR Dubna, 141980, Russia

Hadrons are composite systems built out of colored quarks and described by the theory of strong interaction. These hadrons, proton and neutron being most popular examples of such particles, are excitations of the ground state of the theory. A change in properties of this ground state is deduced from an experimental finding, namely from the observation that the mass of another hadron, the ω meson, is reduced when situated inside nuclear matter, that means embedded in a bulk of protons and neutrons. The properties of this ground state are quantified in so-called condensates, which carry important information on symmetry features of the theory. We emphasize here the specific role of a class of condensates, which up to now lack infor-

mation, the four-quark condensates. We determined how some of these condensates change under the influence of surrounding nuclear matter [1]. Therefore the method of QCD sum rules is applied, which is able to deal with a large variety of hadrons, so our finding and similar considerations for particles other than the ω meson can reveal more insight into changes of hadronic properties within nuclear matter.

The CB-TAPS collaboration observed in the reaction $\gamma + A \rightarrow A' + \omega (\rightarrow \pi^0 \gamma)$ the occurrence of additional low-energy ω decay strength for a Nb target compared to a hydrogen target [2]. Writing out the sum rule equation for the first moment of the spectral distribution function leads to

$$m_\omega^2(n, \mathcal{M}^2, s_\omega) = \frac{c_0 \mathcal{M}^2 \left[1 - \left(1 + \frac{s_\omega}{\mathcal{M}^2} \right) e^{-s_\omega/\mathcal{M}^2} \right] - \frac{c_2}{\mathcal{M}^2} - \frac{c_3}{\mathcal{M}^4} - \frac{c_4}{2\mathcal{M}^6}}{c_0 \left(1 - e^{-s_\omega/\mathcal{M}^2} \right) + \frac{c_1}{\mathcal{M}^2} + \frac{c_2}{\mathcal{M}^4} + \frac{c_3}{2\mathcal{M}^6} + \frac{c_4}{6\mathcal{M}^8} - \frac{\Pi^\omega(0, n)}{\mathcal{M}^2}}.$$

in our notation (\mathcal{M} is the Borel mass, for further details cf. [3]). The coefficients c_j contain condensates and parts of the Wilson coefficients, especially in c_3 enter the flavor-mixing four-quark condensates $\frac{2}{9} \langle \bar{u} \gamma^\mu \lambda_A u \bar{d} \gamma_\mu \lambda_A d \rangle + \langle \bar{u} \gamma_5 \gamma^\mu \lambda_A u \bar{d} \gamma_5 \gamma_\mu \lambda_A d \rangle$ and the pure flavor four-quark condensates (for which we employ $u - d$ isospin symmetry; γ_μ and λ_A stand for Dirac and Gell-Mann matrices) $\frac{2}{9} \langle \bar{q} \gamma^\mu \lambda_A q \bar{q} \gamma_\mu \lambda_A q \rangle + \langle \bar{q} \gamma_5 \gamma^\mu \lambda_A q \bar{q} \gamma_5 \gamma_\mu \lambda_A q \rangle$. The density dependence of these condensates is taken as the linearized density behavior of the squared chiral condensate multiplied by parameters κ . For the given combination of four-quark condensates an effective parameter κ_N describes the strength of their total density dependence. The in-medium modification of the light vector meson masses crucially depends on the density dependence of four-quark condensates, which can already be estimated analytically if one expands the given sum rule equation for small densities and employs standard condensate values and parameters from the full sum rule evaluation

$$m_\omega^2(n) = m_\omega^2(0) + n(4 - \kappa_N) \frac{0.03}{n_0} \text{GeV}^2. \quad (1)$$

The estimate points out that a strong density dependence ($\kappa_N > 4$) is required for an at least not increasing moment m_ω^2 , which in a simple pole/continuum ansatz represents the squared pole mass of the ω meson. In Fig. 1 this critical situation is exhibited, further, the inclusion of the next higher dimensional condensates is shown. It changes the absolute value of the critical κ_N , but not the qualitative requirement of a strong density dependence of the combined four-quark condensates for consistency with the observation

of CB-TAPS. This implies a considerable drop of the four-quark condensate combination considered here.

Although four-quark condensates can not generally be considered as order parameters for chiral symmetry, only specific combinations behave like the chiral condensate $\langle \bar{q}q \rangle$ under chiral transformations, they nevertheless carry information about the complicated structure of the QCD vacuum. Thus, our finding signals significant modifications of this ground state, and the universality of the condensates suggests the study of these effects in other hadronic channels.

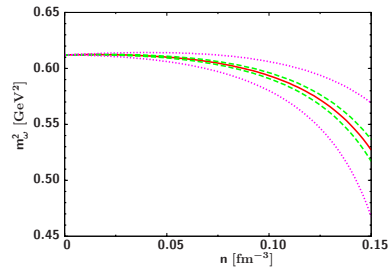


Fig. 1 The mass parameter m_ω^2 from a full QCD sum rule evaluation as a function of the baryon density for $\kappa_N = 4$ and $c_4 = 0$ (solid curve). The effect of a $c_4^{(1)}$ term is exhibited, too ($c_4^{(1)} = \pm 10^{-5} n_0^{-1} \text{GeV}^8$: dashed curves, $c_4^{(1)} = \pm 5 \times 10^{-5} n_0^{-1} \text{GeV}^8$: dotted curves; the upper (lower) curves are for negative (positive) signs).

[1] R. Thomas, S. Zschocke, B. Kämpfer, Phys. Rev. Lett. 95 (2005) 232301

[2] D. Trnka et al. (CB-TAPS), Phys. Rev. Lett. 94 (2005) 192303

[3] S. Zschocke, B. Kämpfer, Phys. Rev. C 70 (2004) 035207

A combined theoretical analysis of ω and ϕ meson production in the processes $pp \rightarrow ppV$, $pn \rightarrow pnV$ and $pn \rightarrow dV$ (here V denotes a vector meson [ω or ϕ], p (n) denotes a proton (neutron), and d stands for the deuteron in the final state) at near-threshold energies is interesting for different aspects of contemporary particle and nuclear physics. For instance, according to the Okubo-Zweig-Iizuka (OZI) rule the production of ϕ mesons in nucleon-nucleon collisions should be strongly suppressed relative to ω production. An enhanced ϕ production would imply some exotic (e.g., hidden strangeness) components in the nucleon wave function. The OZI rule is based on Sakurai's observation that the lowest 1^- vector mesons obey the Gell-Mann SU(3) octet classification and the Gell-Mann-Okubo mass formulae only if one attaches to the eight SU(3) matrices λ_{1-8} a ninth one, $\lambda_9 = \sqrt{2/3}\lambda_0$, so that instead of the 1^- octet one considers a nonet. Then, to reconcile the physical masses of ω and ϕ mesons one introduces a mixing angle θ and forms combinations like $\cos\theta \omega_0 \pm \sin\theta \omega_8$ to reproduce the known masses ($\omega_{0,8}$ are the pure SU(3) meson states). Alternatively, one can determine the mixing angle from the demand to reproduce the quark content of ω ($u\bar{u} + d\bar{d}$) and ϕ ($s\bar{s}$) mesons. The angle θ_0 is the ideal mixing angle. Accordingly, the ϕ meson can contain a small portion of non-strange quarks and, vice versa, the ω can contain some hidden strange components. In spite of the fact that the nonet classification does not have a strict symmetry nature, it has been found to excellently describe the light vector mesons. We have studied ω and ϕ meson production in near-threshold elementary nucleon-nucleon collisions $pp \rightarrow ppV$, $pn \rightarrow pnV$ and $pn \rightarrow dV$ within an effective meson-nucleon theory adjusted to still scarce data, see for instance Fig. 1. A set of effective parameters can be established to describe fairly well the available experimental data of angular distributions and the energy dependence of the total cross sections without explicit implementation of the OZI rule violation. In Fig. 2, the values of the OZI ratio defined at equal excess energies (dashed line) and at equal beam energies (solid line) are exhibited. Corresponding to our approach in both cases the FSI effects are the same (i.e., the deuteron in the final state). The only difference should appear due to the difference in the phase space volumes for ω and ϕ mesons which is estimated to be minimized for the ratio at equal excess energy near the threshold and more pronounced for the ratio at equal beam energies. In both cases the OZI ratio is essentially larger than the one expected from the naive OZI rule restrictions. For more details we refer the reader to [2].

Such an understanding of the elementary production processes of the lightest iso-scalar vector mesons is important for the interpretation of ongoing HADES experiments.

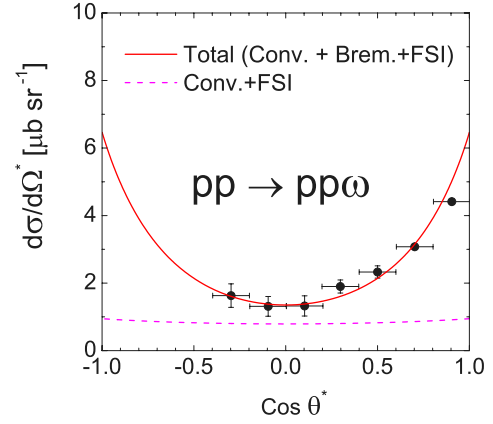


Fig. 1 Angular distributions of ω mesons for the reaction $NN \rightarrow NN\omega$ at the excess energy $\Delta s^{\frac{1}{2}} = 173$ MeV. Dashed lines correspond to contributions of conversion currents (i.e., the ω emerges from an internal boson exchange line with vertex $\rho\pi\omega$), solid lines represent the total contributions of bremsstrahlung and conversion diagrams. Final state interaction (FSI) is included. Experimental data are taken from [1]. The corresponding data set from DISTO for the ϕ meson is too poor to decide the relative strength of bremsstrahlung and internal conversion processes.

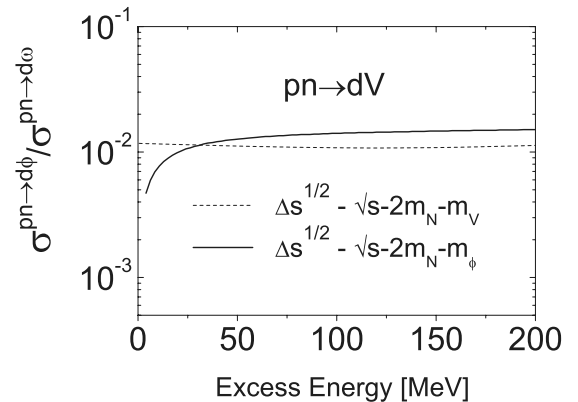


Fig. 2 The OZI rule ratio for $pn \rightarrow dV$ processes as a function of the excess energy. The dashed line represents the ratio at equal values of the excess energy, while the solid line reflects the ratio at equal beam energies and is measured from the threshold of ϕ meson production.

- [1] S. Abd El-Salam et al. (COSY-TOF), Phys. Lett. B 522 (2001) 16
- [2] L.P. Kaptari, B. Kämpfer, Eur. Phys. J. A 23 (2005) 291

¹Bogolyubov Laboratory of Theoretical Physics, JINR Dubna, 141980, Russia

Study of Λ Production in C + C Reactions at 2 AGeV with the HADES Spectrometer^{B,G}

K. KANAKI, F. DOHRMANN, E. GROSSE¹, B. KÄMPFER, R. KOTTE, L. NAUMANN, A. SADOVSKY
for the HADES collaboration

The study of strangeness production in heavy ion collisions contributes valuable information to the comprehension of nuclear matter with consequences for the equation of state and the in-medium properties of hadrons. Several experiments have provided data from elementary p+p reactions up to heavy ion collisions and for a wide range of incident beam energies [1-5]. The aim of our current analysis is the study of strange baryons in C+C reactions at incident beam energies of 2 AGeV, as there are no available data for this particular system at the given energy. An overview of the existing Λ production cross sections, as well as a prediction for the cross section from HADES are shown in Fig. 1.

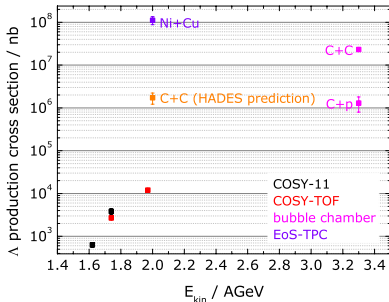


Fig. 1 The existing Λ production cross sections from p+p to heavy ion reactions for medium projectile kinetic energies. The HADES prediction is 1.7 mb and is obtained by appropriate scaling of the known cross sections.

The large phase space coverage and high resolution tracking capabilities make the HADES spectrometer at SIS/GSI, Darmstadt suitable for the reconstruction of Λ hyperons, via their delayed decay $\Lambda \rightarrow p\pi^-$ (64% branching ratio, $c\tau = 7.89$ cm). The analysis steps needed for the Λ reconstruction impose track quality criteria for the single particles of the decay, as well as for the reconstructed momentum vector that corresponds to the parent particle. These criteria are determined by detailed GEANT simulations. The $p\pi^-$ invariant mass distribution finally obtained is depicted in Fig. 2.

The background of the distribution is fitted with a third order polynomial function. After its subtraction, the signal can be fitted with a Gaussian and then integrated, in order to estimate the number of Λ hyperons (see Fig. 3). In a sample of $153 \cdot 10^6$ analyzed events, the counted Λ particles are 357 ± 70 . A series of corrections are needed though, in order to get the true number of the produced particles and the cross section. These corrections are usually calculated and

applied in the two-dimensional space but due to the low statistics, the correction matrix in this case will be momentum and angle integrated.

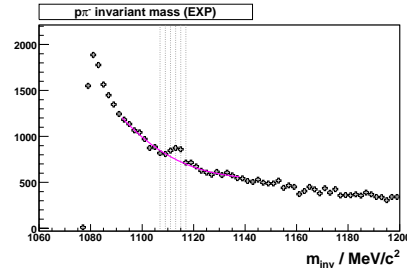


Fig. 2 Invariant mass distribution of $p\pi^-$ pairs. The curve fitting the background is a third order polynomial. The points that belong to the peak are excluded from the fit.

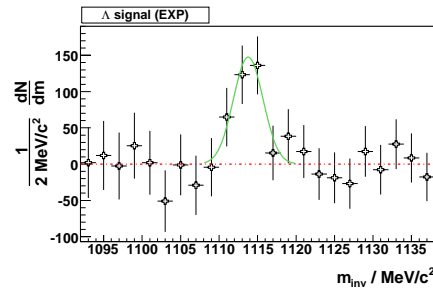


Fig. 3 After subtracting the background contribution, the signal that remains is fitted with a Gaussian. The integral of the surface estimates the number of Λ hyperons.

Thus, after correcting for the geometrical acceptance, the inefficiencies of the tracking algorithm, the reduction due to the enhancement cuts, the electron trigger and the branching ratio of the Λ decay, the multiplicity of Λ in central collisions (charged particle multiplicity > 3) is $\mathcal{M} = (2.00 \pm 0.42) \cdot 10^{-3}/\text{event}$. Correcting for minimum bias and normalizing relatively to another particle whose cross section is independently measured, the multiplicity and the production cross section are expected to decrease. The restricting conditions then are $\mathcal{M} < 2 \cdot 10^{-3}/\text{event}$ and $\sigma_{\Lambda} < \mathcal{M} \cdot \sigma_{geom}(C+C) = 1.9$ mb, in good agreement with the prediction.

- [1] P. Kowina, M. Wolke et al., Eur. Phys. J. A 22 (2004) 293
- [2] J.M. Alexander, P. Chung et al., J. Phys. G 25 (1999) 255
- [3] X. Lopez, Prog. Part. Nucl. Phys. 53 (2004) 149
- [4] D.A. Armutlijski, E. Bogdanovich et al., JINR-P1-85-220, 1985
- [5] M. Justice, 33rd International Winter Meeting on Nuclear Physics, Bormio, Italy, 1995

¹also TU Dresden

Investigation of K^+ Meson Production in C + C Reactions at 2 AGeV with HADES^{B, G}

A. SADOVSKY, R. KOTTE, F. DOHRMANN, E. GROSSE,¹ B. KÄMPFER, K. KANAKI, L. NAUMANN
FOR THE HADES COLLABORATION

A complete K^+ meson analysis of $166 \cdot 10^6$ events recorded in 2002 by HADES for the reaction C + C with kinetic beam energy 2 AGeV on fixed target was performed. The information of two (out of six) fully equipped sectors of HADES was involved in the analysis. The detector description can be found elsewhere [1]. The high-resolution Runge-Kutta tracking was chosen as it provides best results for K^+ particle identification due to high background suppression achieved with the help of specific track-quality parameter.

In the kinematical region in the lab. system of $350 \text{ MeV}/c < p < 700 \text{ MeV}/c$, $46^\circ < \theta < 82^\circ$ about 2200 K^+ mesons (including background contribution of $\approx 23\%$) were registered and were used for an estimate of the K^+ cross section.

Since the number of beam particles was not measured in the experiment, a direct normalization was not possible. Therefore an independent estimate of the total K^+ cross section for C + C @ 2 AGeV was established with respect to π^+ , π^- cross sections which were measured by KaoS collaboration [2] in the reaction C + C @ 1.8 AGeV. Pion cross sections taken as reference were scaled from 1.8 to 2.0 AGeV by a factor of 1.106 due to the beam energy dependence of the multiplicity according to [3, 4]. The correction on registration efficiency of involved detectors was performed with realistic GEANT simulations. Extrapolating to 4π the resulting total K^+ cross section is estimated as

$$\sigma_{K^+} = (6.0 \pm 0.9_{-0.9}^{+1.7}) \text{ mb},$$

where the HADES multiplicity trigger influence and the background contribution were investigated and corrected for.

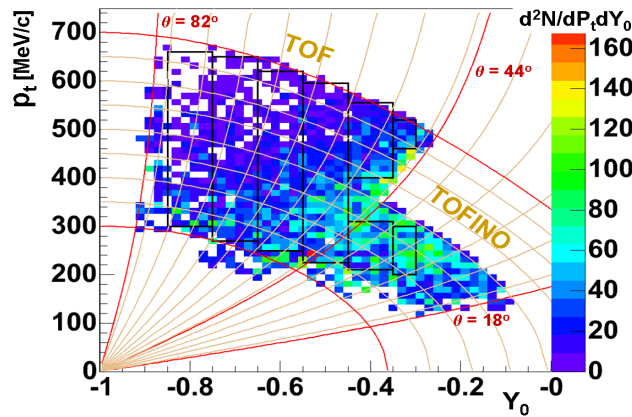


Fig. 1 Detector efficiency corrected $d^2N/dp_t dY_0$ distribution of K^+ mesons. The acceptance grid in laboratory momentum and polar angle θ is indicated by curves. Black boxes depict the regions used for analysis.

Both regions of time-of-flight detectors TOFINO ($350 \text{ MeV}/c < p < 500 \text{ MeV}/c$, $18^\circ < \theta < 44^\circ$) and TOF ($350 \text{ MeV}/c < p < 700 \text{ MeV}/c$, $44^\circ < \theta < 82^\circ$), with total K^+ statistics of about 3700 tracks (including 30% of background) were taken into account to perform $\frac{1}{(m_t)^2} \cdot \frac{d^2N}{dm_t dY_0}$ distributions, where $m_t^2 = p_t^2 + m_{K^+}^2$, m_{K^+} is the K^+ mass. They were fitted independently in 6 different rapidity regions (see Fig. 1) with Boltzmann distributions $C \cdot e^{-m_t/T_B}$ allowing extrapolation to non measured regions and finally integrated over the full m_t range. The resulting dN/dY_0 distribution is shown in Fig. 2. The systematic error is expected to be in the order of 20 - 30%. The distribution was fitted according to isotropic thermal model

$$\frac{dN}{dY_0} = C_0 \cdot e^{-1/k} \cdot \left(2 + \frac{2}{k} + \frac{1}{k^2}\right) \cdot k^3, \quad (1)$$

where $k = T/(m_{K^+} \cdot \cosh(Y - Y_{cm}))$, $Y_0 = \frac{Y}{Y_{cm}} - 1$ represents the normalized rapidity and Y_{cm} is the center-of-mass rapidity. As a result of the fit, the temperature parameter $T \approx (80 \pm 14) \text{ MeV}$, was obtained with an error estimate from the fit.

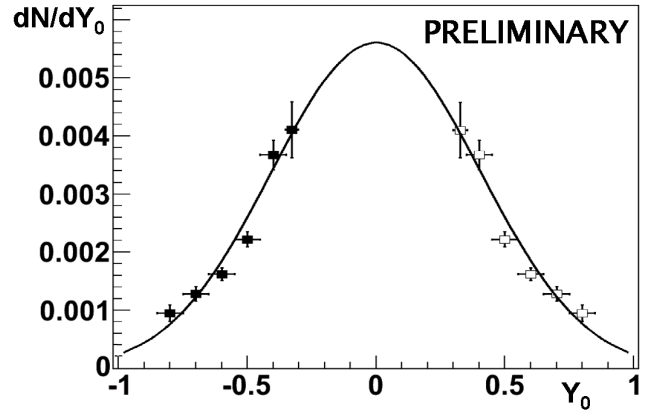


Fig. 2 dN/dY_0 distribution of K^+ mesons. The measured yields (full symbols) are reflected with respect to midrapidity (empty symbols). The full line is the fit function (1) with $T = 80 \text{ MeV}$.

- [1] T. Eberl, G. Agakishiev et al. (HADES), Nucl. Phys. A 752 (2005) 433
- [2] F. Laue, C. Sturm et al., Phys. Rev. Lett. 82 (1999) 1640; F. Laue, I. Böttcher et al., Eur. Phys. J. A9 (2000) 397
- [3] C. Sturm, Dissertation, TU Darmstadt (2001)
- [4] C. Sturm, I. Böttcher et al., Phys. Rev. Lett. 86 (2001) 39

¹also TUDresden

Inclusive K^\pm Production in Proton-Nucleus Collisions near Threshold ^B

W. SCHEINAST, F. DOHRMANN, E. GROSSE,¹ L. NAUMANN, H.W. BARZ, B. KÄMPFER AND THE KAOS COLLABORATION

The $pA \rightarrow K^\pm X$ reaction has been measured by the KaoS collaboration [1, 2], showing the first observation of in-medium effects on phase space distributions of K^- mesons in pA collisions. This data set fills the gap of K^\pm production between pp and AA collisions. A clear effect of the nuclear medium on strangeness production was found by comparing the data from pA collisions with data from pp and AA collisions [1]. The enhancement factor between pp , pA and AA data is significantly larger for K^- than for K^+ . Such an effect is expected for an increasing contribution of strangeness exchange reactions $\pi Y \rightarrow K^- N$ and $NY \rightarrow K^- NN$ to K^- production as well as density dependent in-medium effects. The role of in-medium effects on K^- production in pAu , pC collisions is investigated using the ratio of invariant cross sections of inclusive K^- over K^+ production versus the transverse mass $m_\perp = \sqrt{p_\perp^2 + m_K^2}$ at $E_{\text{beam}} = 2.5$ GeV. Fig. 1 presents the data integrated over the measured angular range compared to results of transport model calculations of BUU type [3]. These calculations take into account strangeness exchange reactions which dominate over the direct K^- production processes, both in AA as well as pA collisions. In pA collisions at 2.5 GeV the contribution of strangeness transfer processes amounts to 50-60%, and for AA collisions it is even larger (70-80%).

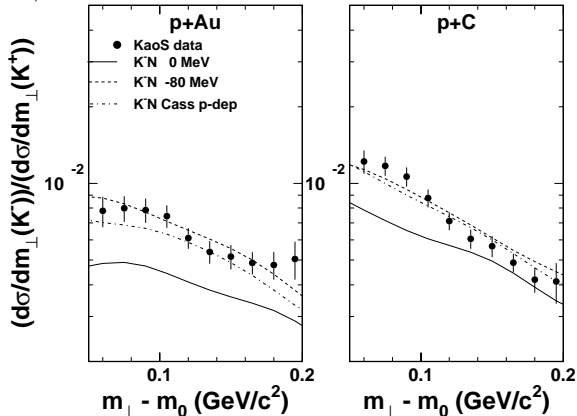


Fig. 1 Ratio of the invariant production cross sections of K^- mesons for inclusive pAu (left panel) and pC collisions (right panel) as function of transverse mass.

In order to discuss the density dependent in-medium potentials, it is important to know at which densities the finally observed K^\pm mesons are produced.

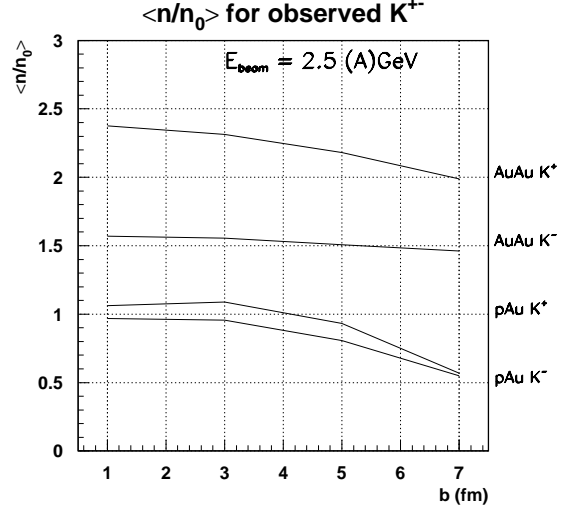


Fig. 2 Average normalized densities at which K^\pm are observed, inferred from BUU calculations for pAu and $AuAu$ collisions.

As an example, Fig. 2 shows these densities for $AuAu$ and pAu collisions vs. the impact parameter b . For pC (Au) collisions at $E_{\text{beam}} = 2.5$ (A) GeV we obtain an average density about 0.8 (0.9) times the normal nuclear matter density n_0 , whereas for CC ($AuAu$) collisions the average value is slightly above 1.1 (1.5) n_0 . The observed K^+ mesons are produced earlier, and hence, at larger average densities: the BUU calculations predict a value of 0.9 (1.0) n_0 for pC (Au) collisions, while for CC ($AuAu$) collisions a value of about 1.4 (2.2) n_0 is obtained for the same beam energy. The data in Fig. 1 (full dots) are compared to the results of BUU calculations with and without in-medium K^-N potentials. The theoretical uncertainties in the K^+ production channels essentially cancel out in the K^-/K^+ ratio. Assuming a K^-N potential of about -80 MeV (Fig 1: dashed curve), the calculations agree reasonably well with the data. The discrepancy between the data and the calculations neglecting K^-N potentials (solid curves) clearly demonstrates the important role of in-medium effects. Within our BUU code, momentum dependent potentials, cf. [4], yield a similar agreement (dash-dotted lines) with the data for an momentum averaged K^-N potential of -80 MeV. A more refined analysis of our data with respect to in-medium effects calls for an improved theoretical approach including off-shell effects and in-medium spectral functions.

- [1] W. Scheinast et al. (KaoS Collaboration), arXiv:nucl-ex/0512028, Phys. Rev. Lett. in print,
 [2] W. Scheinast, Dissertation, TU Dresden (2004)
 [3] H.W. Barz, L. Naumann, Phys. Rev. C 68 (2003) 041901
 [4] A. Sibirtsev and W. Cassing, Nucl. Phys. A 641 (1998) 476

¹also TU Dresden

Effect of K^* Exchange on Azimuthal Asymmetry for Pentaquark Production in pp Collisions ^{A, B}

H.W. BARZ, M. ZÉTÉNYI¹

The question whether the pentaquark Θ^+ exists is not settled at present time. The narrow resonance at 1.53 GeV which decays into the pK^0 or the nK^+ channel could be identified with the pentaquark state predicted in [1]. According to this theory it belongs to a $J^\pi = 1/2^+$ antidecuplet as an isospin singlet with the five quark configuration $uudd\bar{s}$.

If in fact this state exists it would be important to determine spin and parity. Soon it was realized that in $pp \rightarrow \Sigma\Theta^+$ collisions at threshold the parity π of the Θ^+ particle determines the spin of the initial protons via $(-1)^S = \pi$. This has the consequence that, e.g., for positive parity of Θ^+ the spin correlation parameter A_{xx} which controls the cross section in the reaction plane via $1 + A_{xx}P_{1x}P_{2x}$ has the value of -1. Thus the Θ^+ could be generated in this plane only with two protons which have oppositely oriented spins. Therefore, the measurement of the A_{xx} coefficient is one of the tools to determine the parity of the pentaquark.

Here we investigate up to which energy this threshold behavior can be observed in experiment since measurements at threshold are difficult. We describe the interaction in lowest order by a combination of Lagrangians describing K and K^* exchanges. For the spin $J = 1/2$ of Θ^+ the T matrix has the structure

$$T = g_{KN\Sigma}g_{KN\Theta}A + g_{KN\Sigma}^*g_{K^*N\Theta}B \quad (1)$$

with coupling parameters g and g^* from K and K^*

exchanges. If the spin is $3/2$ the respective coupling constants are replaced by f and f^* . For details see [2]. The parameters g are constraint by assuming a production cross section of about $0.4 \mu\text{b}$ and a decay width of 10 MeV for the Θ^+ particle. These values are consistent with the COSY data [3]. On the other hand the data do not allow to determine the ratio of the coupling parameters g^* (or f^*).

For a positive sign of the coupling parameters for the Θ^+ ($g^* = 0.6$ for the $1/2^+$ and $f^* = 2.0$ for the $3/2^+$ state) we have a negative interference which cancels nearly the $L=0$ partial wave in the outgoing channel. This causes a abnormal $\Delta E^{3/2}$ threshold behavior for the cross section σ_0 but at the same time makes the A_{xx} correlation function positive right above threshold. Since the $1 + A_{xx}$ is proportional to ΔE the product $(1 + A_{xx})\sigma_0$ for destructive and constructive interference behave like $\Delta E^{3/2}$. This is shown in Fig. 1. This effect has been found in [4] for spin $1/2$ states at threshold and we see that this behavior holds also for spin $3/2$ up to 100 MeV excess energy.

- [1] D. Diakonov, V. Petrov, M.V. Polyakov, Z. Phys. A 359 (1997) 305
- [2] H.W. Barz, M. Zétényi, Phys. Rev. C 71 (2005) 065207
- [3] M. Abdel-Bary et al. (COSY collaboration), Phys. Lett. B 595 (2004) 127
- [4] C. Hanhart et al., Phys. Lett. B606 (2005) 67

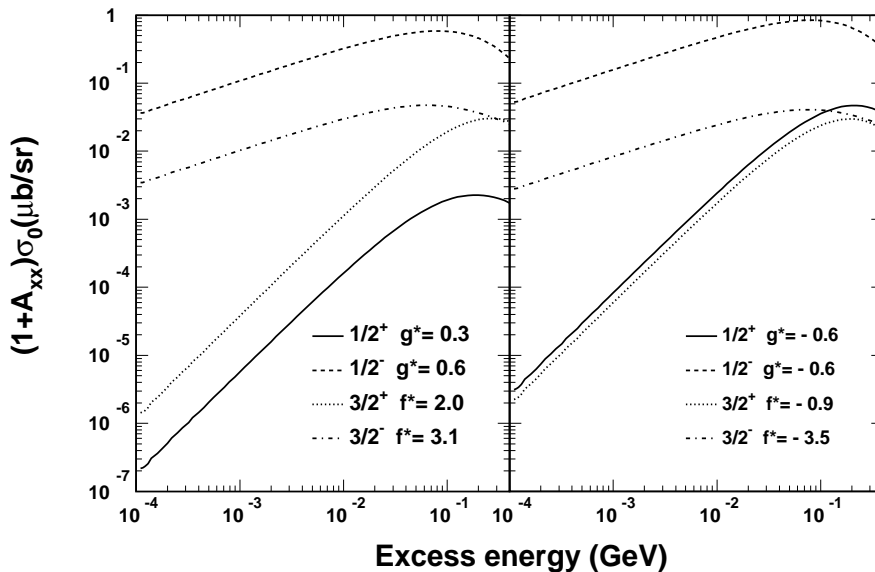


Fig. 1 Excess energy dependence of the combination $(1 + A_{xx})\sigma_0$ for various values of spin and parity. The plot on the left (right) shows the results for positive (negative) coupling strengths of the K^* exchange.

¹KFKI Budapest, Hungary

Coherent Photo-Excitation of Θ^+ B

A.I. TITOV,¹ B. KÄMPFER, S. DATE,² Y. OHASHI²

The pentaquark Θ^+ is a novel hadronic state with the anticipated quark structure $uudd\bar{s}$. The situation is unsettled up to now whether it has been identified unambiguously in experiments. Several measurements have been proposed to pin down the parity of Θ^+ . In [1] we have considered the reaction $\pi^\pm \bar{D} \rightarrow \bar{\Sigma}^\pm \Theta^+$ and calculated, by fairly model independent means, the spin transfer coefficients and deuteron (D) spin anisotropy. Both quantities are correlated in a specific way and may be used to determine the Θ^+ parity. A measurement requires a pion beam at fixed energy impinging on a polarized deuteron target and a detector with large phase space coverage to identify the decay channels $\Theta^+ \rightarrow NK$ and $\Sigma \rightarrow N\pi$. The Σ polarization is accessible by standard procedures relying on the angular distributions in the decay channel. Basically, HADES and FOPI could make such explorations feasible by using the secondary pions beams at the heavy-ion synchrotron SIS.

Signals for Θ^+ are reported mainly in photo-excitation experiments. We have, therefore, studied in some detail the coherent $\Lambda^* \Theta^+$ photo-production in γD reactions [2]. The considered background processes depend strongly on the actual kinematics where the mo-

mentum distribution within the deuteron plays the key role. Thus, at fixed angle of the pK^- photo-production, the nK^+ invariant mass distribution of the considered background processes look like a narrow peak with maximum around the Θ^+ mass. This behavior hampers the extraction of the coherent process at finite mass resolution. Most promising is an experimental analysis of the distributions integrated over the pK^- production angles in the forward hemisphere. In this case the background processes increase monotonously with invariant mass M_{nK^+} in the vicinity of the Θ^+ mass. This allows to extract the coherent $\gamma D \rightarrow \Lambda^* \Theta^+$ channel with finite mass resolution (see Fig. 1). The coherent $\Lambda_{1520} \Theta^+$ photo-production does not depend on the Θ^+ photo-production amplitude, but rather it is defined by the probabilities of Λ_{1520} production and $\Theta^+ \rightarrow NK$ transition. Such models as ours [2] may be considered as examples where the Θ^+ peak is recognized under certain experimental conditions and why it does not stick out the strong background under other conditions. The electron and photon facilities ELSA, ESRF, SPring-8 and JLab are well suited to study in detail the proposed production mechanism.

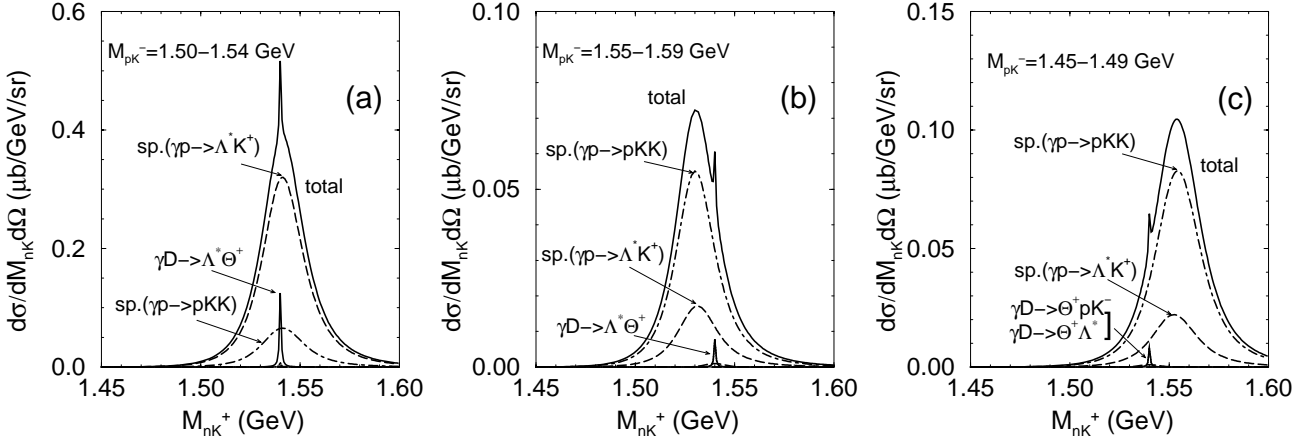


Fig. 1 nK^+ invariant mass distributions in the reaction $\gamma D \rightarrow npK^+ K^-$ at fixed values of the pK^- invariant mass. The angle of the pK^- photo-production in the γD center of momentum system is chosen as 27.5° . Labels are as follows: "sp. ($\gamma p \rightarrow \Lambda^* K^+$)" - non-coherent spectator channel with intermediate Λ^* , "sp. ($\gamma p \rightarrow pKK$)" - non-coherent spectator channel with internal $\gamma p \rightarrow pK^+ K^-$ vertex, " $\gamma D \rightarrow \Theta^+ pK^-$ " - coherent semi-resonant background processes with K^+ exchange and intermediate Θ^+ , " $\gamma D \rightarrow \Lambda^* \Theta^+$ " - coherent $\Lambda^* \Theta^+$ photo-production with both internal Λ^+ and internal Θ^+ .

[1] A.I. Titov, B. Kämpfer, Phys. Rev. C 71 (2005) 062201(R)

[2] A.I. Titov, B. Kämpfer, S. Date, Y. Ohashi, Phys. Rev. C 72 (2005) 014005

¹Bogolyubov Laboratory of Theoretical Physics, JINR Dubna, 141980, Russia

²Japan Synchrotron Radiation Research Institute, SPring-8, 1-1-1 Kouto Mikazuki-cho Sayogun Hyogo 679-5198, Japan

Chemical Freeze-Out in Relativistic Heavy Ion Collisions^B

J. CLEYMANS,¹ B. KÄMPFER, M. KANETA,² S. WHEATON,¹ N. XU³

The statistical-thermal model describes surprisingly well a fairly large set of various hadron multiplicities in heavy-ion collisions over a large range of beam energies. In [1] we analyzed the centrality dependence of strangeness saturation at the RHIC energy of $\sqrt{s_{NN}} = 130$ GeV in reactions of Au+Au. In central collisions, the freeze-out parameters are temperature $T = 168$ MeV, baryon-chemical potential

$\mu_B = 35$ MeV, strangeness-chemical potential $\mu_S = 10$ MeV and strangeness saturation factor $\gamma_S \approx 1$. The strangeness saturation factor falls below unity for peripheral collisions, pointing to some off-equilibrium effects. The centrality dependence turns out to be quite subtle. Examples for selected hadron ratios at mid-rapidity are exhibited in Fig. 1.

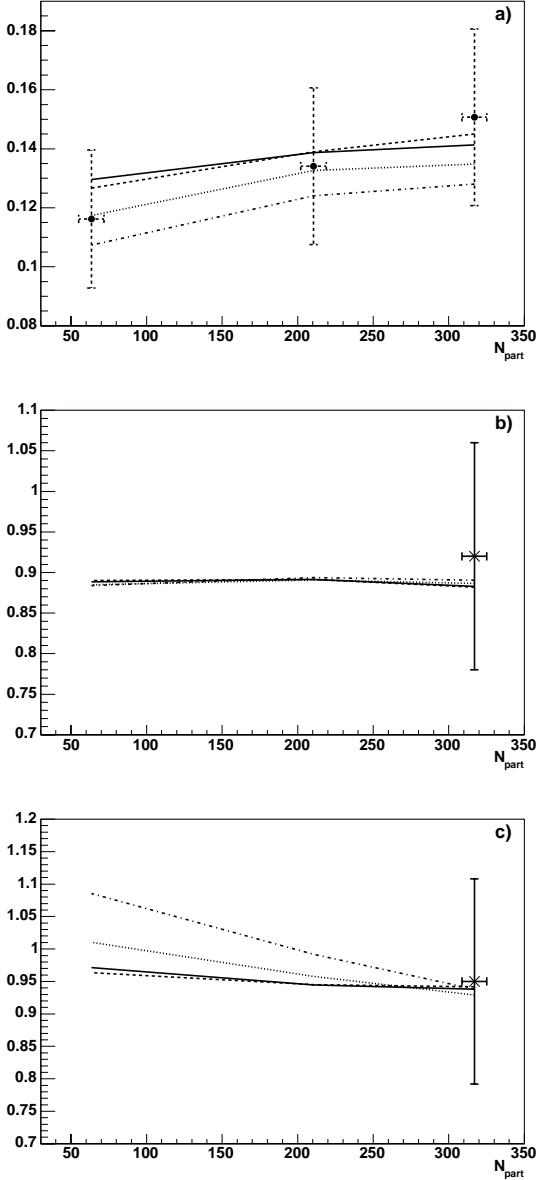


Fig. 1 Centrality dependence of hadron ratios (a: K^-/π^- , b: \bar{K}^{*0}/K^{*0} , c: $\bar{\Omega}^+/\Omega^-$) as derived from fits of many other data binned as in Fig. 1a. The different curves are for different model assumptions; for details see [1].

The combination of freeze-out parameters at various beam energies can be condensed in the formula [2]

$$\mu_B = \frac{1.27372 \text{ GeV}}{1 + 0.257787\sqrt{s}/\text{GeV}} \quad (1)$$

$$T(\mu_B) = (0.16446 - 0.11196\mu^2 - 0.139139\mu^4 + 0.0684637\mu^6) \text{ GeV}, \quad (2)$$

where $\mu = \mu_B/\text{GeV}$ and $\sqrt{s} = 2m_N\sqrt{1 + \frac{T_{lab}}{2m_N}}$ for fixed-target experiments. This allows to predict the freeze-out parameters in planned CBM experiments at FAIR. As an example we exhibit in Fig. 2 temperature and chemical potential for beam energies ranging from 10 to 50 AGeV. The CBM detector set-up is going to be optimized for a nominal beam energy of about 25 AGeV. The freeze-out points may also serve for an orientation of the isentropic equation of state.

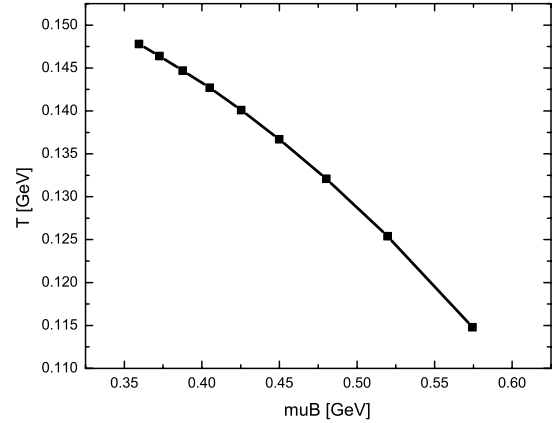


Fig. 2 Chemical freeze-out curve in the temperature T and chemical potential μ_B plane. The squares are for beam energies ranging from 10 AGeV (right bottom point) to 50 AGeV (left top point) in steps of 5 AGeV, as envisaged for SIS100/300 at FAIR.

- [1] J. Cleymans, B. Kämpfer et al., Phys. Rev. C 71 (2005) 054901
- [2] S. Wheaton, PhD, University of Cape Town, 2005

¹UCT-CERN Research Centre, Department of Physics, University of Cape Town, Rondebosch 7701, Cape Town, South Africa

²RIKEN BNL Research Center, Brookhaven National Laboratory, Upton, New York 11973, USA

³Lawrence Berkeley National Laboratory, Berkeley, California 94720, USA

Critical End Point Effects on the QCD Equation of State^{A,B,G}

M. BLUHM, B. KÄMPFER

In the QCD phase diagram, hadronic and quark gluon fluid phases are separated by a (pseudo-) critical line. The phase transition across this line is expected to be first order for large baryo-chemical potentials μ_B and finite temperatures T ending in a critical point (CEP) of second order.

Formulating the equation of state (EoS) in terms of the entropy density, it can be decomposed into an analytic and a non-analytic contribution $s = s_a + s_n$. s_a is adjusted to the known EoS outside the critical region whereas s_n includes CEP assuming that it belongs to the static universality class of the 3D Ising model. For elucidating observable consequences of the CEP existence, one can study the manner isentropic trajectories $s/n_B = \text{const}$ become modified. First, we consider a simple toy model,

$$s_a(T, \mu_B) = 4\bar{c}_0 T^3 + \frac{2}{9}\bar{c}_2 \mu_B^2 T, \quad (1)$$

$$s_n(T, \mu_B) = \frac{2}{9}\bar{c}_2 \mu_B^2 T A \tanh(S_c(T, \mu_B)) \quad (2)$$

with constant coefficients $\bar{c}_0 = (32 + 21N_f)\pi^2/180$, $\bar{c}_2 = N_f/2$ for $N_f = 2$ and strength parameter A . The net baryon density n_B follows from s . $S_c(T, \mu_B)$ is defined according to [1] with adjustable parameters characterizing the unknown extension of the critical region around CEP. We locate CEP at $\mu_{B,c} = 360$ MeV in line with [2]. Results are exhibited in Fig. 1 (cf. [3] for details). The trajectories are bent to larger μ_B where CEP acts as attractor (repulsor) on isentropes on the left (right) of it. As shown in Fig. 1 (lower panel), the influence of CEP on the isentropic trajectories decreases by shrinking the extension of the critical region.

In agreement with lattice QCD simulations, s_a can be constructed as Taylor series expansion in (μ_B/T) including expansion coefficients $c_{0,2,4,6}(T)$ which are reproduced by our quasi-particle model (QPM). We include CEP in line with the procedure outlined above and assume a small critical region. As exhibited in Fig. 2, CEP effects become visible only for large μ_B but with negligible impact on the hadronic sections [3].

[1] C. Nonaka, M. Asakawa, Phys. Rev. C 71 (2005) 044904

[2] Z. Fodor, S. D. Katz, JHEP 0404 (2004) 050

[3] B. Kämpfer, M. Bluhm et al., Nucl. Phys. A (2006) in print

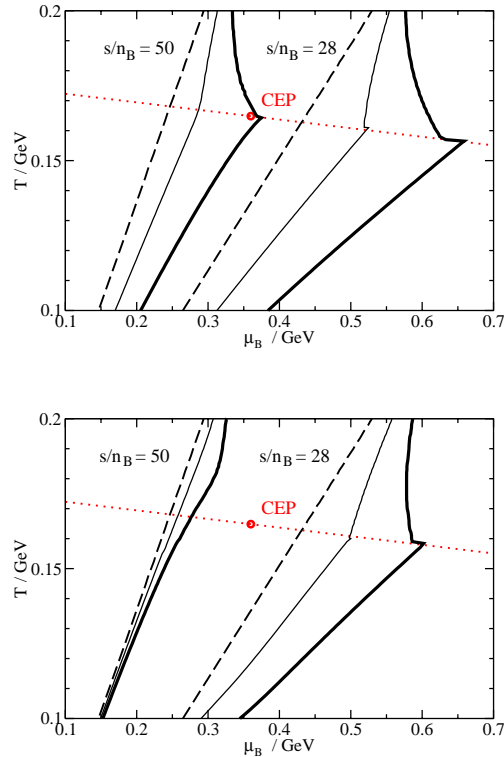


Fig. 1 Isentropic trajectories of the toy model (1, 2) depending on $A = 0, 0.5, 1.0$ (dashed, thin and solid lines, respectively). Dotted line indicates tangent on estimated phase border line at CEP. Upper panel: $\Delta T = 100$ MeV, $\Delta\mu_B = 200$ MeV, $D = 0.15$; lower panel: $\Delta T = 10$ MeV, $\Delta\mu_B = 10$ MeV, $D = 0.06$ as parameters characterizing the extension of the critical region (cf. [1]).

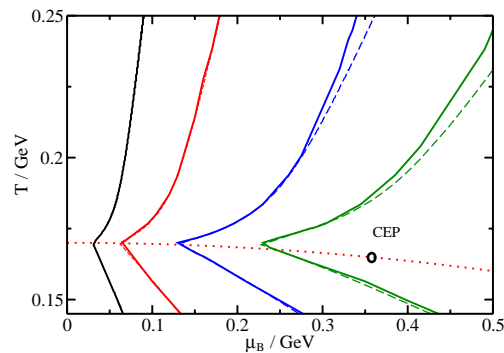


Fig. 2 Isentropic trajectories of the QPM adjusted to lattice QCD without CEP (dashed) and with CEP (solid lines) for $s/n_B = 200, 100, 50, 33$ (from left to right) with $\Delta T = 10$ MeV, $\Delta\mu_B = 10$ MeV, $D = 0.06$ and $A = 0.5$. Dotted line indicates phase border line.

The QCD phase diagram exhibits an astonishingly rich structure. Although the true nature of the transition separating hadrons and resonances from the quark gluon fluid phase is still matter of debate, large fluctuations of energy and various susceptibilities across this transition are expected. Susceptibilities are measurable through event-by-event fluctuations of the according conserved quantities in heavy-ion collisions such as net quark number n_q , isospin number or electric charge. Here, we focus on fluctuations of the net baryon number $n_B = n_q/3$.

Recent progress in evaluating thermodynamic bulk properties by means of first principle lattice QCD simulations was achieved for non-vanishing baryochemical potential μ_B at finite temperature T . Applying a Taylor series expansion in (μ_B/T) , the first expansion coefficients $c_{2,4,6}(T)$ were analyzed in [1]. Starting from the pressure p of our quasi-particle model (QPM), the expansion coefficients follow through $c_n(T) = \frac{T^{n-4}}{n!} \frac{\partial^n p}{\partial \mu^n} \Big|_{\mu=0}$ where $\mu = \mu_B/3$ is the quark chemical potential. They read

$$c_2(T) = -\frac{d_q}{2\pi^2} \int dk \frac{k^2}{T^3} f_q^{(1)}(\epsilon_0) \quad (1)$$

$$c_4(T) = -\frac{1}{4!} \frac{d_q}{2\pi^2} \int dk \frac{k^2}{T^3} \left(2f_q^{(3)}(\epsilon_0) + \frac{3}{\epsilon_0} f_q^{(2)}(\epsilon_0) \frac{\partial^2 m_q^2}{\partial \mu^2} \Big|_{\mu=0} \right), \quad (2)$$

with $\epsilon_0 = [k^2 + m_q^2(T, \mu = 0)]^{1/2}/T$, $d_q = 2N_c N_f = 12$ and $f_q^{(n)}(y)$ as the derivative of order n of the Fermi distribution function for quarks $f_q(y) = (e^y + 1)^{-1}$ at ϵ_0 . Details of $c_6(T)$ and the derivative of the quasi-particle self-energy m_q^2 are presented in [2].

As exhibited in Fig. 1, the QPM reproduces the $c_i(T)$, in particular the peak and double peak structure in $c_4(T)$ and $c_6(T)$, respectively, fairly well. The pronounced structure of e. g. $c_4(T)$ at the (pseudo-)critical temperature T_c indicates a strong sensitivity of higher order Taylor expansion coefficients on details of the transition. Consequently, measurable quantities which can be expressed in terms of these coefficients should show a pronounced behavior in the vicinity of T_c as higher orders become important. As an example, the baryon number susceptibility $\chi_B/T^2 = \frac{2}{9}c_2(T) + \frac{12}{9}c_4(T) \left(\frac{\mu}{T}\right)^2 + \frac{30}{9}c_6(T) \left(\frac{\mu}{T}\right)^4 + \dots$

is depicted in Fig. 2.

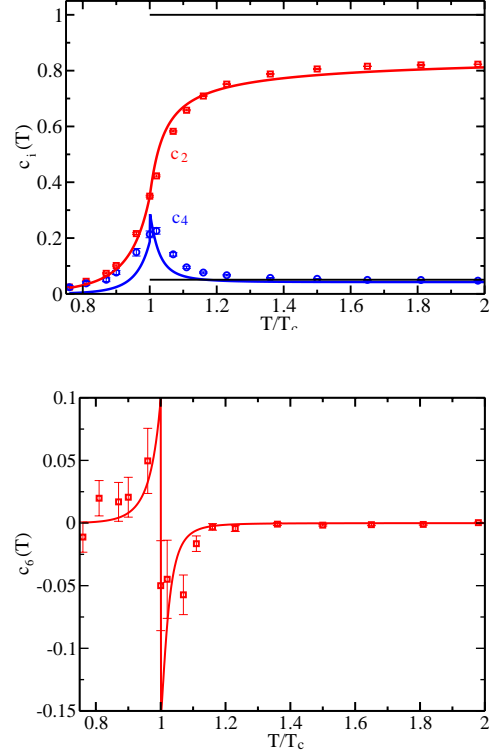


Fig. 1 Taylor series expansion coefficients $c_i(T)$ from the QPM (lines) compared to lattice data [1] (symbols). Horizontal lines in upper panel depict the coefficients for a massless non-interacting gas of quarks and gluons.

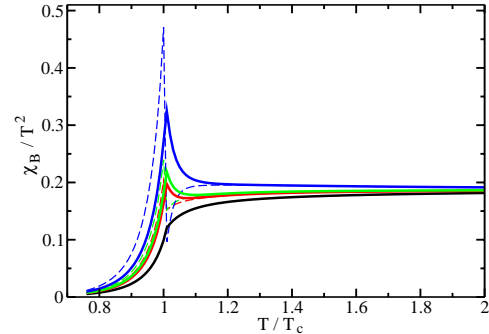


Fig. 2 Baryon number susceptibility χ_B/T^2 for $\mu_B = 450, 330, 300, 150$ MeV (from top to bottom) without $c_6(T)$ (solid) and with $c_6(T)$ (dashed lines).

[1] C. R. Allton, M. Döring et al., Phys. Rev. D 71 (2005) 054508

[2] M. Bluhm, B. Kämpfer, G. Soff, Phys. Lett. B 620 (2005) 131

¹TU Dresden

Imaging the Proton Emission Source in Central Al+Al Collisions at 1.9 A·GeV^G

R. KOTTE FOR THE FOPI COLLABORATION

Previous detailed studies of two-proton intensity interferometry [1, 2, 3] have been extended to central collisions of Al+Al at a beam energy of 1.9 A·GeV, the smallest symmetric heavy-ion collisions system investigated so far by the FOPI collaboration at SIS/GSI Darmstadt. Here, we report on the method of source imaging by numerical inversion of the correlation function [4].

Let $Y_{12}(\mathbf{p}_1, \mathbf{p}_2)$ be the coincidence yield of pairs of particles having momenta \mathbf{p}_1 and \mathbf{p}_2 . Then the experimental two-particle correlation function is defined as

$$1 + R(\mathbf{p}_1, \mathbf{p}_2) = \mathcal{N} \frac{\sum_{events,pairs} Y_{12}(\mathbf{p}_1, \mathbf{p}_2)}{\sum_{events,pairs} Y_{12,mix}(\mathbf{p}_1, \mathbf{p}_2)}. \quad (1)$$

The sum runs over all events fulfilling cuts on high charged-particle multiplicities, hence allowing for the selection of the most central 10% events, and over all pairs satisfying certain conditions like, e.g., cuts on the pair momentum $\mathbf{P} = \mathbf{p}_1^{cm} + \mathbf{p}_2^{cm}$. Here, \mathbf{p}_i^{cm} are the particle momenta calculated in the c.m. system of the colliding nuclei. Event mixing, denoted by the subscript "mix", means to take particle 1 and particle 2 from different events. \mathcal{N} is a normalization factor fixed by the requirement to have the same number of true and mixed pairs. The correlation function (1) is then projected onto the relative momentum $q = |\mathbf{q}| = \frac{1}{2} |\mathbf{p}_1^{cm} - \mathbf{p}_2^{cm}|$.

Figure 1 shows the experimental results (symbols) of the pp-correlation function at small relative momenta. At $q \simeq 20$ MeV/c a strong peak is visible. This "²He"-resonance is the result of the common action of the enhancement due to the attractive nucleonic potential and the suppression due to both the mutual Coulomb repulsion and the antisymmetrization of the pp wave function. The data are confronted to simulations performed with a final-state-interaction (FSI) model assuming either a static Gaussian source with zero lifetime [1, 2] or feeding it with the one-body phase-space distribution at particle freeze-out provided by a BUU transport approach [1]. The theoretical correlation function can be written as

$$1 + R(\mathbf{P}, \mathbf{q}) = \int d^3\mathbf{r} S(\mathbf{P}, \mathbf{r}) |\Psi_{\mathbf{q}}(\mathbf{r})|, \quad (2)$$

where S is the source function. The wave function $\Psi_{\mathbf{q}}$ describing the relative motion of two particles is generated by partial wave expansion, i.e. analytical integration of the angular part and taken the radial wave functions from numerical solution of the Schrödinger equation with Coulomb and nuclear potentials. Taking advantage of a simple geometrical (sharp cut-off) model the experimental selection of the most central 10% events translates into an average impact parameter of about 2 fm as used in BUU.

While the correlation peak height can be well fitted by the output of the FSI model using the static source with apparent (i.e. not corrected for finite lifetime and radial flow [2, 3]) Gaussian radius of $R_0^* = \sqrt{\langle r^2 \rangle / 3} = 2.2$ fm (dashed line), the shape of the correlation function - especially at relative momenta between 35 and 80 MeV/c - is only poorly reproduced. Indeed, as obvious from Fig. 2, the source image derived from numerical inversion of the correlation function is not of Gaussian but rather of exponential shape. In contrast to the Gaussian source, the BUU+FSI model output well reproduces both height and shape of the correlation peak (full line in Fig. 1).

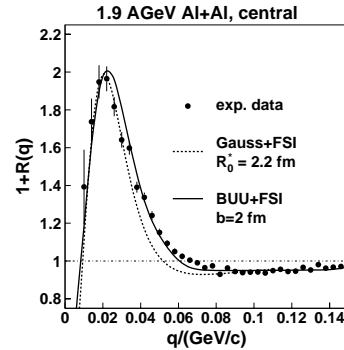


Fig. 1 The two-proton correlation function at small relative momenta in central collisions of Al+Al at 1.9 A·GeV. Dots: experimental data, dashed line: FSI-model simulations for zero lifetime and apparent Gaussian radius of 2.2 fm, full line: BUU+FSI model simulation. The simulated correlation functions are folded with the experimental q resolution of 6 MeV/c.

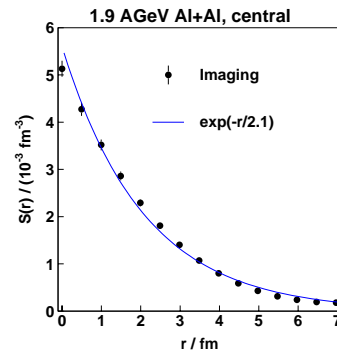


Fig. 2 The source image of the experimental correlation function of Fig. 1 (dots). The full line is an exponential distribution with inverse slope of 2.1 fm.

- [1] R. Kotte, J.P. Alard et al. (FOPI collaboration), Eur. Phys. J. A 23 (2005) 271
- [2] R. Kotte, H.W. Barz et al. (FOPI collaboration), Eur. Phys. J. A 6 (1999) 185
- [3] R. Kotte, J. Biegansky et al. (FOPI collaboration), Z. Phys. A 359 (1997) 47
- [4] D.A. Brown, P. Danielewicz, Phys. Lett. B 398 (1997) 252; Phys. Rev. C 57 (1998) 2474; Phys. Rev. C 64 (2000) 014902

Particle Production in Antiproton-Proton Interactions

R. KLIEMT,¹ H. MÜLLER, K.-T. BRINKMANN,¹ R. JÄKEL¹

The PANDA collaboration is constructing a universal detector for strong interaction studies with antiprotons at the high energy storage ring HESR at the international FAIR facility. A description of the PANDA detector can be found at [1] and in [2]. At PANDA antiproton-proton as well as antiproton-nucleus interactions in the momentum region from 1.5 to 15 GeV/c are to be investigated.

Simulation calculations are the only way to understand and to optimize such a rather complex detector set-up. The PANDA software environment (more informations at [3]) contains a comprehensive set of tools for simulating interactions of particles and their propagation through various detector components. We intend to use the Rossendorf Collision (ROC) model [4, 5, and references therein] as a possible external event generator which we adopt to our special needs. The ROC model describes hadron production in the center-of-mass energy region from threshold up to several tens of GeV. It is implemented as an event generator which yields complete events. This enables the simultaneous consideration of the reactions of interest as well as of the physical background.

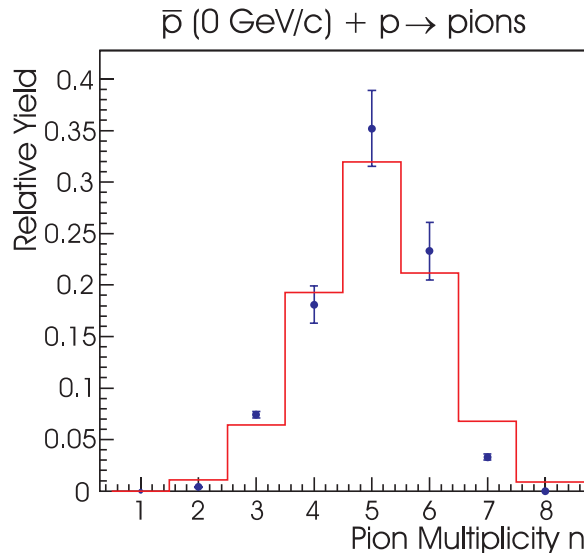


Fig. 1 Pion multiplicity distribution for $\bar{p}p$ at rest. Data (dots) from Crystal Barrel [8] are compared with ROC results (histogram).

The model has been successfully applied to the preparation of experiments at COSY (Jülich) for investigating subthreshold production of kaons in proton-nucleus interactions [6]. An application of the ROC model to antiproton induced reactions demands for the extension of the model due to the presence of a strong annihilation component in the cross section. The result from a first implementation of the anni-

hilation process is shown in Fig. 1. There the multiplicity distribution of pions produced in $\bar{p}p$ annihilation at rest from the Crystal Barrel experiment [8] is compared with ROC-model results. By adopting the parameter describing the probability for the annihilation of a $q\bar{q}$ pair a good description of the measured distribution is achieved. However, this picture has to be studied further to achieve a more detailed description. At high energies annihilation becomes negligible and the ROC model yields reasonable results with the same parameters [4] as deduced from pp interactions. This is demonstrated in Fig. 2 for the multiplicity distribution of charged particles from $\bar{p}p$ interactions at 100 GeV/c [7].

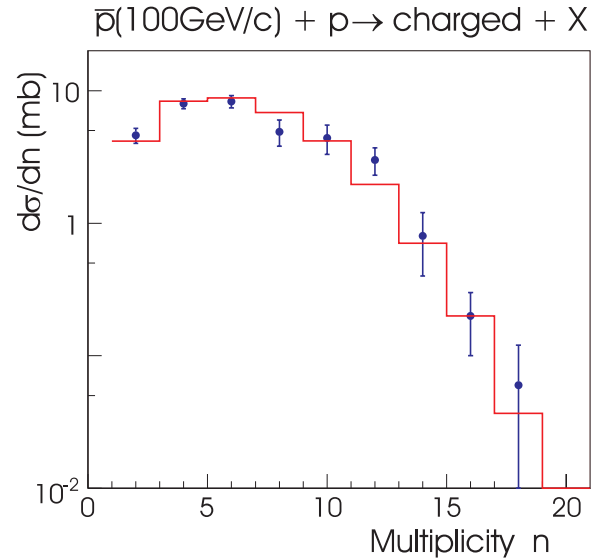


Fig. 2 Multiplicity distribution of charged particles from $\bar{p}p$ at 100 GeV/c. Data (dots) from [7] are compared with ROC results (histogram).

In a next step of investigation it is necessary to establish a smooth transition between these two energy regions to find a reasonable description of antiproton induced reactions in the energy range of the PANDA detector.

- [1] <http://www.gsi.de/fair/experiments/hesr-panda/index.html>, (07.07.2005)
- [2] PANDA Collaboration, Technical Progress Report (2005)
- [3] http://www.ep1.rub.de/~panda/auto/com/_home.html, (24.01.2006)
- [4] H. Müller, Eur. Phys. J. C 18 (2001) 563
- [5] H. Müller, V.I. Komarov, J. Phys. G 31 (2005) 285
- [6] T. Kirchner et al., COSY Proposal #21, Jülich (1996)
- [7] A. E. Brenner et al., Phys. Rev. D 26 (1982) 1497
- [8] E. Klempt, C. Batty, J.M. Richard, Phys. Rep. 413 (2005) 197

¹TU Dresden, Institut für Kern- und Teilchenphysik

The QCD sum rule method aims at predicting the physical properties of hadrons both in vacuum and in medium. Some uncertainties stem mainly from poorly known in-medium quark condensates [1, 2]. While pion matrix elements can be evaluated by means of the algebraic soft pion theorem, no such theorem is available yet for nucleon matrix elements. Therefore, in [3] we have developed a new algebraic approach which allows for an evaluation of nucleon matrix elements, analogously to the soft pion theorem.

From deep inelastic lepton-nucleon scattering experiments one knows that nucleons are composite color-singlet systems made of partons. In the language of QCD these are three valence quarks, accompanied by virtual sea quarks and gluons. In the low energy region many properties of the nucleon can be rather successfully explained by approximating the virtual sea quarks and gluons by a cloud of mesons, especially pions, surrounding the bare valence quark core. Accordingly, in the pion-cloud model the physical nucleon is considered as a so-called bare valence quark core accompanied by the pion-cloud, which accounts for the sea-quarks and gluons. The corresponding Fock representation for the nucleon reads

$$|N\rangle_{\text{phys}} = |N\rangle + \phi_1 |N\pi\rangle + \phi_2 |N\pi\pi\rangle + \dots \quad (1)$$

The coefficients ϕ_n are the amplitudes to find the physical nucleon in the state $|N n\pi\rangle$. Using (1) the nucleon expectation value of an operator \hat{O} is given by

$$\langle N | \hat{O} | N \rangle_{\text{phys}} = \langle N | \hat{O} | N \rangle + \phi_1^2 \langle N\pi | \hat{O} | N\pi \rangle + \dots \quad (2)$$

In our investigation we have concentrated on the first term, i.e. the valence quark contribution. To derive a formula for this matrix element between bare nucleons with momentum k , spin σ and mass M_N we first apply the LSZ reduction formalism (cf. [3] for references) to the right nucleon state:

$$\begin{aligned} & \langle N(k_2, \sigma_2) | \hat{O}(x) | N(k_1, \sigma_1) \rangle \\ &= -i \int d^4 x_1 \langle N(k_2, \sigma_2) | T \left(\hat{O}(x) \hat{\Psi}_N(x_1) \right) | 0 \rangle \\ & \times \left(i\gamma^\mu \overleftarrow{\partial}_\mu + M_N \right) u_N(k_1, \sigma_1) e^{-ik_1 x_1} . \end{aligned} \quad (3)$$

We approximate the nucleon field operator $\hat{\Psi}_N$ in (3) by a noninteracting field operator. Applying LSZ on both nucleon states yields

$$\begin{aligned} & \langle N(k_2, \sigma_2) | \hat{O}(x) | N(k_1, \sigma_1) \rangle \\ &= \int d^4 x_1 \int d^4 x_2 e^{-ik_1 x_1} e^{ik_2 x_2} \delta(t - t_1) \delta(t - t_2) \\ & \times \langle 0 | [\hat{\Psi}_N^{\alpha_2}(x_2), [\hat{O}(x), \hat{\Psi}_N^{\alpha_1}(x_1)]_-]_+ | 0 \rangle \\ & \times \bar{u}_N^{\beta_2}(k_2, \sigma_2) (\gamma_0)_{\beta_2 \alpha_2} (\gamma_0)_{\beta_1 \alpha_1} u_N^{\beta_1}(k_1, \sigma_1) . \end{aligned} \quad (4)$$

To make the relation (4) applicable for matrix elements of quark operators, the nucleon field operator $\hat{\Psi}_N$ is replaced by an interpolating field operator $\hat{\psi}_N$ of quark fields, carrying the quantum numbers of nucleons. For instance, for the proton it is given by [3]

$$\begin{aligned} \hat{\psi}_p(x) &= A_p \epsilon^{abc} (u^a T(x) C \gamma_5 d^b(x)) \hat{u}^c(x) \\ &+ B_p \epsilon^{abc} (u^a T(x) C \gamma_5 u^b(x)) \hat{d}^c(x) , \end{aligned} \quad (5)$$

basing on the quark-diquark approximation where effectively only one quark of the nucleon interacts with the hadronic environment, while the other two quarks of nucleon are tightly bound to a heavy bosonic quasiparticle. The coefficients A_p and B_p can be determined unambiguously by means of the valence quark content of nucleons [3]. The nucleon formula (4) in combination with the field operator (5) allows to evaluate the valence quark contribution of quark operators. In such a way, two-, four- and six-quark operators have been evaluated by means of this new algebraic approach. The outcome has first been compared with known two-quark operators, finding an agreement for the expected results of the electromagnetic and pseudo-vector current, and for the known results for the chiral condensate inside nucleon. For instance, for the valence quark contribution to the chiral condensate the algebraic approach yields $\sigma_N^v = 3m_q$, which is, with a light quark mass of $m_q \simeq 7$ MeV, in agreement with $\sigma_N^v = 20$ MeV determined in [4]. Similar, for the valence quark contribution of four-quark operators we have found an interesting agreement with the factorization approximation. For six-quark operators our findings are the first available results inside nucleons.

The main intention of the new algebraic approach presented is to establish a purely algebraic approach for evaluating matrix elements of operators taken between physical nucleon states. Accordingly, for the time being the application of nucleon formula (4) in combination with the field operator (5) has to be considered as a first step. An algebraic approach for taking into account the pion cloud is presently under consideration.

- [1] S. Zschocke, O.P. Pavlenko, B. Kämpfer, Phys. Lett. B 562 (2003) 57
- [2] S. Zschocke, B. Kämpfer, Phys. Rev. C 70 (2004) 035207
- [3] S. Zschocke, B. Kämpfer, G. Plunien, Phys. Rev. D 72 (2005) 014005
- [4] L.S. Celenza, C.M. Shakin et al., Phys. Rev. C 48 (1993) 159

¹TU Dresden, Institut für Theoretische Physik

Impact of Nucleon Mass Shift on the Freeze-Out Process^E

S. ZSCHOCKE, L.P. CSERNAI,¹ E. MOLNAR,¹ J. MANNINEN,² A. NYIRI¹

Nucleus-nucleus collision experiments provide a unique way to detect new states of matter (Quark-Gluon Plasma, Color Superconductivity) and to test the validity of theoretical approaches of physics describing these scenarios. An inevitable problem of collision experiments is that in-medium modifications of hadrons and the expected new states of matter disappear by the end of the reaction. Accordingly, one has to probe the initial stages of the collision indirectly by using theoretical models to reproduce the observed final particle spectra. A detailed understanding of the different stages of a relativistic heavy-ion collision process becomes therefore very compelling. However, due to the complexity of the problem, in most of the former evaluations of the freeze out process, vacuum parameters of the particles have been implemented. In [1] investigations are listed, where the impact of in-medium hadron masses on the particle ratios during the *chemical* freeze out has been studied. A systematic study concerning the impact of in-medium hadron masses on the *kinetic* freeze out process has not been performed yet. Therefore, in our investigation [2], we have studied a nucleon gas and investigate the impact of an in-medium nucleon mass shift on the freeze-out profile. The frozen out particles are formed in a layer of finite thickness L , bounded by two hyper-surfaces: the pre-freeze-out hyper-surface with $T_{\text{preFO}} \leq T_c \simeq 170$ MeV, and a post-freeze out hyper-surface where a temperature becomes ill-defined. As the system expands and cools down the number of interacting particles decreases up to the post-freeze-out surface of a finite layer, where by definition the density of interacting particles vanishes. Accordingly, the thermal freeze-out process inside the layer can be described by decomposing the particle distribution function into two components of the matter, an interacting part f_i and a non-interacting part f_f , thus

$$f(x, k) = f_i(x, k) + f_f(x, k), \quad (1)$$

where x is the four-coordinate inside the layer, and k is the four-momentum of the nucleons. The space-time evolution of the interacting and non-interacting components inside the layer is governed by the following differential equations [2]:

$$\begin{aligned} \partial_t f_i &= -\frac{1}{\tau} \left(\frac{L}{L-t} \right) \left(\frac{k^\mu d\sigma_\mu}{k_\mu u^\mu} \right) f_i \\ &+ \frac{1}{\tau_0} [f_{eq}(t) - f_i], \end{aligned} \quad (2)$$

$$\partial_t f_f = +\frac{1}{\tau} \left(\frac{L}{L-t} \right) \left(\frac{k^\mu d\sigma_\mu}{k_\mu u^\mu} \right) f_i, \quad (3)$$

with the time τ between collisions among the nucleons, and f_{eq} stands for the Jüttner distribution. The second term in (2) is the re-thermalization term which describes how fast the interacting component approaches the Jüttner distribution within the relaxation time τ_0 .

The distribution functions f_i and f_f are functions of nucleon density n , temperature T , flow velocity v and energy density e , for which four partial differential equations have to be solved [2]. We have found a substantial change in the distribution function by comparing an evaluation using vacuum nucleon mass (Fig. 1) with an evaluation implementing the in-medium nucleon mass (Fig. 2).

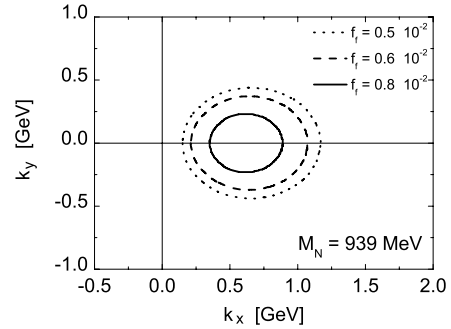


Fig. 1 Contours of freeze-out distribution functions $f_f(k_x, k_y)$ with the vacuum nucleon mass $M_N(0) = 939$ MeV.

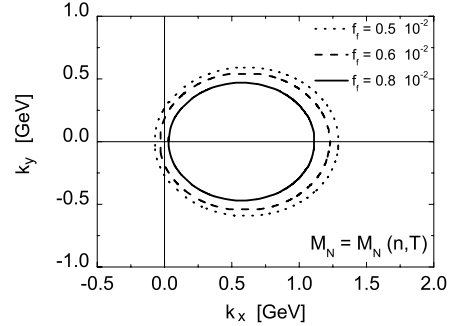


Fig. 2 The same as in Fig. 1, but with the in-medium nucleon mass $M_N(n, T)$. The overall norm has increased by a factor of $\simeq 4$ compared to Fig. 1.

- [1] W. Florkowski, W. Broniowski, Phys. Lett. B 477 (2000) 73; D. Zschieche, S. Schramm et al., Phys. Lett. B 547 (2002) 7
 [2] S. Zschocke, L.P. Csernai et al., Phys. Rev. C 72 (2005) 064909

¹Section for Theoretical and Computational Physics, University of Bergen, 5007 Bergen, Norway

²University of Oulu, Department of Physical Science, 90571 Oulu, Finland

Effect of Four-Quark Condensates on In-Medium Nucleon Self-Energies^{B, G}

R. THOMAS, S. ZSCHOCKE, B. KÄMPFER

Protons and neutrons are the important constituents in the microscopic description of normal nuclear matter and provide the explanation of coarse properties of the observed nuclei. However, the strong interaction between nucleons and even the existence of nucleons is described by Quantum Chromodynamics (QCD) where the fundamental degrees of freedom are quarks and gluons. QCD sum rules - a method to relate properties of the QCD ground state to observable hadronic properties - is applied to derive predictions on the in-medium behavior of self-energies of nucleons. The self energy Σ of the nucleon which influences its propagation function

$$G(q) = \frac{1}{q_\mu \gamma^\mu - M_N - \Sigma(q)}$$

can be decomposed into parts using the two characteristic Lorentz vectors of the problem, the nucleon momentum q_μ and the medium velocity v_μ , γ^μ are the Dirac matrices. This decomposition together with the pole structure of $G(q)$ lead to the definition of the scalar and vector self-energies Σ_s and Σ_v . The first accounts for the deviation from the nucleon vacuum mass M_N . In-medium chiral perturbation theory for example predicts large cancellation effects between these two quantities [1], i.e. the self-energies should be comparable in magnitude but have opposite signs.

QCD sum rule evaluations showed a significant dependence of the self-energies on the density behavior of four-quark condensates [2]. The standard treatment for four-quark condensates, QCD ground state expectation values of four quark operators like $\langle \bar{q}q\bar{q}q \rangle$, is to simplify it to squares of the di-quark condensate $\langle \bar{q}q \rangle$ (ground state saturation approximation), which is supported by large N_c arguments. We test this approximation while we apply our parameterization of four-quark condensates for the full set of structures which appear in the operator product expansion for the nucleon interpolating fields. The sum of all parameterized four-quark condensates up to a linear dependence in baryon density n

$$\sum_{\Gamma, C, f_1, f_2} \alpha_{\langle \cdot \rangle} \langle \bar{q}_{f_1} \Gamma_1 C_1 q_{f_1} \bar{q}_{f_2} \Gamma_2 C_2 q_{f_2} \rangle = A \kappa_N^{\text{vac}} + B \kappa_N^{\text{med}} n$$

yields effective parameters κ_N^{vac} and κ_N^{med} which describe deviations from the standard treatment. The sum runs over all four-quark condensates with weight factors $\alpha_{\langle \cdot \rangle}$ and extends the condensate list for the vacuum case [3], Γ, C and f denote Dirac, color and flavor structures; A and B are constants and estimate the order of magnitude as given by the factorization limit. A value of $\kappa_N^{\text{med}} = 0$ corresponds to no density-dependence of the combined four-quark condensates, a value of $\kappa_N^{\text{med}} = \kappa_N^{\text{vac}}$ to a density behavior similar to that of the squared di-quark condensate (κ_N^{vac} is

adapted to the correct vacuum nucleon mass). The results in Fig. 1 exhibit the variation of the dominant κ_q and its consequences for the self-energies as function of the Fermi momentum of the nucleon. The sum rules for the nucleon actually involve three equations each of them containing its own set of four-quark condensates, we consider here the most sensitive part with κ_q . A symmetric picture of self-energies is achieved if the combined four-quark condensates are constant, expressed by $\kappa_q = 0$. Calculations of four-quark condensates in a perturbative chiral quark model support this choice [4].

The four-quark condensates in sum rules for baryons like the nucleon differ significantly from those in meson sum rules. The three quark systems generically cause the occurrence of linear combinations of these condensates in two different color structures. This leads interestingly to a reduction of the list of independent four-quark structures for baryons, contrary it makes a connection to meson four-quark condensates partially impossible, since the latter appear only with one type of color contraction. Therefore a consideration of structures in other baryon sum rules, for example the Δ , could provide more information on four-quark condensates and especially how the sum rules of nucleon and other baryons are related in this respective. Since the condensates represent universal parameters for all hadrons an understanding of the nucleon self-energies, clearly a fundamental question, is inevitable incorporated with the density-dependent properties of all low-lying hadrons.

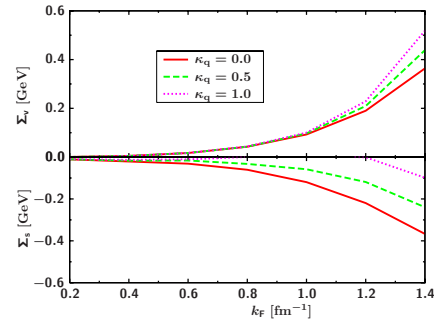


Fig. 1 The scalar and vector self-energies Σ_s and Σ_v of the nucleon as function of the nucleon Fermi momentum k_F for different density dependencies of the combined four-quark condensates. The preferred symmetric picture is realized if this dependence is weak ($\kappa_q = 0$).

- [1] D. Vretenar, W. Weise, Lect. Notes Phys. 641 (2004) 65
- [2] R.J. Furnstahl, D.K. Griegel, T. Cohen, Phys. Rev. C 46 (1992) 1507
- [3] R. Thomas, K. Gallmeister et al., hep-ph/0501202
- [4] E.G. Drukarev, M.G. Ryskin et al., Phys. Rev. D 68 (2003) 054021

Implications of Modified Gluon Bremsstrahlung in Charm Stopping^{A,B}

H. SCHADE,¹ R. THOMAS, B. KÄMPFER, G. BARNAFÖLDI²

In relativistic heavy-ion collisions bunches of hadrons, the so-called jets, are observed, which can be understood as consequences of elementary parton collisions. Before the partons (quarks or gluons) hadronize they can interact with the surrounding particles assuming secondary collisions take place in the hot and dense zone transiently created in a relativistic heavy-ion collision. Selection of different target ions and beam energies allows for systematic study of "temperature" and "density" scenarios. It was found that in very dense events the leading particles of jets appear to have lost significant parts of their energy prior to hadronization (jet quenching).

An effect which can explain this energy loss is the emission of gluon bremsstrahlung off an incident projectile quark scattering in a deconfined medium of colored targets. We study the influence of the quark mass and polarization effects in such model calculations which have been developed at first for massless projectiles. Indeed, RHIC data [1] suggest a suppression of energy loss for heavy charm quarks compared to the lighter up or down flavored quarks. As well-known from electrodynamics the photon emission of a relativistic electron is peaked to forward angles and suppressed inside an angular cone $\theta < \theta_0$ around the projectile direction - the dead cone. This was numerically studied for QCD, where in addition non-abelian effects can become relevant outside the soft gluon limit [2]. Here we present an extension of the numerical analysis of the leading-order effect, i.e., the single scattering off a massive on-shell quark on a static screened potential including the Ter-Mikaelian effect, that is we incorporate the polarization of the medium. Therefore the gluon is assigned an effective on-shell mass ω_0 [3], so that the zeroth component of the gluon four-momentum is modified

$$k_0 = \omega \equiv |\vec{k}|c \longrightarrow k_0 = \sqrt{\omega^2 + \omega_0^2} \quad .$$

In the static Debye screened potential underlying our calculation this acts like an additional screening parameter. In Fig. 1 the probability for emission of a gluon is shown as a function of the emission angle θ : The upper panel exhibits the influence of only the quark mass m ; the peak and, with this the dead cone, is shifted to higher angles with increasing masses, and the magnitude of the radiation probability decreases for heavier particles. This points to a reduction in radiative energy loss. The variation of ω_0 for very light quarks in the lower parts of Fig. 1 works similar to a finite quark mass. Therefore one can define, in the soft gluon limit and with some further assump-

tions, an effective dead cone angle $\theta_d = \sqrt{\theta_0^2 + \theta_p^2}$. It takes into account the quark mass effect $\theta_0 = m/E$ and the gluon polarization $\theta_p = \omega_0/k_0$. Here, E denotes the energy of the incident quark. This definition reveals the interplay of both effects and it will be necessary for more quantitative statements to obtain numerically an expression for the integrated energy loss as a function of external parameters.

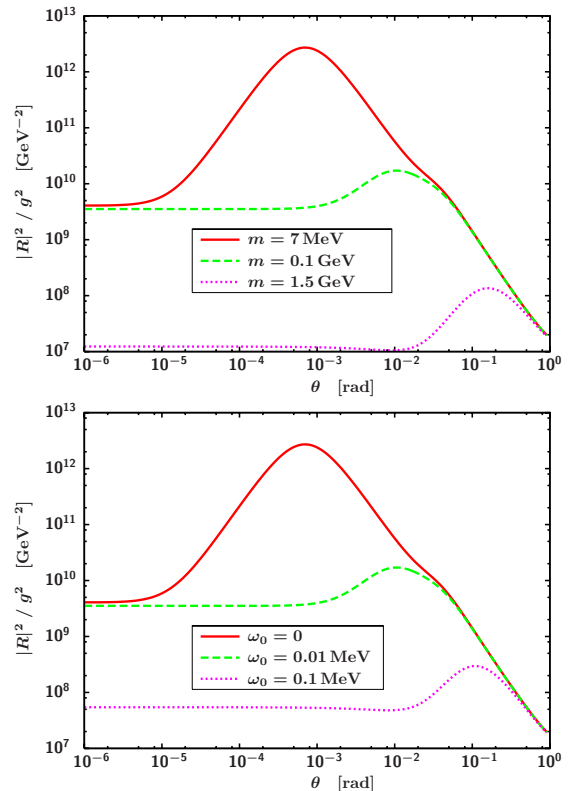


Fig. 1 The radiation amplitude R as a function of the gluon emission angle θ for different parameters. Curves are shown for different quark masses m without polarization effects (upper panel, $\omega_0 = 0$) and for various polarization parameters ω_0 with fixed quark mass (lower panel, $m = 7$ MeV). The radiation is suppressed at angles smaller θ_d - is the dead cone. Further the magnitude of radiation changes drastically. The figure demonstrates the common consequences of both effects. Parameters in this calculation are $\omega = 1$ MeV, $\phi = \pi/2$, $\vec{p}_i = (0, 0, 10)$ GeV, $\vec{q}_\perp = (0.3, 0.2)$ GeV, $\mu = 0.5$ GeV.

- [1] K. Adcox et al. (PHENIX), Phys. Rev. Lett. 88 (2002) 192303
- [2] R. Thomas, B. Kämpfer, G. Soff, Heavy Ion Phys. A 22 (2005) 83
- [3] B. Kämpfer, O.P. Pavlenko, Phys. Lett B 477 (2000) 171

¹TU Dresden, Institut für Theoretische Physik

²RMKI-KFKI Budapest, Hungary

Neutron Beam Characteristics, Collimator Design and Detector Simulations for ELBE-nToF ^D

J. KLUG, E. ALTSTADT,¹ C. BECKERT,¹ R. BEYER,² H. FREIESLEBEN,³ M. GRESCHNER,³ E. GROSSE,^{also3}
A.R. JUNGHANS, D. LÉGRÁDY,¹ B. NAUMANN,⁴ K. NOACK,¹ S. SCHNEIDER,⁵ K. SEIDEL,³ A. WAGNER, F.-P. WEISS,^{2,6}

The neutron time-of-flight (nToF) system at ELBE uses the electron beam to produce neutrons in a liquid-lead neutron radiator. The neutron energies that can be used for nToF measurements range from 70 keV up to 10 MeV when ELBE delivers a beam repetition rate of 0.5 MHz. In this energy interval there is a need for neutron cross section data relevant for transmutation and for testing materials of fission and fusion reactors [1]. In addition, energies in the 30–70 keV range, accessible with a reduced repetition rate, can be utilized for nuclear astrophysics experiments.

By using the neutrons emitted from the radiator perpendicular to the direction of the electron beam a high suppression of the forward-peaked bremsstrahlung photons is obtained. The neutrons will be shaped by a collimator into a beam entering the experimental site in the adjacent room.

Monte Carlo simulations were performed using MCNP4C3 [2] to characterize neutron and photon intensities at the sample position, time and energy distributions, and resolutions. The main parameters determining these are the radiator dimensions, the energy of the beam electrons, the beam current, and the length of the neutron flight path. Tab. 1 shows a compilation of predicted source strengths and fluxes at the measuring position 3.9 m from the radiator, for different electron energies.

Tab. 1 Simulated neutron source strength and flux at the measuring position (electron beam current $I_e = 1$ mA).

Electron energy / MeV	Radiator source strength / s^{-1}	Flux / $cm^{-2} s^{-1}$
20	$7.9 \cdot 10^{12}$	$4.3 \cdot 10^6$
30	$1.9 \cdot 10^{13}$	$1.0 \cdot 10^7$
40	$2.7 \cdot 10^{13}$	$1.5 \cdot 10^7$

It was found that only the radiator gives significant contributions to the neutron flux at the measuring position—almost 92% stem directly from the lead in the radiator, while about 8% of the neutrons were created or scattered in the molybdenum channel confining the lead. A very small fraction ($< 0.1\%$) was scattered in the steel housing accommodating the radiator.

A further objective of the simulations was to optimise the geometry and material composition of the collimator and of a beam filter. This aimed at (i) eliminating neutrons and photons scattered or produced in

the collimator, thereby creating a well-defined beam of unscattered neutrons, having a minimal background of both neutrons and photons outside the beam, and (ii) minimizing the component of slow neutrons coming directly from the radiator, overlapping into the next beam pulse and creating measurement ambiguities.

Fig. 1 shows five examples of investigated collimator compositions placed in the wall consisting of 1.2 m concrete and 1.2 m of heavy concrete (seen from left to right). Dark-coloured collimator insertions are made from lead and light ones from borated polyethylene (CHB), while uncoloured regions do not contain any material. The neutrons travel from left to right, and the lead insertions are placed behind the CHB sections in order to absorb photons created in (n,γ) reactions. An additional 10 cm thick lead shield is placed after the wall.



Fig. 1 Examples of investigated collimator designs. Dark sections: lead; light sections: borated polyethylene.

Collimator types Q, R and S have the same thickness of CHB and lead in the axial direction, but distributed mainly in 4, 2 and 3 groups, respectively. Types T and U are completely filled; the former with the same ratio between materials as the types mentioned first, and the latter with 50% each of CHB and lead. All collimators have an opening (beam diameter) of 3 cm, and increasingly larger outer radii of 5, 6 and 7 cm, defined by a stainless steel tube with 1 cm thick walls.

The neutron beam profile for the different collimators is shown in Fig. 2, given by detectors at an axial distance of 3.9 m from the radiator (50 cm after the collimator opening), and at increasing radial distances from the beam center. All collimators shape a neutron beam with a sharp edge, indicated by the intensity drop between $r = 1.5$ cm and $r = 2.0$ cm. At larger distances, the intensity is four orders of magnitude less

¹FZ Rossendorf, FWS

²also Friedrich-Schiller-Universität Jena

³TU Dresden, Institut für Kern- und Teilchenphysik

⁴FZ Rossendorf, FKT

⁵FZ Rossendorf, FWF

⁶TU Dresden, Institut für Energietechnik

than in the beam. A similar trend has been shown for photons.

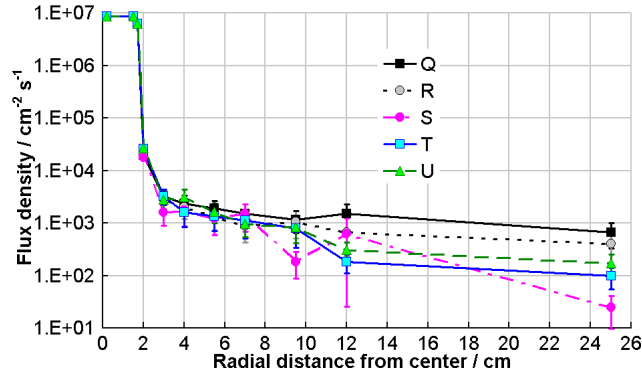


Fig. 2 Neutron fluxes after the collimator (3.9 m from the neutron radiator), at different distances from the beam center ($E_e = 30$ MeV and $I_e = 1$ mA).

A close inspection of the fluxes at points with small errors (at $r = 1.7, 2,$ and 3 cm) shows that collimators not fully filled (i. e., Q, R, S) produce less neutron background outside the beam than those without air gaps. Among these, the S-type collimator shows the best performance. In addition, it was found that a conical beam channel (with a smaller entrance diameter) improves the beam profile even more.

With an accelerator repetition rate of 13 MHz, most of the neutrons will overlap into the following pulses, making unambiguous measurements impossible. This problem can be overcome by lowering the repetition rate to 0.5 MHz and by placing a filter in the beam. The intensity loss due to a lower rate will be compensated for with a superconducting RF photo electron injector being developed, allowing for a beam current of 1 mA at a repetition rate of 0.5 MHz [3]. The effect of different filters is shown in Fig. 3.

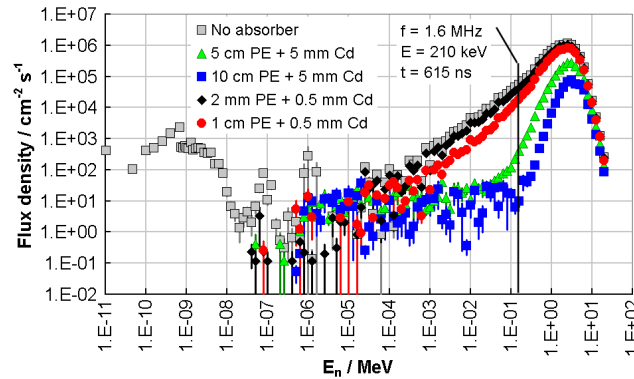


Fig. 3 Neutron fluxes with different absorbers placed in the collimator entrance. Neutrons with $E_n < 210$ keV should be prevented from creating background in subsequent beam pulses.

With a frequency of 1.6 MHz, the next pulse comes 615 ns later (indicated). Thus, neutrons with $E_n < 210$ keV must be suppressed. With a 5 cm thick slab

of polyethylene and a thin disc of Cd placed at the collimator entrance (triangles), the neutron flux below 210 keV drops two orders of magnitude, compared to the situation with no filter (light squares).

The cost of using the filter is a decrease in peak intensity by a factor of 5, but the relative background reduction is considerable—up to two orders of magnitude. The correlation between neutron kinetic energy and time of flight, as well as the energy resolution shown earlier [4], is preserved.

Lithium-glass detectors (diam. 46 mm, thickness 10 or 25 mm) and plastic scintillator stripes (cross sections of 11×42 mm² or 22×42 mm²) were simulated to obtain neutron detection efficiencies, time spectra and energy resolutions. The share of events with lost timing information due to neutron scattering before detection was also determined. This is shown for different detectors in Fig. 4 (lowest histograms).

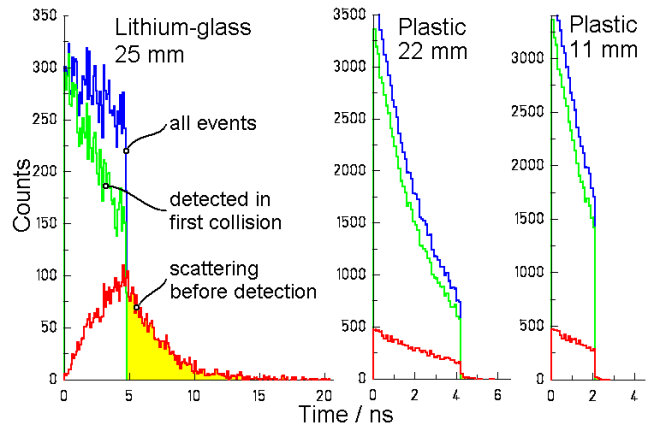


Fig. 4 Simulated detector time spectra. $E_n = 144$ keV.

For Li-glass detectors, 34 % of all events have lost their timing information, and 16 % (shaded area) of all events lie outside the time range related to the detector thickness. These significantly worsen the energy resolution. For the plastic scintillators, a threshold of 5–10 keV can be applied by triggering in the single-electron peak and using a coincident readout with two photomultiplier tubes [5], reducing the share of events with lost timing to 15 % and the fraction outside the detector thickness to below 1 %. The detection efficiencies are also in favour of plastic scintillators (60–80 %, depending on thickness) compared to Li-glass detectors (< 5 %).

- [1] Long Term Needs for Nuclear Data Development, comp. M. Herman, INDC(NDS)-428, IAEA Nuclear Data section, Vienna, Austria (2001)
- [2] MCNP—a General Monte Carlo N-Particle Transport Code (Report LA13709), ed. J. F. Briesmeister, Los Alamos National Laboratory (2000)
- [3] J. Teichert, FZR, private communication (2005)
- [4] E. Altstadt, C. Beckert et al., IKH Annual Report 2004, FZR-423 (2005) 19
- [5] R. Beyer, E. Grosse et al., this report, p. 40

Development of Neutron-Time-of-Flight Detectors for the Investigation of Astrophysically Relevant (γ,n) Reactions

R. BEYER,¹ E. GROSSE,² A. HARTMANN, K. HEIDEL, L. HEINRICH, J. HUTSCH, A.R. JUNGHANS, J. KLUG,
W. SCHULZE, M. SOBIELLA, A. WAGNER

In (γ,n) reactions of importance for the formation of the chemical elements in the universe, neutron energies in a range from a few tens of keV to several MeV, i.e., fast neutrons, play a decisive role. For these energies there are very few established types of neutron detectors. Three different types, normally used for much lower or higher energies, were tested in this energy range: Li-glass, plastic and ZnS scintillators [1]. The neutron-energy determination was done by time-of-flight technique.

Every scintillator is read out by high-gain Hamamatsu R2059-01 photomultiplier tubes. The detector signals, having rise and fall times of a few ns, are processed by very fast CFDs developed at our institute. The dead time of these CFDs is about 30 ns and the threshold can be set to a minimum of 10 mV with little walk. For signals of 1 ns rise and fall times, the walk from 1 V to 10 mV amplitude was about 400 ps.

The time measurement was done by means of a state-of-the-art multichannel multihit TDC CAEN V1190A. At the same time the charge of the detector signal was measured using a multichannel QDC CAEN V792. With the whole electronics setup one can determine the correlated energy and time signals of up to ten detectors simultaneously, what can easily be extended. The measured values are read out via VME Bus using a RIO3 Power PC running the GSI software MBS. The data taking is triggered by the logical OR of the CFD signals of all detectors used. To ensure the correlation of the time and energy signal, this logical OR is vetoed by the trigger signal itself, delayed by some ns, by the busy signal of the QDC, and by the dead time of the read-out electronics. This results in a total dead time per event of about 72 μ s, corresponding to a maximum average detection rate of $13 \cdot 10^3$ events per second. The data reduction was done by means of the GSI software LEA, executing an individual analysis program for every detector type. These programs can be executed online with the experiment or afterwards using the list-mode data created by MBS.

To investigate the properties of the different detectors, i.e., time resolution and efficiency, a ^{252}Cf neutron source was used. The well known neutron-energy spectrum of ^{252}Cf [2] is normalized by means of the activity of the source, the number of emitted neutrons per fission, the branching ratio, the solid angle of the detector and the efficiency of a BaF_2 detector, used to determine the moment of fission giving the start of the time-of-flight measurement.

The Li-glass scintillators, containing 70 mg/cm³ ^6Li ,

are cylindric discs with a diameter of 46 mm and thicknesses of 10 or 25 mm. To detect neutrons with these detectors the reaction $^6\text{Li} + n \rightarrow \alpha + ^3\text{H} + 4.78 \text{ MeV}$ is applied. The positive Q-value can be used to reduce the background of low-energy photons and of events produced by afterpulses by setting a threshold just below the corresponding peak in the QDC spectrum. From the difference of this Q-value peak for a free-running neutron detector compared to a measurement in coincidence with the BaF_2 detector one gets the efficiency of the BaF_2 detector. The efficiency of the neutron detector is determined by the comparison of the measured time-of-flight spectrum and the normalized spectrum of the ^{252}Cf source and is found to be in the order of 5%.

The ZnS scintillators are cylindrical discs of 46 mm diameter and with a thickness of 6 mm. They contain 9 mg/cm³ ^6Li . The advantage over the Li-glass detectors is the capability of pulse shape discrimination. By this technique one can reduce the photon background by several orders of magnitude, whereas the neutron events stay unaffected. The disadvantage of this type of detectors is the very low detection efficiency of less than 1% for fast neutrons.

The plastic scintillators were stripes with a rectangular cross section of 11 x 42 mm² and lengths of 125, 250 or 1000 mm, respectively. Each strip was directly coupled to two photomultiplier tubes, one at each end, to get a position information by means of the time difference between both signals. These tubes were operated at the highest gain, so that one is able to put the CFD threshold just below the single-electron peak. By doing this one can adjust a stable and reproducible detection threshold and on the other hand can use these proton recoil detectors to detect neutrons of energies down to a few tens of keV [3]. The efficiency was found to be almost 90% at neutron energies of 50 keV. The position resolution was determined by means of a collimated ^{90}Sr electron source to be about 5 cm (FWHM). The time resolution of about 0.6 ns (FWHM) is the same as for the Li-glass detectors and twice as good as for the ZnS scintillators.

In summary, for the measurements of cross sections of astrophysically relevant (γ,n) reactions the plastic scintillator is the best choice of the three tested types because of its good timing characteristics and high efficiency.

- [1] R. Beyer, Diplomarbeit (2005), to be published
- [2] W. Mannhart, IAEA-TECDOC 410 (1987) 158
- [3] N.W. Hill, J.A. Harvey et al., IEEE Trans. Nucl. Sci. NS-32 (1985) 367

¹also Friedrich-Schiller-Universität Jena

²also TU Dresden

Absolute Efficiency Calibration of HPGe Detectors for Photoactivation Experiments

C. NAIR, A.R. JUNGHANS, M. ERHARD, E. GROSSE,¹ K.D. SCHILLING, R. SCHWENGER, A. WAGNER

An absolute efficiency calibration of the High Purity Germanium detectors (HPGe) used in the photo activation experiments were done with eight different nuclides, all under the same geometry. The systematic uncertainties from the source calibration certificate was about 1.05%. The samples were put directly on the top of three cadmium absorber layers with an overall thickness 1.535(4) mm which minimizes the coincidence summing with X-rays in case of multi- γ emitting nuclides [1].

The full-energy-peak efficiency as is defined as

$$\epsilon_p(E_\gamma) = \frac{N_\gamma}{N_s} = \frac{N_\gamma}{t_r p A_0 \exp \frac{-\Delta t}{\tau}}$$

with N_γ = Number of counts in the photopeak, corrected for dead-time and pile-up losses and N_s = Number of photons emitted from the source. The other terms describe themselves as Δt - time elapsed since calibration up to measurement, A_0 - activity of the source on the reference date, p - branching ratio corresponding to the energy E_γ , τ - the mean lifetime and t_r denotes the real time taken for the data run.

For a precise measurement of the efficiency, one of the important corrections to be applied arises from coincidence summing and one well known example for this type of nuclides is ^{133}Ba which owns a very complex decay scheme as in Fig. 1. In this particular case, two or more photons can be emitted in cascade for a single decay and an empirical method to correct for them is complicated [2].

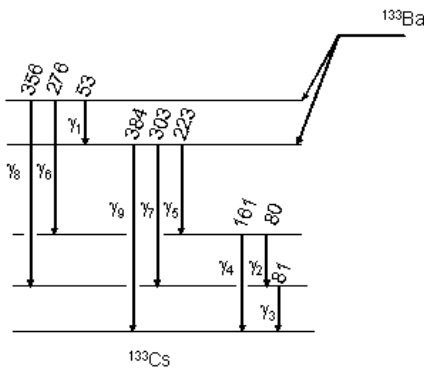


Fig. 1 Decay scheme of ^{133}Ba with energies displayed in units of keV.

Taking the example of 276 keV (γ_6) transition of this decay, we can divide the correction factors into two: One which comes out from the "summing-out" effects due to coincidence of γ_6 with γ_4 , with γ_2 - γ_3 cascade and the other factor from "summing-in" effects due to γ_1 - γ_5 cascade. The correction factor for this decay is

given by the expression

$$\frac{1}{C_6} = \left(1 - f_{64}\epsilon_{t4} - f_{62}\epsilon_{t2} - \frac{\epsilon_{t3}}{(1 + \alpha_3)} \right) \cdot \left(1 + \frac{p_1 f_{15} \epsilon_1 \epsilon_5}{p_6 \epsilon_6} \right)$$

with

$$f_{64} = \frac{p_4}{p_4(1 + \alpha_4) + p_2(1 + \alpha_2)}$$

$$f_{15} = \frac{p_5}{p_5(1 + \alpha_5) + p_7(1 + \alpha_7) + p_9(1 + \alpha_9)}$$

etc. Here C_i denotes the correction factor, α_i - total internal conversion coefficients, p_i - γ emission probabilities, ϵ_i - full energy peak efficiencies and ϵ_{ti} - total efficiencies for the detector used with $i = 1, \dots, 9$.

For analyzing the source spectra and extracting the peak area, the fit routine was designed manually so as to meet the experimental peculiarities [1]. The total and photopeak efficiencies were simulated using GEANT3 [3] and compared with the measured values. Corrections were applied for the self absorption in the source material and for the source-detector geometry offsets. An example of efficiency curve is shown in Fig. 2, which clearly shows that the absolute peak efficiency can be determined to an accuracy of 1.5% by including the coincidence summing corrections.

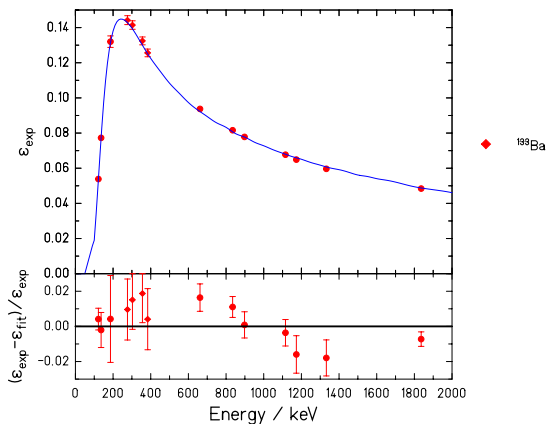


Fig. 2 Efficiency curve for the HPGe detector with 100% efficiency relative to a $3'' \times 3''$ NaI detector. The χ^2 of the fit is 19.4 with 13 degrees of freedom. The upper part is the fit curve overlaid on experimental data and the lower part shows the residuals with error bars of the data points on the same scale.

- [1] C. Nair, A.R. Junghans et al., IKH Annual Report 2004, FZR-423 (2005) 18
- [2] K. Debertin, R.G. Helmer, "γ and X-ray Spectrometry with Semiconductor Detectors", Elsevier Science Publ. (2001)
- [3] CERN program Library Long Writeup Q121, CERN, Geneva (CH), 1994

¹also TU Dresden

Pneumatic Delivery System for Photoactivation Experiments at the Bremsstrahlung Facility at ELBE

K.D. SCHILLING, A. WAGNER, J. CLAUSSNER,¹ M. SOBIELLA, M. ERHARD, E. GROSSE,² A. HARTMANN, A.R. JUNGHANS, M. LANGER, C. NAIR, A. SAAFY, R. SCHWENGER, A. SEIFERT, J. STEINER

The photoactivation method has been introduced at ELBE [1] for the studies of p-process nuclei via (γ, n) -, (γ, p) - and (γ, α) -reactions and for the determination of energy-dependent cross sections needed as input data for nucleosynthesis network calculations.

In order to substantially reduce the limited access time of the procedure described in [2], a pneumatic delivery system has been installed at the bremsstrahlung facility of ELBE [3] allowing spectroscopic investigations of nuclei with very short half-lives.

The new system is based on the pneumatic-tube transport of the samples that are to be investigated from the irradiation position to the measurement site. The diagram displayed in Fig. 1 illustrates this new procedure. The samples are enclosed in cartridges made of polyethylene or aluminum. A stack of up to 10 of such prepared cartridges is stored in station A (cartridge magazine). The cartridges are shot by compressed air through a polyamide (PA) tube to station B into their irradiation position inside the iron casing of the electron beam dump. They are adjusted just behind the vacuum steel vessel containing the graphite electron

beam stopper on the axis of the electron beam, thus utilizing the highest bremsstrahlung flux density for the activation of the samples. Immediately after the activation period, the cartridges are transported to the low-level counting setup (station C) directly onto the top of the HPGe detector inside the lead castle that shields efficiently against background radiation. The PA tube lengths between the stations A resp. C (outside the accelerator hall) and station B (inside the accelerator hall) are approximately 30 m. The transport times amount to about 3-5 seconds. The samples are precisely positioned on the detector to enable definite efficiency corrections. After each measurement, the cartridges are collected in a radiation shielded container (depot). The pneumatic transport is realized by a compressor and pneumatically controlled by using a diverter and several valves. The whole procedure of activation and measurement is completely automatically controlled for up to 10 cartridges. Moreover, activation and decay measurement can proceed simultaneously.

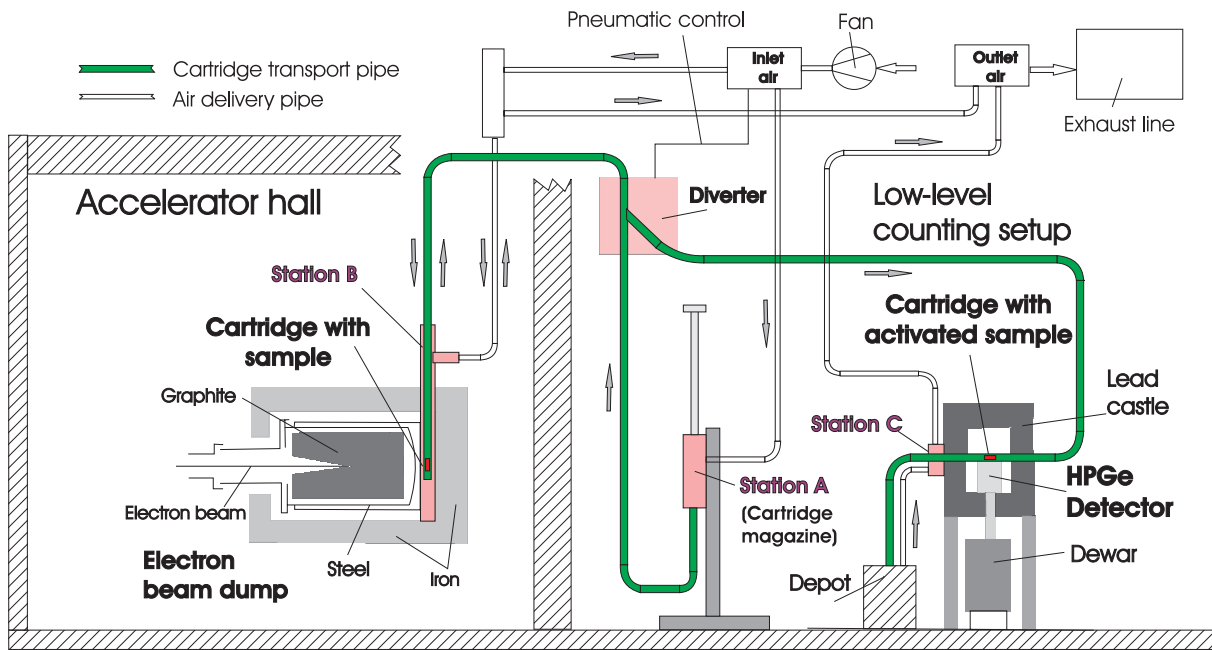


Fig. 1 Diagram of the pneumatic delivery system for photoactivation experiments at the bremsstrahlung facility.

- [1] M. Erhard, A. Wagner et al., IKH Annual Report 2003, FZR-401 (2004) 13
 [2] M. Erhard, E. Grosse et al., IKH Annual Report 2004, FZR-423 (2005) 13, 14
 [3] K.D. Schilling, M. Döring et al., IKH Annual Report 2004, FZR-423 (2005) 15

¹FZ Rossendorf, FWF

²also TU Dresden

Liquid Nitrogen Filling Control System for Cryogenic Detectors at ELBE

J. STEINER, A. WAGNER, U. WOLF

Cryogenic photon detectors used in nuclear physics experiments at ELBE require regular replenishment of liquid nitrogen (LN). Up to now, the commercially available system by Ortec (Ortec 785 + 786) does not allow for remote control since all malfunctions are causing only audible signals. Consequently, the process starts automatically but must be observed by a person and if an error occurs while filling, no one is informed. Therefore, an extension allowing for remote control and system information logging has been developed which reports detected errors and displays the status of actual and past filling operations. A cheap solution (<100€) is to use the c't Com2Lan adaptor[1] collaborating with a dedicated LabVIEW [2] program.

The Com2Lan adaptor is a cheap non-assembled kit consisting of three modules. The first module supports a hardware connection between a serial and an Ethernet port (XPort), which includes a small Java based web server. The second module extends it with a micro-controller (Atmel ATMEGA8535) being able to perform calculations and manipulations of analog or digital data received or transmitted by the XPort module. The third but not used module supports a wireless network adaptor. See Fig. 1 for details.



Fig. 1 Com2Lan adaptor / XPort with 32 I/O lines

The LN-filling hardware at ELBE consists of three modules developed by Ortec, one main module (one back plane connector for filling and one for alarm indication) and two extension modules (4 back plane connectors each, for filling indication). Line drivers are added into all modules and the signals from the three modules are combined into one SUB-D37 connector which is attached to the Com2Lan adaptor. The signals are at 0 V (active) / +5 V (inactive) level.

The program for the Atmel micro-controller is written in C. Its main task is to send the filling and alarm status to the XPort every second using the 4 byte data format as shown in Fig. 2. It allows for automatic synchronization to the XPort when starting the program and re-synchronization after the connection was lost.

This feature provides easy error recovering in case of power outage or network problems.

Header FF	Header Alarm F 0/E	Fill status	Fill status 9
--------------	-----------------------	-------------	---------------

Fig. 2 4 byte data format sent by XPort

The fill status is encoded bit-wise into byte #3 and #4. The XPort itself features a network address and a special port number where these data can be read by other network devices. For controlling the LN-filling, a computer running a LabVIEW program is used. The program is called ALNFScontrol, i.e. Automatic Liquid Nitrogen Filling System Control. It sets up a connection to the XPort, synchronizes to the header and analyzes the received data. After a fill process (usually after 24 hours) the program creates a file entry with the filling valve number, date, time, filling duration and alarm status. These data are also sent as an email to a specified recipient or a group of recipients. After successful filling or if an alarm occurs, a message will be sent as an email and mobile phone short message (SMS) to specified recipients.

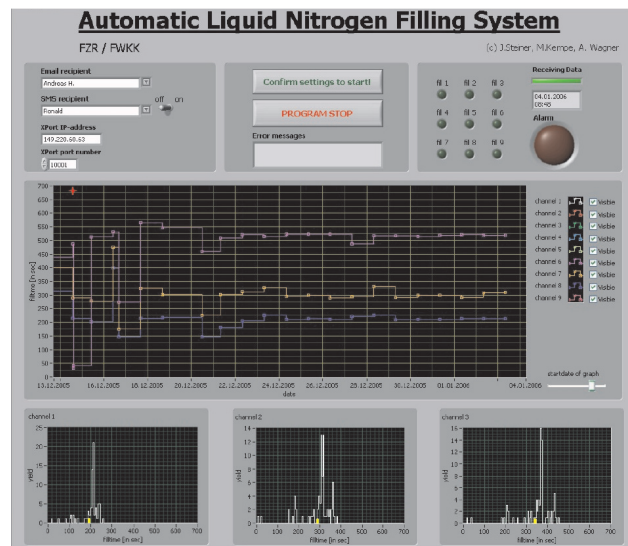


Fig. 3 Screenshot of the program "ALNFScontrol"

The file created in LabVIEW is connected to a website where the actual status with all filling and alarm messages is available. Moreover, a statistical analysis of the operating (time used for filling) is done and displayed as a time sequence and as a histogram for each detector, see Fig. 3. This feature allows for an easy detection of faulty detectors indicating an increased consumption of liquid nitrogen.

- [1] c't 13/2004, p. 200, c't 14/2004, p. 214, c't 22/2004, p. 236, c't 26/2004, p. 228, Heise ZeitschriftenVerlag GmbH & Co. KG, Hannover, 2004
- [2] Software of National Instruments, Version 7.11, 2005

Investigation of the HADES Alignment Quality by Improved Trigger Simulations^G

J. WÜSTENFELD

The knowledge of the exact positions of the detector components are crucial to achieve the high resolution the dilepton spectrometer HADES was designed for [1].

The tracking of particles in HADES has to be done in 3 dimensional space, as the magnetic field of the spectrometer applies in addition to the deflection in polar angle θ also a small deflection in azimuthal ϕ direction. Tracking is done by first calculating the position of a hit in each detector individually, and then matching the hits of different detectors to a track segment, one segment before the magnet, and one behind the magnet. The positions of a hit are calculated in a detector coordinate system and thus only the positions of the sensitive components relative to the detector are needed. But for the next stage of matching different detectors, one needs the positions of the detectors relative to each other. Figure 1 shows the principle method of the tracking.

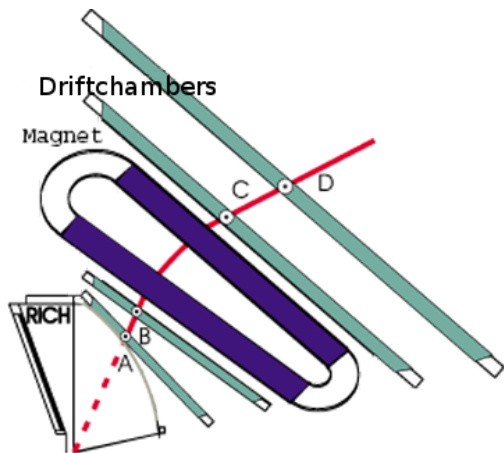


Fig. 1 Tracking principle. Shown are the four tracking stations in one sector together with the magnet. The dashed and solid curve represents the track of a particle.

These track segments are the start points for the tracking through the magnetic field. The algorithm determines from the curvature of the track the momentum and the polarity of the track. Errors in the track direction propagate into errors in the momentum calculation, and for particles with high momenta also errors in the polarity determination are possible (straight tracks). As the overall resolution of the detectors is in the order of $120 \mu\text{m}$, and the matching of the hit-points is done by projecting the hitpoints from two

drift chambers onto a plane inbetween them and then searching for overlaps of this points, it becomes clear that the position of the chambers has to be known with a precision of $150 \mu\text{m} - 200 \mu\text{m}$.

During the analysis of the $C + C$ data, taken at a kinetic beam energy of 2 AGeV it was found, that the assumption on the position of the MDC detectors in the HADES setup, as extracted from the technical design drawings, was not precise enough to achieve the anticipated mass resolution. To correct the position information of the multiwire drift detectors, a special method to extract the real positions from the data was developed [2] and successfully applied to the data. Recent improvements of the alignment method include better start values, extracted from photographic pictures of the detector setup and the inclusion of mechanical constraints, to limit the number of degrees of freedom in the functional used to calculate the correct positions [3]. This lead to a improvement in the quality of the alignment which manifested in a better track quality, which is essential for the momentum calculation.

To be able to compare the results from the experiment with simulations, one needs to apply the exact same conditions on the simulated events as they where used during the experiment. Event selection in the experiment is done by a trigger that decides on the event characteristics whether it will be recorded or not. HADES uses two levels of triggering. The first level is straight forward to implement in software, as it only cuts on the number of hits in the TOF (Time of flight) detector. The second level trigger is more complex, as it combines the information from RICH, TOF and SHOWER detector together, to search for leptons [4]. This is done by searching in each detector individually for specific hit patterns and then matching those within one sector. For previous simulation runs, this conditions have only been applied for the search for leptons, but not as a tool for data reduction and check of the trigger efficiency. This was changed especially to investigate the quality of the alignment as effects here can be most prominently seen with selected pure events.

This work is ongoing and first results look promising.

- [1] HADES Technical Design Proposal, GSI 1994
- [2] Hector Alvarez Pol, On the Multiwire Drift Chamber alignment of the HADES dilepton spectrometer, PhD thesis, 2002, Universidade Santiago de Compostela
- [3] A. Schmah, Alignment report, GSI 2006
- [4] Alberica Toia, Performance of the HADES Spectrometer for Dilepton Identification in the Reaction $C + C$ at 1 - 2 AGeV, PhD thesis, 2004 Justus Liebig Universität, Giessen

Studies of a Separator Dipole Magnet for Tagging Experiments for Photon-Induced Transmutation at ELBE^E

F. DOHRMANN, A. SYTCHEVA, E. GROSSE¹

The outstanding properties of the ELBE electron linac provide, in addition to primary electrons, high intensity and highly collimated secondary beams. When irradiating a probe with electrons, photons from bremsstrahlung have to be taken into account.

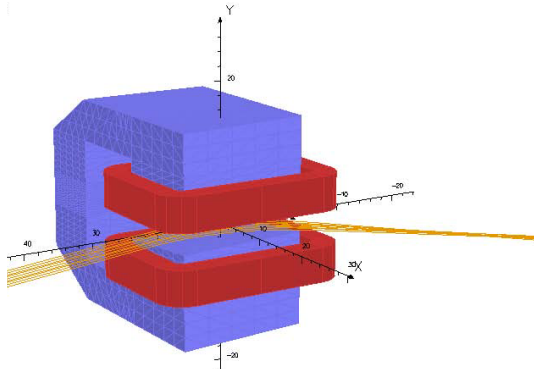


Fig. 1 Simulation of a clam magnet with trapezoidal pole shoes. Magnetic flux density 0.65 T, gap 5 cm, deflection angle 45 deg, bending radius 30 cm. The electron beam of 35 MeV kinetic energy is focussed in the vertical plane.

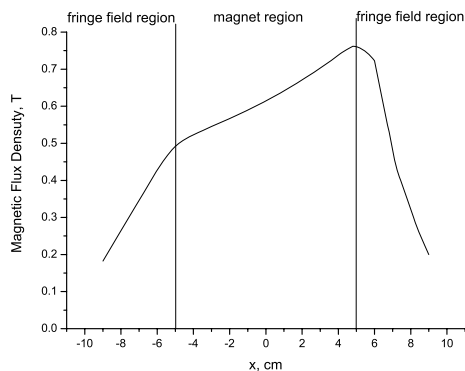


Fig. 2 Magnetic flux density along the x-axis in the middle between the poles. The slope of the curve in the middle region (magnet region) shows the focussing of the beam in the vertical plane. Fringe fields have still to be reduced.

A separated beam of bremsstrahlung photons will not only provide the means of quantifying this contribution but may well be used for experiments itself. Complementary to secondary beams of neutrons this facility will yield the opportunity to study structural or nuclear transmutation of specific probes. In particular these may include valuable information on cross sections for transmutation of radioactive waste from

fission reactors. Moreover, highly intensive photon beams may be used for studying structural defects and ageing due to high radioactive doses within material. For achieving a separation of the primary electron beam and the bremsstrahlung photons, a conceptual design of a dedicated dipole magnet has been started. This dipole magnet should be part of a spectrometer setup with which the residual energy of the electron beam should be characterized.

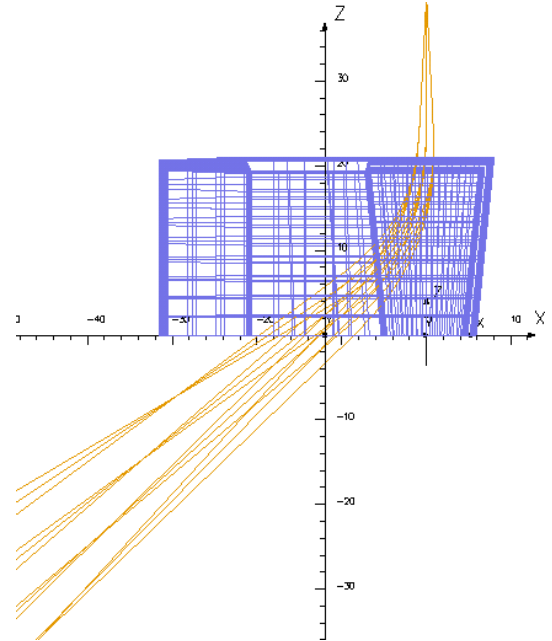


Fig. 3 Simulation of deflection of electrons of different energies (30 - 45 MeV) by dipole magnet.

We have started simulation with different codes, in particular using the Opera-3D/TOSCA [1] program for studying such a separator magnet. A possible use of non-flat pole shoes (clam design) is under discussion, which may provide additional focussing as shown in Fig. 1. This figure shows a simulation using Opera, for a beam of electrons of 35 MeV, a deflection of 45 deg, with additional focussing. The profile of the magnetic flux density is given in Fig. 2. Fringe fields of such a design have yet to be minimized. Fig. 3 shows the focussing of electrons for 30 - 45 MeV beam energies in steps of 5 MeV in order to study the location of the focal plane.

[1] Opera-3D user guide, Vector Fields Ltd., Oxford, England <http://www.vectorfields.co.uk>

¹also TU Dresden

Testing the Performance of Timing RPC Detectors at ELBE^E

R. KOTTE, L. NAUMANN, F. DOHRMANN, D. STACH

Resistive Plate Chambers (RPCs) are potentially suited for cost-efficient large-area time-of-flight (TOF) arrays needed for the identification of minimum ionizing particles (MIPs) in large-scale heavy-ion experiments [1-6]. Since the specific energy loss of 10-40 MeV electrons is quite similar to that of MIPs, a test setup is installed at the radiation source ELBE where scattered electrons are used to mimic the behavior of MIPs within RPC detectors. Furthermore, the high precision of the accelerator R.F. signal allows for a well defined time reference. No high-resolution start counter requiring an additional pulse height correction (time slewing) is necessary. Electrons from ELBE are scattered (quasi) elastically off a thin (18 μm) Al target. Passive (Pb shielding) and active collimation (various scintillation counters) allows selection of a small solid angle and sufficient background suppression. The test detector is positioned 2 m away from the target at scattering angle of 45 degrees.

Here, we present results derived with a 20 cm long prototype of the symmetric Multistrip-Multigap Glass RPC (central anode with 16 strips of 2.5 mm pitch, six gas gaps of 250 μm , eight float-glass plates of 1 mm)

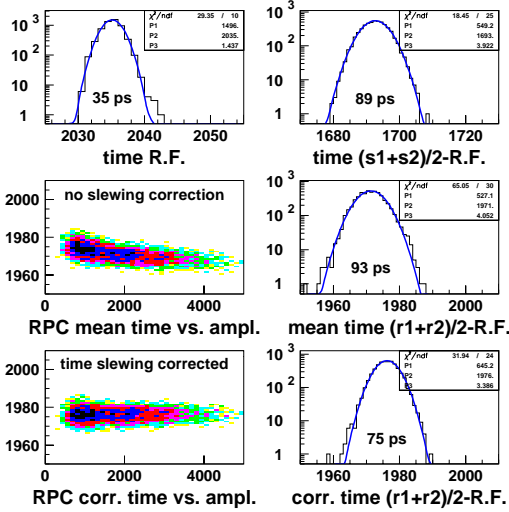


Fig. 1 The time resolution, σ_t , of different measured quantities (full lines: Gaussian fits, TDC time slope 24.5 ps/ch). Upper left panel: The 13 MHz time reference signal of ELBE fed into two TDC channels (self-coincidence). For the resolution values given in the right side panels this TDC contribution is quadratically subtracted. Upper right: Mean timing $(t_{left} + t_{right})/2$ of a $2 \times 2 \text{ cm}^2$ (5 mm thick) scintillator read out on two sides by XP2020 photo tubes. Middle (lower) left: Dependence of a similar mean timing of a RPC strip on integrated charge before (after) time slewing correction. The corresponding right panels show the projections onto the time axis. The RPC potential voltage was set to 8.2 kV and the corresponding rate was limited to 50 Hz/cm².

developed for the upgrade of the TOF barrel of the FOPI experiment at SIS/GSI [4, 5, 6]. The counter is operated with a gas mixture of 85 % C₂H₂F₄ + 10 % SF₆ + 5 % iso-C₄H₁₀ at a flow of 1.8 l/h.

Typical results of time resolution measurements are summarized in Figs. 1-3. Reproducibility is achieved within ± 10 ps. Note that the given resolution values are corrected for the finite resolution of the time-to-digital-converter (TDC, here: CAEN V1290N) but not for any jitter of the R.F. signal and the front-end electronics (FEE, here: GSI development precursor with 4 channels, single-ended 50 Ω input, gain $\lesssim 250$, bandwidth ~ 1 GHz, threshold $\lesssim 100$ mV [6]).

The authors thank J. Pawelke and W. Wagner for their kind hospitality in the radiation physics cave at ELBE.

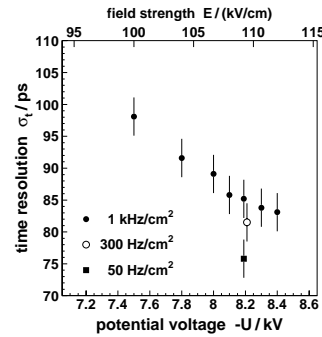


Fig. 2 The time resolution vs. potential voltage applied to the RPC detector (bottom axis). The apparent field strength being the ratio of potential voltage over sum of gas gap sizes per detector half is provided as top axis. The various symbols indicate measurements taken at different count rates.

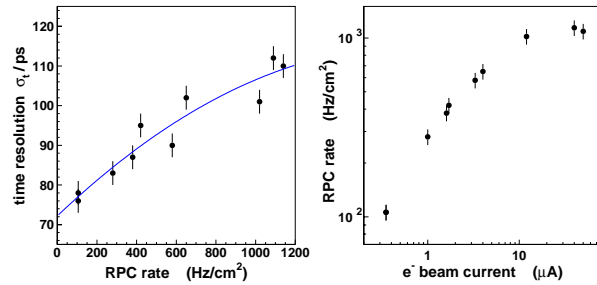


Fig. 3 Left panel: The time resolution vs. RPC detector count rate. The apparent field strength was 110 kV/cm. Right panel: The count rate vs. primary e⁻ beam current. A clear saturation effect due to signal degradation as result of the finite RPC-glass conductivity is visible.

- [1] P. Fonte et al., Nucl. Instr. Meth. A 443 (2000) 201
- [2] P. Fonte et al., Nucl. Instr. Meth. A 449 (2000) 295
- [3] A. Blanco et al., Nucl. Instr. Meth. A 485 (2002) 328
- [4] M. Petrovici et al., Nucl. Instr. Meth. A 487 (2002) 337
- [5] M. Petrovici et al., Nucl. Instr. Meth. A 508 (2003) 75
- [6] A. Schüttauf, Nucl. Instr. Meth. A 533 (2004) 65

A Straw Tube Based Transition Radiation Tracker for the CBM Experiment at FAIR^{E, G, W}

L. NAUMANN, J. MARZEC¹, V. PESHEKHONOV², D. SELIVERSTOV³, V. TIKHOMIROV⁴, P. WINTZ⁵, K. ZAREMBA¹

The Facility for Antiproton and Ion Research (FAIR) was proposed in 2001 as an international scientific center with a variety of accelerators to deliver protons, antiprotons, radioactive and stable ion beams [1]. At FAIR up to four different kinds of ions should be accelerated in parallel. The Compressed Baryonic Matter (CBM) experiment [2] is designed to explore the phase diagram of strongly interacting matter at high baryon densities. The research program includes the search for the deconfinement phase transition and the critical endpoint, the study of the chiral symmetry restoration and the nuclear equation of state. Promising probes are hadrons containing charm or strangeness and leptons. The experiments require proton beams with intensities of 10^{10} /s up to 90 GeV and heavy-ion beams with 10^9 /s up to 45 AGeV. The spectrometer should select very rare probes, e.g. in central collisions of heavy ions, where up to 10^3 charged particles will be created at reaction rates of up to 10^7 /s. The setup consists of a dipole magnet with a silicon tracker inside, a ring imaging Cerenkov counter, transition radiation detectors (TRD), a resistive plate chamber (RPC) and an electromagnetic calorimeter.

The FZR is involved in the development of two new types of detectors, the RPC for time-of-flight measurement with a resolution below 100 ps and the TRD to provide electron identification and tracking of all charged particles. The required pion suppression is about 10^2 and the position resolution is in the order of $200 \mu\text{m}$. Transition radiation (TR) may be emitted when a charged particle intersects the interface between two dielectrics. The energy of the emitted photons increases with rising Lorentz factor γ . The velocity β of considered electrons or pions is closed to 1, while γ of electrons is noticeably larger than that of pions. The energy of electron generated TR amounts to 6 keV whereas the pion TR is significantly below the energy loss caused by ionization. This makes it possible to provide a discrimination of pions by more than two orders of magnitude.

The TRD module (Fig.1) consists of six regular radiator stacks (120 Mylar foils of $15 \mu\text{m}$ thickness and $200 \mu\text{m}$ gap); straw tube detectors (4 mm, gas Xe/CF₄/CO₂) are located behind the stacks. Fig.2 shows a Monte Carlo simulation of the pion discrimination for one detector module. The rate capability of a single straw tube (4 mm) has been measured with X-rays (Fig.3) and amounts to 8 MHz/cm^2 [3]. A

measurement of the spatial resolution is in preparation.

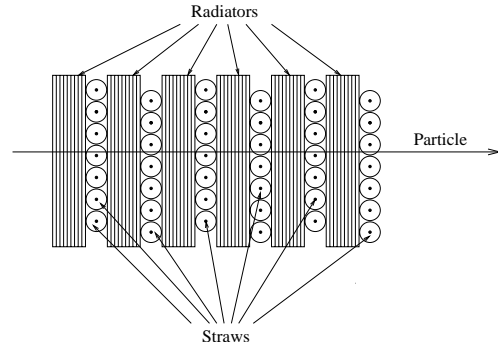


Fig. 1 Arrangement of the straws and radiator foils. The straws are tilted under stereo angles ($\pm 0, \pm 10$ deg) to improve the spatial resolution and the rate capability.

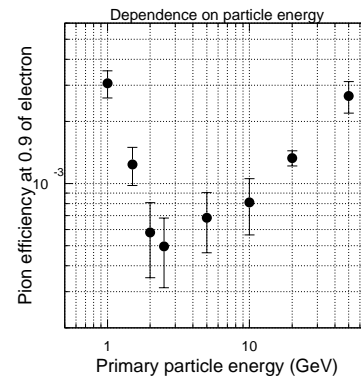


Fig. 2 Dependence of the pion detection efficiency on the energy. The suppression of the pions amounts to more than 10^3 around 2 GeV .

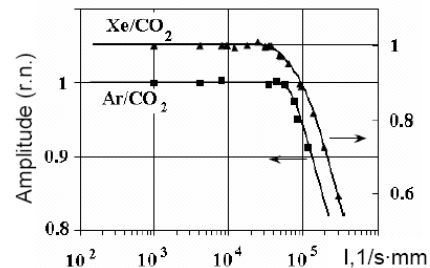


Fig. 3 Signal amplitude in dependence of the X-ray rate. A reduction of 10 % is caused by rates of 10^5 /s-mm

¹University of Technology, Warsaw, Poland

²Joint Institute for Nuclear Research, Dubna, Russia

³Petersburg Nuclear Physics Institute, Russia

⁴Lebedev Physical Institute, Moscow, Russia

⁵Forschungszentrum Jülich, Germany

[1] see <http://www.gsi.de/fair/>
 [2] CBM Technical Status Report, GSI January (2005)
 [3] I.A. Shukov et al., Dubna Preprint P13 (2005) 126

Study of the Reaction $pp \rightarrow pp\omega$ ^J

R. SCHLEICHERT,¹ S. TROUSOV FOR THE ANKE COLLABORATION

The study of ω -meson production in nucleon-nucleon collisions near threshold is of significant interest in connection with the OZI rule violation observed in the ϕ/ω production ratio which may be interpreted as an admixture of strange quarks to the nucleon wave function. However, the interpretation is sensitive to the production mechanism which is not well established even for the most investigated $pp \rightarrow pp\omega$ reaction.

In a 1-day evaluation measurement at COSY-ANKE about 9000 $pp \rightarrow pp\omega$ events have been taken at excess energies of 60 MeV and 92 MeV. The later corresponds to the lowest energy measured at COSY-TOF while SATURNE data has been taken below 31 MeV. Having both protons detected in the ANKE detection system the ω -meson is identified by the missing mass method. The separation of the $pp \rightarrow pp\omega$ events from the large $pp \rightarrow ppX$ background was found to be possible at ANKE using kinematical transformations as a model-independent approach. It was also tested to obtain the angular distribution over the ω center-of-mass angle Θ_{cm}^ω and the distribution over relative kinetic energy $\epsilon(pp)$ of two protons in final state presented in Fig. 1.

In average the measured distributions do not significantly deviate from the results of a phase space simulation. Still there is some systematics which can be related to the background subtraction procedure and needs further investigation. Assuming a pure phase-space distribution and not taking into account the final-state interaction of the 2-proton system, the analysis leads to a total cross-section of $\sigma_{tot}(Q = 60 \text{ MeV}) = 5 \mu\text{barn} \pm 30\%$ and $\sigma_{tot}(Q = 92 \text{ MeV}) = 10 \mu\text{barn} \pm 20\%$.

Due to the trigger conditions in this particular experiment the obtained data is neither sensitive to the final state interaction of the two protons nor to their relative angular dependence. Small relative kinetic energies $\epsilon(pp)$ are suppressed. For the same reason the extraction of relative angular distribution of two protons from these data is not possible. For the actual data sample this introduces an additional systematic uncertainty as large as 50% to the total cross section. This can be significantly improved either in a future experiment at ANKE getting additional information on the two proton state or by extracting the relative protons distributions from the COSY-TOF data.

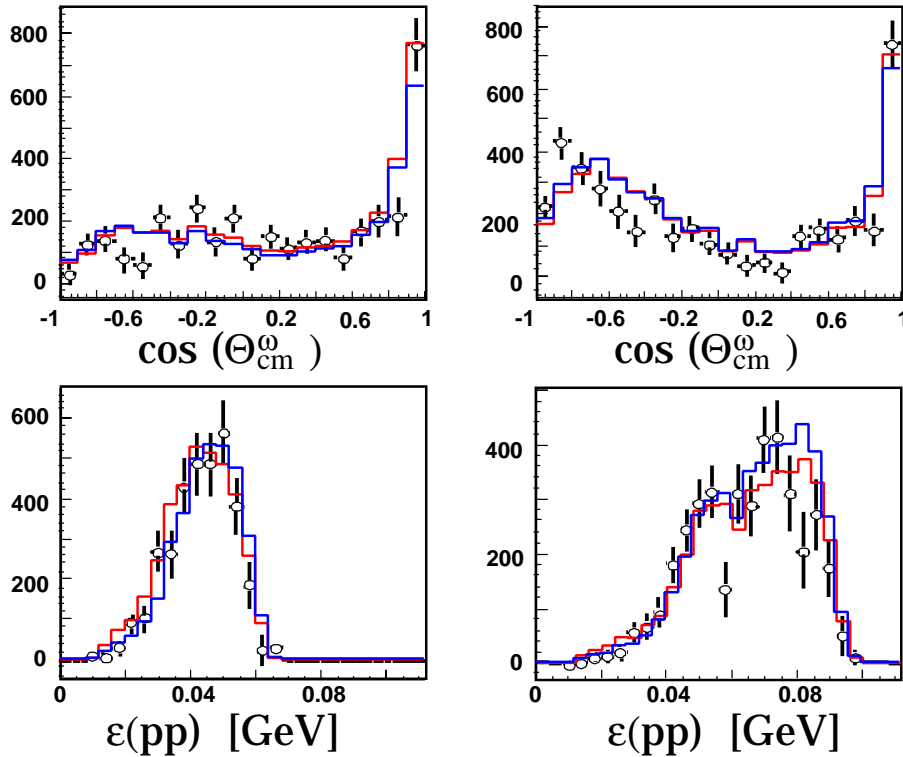


Fig. 1 Differential distributions of $pp \rightarrow pp\omega$ events along the the ω center-of-mass angle Θ_{cm}^ω and along the relative kinetic energy $\epsilon(pp)$ of two protons obtained at $Q=60$ MeV (left column) and at $Q=92$ MeV. Phase space simulations assuming an isotropic angular distribution of the two protons are shown by gray lines. The black lines correspond to a $\cos^2(\Theta_{cm}^{pp})$ angular dependence.

¹FZ Jülich

Life Sciences:

Biostructures and Radiation

Biomedical research in the Institute of Nuclear and Hadron Physics focusses onto three main topics

- (i) Studies on the structural dynamics of biomolecules by means of infrared light,*
- (ii) Radiation biology with soft, quasi-monochromatic X-rays,*
- (iii) In-beam positron emission tomography (PET) for quality assurance of charged hadron therapy.*

Structural dynamics of biomolecules: *The extremely diverse functions of biomolecules are determined by their structure. Structural transitions are thus the key mechanism by which nature controls the vast majority of cellular processes. Whereas crystallography has provided insight into the static three-dimensional structure of many proteins, the direct observation of their structural transitions remains a major challenge in the elucidation of biomolecular mechanisms. At the IKH, IR-based spectroscopic methods are at the heart of these investigations because structural information can be gathered under native conditions and with time-resolution. We are particularly interested in the detection of structural alterations in proteins and DNA as these molecules are the most important carriers of biological information. We have focused on G-protein-coupled receptors, looking for conserved physicochemical activation mechanisms that are of salient importance for pharmacological applications. In the field of DNA research, structure-sensitive IR-based methods are of special interest as the irregular structure of long DNA stretches prevents crystallography. Recent progress has been achieved in the combination of time-resolved detection of FEL IR-pulse-induced structural changes of the optical properties in DNA with spatial resolution in microsamples (see cover picture). An experimental platform has thus been established that allows to induce and follow from ps to ms the motion of complex biological molecules using the unique properties of the IR-FEL at ELBE.*

Cell radiobiology: *Photon radiation in the energy range from 10 to 100 keV is widely used in diagnostic and therapeutic radiology. Therefore, a precise determination of the relative biological effectiveness (RBE) of such X-rays and moreover of the RBE dependence on photon energy for different cell types and biological endpoints is highly desirable. The necessary intensive quasi-monochromatic X-ray beam of variable energy can be produced at the ELBE superconducting electron accelerator by channeling of the relativistic electrons in single crystals. In a series of experiments channeling radiation (CR) has been produced in diamond crystals at low beam intensity which allowed to measure the X-ray energy distribution. The energy, energy width and yield of the channeling X-rays in dependence on the energy of the electron beam and on the thickness of the diamond crystal have been investigated. Furthermore, the spatial and spectral distribution of the radiation background at the irradiation site has been measured proving that the commissioning of the second LINAC section at ELBE not only allowed to increase the electron and the corresponding CR energy but also to reduce the radiation background level by more than one order of magnitude at low electron energy. The encouraging results initiated the next step, which will be the increase of the CR intensity by enhancement of the corresponding electron beam intensity in order to meet the photon flux requirements of cell irradiations. In parallel with the CR experiments at ELBE, the cell irradiation studies at conventional polychromatic X-ray tubes have been continued. Chromosomal aberrations in a human mammary epithelial cell line show a strong dependence of the RBE on the type of aberration. Results obtained for different tube voltages indicate a RBE dependence on photon energy which has to be further investigated. In addition to the Giemsa staining, the technique*

of fluorescence in-situ hybridisation (FISH) was established and allows to extend the studies on the investigation of aberrations for specific chromosomes. After the coupling of photon and electron transport in the Monte Carlo program AMOS the implemented algorithms were validated by two different dosimetric methods. The very good agreement prove AMOS to be a multi-purpose tool which can be used for various applications including the simulation of primary and secondary radiation down to cellular dimensions.

In-beam PET for quality assurance of charged hadron therapy: During the three therapy beam times of the year 2005 another 48 patients have been treated with ^{12}C ion beams at the experimental heavy ion therapy facility at GSI Darmstadt. The tumors treated were predominantly located in the head and neck but also in the sacral region. For quality assurance all irradiation fractions have been monitored by means of in-beam PET. Besides these clinical activities extensive work on the development of in-beam PET towards a routine clinical method has been performed. This comprises: (i) dedicated algorithms for real-time tomographic reconstruction of in-beam PET data, which will allow the activity build-up to be visualized during therapeutic irradiation: (ii) The optimization of detector arrangements for in-beam PET on the basis of experimental studies and on Monte Carlo simulations of clinical cases. (iii) The quantification of the metabolic washout of positron emitters generated during irradiation. Furthermore, first experiments on the quantification of the β^+ -activation of organic targets by hard photon beams have been started at the ELBE beam. This study is devoted to the investigation of the technical feasibility and the possible clinical impact of in-beam PET at therapeutic beams of hard photons. To support education on tomographic techniques a dedicated PET-scanner has been designed and successfully installed.

Structural Dynamics of Biomolecules

- Rockefeller University, New York
- Universität Orenburg
- Universität Erlangen-Nürnberg
- MPI für Zellbiologie und Genetik, Dresden
- ISAS, Berlin
- ENEA, Frascati (Italien)
- CLIO, Paris (Frankreich)

Cell radiobiology

- Institut für Bioanorganische und Radiopharmazeutische Chemie (FZ Rossendorf)
- Klinik für Strahlentherapie und Radioonkologie, TU Dresden
- Institut für Kern- und Teilchenphysik, TU Dresden
- GSI Darmstadt
- Medizinische Fakultät, Universität Göttingen

In-beam PET for quality assurance of charged hadron therapy

- DKFZ Heidelberg
- Universität Heidelberg
- GSI Darmstadt
- Soltan Institute for Nuclear Studies, Otwock Swierk, Poland
- MedAustron, Wiener Neustadt, Österreich
- Atominstitut der Österreichischen Universitäten an der TU Wien, Österreich
- Universite Claude Bernard Lyon 1, Frankreich
- CERN, Genf, Schweiz
- Harvard Medical School, Boston, USA

FEL-Light-Induced Changes in DNA Observed by Dynamic Brewster Angle Microscopy

M. SCZEPAN, G. FURLINSKI, D. WOHLFARTH, W. SEIDEL, K. FAHMY

Brewster angle microscopy is a proven technique for the evaluation of thin organic films [1]. If a sample is observed under Brewster angle conditions, small changes in the refractive index of the surface can be observed and thus thin layers on the surface of a substrate or liquid can be made visible. Coupling a Brewster angle microscope (BAM) with a powerful light source like the FEL allows the investigation of IR-induced changes of the reflectivity (R) in thin organic films. Using the temporal characteristics of the pump and sample illumination light, fast processes can be tracked.

Our aim is to study of IR-pulse-induced structural changes in biopolymers, since the function of biopolymers is determined by their structural dynamics. In this study we want to explore the feasibility of using FEL light-induced changes for the investigation of the structural dynamics of biomolecules. A large number of superstructures is particularly important for DNA function. Our experiments aim at the induction and kinetic analysis of the IR-induced transitions between such states. The microscope setup consists of illumination, imaging and pump beam delivery systems as described earlier [2].

First experiments have been performed using thin layers of DNA which were formed by drying small amounts of DNA solution (pUC21 plasmid DNA, PlasmidFactory) on ZnSe and CaF₂ substrates. The thickness of the layers has been estimated to be 400 - 800 nm by interference fringe counting. These samples were irradiated with FEL light (9.21 μm wavelength, single pulse energy 20 - 100 nJ, macro bunch length 200-1200 μs). Fast changes of reflectivity - following the temporal structure of the FEL light intensity were observed (Fig. 1b). The fast (some ten microseconds) processes during and shortly after the macro pulse are followed by slow relaxation processes in the millisecond (typical time constant ca. 30 ms) time range (Fig. 1a). First experiments to determine the influence of the micropulse energy (Fig. 1b), macro bunch length and humidity conditions have been performed and revealed a strong influence of those parameters.

We assign the observed changes in reflectivity in the irradiated spots of the layer to changes in the refractive index and/or the thickness of the DNA film. These changes in the physical properties of the sample can be attributed to structural changes of the DNA molecules such as unstacking and base pair opening. The refrac-

tive index of single strand DNA differs significantly from the refractive index of double strand DNA [3]. Base pair opening and re-closing would thus result in changes of the reflectivity. Partially, also thickness changes of the film and surface deformation of the sample due to local heating may be involved in the observed reflectivity changes.

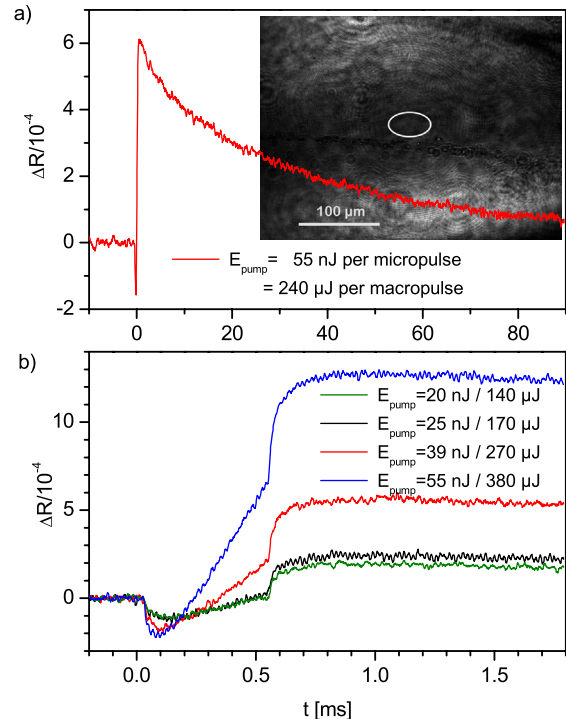


Fig. 1: Change of reflectivity of a DNA film (central spot in BAM image (a), $R = 0.007$) during and past FEL irradiation in long (a) and short (b) time scale. Fig. 1b also shows the effect of different light intensities/micro bunch energies.

The first experiments demonstrate the feasibility of high signal/noise detection of IR-pulse induced processes in biofilms and give first insight into the dynamics of these processes.

- [1] S. Hénon, J. Meunier, Rev. Sci. Instr. 62 (1991) 936
- [2] M. Sczepan, G. Furlinski et al., IKH Annual Report 2004, FZR-423 (2005) 63
- [3] S. Elhadj, G. Singh, R. Saraf, Langmuir 20 (2004) 5539

Structure and pH-Sensitivity of the Transmembrane Segment 3 of Rhodopsin

S. MADATHIL, G. FURLINSKI, K. FAHMY

G protein-coupled receptors (GPCRs) are heptahelical membrane proteins that reside in the plasma membrane of eucaryotic cells, where they transmit a large variety of extracellular signals. Rhodopsin, the visual photoreceptor, is the only GPCR for which crystal structures have been solved serving as a model for structure and function of class I (rhodopsin-like) GPCRs [1]. Protonation of the carboxylate in the conserved D(E)RY motif in transmembrane helix 3 (TM3) may be a general property of the active state of class I GPCR [2]. We have used synthetic TM3 peptides to study the impact of protonation at Glu¹³⁴ on the TM3 structure of rhodopsin using FTIR and fluorescence spectroscopy.

The synthetic peptide TM3(108-138) adopts an α -helical structure in lipidic vesicles as evident from the amide I mode at 1655 cm⁻¹ (Fig. 1). The angular dependence of the dichroic ratio R of the amide I and amide II bands ($R = A_p/A_v = 1 + 3\sin^2\omega S/[n^2(1-S)]$) measured with a polarized IR beam corresponds to a tilt of the helical axis of of 44°-50° relative to the membrane normal (Fig. 1). TM3(108-138) is also helical in dodecyl-maltoside micelles where the amide I mode is found at 1655 cm⁻¹ with a shoulder at 1624 cm⁻¹ which is more pronounced at pH 8.8 than at pH 2. The helix-forming propensity is reduced in the 15-mer TM3(123-137) showing distinct amide I modes at 1655 and 1624 cm⁻¹. Acidic pH favors the helical content. The IR data evidence that protonation of Glu¹³⁴ is coupled to conformational changes at the C-terminal end of the helical TM3.

This is supported by the fluorescence of Tyr¹³⁶ at 312 nm in TM3(108-138) exhibiting a pK_a of ~6 of its pH-dependent emission (Fig. 2) which is largely abolished when Glu¹³⁴ is replaced by Gln. In combination with the FTIR data, the results show that the conserved carboxylate confers pH sensitivity to the TM3 peptide secondary structure specifically in the environment of the conserved ¹³⁴D(E)RY¹³⁶ motif [3]. We propose that the conserved hydrophobicity profile renders the carboxylate to be a critical side chain for the pH-dependent positioning of TM3 in GPCRs by allowing the proton-induced formation of a contiguous hydrophobic stretch at the lipid water interface of TM3, thereby, regulating helix insertion and / or rotation.

Peptide sequences: native sequence TM3(108-138): T¹⁰⁸GCNLA(E)GFFATLGGA(E)IALWSLVVLAIER-YVV¹³⁸; TM3Q(108-138): T¹⁰⁸GCNLA(E)GFFATLGA-(E)IALF(W)SLVVLAIQ(E)RYVV¹³⁸; TM3(123-137): I¹²³-ALWSLVVLAIERV¹³⁷.

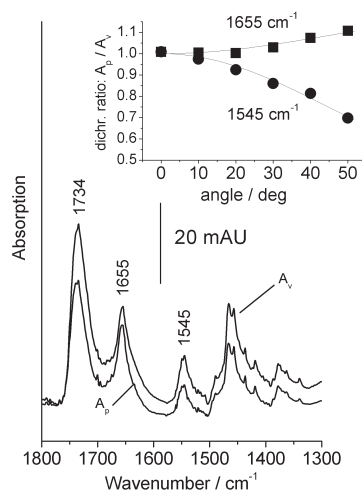


Fig. 1: Polarized transmission FTIR spectra of PC vesicles reconstituted with TM3(108-138). The sample (on CaF₂) was tilted by 60° relative to the IR beam. The inset shows the dichroic ratio of the amide I and amide II bands as a function of the angle of incidence of the IR beam. Solid lines are calculated with $n = 1.4$ and S values of 0.39 and -0.49 for the amide I and II mode, respectively.

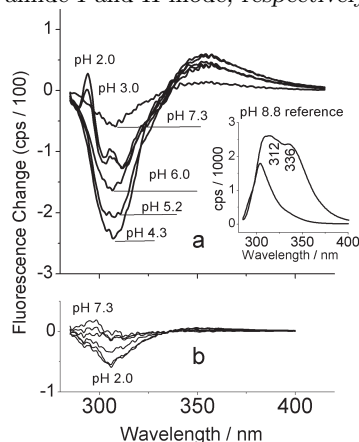


Fig. 2: Fluorescence emission from detergent-solubilized TM3(108-138). a) pH-dependent emission from Tyr¹³⁶ (312 nm) after subtraction of a pH 8.8 reference spectrum. Inset: Reference emission spectra of TM3(108-138) in the upper and TM3Q(108-138) in the lower trace (removal of Trp¹²⁶ abolishes the 336 nm emission). b) as in (a) but for TM3Q(108-138).

- [1] S. Filipek, D.C. Teller et al., Ann. Rev. Biophys. Biomol. Struct. 32 (2003) 375
- [2] S. Cotecchia, L. Stanasila et al., Biol. Cell, 96 (2004) 327
- [3] S. Madathil, G. Furlinski, K. Fahmy, Biospectroscopy (2006) in press

Photothermal Beam Deflection Spectroscopy on Uranyl Compounds at the Free Electron Laser Facility FELBE

H. FOERSTENDORF,¹ K. HEIM,¹ W. SEIDEL, G. BERNHARD¹

FELBE is an acronym for the free electron laser (FEL) at the **E**lectron **L**inear accelerator with high **B**rilliance and low **E**mittance (ELBE) located at the FZR. This FEL is a source of pulsed, coherent light which is continuously tunable over the infrared wavelength range (see Tab.1). The FELBE facility is a member of the EC-funded "Integrating Activity on Synchrotron and Free Electron Laser Science (IA-SFS)", which comprises most synchrotron and FEL facilities in Europe and provides financial support to users from the EC and associated states.

Tab. 1 Parameter of the FEL

Wavelength range	4 – 22 μm (15 – 150 μm)	U27 (U100; operation 2006)
Pulse energy	$\leq 1 \mu\text{J}$ (U27)	depending on λ
Pulse length	1 – 10 ps	depending on λ and cavity detuning
Repetition rate	13 MHz	3 modes: - cw - Macropulse structure: 0.1 – 36 ms (duration) 1 – 25 Hz (rate) - single-pulse selection: 1 – 1000 Hz (projected)

At the FELBE facility a laboratory suitable for radiochemistry research was installed. This laboratory is classified as a controlled zone for investigations of certain radionuclides obeying to all aspects of radiation protection (Tab. 2). The maximum activity of the investigated radioactive samples can add up to 10^5 times of the admissible limit.

Tab. 2 Table of radionuclides which can be handled at FELBE.

Nuclide	$T_{1/2}$	Molar activity	Max. allowed activity in lab
	[s]	[Bq]	[Bq]
C-14	1,81E+11	2,31E+12	9,00E+04
Tc-99	6,62E+12	6,30E+10	5,73E+05
Th-232sec	4,42E+17	9,46E+05	3,66E+00
Pa-231	1,04E+12	4,01E+11	1,56E+06
Np-237+	6,75E+13	6,19E+09	2,35E+04
U-238sec	1,41E+17	2,96E+06	1,12E+01
Pu-239	7,57E+11	5,52E+11	2,08E+06
Pu-242	1,18E+13	3,53E+10	1,31E+05
Am-243+	2,32E+11	1,80E+12	6,66E+06
Cm-244	5,71E+08	7,31E+14	4,99E+07
Cm-248	1,07E+13	3,89E+10	1,41E+05

A glove box provides the possibility to perform experiments on sensitive samples which have to be kept in an inert gas atmosphere.

Recently we have shown that photothermal beam deflection (PTBD) spectroscopy performed with a pulsed free electron laser (FEL) can provide reliable infrared spectra throughout a distinct spectral range of interest [1]. In our first experiments at FELBE we have used

uranyl model compounds to analyze the antisymmetric stretching vibration (ν_{as}) mode of

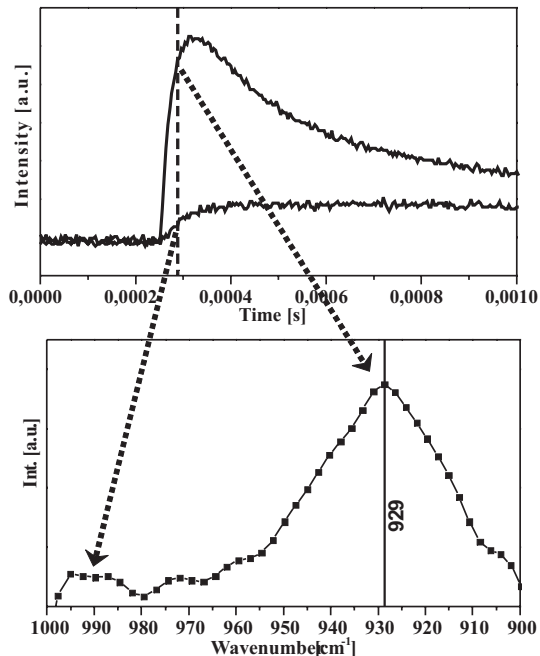


Fig. 1 PTBD signals recorded at the maximum (top, upper trace) and at the edge of UO_2^{2+} - absorption band (top, lower trace). The amplitudes of the signal provide the spectral intensities after normalization (below).

the UO_2^{2+} -cation since the position and shape of this band can help to identify uranium complexes sorbed on mineral surfaces. Fig. 1 (upper part) shows typical deflection curves of a uranium model compound recorded with different FEL wavelengths. The amplitude of the deflection curves correlates with the absorption coefficient of the sample. Since the wavelength of the FEL light can be tuned over a certain range, absorption spectra can be calculated from the deflection curves by extracting the values of the amplitude at a certain time and normalizing to the reference signal of the FEL (Fig. 1 bottom). The obtained spectrum is in good agreement to spectra recorded by conventional FT-IR spectroscopy [2].

In further studies we will evaluate the minimal concentration of the actinide compounds which will be necessary for detection by PTBD. Another topic will be the investigation of neptunium(V) model compounds at longer FEL wavelengths.

- [1] W. Seidel, H. Foerstendorf et al., Eur. Phys. J. Appl. Phys. 25 (2004) 39
- [2] A.A. Zazhugin, H.D. Lutz, A.I. Komyak, J. Mol. Struct. 482/483 (1999) 189

¹FZ Rossendorf, FWR

Selection of FELBE Radiation Pulses Using a Laser-Activated Plasma Switch

S. Friebel,¹ S. Winnerl,¹ W. Seidel, H. Schneider,¹ M. Helm¹

In order to adapt the infrared radiation of the free-electron laser (FEL) to the needs of the internal and external users, a laser-activated plasma switch selecting infrared FEL radiation pulses was put up and examined. With this switch it is possible to reduce the repetition rate of FEL radiation from 13 MHz to 1 kHz and hence reduce the average radiation power. The intensity of every individual radiation pulse is nearly unchanged. This infrared radiation with lower average power can be used for examination of sensitive samples. These samples would be damaged through the high thermal load when exposed to the FEL radiation at full power. Furthermore the reduced repetition rate allows investigating effects with timescales larger than 100 ns (13 MHz corresponds to 77 ns).

The plasma switch selects the individual FEL radiation pulses using the principle of photo-induced reflectivity [1]. For that propose an undoped semiconductor, e. g. Germanium and Silicon, is illuminated by a Ti:sapphire laser. Due to absorption of photons an electron-hole plasma on the front surface of the semiconductor is generated. When the plasma frequency is higher than the FEL radiation frequency the optical semiconductor properties are changed for the FEL radiation. The plasma frequency influences the refraction index of the semiconductor material, there by leading to a variation of the semiconductor reflectivity for the infrared radiation.

For the examinations, shown here, the semiconductor material Germanium was used for the plasma switch. The radiation of the FEL had a wavelength of $9.2 \mu\text{m}$. The Ti:sapphire laser used for illuminating the semiconductor had a wavelength of 800 nm and a pulse duration of $< 100 \text{ fs}$. For realizing the pulse selection the frequencies of both laser sources were synchronized with RF-electronics. For the exact timing of both

were detected with a photon-drag detector (FEL) and a photo diode (Ti:sapphire) and were adjusted on each other trough moving a precision linear stage. The selected FEL pulses were detected by a fast MCT detector with a bandwidth of 20 MHz and were monitored with an oscilloscope. A gold mirror served as a reference for determining the reflectivity of the Germanium [2].

Fig. 1 shows the time-resolved reflectivity for two different values of the average Ti:sapphire laser power. The rise time of ca. 7 ps can be mainly attributed to jitter of the synchronization of both laser sources. The reflectivity drops exponentially with a decay time of 110 ps. This decay of the reflectivity is fast enough, before the next FEL pulse hits the semiconductor. For the highest value of the Ti:sapphire laser fluence ($1.75 \text{ mJ}/\text{cm}^2$) a reflectivity of Germanium for FEL radiation of 85 % was achieved. With a lower fluence ($0.67 \text{ mJ}/\text{cm}^2$) a reflectivity of 65 % could be measured.

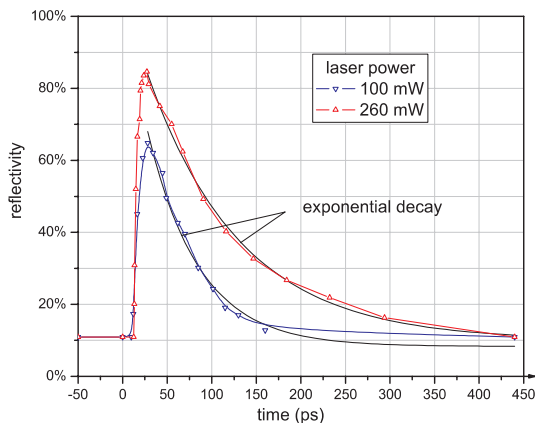


Fig. 1 Time-resolved measurement of the reflectivity for two different values of the average Ti:sapphire laser power. laser pulses, when they hit the semiconductor, they

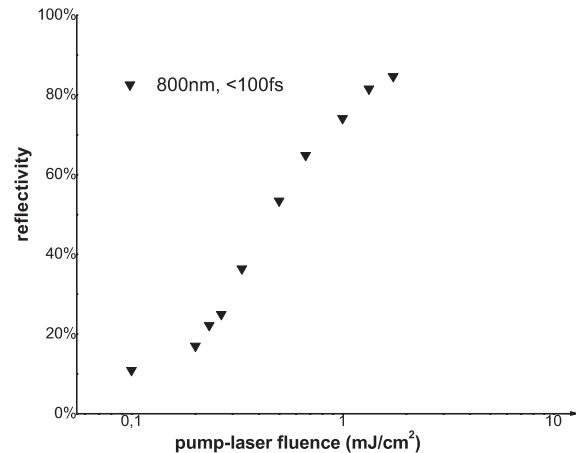


Fig. 2 Dependence of reflectivity on the pump-laser fluence

The dependence of the reflectivity on the pump-laser fluence is shown in Fig. 2. The fluence was changed in the range from $0.1 \text{ mJ}/\text{cm}^2$ to $1.75 \text{ mJ}/\text{cm}^2$, the latter corresponds to an average pump-laser power of 260 mW. In conclusion, these results demonstrate that plasma switch is most suitable for the Rossendorf FEL. During further examinations it should be shown that similar results can be achieved using a Nd:YAG laser amplifier ($\lambda = 1064 \text{ nm}$, $\tau < 16 \text{ ps}$), which is planned for excitation of the semiconductor material.

- [1] P. Haar: Pulse stacking in the Stanford external cavity and photo-induced reflectivity in the infrared, Dissertation Univ. Stanford, 1996
- [2] S. Friebel: Aufbau und Test eines Plasma-Schalters für Laserstrahlung, Diploma thesis FZ Rossendorf, 2006

¹FZ Rossendorf, FWI

Single Shot Infrared Ellipsometry with a Free Electron Laser

M. GENSCH¹, J.S. LEE², K. HINRICHS¹, K. FAHMY, N. ESSER¹, W. SEIDEL, U. SCHADE²

We present the concept of a single shot ellipsometer for the mid infrared spectral range using a novel "division of amplitude polarimeter" (DOAP) principle [1]. It has the potential to circumvent present limitations in spatial and time resolution of state of the art infrared ellipsometers by using radiation from the FELBE free electron laser and can easily be extended into the far infrared. Ellipsometry is a routine technique to investigate thin films and surface layers [2]. Its strength stems from the fact that it is reference-free because the optical properties (e.g. the dielectric function) are derived from the change of the polarization upon reflection/transmission of radiation at/through the sample, respectively. The current detection limit of infrared ellipsometry allows to investigate organic monolayers and submonolayers of hydrogen or silicon suboxides [3]. The quantities derived in the experiment are the so called ellipsometric parameters $\tan\Psi$ and Δ (for definitions see Fig.1).

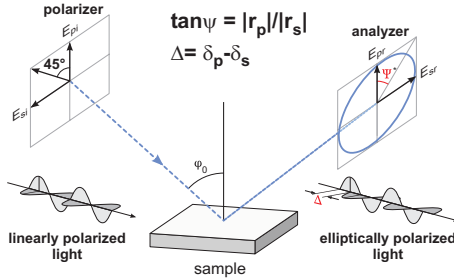


Fig. 1 Principle of an ellipsometric measurement and meaning of the ellipsometric parameters. $\tan\Psi$ and Δ are defined as the real and imaginary part of the ratio of the complex reflection coefficients: $\rho := r_p/r_s = |r_p|/|r_s|e^{i(\delta_p - \delta_s)} = |r_p|/|r_s|e^{i\Delta} = \tan\Psi e^{i\Delta}$.

The most common ellipsometers use rotating analyzers (RAE), rotating compensators (RCE) or phase modulation concepts (for details see [2]). However, the time resolution of the concepts is limited by the necessity to move optical components or to change properties of optical elements (e.g., birefringence of the photoelastic modulator). Only multichannel approaches allow the instant "single shot" determination of the ellipsometric parameters and are, therefore, particularly suitable for fast measurements and utilization of pulsed sources [4]. Here, we present a first concept for a single shot ellipsometer for the use with an IR FEL (Fig. 2). The set-up utilizes electrical lock-in technique to the macro pulse structure of the FEL.

The multi-channel detection scheme for $\tan\Psi$ and Δ by measurement of 2 intensity ratios, makes the method robust against pulse to pulse power fluctua-

tions. The high average power of the FELBE source allows to constrain the waist of the beam by an aperture stop in front of the setup. No further focussing is needed. The intensity of the source was further attenuated by absorbers to optimize the intensity incident on the detectors.

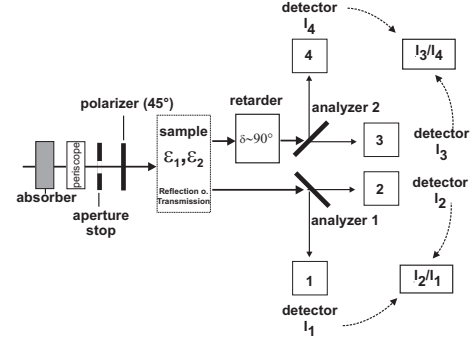


Fig. 2 Sketch of the DOAP concept. - The waist of the beam is constrained by the use of an aperture stop of 1mm in diameter. The beam is rotated azimuthally by a periscope to align the intrinsic linear polarization of the FEL radiation with an angle of 45° to the plane of incidence. After reflection at the sample or transmission through the sample, the radiation is analyzed by up to 4 DTGS detectors to determine the intensity ratios $I(0^\circ)/I(90^\circ)$ and $I(45^\circ)/I(135^\circ)$ from which $\tan\Psi$ and Δ can be calculated [1, 5]. For the division of the amplitude 2 analyzers (metal wire grids on KRS-5 substrates - Grasby Specac) are used as polarizing beam splitters. A prism retarder (made of KRS-5) is used to enhance the accuracy of the measurement of Δ .

During the first beam time in November 2005, we determined successfully the optical response of thin polymeric films on silicon for 2 different wavelengths ($10.6\ \mu\text{m}$ and $6\ \mu\text{m}$, macro pulse duration $340\ \mu\text{sec}$ at 25 Hz). Thus, the proof of principle could be established and the sensitivity of the instrument for thickness differences on the nanometer-scale could be shown [1]. Potential applications may range from micro-focus ellipsometry (possibly down to the diffraction limit), imaging (when making use of detector arrays) to time resolved ellipsometry.

- [1] M. Gensch et. al. to be published
- [2] R.M.A. Azzam and N.M. Bashara, "Ellipsometry and polarized light", North-Holland Personal Library 2003
- [3] J. Rappich et. al., J. Phys. Chem. B 110 (2006) 1332
- [4] R.M.A Azzam, Thin Solid Films 234 (1993) 371 and Ref. therein
- [5] A. Roeseler, Thin Solid Films 234 (1993) 307

¹ISAS - Inst. for Analytical Sciences, Dep. Berlin, Germany

²Bessy GmbH, Berlin, Germany

The Optical Beamline to the High Magnetic Field Laboratory (HLD)

R. WÜNSCH, T. HERRMANSDÖRFER¹

Since May 2004 the mid-infrared FEL at the radiation source ELBE is producing laser light. In 2006 it will be complemented by another FEL producing infrared light from 20 up to 150 μm . A beamline consisting of 10 cm wide vacuum tubes with plane and focusing mirrors delivers the beam to six user laboratories. First, the beam is transported from the respective FEL resonator to a diagnostic table, where its parameters are measured and, if needed, modified. From there the

beam is transported by a common beamline [1].

The High Magnetic Field Laboratory (HLD) represents another outstanding new research facility of the FZR where fields up to 100T will be created. The IR-FELs of ELBE are an appropriate tool for investigating the effects of such strong magnetic fields on matter [2]. Therefore a few meter behind the diagnostic table the beamline to the HLD branches off, and

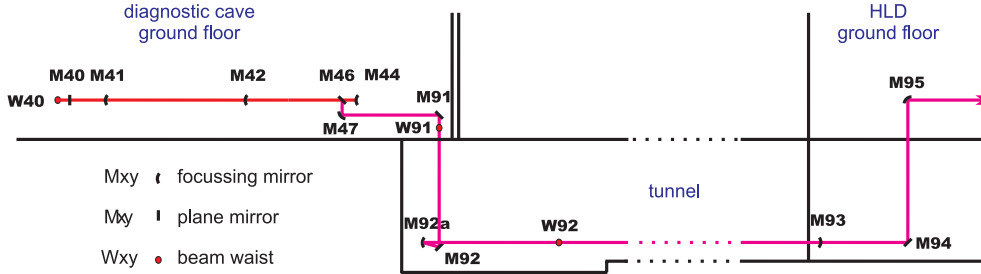


Fig. 1 Unrolled side-view of the IR-beamline from the beam waist (W40) on diagnostic table to the HLD.

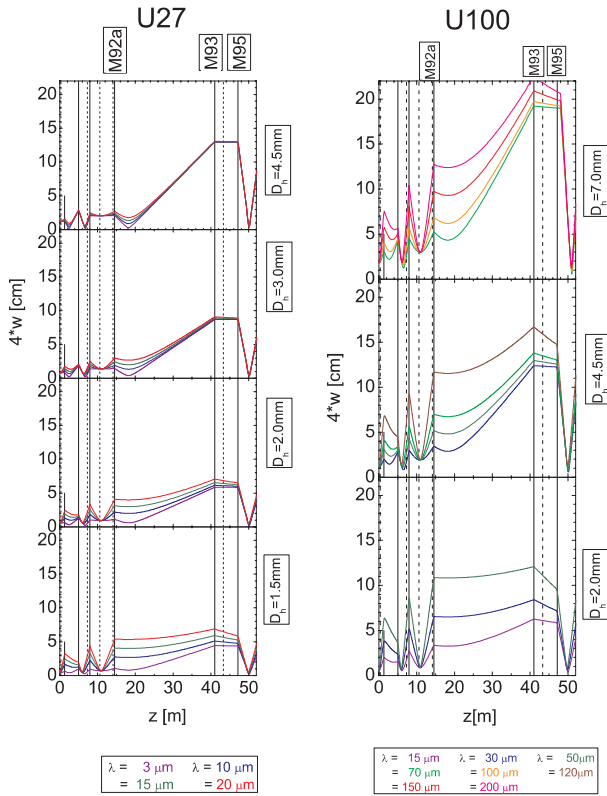


Fig. 2 Beam envelope ($4 \cdot w$) along the beamline for different wavelengths and outcoupling holes D_h .

from there the beam runs through a vacuum tube in a tunnel which connects the ELBE building with the

HLD. There it will be distributed to several magnets. Fig.1 shows the beamline from the diagnostic cave (left side) through the tunnel to the HLD building. The beam starts at the beam waist on the diagnostic table (W40). The position of this waist is independent of the wavelength and the same for both FELs. Its size is proportional to the size of the outcoupling hole in the resonator mirror of the FEL.

Behind the diagnostic table the beam is focused and deflected by several mirrors (M40, M41, M42). Mirror M46 deflects the beam into a particular beamline. M47 and M91 guide the beam into the tunnel. There it is deflected by M92 and focused by M92a. To cross the tunnel without refocussing a thicker beam tube is necessary. At the end of the tunnel the beam is refocussed and guided to the ground floor of the magnetic field laboratory. Mirror M93 produces a weakly converging beam (see Fig. 2) which can be focussed on almost any place in the laboratory and then guided into one of the kryostats of the magnets. By means of an additional removable mirror the beam can be delivered to other kryoastats.

Fig.2 shows the envelopes for the various beams of the ELBE FELs at several wavelengths. Upstream of M92a a 10 cm beam tube is sufficient. Downstream the tube has to be expanded to 20 cm.

- [1] Th.Dekorsy et al., Proc. 24th Int. Conf on Free Electron Lasers, Argonne (USA), p. II-35
- [2] F. Herlach, N. Miura, High Magnetic Fields, Vol. 2: Science and Technology, World Scientific, New Jersey, London, Singapore, (2003)

¹FZ Rossendorf, FWH

Mode Conversion in the Partial Waveguide of FEL2

R. WÜNSCH, C.A.J. VAN DER GEER¹

At wavelengths around $150\ \mu\text{m}$ a freely propagating resonator mode in the long-wavelength FEL2 at the radiation source ELBE is roughly 4 cm thick ($4 \cdot w_0$). This is in conflict with a reasonably small undulator gap and a sufficiently high magnetic field on the undulator axis. For that reason a waveguide will be installed [1]. It spans from the entrance into the undulator to the downstream resonator mirror and compresses the optical beam vertically. It is 1 cm high (inside height) and wide enough to allow a free propagation of the resonator beam in horizontal direction (parallel-plate waveguide). On the upstream side the elements necessary for a correct electron beam formation do not allow to install bulky waveguide plates. Here, the beam propagates freely both horizontally and vertically.

The waveguide allows a minimal undulator gap of 24 mm with an undulator parameter $K_{\text{rms}} \approx 2.7$. A particular hybrid waveguide mode [2] carries the optical energy practically without loss. Losses arise solely at the waveguide exit where the mode is converted from a waveguide into a freely propagating Gaussian mode and vice versa. The hybrid waveguide $H_{m,n}$ mode shape is Gauss-Hermitian horizontally and sinusoidal vertically. Apart from the principal mode ($m = 0, n = 1$) a number of higher modes with additional maxima may be excited. These modes have a broader field distribution and hence a smaller overlap with the electron beam. Fig. 1 shows that the power density of the principal mode ($m = 0$) in the center, where the beam overlaps with the electrons, is twice as large as that of an $m = 2$ mode. Its gain is correspondingly larger.

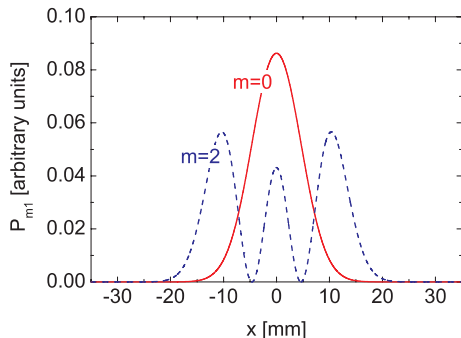


Fig. 1 Horizontal power distribution of the principal optical mode ($m = 0$) and the $m = 2$ mode.

Modes with more than one field maximum in vertical direction ($n > 1$) propagate with a slightly lower group velocity which reduces the overlap with the electron bunch additionally. At $150\ \mu\text{m}$ the $n = 3$ radiation pulse is roughly 2 mm behind the $n = 1$ pulse after one roundtrip. At a resonator length fitted to the

$n = 1$ mode the $n = 3$ mode does practically not overlap with the short electron bunch and is not amplified. At shorter wavelengths higher vertical modes can be amplified simultaneously with the principal one.

Using a partial waveguide higher order modes can be generated by the conversion of a waveguide mode into a freely propagating one and vice versa. When calculating lasing gain and power [3] and estimating the coupling losses between freely propagating and waveguide modes [4] the assumption was made that solely the principal mode $H_{0,1}$ is present in the waveguide when the appropriate mirror curvature has been selected. We have verified this assumption by means of the software package GPT [5] extended by a code describing the propagation of the optical beam inside and outside the waveguide without the restriction to the principal mode.

	m=0	m=2	m=4	m=6	m=8
no hole	0.982	0.000	0.002	0.002	0.001
$d_h = 7\ \text{mm}$	0.968	0.010	0.010	0.006	0.006

Table 1: Coupling matrix of the principal waveguide mode ($m = 0$) with higher modes calculated for one roundtrip of a $150\ \mu\text{m}$ beam through the FEL2 resonator.

Table 1 illustrates the coupling between the various waveguide modes. It verifies that an optical field starting as a principal waveguide mode basically returns as a principal mode after freely propagating through the downstream side of the resonator. Only a few percent of the power (3.6% without outcoupling and 6.3% for a 7 mm hole) is converted into higher modes. These values are in nice agreement with the losses calculated by means of the computer code GLAD [6].

Due to the larger absorption and the lower gain of higher order modes they are less amplified during the lasing process and, after a sufficient number of roundtrips the final profile contains less than 1% of higher order modes at the outcoupling mirror even at 7 mm hole. Altogether the results confirm the assumptions and restrictions made when calculating the roundtrip losses by means of the optical code GLAD.

- [1] Th. Dekorsy et al., IKH Annual Report 2004, FZR-423 (2005) 65
- [2] L.R. Elias and J. Gallardo, Appl. Phys. B31 (1983) 229
- [3] R. Wünsch, IKH Annual Report 2004, FZR-423 (2005) 67
- [4] R. Wünsch, IKH Annual Report 2004, FZR-423 (2005) 66
- [5] Pulsar Physics, General Particle Tracer (GPT), <http://www.pulsar.nl>
- [6] E. Grosse et al., Proc. 27th Int. Conf on Free Electron Lasers, Stanford, USA, <http://accelconf.web.cern.ch/AccelConf/f05/PAPERS/TUPP031.PDF>

¹Pulsar Physics, The Netherlands

Analysis of MLEM and OSEM Reconstruction Algorithms for Different Geometries of PET Scanners^{E,G}

G. SHAKIRIN, P. CRESPO, W. ENGHARDT¹

At the experimental heavy ion tumor therapy facility at the GSI Darmstadt in-beam PET is operated. The in-beam PET data should be reconstructed as fast as possible (ideally, in real time), because they allow monitoring irregularities in beam delivery. To find a fast reconstruction algorithm with acceptable quality, MLEM [1] and OSEM [2] algorithms were compared for full-ring and dual-head geometries of the PET scanner with different parameters of reconstruction. An activity distribution to be reconstructed was generated by the simulation routine. Quality assurance of reconstructions was performed by numerical and visual comparison of the reconstructed and generated activity distributions.

The simulated activity was homogeneously distributed within a hollow sphere. Then it was reconstructed using the projection data by means of MLEM and OSEM algorithms. Results of these reconstructions were compared using the Mean Absolute Error (MAE) [3]. For the OSEM algorithm projection data were grouped into different number of subsets.

Reconstructions with OSEM 6, 8, 10 and 12 subsets were compared with the reconstruction result after 50 iterations of MLEM for a full-ring PET scanner (see Fig. 1). Best result in terms of MAE showed the reconstruction with OSEM 8 subsets. It achieved the quality after 50 iterations of MLEM in 9 iterations.

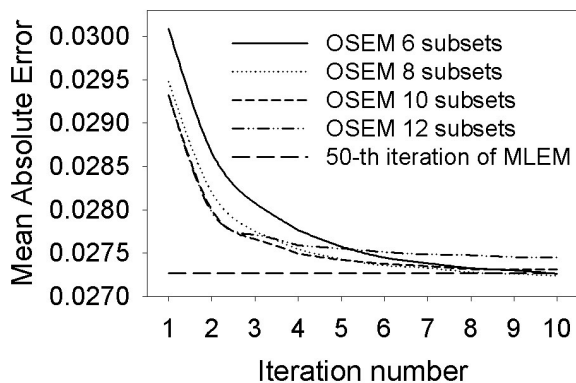


Fig. 1 Mean Absolute Error for reconstructions within the full-ring PET scanner.

In case of a dual-head PET scanner MAE has a minimum at the 35-th iteration for MLEM and then increases. Finally MAE of MLEM and OSEM algorithms converges to the same value (see Fig. 2).

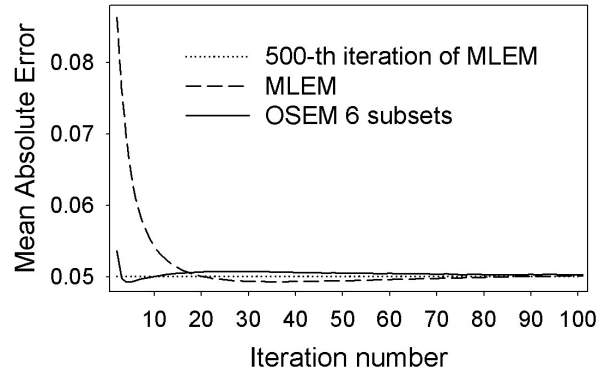


Fig. 2 Convergence of MLEM and OSEM for the dual-head PET scanner geometry.

The best reconstruction result showed the OSEM algorithm with decreasing number of subsets from iteration to iteration. It achieved the quality of the 35-th iteration of MLEM in 2 iterations (see Fig. 3).

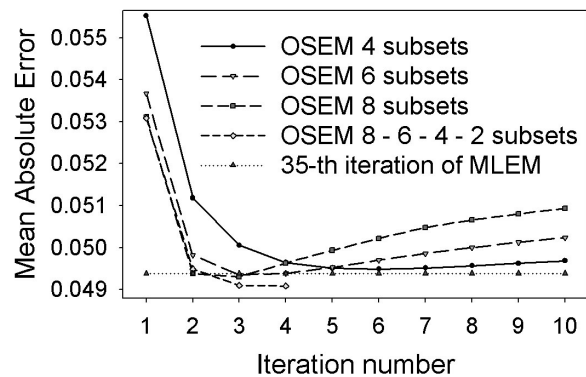


Fig. 3 Mean Absolute Error for reconstructions within the dual-head PET.

- [1] L.A. Shepp and Y. Vardi Maximum likelihood reconstruction for emission tomography, IEEE Trans. Med. Imag., vol MI-2 (1982) 113
- [2] H.M. Hudson and R.S. Larkin, Accelerated Image Reconstruction Using Ordered Subsets of Projection Data, IEEE Trans., vol 13 No 4 (1994) 601
- [3] J. Sheng and D. Liu, An Improved Maximum Likelihood Approach to Image Reconstruction Using Ordered Subsets and Data Subdivisions, IEEE Trans. Nucl. Science Vol 51 No 1 (2004) 13

¹also TU Dresden

First Experiments on In-Beam PET at Hard Photon Beams ^E

D. MÖCKEL, J. PAWELKE, M. SOMMER¹, E. WILL², W. ENGHARDT³

Since there are good experiences with in-beam PET for quality assurance in carbon ion therapy [1] it is highly desirable to extend this method to the more widely used radiation therapy with photon beams. In-beam PET seems to be feasible also for high energy photon irradiation with energies above ~ 20 MeV because of the generation of positron emitters ^{11}C and ^{15}O in tissue by (γ, n) reactions as already shown in simulations [2].

First quantitative results on the activation of phantoms at hard photon beams were obtained by performing off-beam PET experiments. Homogeneous PMMA phantoms were irradiated with high energy photons. After the irradiation the distribution of the generated positron emitters in the phantom was measured using the PET scanner Siemens ECAT EXACT HR+ (cf. Fig. 1). Furthermore, the depth dose distribution was measured by means of optical stimulated luminescence detectors (BeO).

For the experiments an electron beam at ELBE with a current of $\sim 70 \mu\text{A}$ and different energies $E = \{21, 23, 25, 30, 34\}$ MeV was used to generate bremsstrahlung in a $18 \mu\text{m}$ thick Al target. The accelerator was operated in the continuous wave mode at a frequency of 13 MHz.

The activity concentration determined by the PET measurement was recalculated to the end of the irradiation. It was assumed that only the annihilation photons of positrons emitted by ^{11}C were detected because of the ~ 30 min time interval between the end of the irradiation and the start of the PET measurement, which corresponds approximately to 15 half-lives of ^{15}O and 1.5 half-lives of ^{11}C .

By dividing this recalculated activity concentration and the measured dose of the BeO detectors the dose related activity concentration was calculated. In Fig. 2 the absorbed dose and the PET activity concentration at the end of the irradiation in the PMMA phantom (top) and the dose related activity concentration (bottom) are shown for $E_{e^-} = 34$ MeV.

Increasing the electron energy results in a rising of the generated activity (cf. Fig.3). Energies larger than ~ 23 MeV are required to obtain a sufficient amount

of positron emitters.

A remarkable increase of the measured activity is expected if also ^{15}O is detected. Therefore, experiments with in-beam PET at ELBE are in planning.

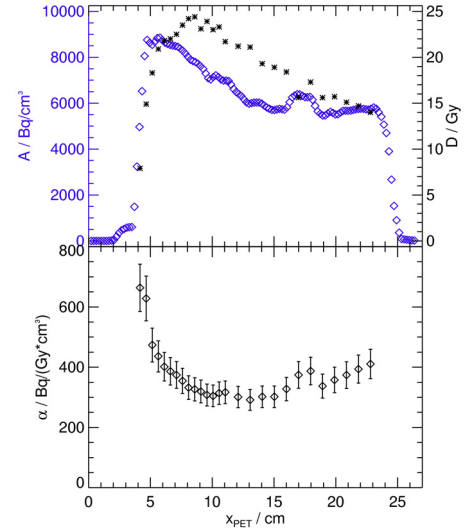


Fig. 2 Depth dose distribution D and activity concentration A (top) as well as dose related activity concentration α (bottom) in dependency of the penetration depth in a PMMA phantom at the end of the irradiation ($E_{e^-} = 34$ MeV).

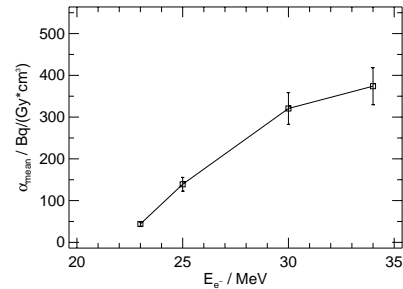


Fig. 3 Mean dose related activity concentration α_{mean} in a PMMA phantom in dependency of the electron energy E_{e^-} .

- [1] W. Enghardt, P. Crespo et al., Nucl. Instr. Meth. A 525 (2004) 284
 [2] H. Müller and W. Enghardt, Phys. Med. Biol. (2006), in press

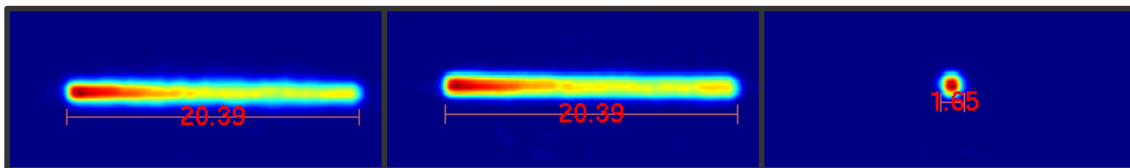


Fig. 1 Two dimensional distribution of the generated positron emitters (^{11}C) in a PMMA phantom for an electron energy of 34 MeV in transaxial, coronal and sagittal view (from left to right).

¹TU Dresden, Institut für Kern- und Teilchenphysik

²FZ Rossendorf, FWP

³also TU Dresden, Medizinische Fakultät

Experimental Setup of a PET-Scanner for Educational Purposes

T. WÜRSCHIG, W. ENGHARDT¹



Fig. 1 Picture of the PET-scanner 'PET-TW 05' Right: Front side with the integrated hardware components (above) and picture of the detector system (below)

The positron emission tomography has been established as one of the standard technologies for molecular imaging in clinical practice as well as in medical, biological and pharmaceutical research. Hence, for students with a corresponding specialization a practical introduction to this technique is highly desirable. Therefore, the PET scanner 'PET-TW 05' was realized which allows to demonstrate the principles of computer tomography (CT) and the basics of PET. Moreover, the technical requirements and the signal processing needed for a PET system are shown in a simplified way.

For the coincident registration of the annihilation photons two commercial block detectors

(*ECATEXACT*, [1]) are used. They are fixed in opposite to each other to coupled linear axes which are mounted on a revolving table. Like this it is possible to move the detectors along the linear axes and to rotate them, respectively. The motion is realized by step motors. Centered in the projection plane objects with an extension up to 20 cm can be examined. The data acquisition is proceeding continuously during the translation of the detectors at a fixed projection angle. Afterwards the system is rotated by 2°. Thus, a complete data set for the reconstruction is reached after ninety projections.

The image reconstruction is running parallel to the measurement. After each projection the measured intensity profile, the actualized sinogram (2D diagram of the intensity profiles versus the projection angle) and the images of the simple and the filtered backprojection deduced from the collected data are displayed on the screen. So it is possible to follow the successive build up of the reconstructed image using the method of the filtered backprojection during the measurement. To avoid an off-line analysis after the measurement, the data for each projection is stored in a binary file additionally.

The scanner has an intrinsic spatial resolution of 6.75 mm. The time resolution of 4.5 ns is better than the 8 to 12 ns usually achieved with comparable PET systems (same detectors, analog signal processing).

[1] M. Casey, R. Nutt; IEEE Trans.Nucl.Sci. 33 (1986) 460

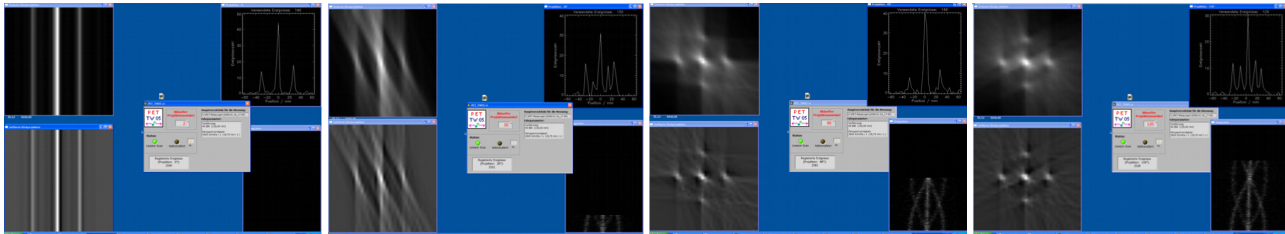


Fig. 2 Build up of the reconstructed images - screenshots during a measurement with 5 sodium (²²Na) point sources: (a) after the first projection, (b) after 15, (c) after 45, (d) after 60 of 90 projections

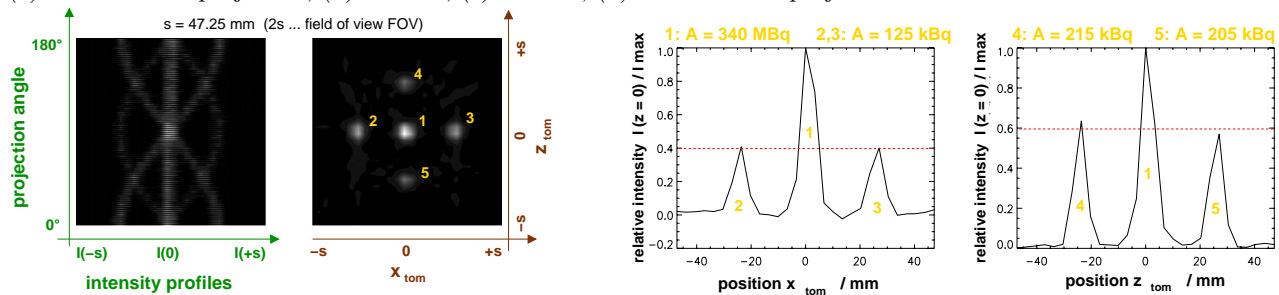


Fig. 3 Sinogram and image of the filtered backprojection after 90 projections (left). Besides the position of the sources their relative intensity to each other can be analyzed (peakheight in line diagrams of the reconstructed image at right).

¹also TU Dresden

Washout studies performed via in-beam PET ^{G,E}

F. FIEDLER, M. SELLESK,¹, W. ENGHARDT²

In the experimental carbon ion treatment facility at the Gesellschaft für Schwerionenforschung (GSI) Darmstadt, Germany, a double-head PET scanner has been installed [1]. Patients suffering from tumors mostly in the head and neck region are irradiated with ¹²C-ions [2].

Since dose and activity do not match, for a clinical application of in-beam PET a prediction is performed using a dedicated simulation [3]. By comparing the simulated β^+ -activity distribution to the measured one, information on beam portal position, anatomical changes and range deviations can be deduced. Since washout processes are not considered in the simulation up to now, the objective of this study was to find dependencies of washout processes on different parameters and to implement this process into the simulation. The PET measurement is done for each irradiation. If there is more than one, only the first irradiated portal per day is usually evaluated, since the results for the subsequent portals are corrupted by the radioactivity deposited by the previous ones. Usually the order of the portals alternates from day to day. The measurement includes the patient irradiation followed by 40s measuring the decay after the end of the irradiation. To calculate a biological half life T_{biol} from measured patient data also experiments done with carbon and water phantoms [4] were evaluated to come to an effective half life which is equivalent to the physical one T_{phys} due to the missing washout in the phantoms. Considering the O/C=3.15 ratio in the human, the effective half life T_{eff} was calculated as a weighted mean of the measured effective half lives in the phantoms fitted 40s after the end of the irradiation and found to be $T_{eff} = 128.1 \pm 3.3$. In this study [5] data from patients with tumors in the head and neck region treated at GSI between July 2003 and June 2005 at GSI Darmstadt were evaluated, only patient data from patients with two opposite portals and an irradiation protocol of 15 fractions plus 5 fractions boost were taken into account. Using a patient CT, along each coincidence line the mean and standard deviation

of the Hounsfield Units (HU) are calculated excluding all voxels without dose and air ($HU < 600$). Different subsets of the patient data were analyzed finding no dependence on the T_{eff} on the mean HU, the values for the effective half lives for the subsets can be found in Tab. 1.

Range HU	σHU	T_{eff}/s
$-50 < HU < 75$	$0 \leq \sigma < 100$	77.3 ± 3.4
$0 < HU < 250$	$100 \leq \sigma < 500$	75.8 ± 2.6
$250 < HU < 600$	$0 \leq \sigma < 750$	72.8 ± 1.6

Tab. 1 Effective half lives in dependence on the HU.

The dependence of the T_{eff} on T_{phys} and T_{biol} is given by [6]

$$\frac{1}{T_{eff}} = \frac{1}{T_{phys}} + \frac{1}{T_{biol}}. \quad (1)$$

A weighted mean T_{eff} was found to be 75.4 ± 2.5 s for patient irradiation and from eq. 1 results $T_{biol} = 183.1 \pm 21.3$. Furthermore, the dependence of T_{eff} on the dose was analyzed (cf. Tab. 2) and the T_{biol} was calculated due to eq. 1.

Range dose / %	T_{eff}/s	T_{biol}/s
0-90	71.8 ± 0.6	163.2 ± 8.3
90-100	79.5 ± 1.8	209.3 ± 21.1

Tab. 2 Effective and biological (cf. eq. 1) half lives in dependence on the dose.

The T_{biol} in the tumor is higher due to the lower perfusion in this tissue. So in the simulation in dependence on the dose two different additional biological half lives were introduced improving the fit to the measurement in some instances (cf. Fig. 1).

- [1] W. Enghardt et al. Nucl. Instr. Meth. A 525 (2004) 284
- [2] D. Schulz-Ertner et al. Strahlenther. Onkol. 179 (2003) 598
- [3] F. Pönisch et al. Phys. Med. Biol. 49 (2004) 5217
- [4] F. Fiedler et al. IEEE Nucl. Sci. Symp. Conference Records J01-2 (2005) 2757
- [5] M. Sellesk, Studienarbeit, 2005
- [6] H. Krieger Strahlenphysik, Dosimetrie und Strahlenschutz, B. G. Teubner Stuttgart 1998

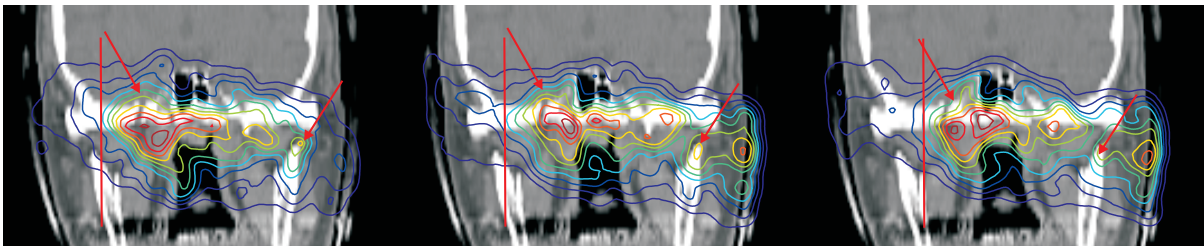


Fig. 1 β^+ -activity distribution superimposed on a patient CT. Left: measurement, middle: simulation with consideration of washout, right: simulation without washout. The range is marked by a line and differences in the simulations are shown by arrows.

¹also TU Bergakademie Freiberg ² also TU Dresden

Optimum Detector Arrangements for In-Beam PET with Direct Time-of-Flight

B,G

P. CRESPO, F. FIEDLER, J. PAWELKE, G. SHAKIRIN, W. ENGHARDT¹

Due to its effectiveness in monitoring highly tumor-conformed charged hadron therapy, in-beam positron emission tomography (in-beam PET [3]) is strongly desirable at charged hadron facilities under construction [2] or planning [3]. We present, therefore, optimized arrangements of the γ -ray detectors for next-generation in-beam PET scanners. A versatile, fully 3D, rebinning-free maximum likelihood expectation maximization (MLEM) algorithm coupled to a simulation routine was applied to several high-resolution closed-ring or dual-head tomographs. The use of the time-of-flight (TOF) information between each pair of annihilating photons [4, 5] was also investigated. In order to evaluate the quality of images obtained with several camera configurations in real therapeutic situations, β^+ -activity distributions calculated from real treatments with the PosGen Monte-Carlo code [6, 7] were considered. Results regarding the optimization of in-beam PET for monitoring head-and-neck irradiation can be found in [4, 5, 8]. Here we refrain to the more challenging situation, due to the large image volume, of monitoring the irradiation of the pelvis.

Fig. 1 depicts the positioning strategy for monitoring irradiation of the pelvis with in-beam PET. The closed-ring tomograph (left) has substantial larger volume in respect to conventional nuclear medicine PET scanners, from which the dual-head tomographs are composed (right). Fig. 2 shows the corresponding reconstructed images obtained without (top and middle rows) and with (bottom) time-of-flight (TOF) capable detectors. The sagittal views in Fig. 2 show the rectum of the patient, a radiosensitive organ, lying adjacent to the irradiated tumor and, therefore, elucidate how in-beam PET monitoring brings important information to the radiooncologist. Clearly, the closed-ring detector configuration (top row) yields the best images and its implementation feasibility is discussed in [4, 8]. Although the field of view of the dual-head tomograph with $\phi = 46^\circ$ (middle row) covers the irradiated volume completely, the corresponding reconstructed images contain less information due to the image degradation arising from the gaps between the two detector heads [4, 8]. This degradation is refrained [4, 5] if TOF-capable detectors with sufficiently good coincidence time resolution are used (bottom row).

In summary, in-beam PET monitoring of large fields benefits most from a closed-ring tomograph as long as ultra-fast, TOF-capable detectors are not available at large production scales. A non-TOF dual-head tomograph with $\phi = 46^\circ$ yields satisfactory results for monitoring head-and-neck irradiation due to the smaller target volume (not shown).

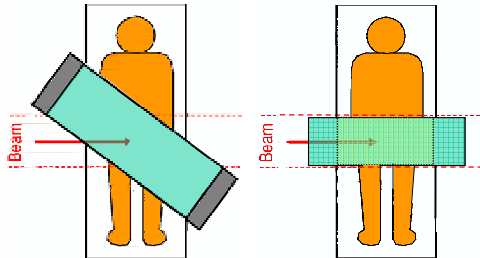


Fig. 1 Patient positioning with closed-ring (left) and dual-head (right) tomographs for pelvis irradiation.

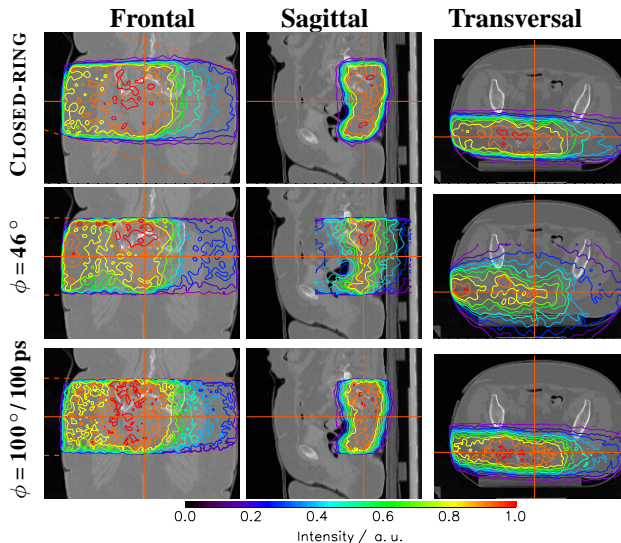


Fig. 2 Reconstructions of a realistic pelvis irradiation (simulation). The dashed lines (frontal views) depict the margins of the tomograph (cf. Fig. 1). The angle ϕ (dual-head scanners only) is formed between the edge of the top and bottom detector heads with the isocenter of the tomograph. Top and middle rows obtained without TOF-capable detectors and with MLEM reconstruction. Bottom row with detectors yielding 100 ps FWHM coincidence time resolution and with an ultra-fast (potentially real-time) direct-TOF algorithm [4, 5].

- [1] W. Enghardt, P. Crespo et al., NIM A 525 (2004) 284
- [2] H. Eickhoff, R. Bär et al., PAC'03, Portland, OR, p. 694
- [3] Siemens Medical Solutions, "Particle therapy, getting to the point", Order No. A91100-M2600-C689-2-7600
- [4] P. Crespo, Thesis, Technische Universität Darmstadt (2005)
- [5] P. Crespo, F. Fiedler et al., Phys. Med. Biol. (2006) to be submitted
- [6] B.G. Hasch, Thesis, Technische Universität Dresden (1996)
- [7] F. Pönisch, K. Parodi et al., Phys. Med. Biol. 49 (2004) 5217
- [8] P. Crespo, G. Shakirin et al., Phys. Med. Biol. (2005) submitted

¹also TU Dresden

Despite its many advantages as a scintillator for PET [1], the lutetium in LSO (Lu_2SiO_5) contains approximately 2.6% ^{176}Lu , a natural radioisotope. This leads to an LSO background activity density of approximately 240 Bq cm^{-3} [2] which induces an intrinsic background activity onto LSO-based PET scanners. The intensity of this background depends on several parameters like the volume of scintillator and the geometry of the tomograph, or the coincidence time resolution of the readout detectors and electronics. We report the influence of this intrinsic activity onto very low activity images obtained with two LSO-based PET scanners: the Pico Hi-Rez from the Biograph 16 PET/CT and the microPET P4. A low-activity phantom was positioned in the field of view (FOV) of the tomographs. In order to evaluate the potential use of LSO for next-generation, in-beam PET scanners, the intensity and shape of the activity distribution resembled those obtained with in-beam PET imaging for ion therapy monitoring [3]. The phantom consisted of a 12 cm long hollow cylinder of polyethylene (PE) with outer and inner diameter of 19 and 8.5 cm, respectively. An ^{18}F -fluoro-deoxyglucose (FDG) solution with an initial activity density of approximately 1 kBq cm^{-3} was inserted into the hollow cylinder. The PE cylinder is expected to attenuate the annihilation photons by about the same factor observed when performing brain scans. The total measuring time was ten hours, corresponding to 5.5 half-lives of ^{18}F . During each half-life a long and a short scan of 70 and 5 minutes, respectively, was performed.

Fig. 1 shows images sampled with the Pico Hi-Rez with a phantom activity density similar to that induced by fractionated carbon ion irradiation at the Gesellschaft für Schwerionenforschung (GSI), Darmstadt. This activity is of the order of $200 \text{ Bq cm}^{-3} \text{ Gy}^{-1}$ [3], which amounts to about 60 Bq cm^{-3} for irradiation portals delivering as low as 0.3 Gy. The quality of the images sampled with a long acquisition time of 70 minutes is quite high. For a very short sampling time of 5 minutes the central region of the FOV where the phantom was located appears hot in the attenuation-corrected image. This is because the uniform background was amplified more heavily in the area with higher density. Due to its much smaller scintillator volume, the randoms-to-trues ratio (RTR) measured with the animal PET scanner microPET P4 (Fig. 2) is always smaller than unity. Therefore, the images obtained with that tomograph do not show artefacted hot areas (not shown). Because of the good agreement with the RTR measured here and those calculated in [4] we conclude that the influence onto in-beam PET of the intrinsic activity of LSO-based tomographs can

be eliminated by fulfilling two requisites [4]: the use of optimum electronics providing low enough coincidence time resolution together with a reconstruction algorithm dedicated to low-statistics datasets.

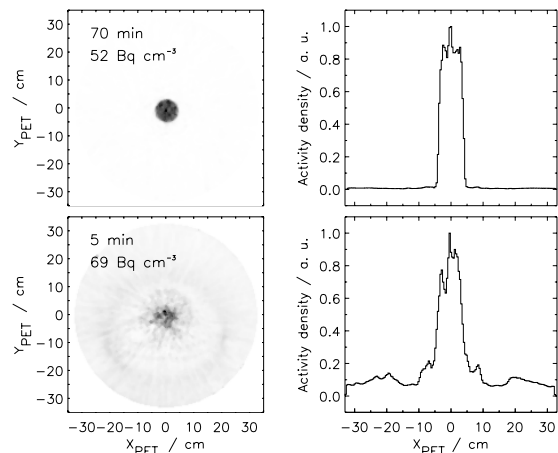


Fig. 1 Low activity imaging with long (top) and short (bottom) sampling times. The 2D images show the central slice of the tomograph. The line profiles show the average of the seven middle pixels along the center of the 2D image. Data were sampled in 3D with the Pico Hi-Rez PET scanner and reconstructed with an attenuation correction algorithm (OSEM-2D, 4 subsets, 8 iterations).

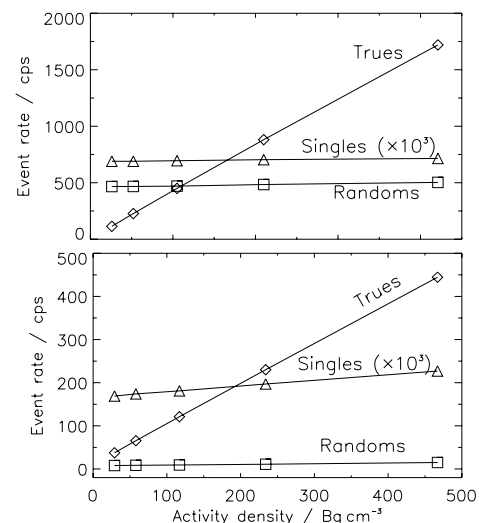


Fig. 2 Event rates registered with the Pico Hi-Rez (top) and with the microPET P4 (bottom) PET scanners for different phantom activity densities.

- [1] W.W. Moses, S.E. Derenzo, IEEE Trans. Nucl. Sci. 46 (1999) 474
- [2] J.S. Huber, W.W. Moses et al., Phys. Med. Biol. 47 (2002) 3535
- [3] W. Enghardt, P. Crespo et al., NIM A 525 (2004) 284
- [4] P. Crespo, Thesis, Technische Universität Darmstadt (2005)

¹ TU Dresden, Zentrum für Innovationskompetenz Oncoray

² FZ Rossendorf, FWP

Systematic Measurement of Channeling Radiation Yields for Diamond

W. WAGNER, B. AZADEGAN, J. PAWELKE

In the face of a powerful channeling radiation (CR) production for application as a novel quasi-monochromatic X-ray source, a systematic study of the dependence of the yield (Y) of planar CR from the most intense $1 \rightarrow 0$ transition in the (110) plane of diamond has been performed. Diamond type IIa crystals of thickness 42.5, 102, 168 and 500 μm have been investigated at electron energies of 14.6, 17, 30 and 34 MeV.

The quantum theory of CR predicts that the yield of planar CR scales with the electron energy nearly like $Y \sim \gamma^{5/2}$ where γ denotes the Lorentz factor. According to newer measurements [1,2], the yield, however, should also increase with the crystal thickness (z) like $Y \sim z^{1/2}$ due to the effect of in-plane multiple scattering.

Recently, it could be found that the Doppler broadening of the CR linewidth associated with multiple scattering during channeling is remarkably weaker than expected by the formal assumption that multiple scattering acts on channeled particles in the same manner as on nonchanneled ones [3].

This opens the possibility to enhance the CR intensity without extensive loss of quasi-monochromacy by optimal choice of electron energy and crystal thickness as well. Although self absorption of radiation in the crystal depth becomes the limiting parameter now, at the electron energies considered here, this is less crucial because of the low atomic number of carbon.

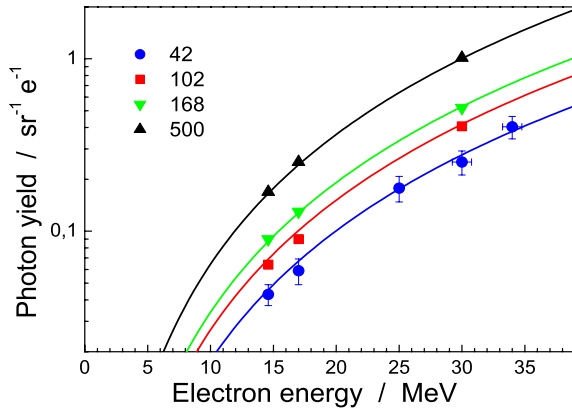


Fig. 1 Yields of channeling radiation from the $1 \rightarrow 0$ transition in the (110) plane of diamond (preliminary).

Some preliminary results of our measurement series are shown in Fig. 1. It should be mentioned that yield measurements with diamond performed earlier usually concerned thinner crystals (i.e., 13-55 μm [4]),

and there was only one previous work where a 200 μm thick diamond type IaA crystal has been sampled [1]. The data shown in Fig. 1 can be uniformly interpreted by the above mentioned dependence on the electron energy. The lines drawn in Fig. 1 for every crystal thickness i represent the function $Y = c_i \times \gamma^{5/2}$ where the coefficients c_i have been chosen to approach the data points, respectively. For more clearness, error bars are only shown at the values measured for the thickness 42.5 μm but they are typical for the entire measurement series.

Since the numerical values of the coefficients c_i provide the relative dependence of the CR yield on the crystal thickness, they are drawn versus this parameter in Fig. 2. The indicated error bars have been determined by variation of c_i such that all data points obtained for a given thickness were enveloped. The thickness of the crystals has been measured by means of a submicron stylus profiler (VEECO DEKTAK 8).

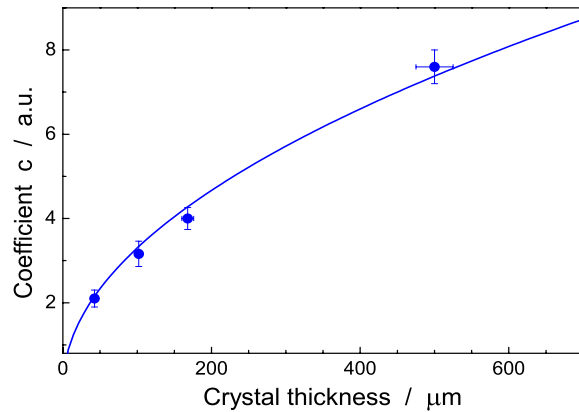


Fig. 2 Coefficients as determined from Fig. 1 in dependence on the crystal thickness (see text). The line represents an approximation of the data points by a curve proportional to $z^{1/2}$.

From Fig. 2 one can conclude that the yield of CR from the transition between the most tightly bound channeling states in the (110) plane of diamond depends on the crystal thickness like $\sim z^{1/2}$, and this proportionality holds up to rather large values of crystal thickness as well as over the entire range of electron energy considered.

- [1] I. Reitz, Diploma thesis, TU Darmstadt (1999)
- [2] W. Wagner, B. Azadegan et al., SPIE vol. 5974 (2004)
- [3] B. Azadegan, J. Pawelke, W. Wagner, this report, p. 65
- [4] H. Genz, L. Groening et al., Phys. Rev. B 53 (1996) 8922

Peak Shape Analysis of Channeling Radiation Spectra

B. AZADEGAN, J. PAWELKE, W. WAGNER

Spectra of planar channeling radiation (CR) have been measured for diamond crystals of thickness 42.5, 102, 168 and 500 μm at electron energies of 14.6, 17, 30 and 34 MeV. The influence of different line-broadening mechanisms on the line shape of CR from the $1 \rightarrow 0$ transition in the (110) plane has for the first time been investigated at relatively large variations of crystal thickness and beam energy as well.

Recently, the transition energies have been calculated by means of the many-beam method [1]. Several mechanisms, however, govern the formation of the CR line shape registered. It depends on the coherence length, finite crystal thickness, Bloch-wave broadening, beam-energy spread, beam divergence, detector resolution and the Doppler broadening (Γ_{Dopp}). Multiple scattering during channeling can remarkably affect the CR line shape because small-angle scattering of the electrons on their path through the crystal effectively increases the beam divergence. This leads to an energy shift, peak broadening and an asymmetric CR line shape as well.

If the CR peaks are sufficiently well separated, the mean multiple-scattering angle can be obtained from measured spectra. To account for multiple scattering, we approximated the registered CR lines by a convolution of a Lorentzian (bandwidth Γ_T) with a Gaussian-like distribution of the multiple-scattering angle [2]

$$P(E_x)dE_x = \pi^{-3/2}dE_x \times \int_0^\infty \frac{t^{-1/2}\Gamma_T(1+2\alpha^2t)e^{-t}}{(E_x(1+2\alpha^2t) - E_0)^2 + 0.25(1+2\alpha^2t)^2\Gamma_T^2} dt \quad (1)$$

where $\alpha = \gamma\theta_{ms,ch}$, $\theta_{ms,ch}$ denotes the dispersion of the multiple-scattering angle for planar channeled electrons, E_x is the CR peak energy and E_0 is the maximum photon energy at zero degree.

The measured spectra were corrected for detector efficiency, self absorption in the crystal and attenuation in other window materials. After subtraction of the bremsstrahlung background, functions as given by Eq. (1) have been fitted to the CR lines, and the remaining background was approximated by a low-order polynomial (Fig. 1).

Fig. 2 shows the values of the squared asymmetry parameter (α^2) resulting from the peak-shape analysis of our measurements at the electron energy of 17 MeV in dependence on the crystal thickness (L). This dependence is by far not linear as predicted for nonchanneled particles but can be described by a function of the form $\alpha^2 = bL^c$ with $c=0.37$ and b being a scaling factor. This means that the effect of multiple-scattering during planar channeling is weaker.

Tab. 1 lists the parameters Γ_T and Γ_{Dopp} as deduced from the fitting procedure and the total (FWHM) linewidth of the asymmetric profiles (Γ_{tot}) for the $1 \rightarrow 0$

transition obtained at 17 MeV electron energy. As an effect of multiple scattering during channeling, Γ_{tot} only slightly increases with the crystal thickness while Γ_T is found to be rather constant. With respect to some application of CR as a quasi-monochromatic X-ray source, this finding enables the usage of thicker crystals for more effective CR production [3].

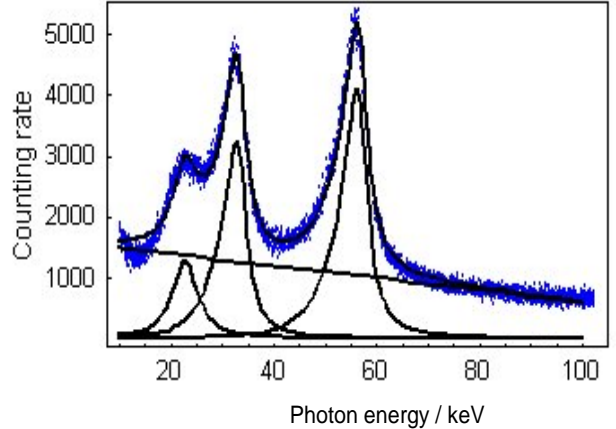


Fig. 1 Least squares fit of the spectrum of (110) planar channeling radiation for a 168 μm thick diamond crystal at an electron energy 30 MeV.

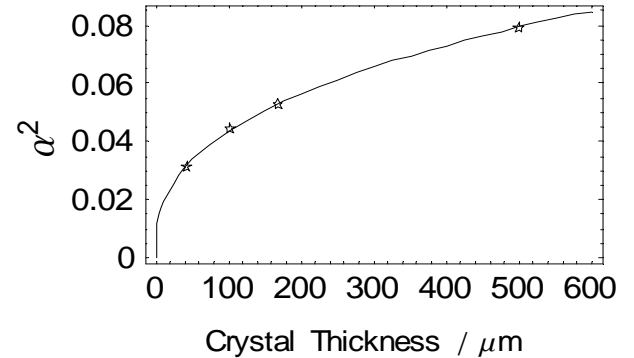


Fig. 2 Squared asymmetry parameter as obtained for the electron energy of 17 MeV drawn versus the crystal thickness.

Tab. 1 Planar CR linewidths for the $1 \rightarrow 0$ transition in the (110) plane at 17 MeV electron energy.

$L/\mu\text{m}$	Γ_{tot}/keV	Γ_T/keV	Γ_{Dopp}/keV
42.5	2.00	1.45	0.69
102	2.19	1.45	0.98
168	2.47	1.44	1.16
500	2.77	1.26	1.74

- [1] B. Azadegan, L.Sh Grigoryan et al., IKH Annual Report 2004, FZR-423 (2005) 68
- [2] M. Gouanere, D. Sillou et al., Phys. Rev. B 38 (1988) 4352
- [3] W. Wagner, B. Azadegan et al., IKH Annual Report 2004, FZR-423 (2005) 69

Planar Channeling Radiation from 17 - 34 MeV Electrons in Quartz

B. AZADEGAN, W. WAGNER, J. PAWELKE, L.SH. GRIGORYAN¹

At moderate electron energies, channeling radiation (CR) has been studied with crystals of diamond, ruby, Si, Ge, Ni and LiF. We performed measurements of planar CR spectra on quartz (SiO₂) at electron energies of 17, 25 and 34 MeV.

A quartz crystal is characterised by a hexagonal structure containing 3 Si and 6 O atoms in the unit cell. Its lattice is defined by two primitive vectors \mathbf{a}_1 , \mathbf{a}_2 of equal length, which open an angle of 120°, and a third one \mathbf{c} directed perpendicular to both the others. Conventionally, a crystal plane is given by four indices $(hki\bar{l})$ with $i = -(h + k)$. Therefore, some crystal planes are segregate and others are mixed.

Continuum potentials for different planes of quartz have been calculated using the Doyle-Turner potential [1]. The eigenvalues of channeled electrons were found by means of the many-beam formalism [2]. For illustration, the continuum potential of the $(20\bar{2}3)$ plane is shown in Fig. 1 together with the eigenvalues calculated for an electron energy of 34 MeV.

The spontaneous transition rate of planar CR per unit of solid angle, per unit of photon energy, per unit of crystal thickness, and per electron is given in [3]. For CR directed along the electron motion, one finds

$$\frac{d^2 N_{i-f}}{d\Omega dz} = \frac{\alpha \lambda_c^2}{\pi \hbar c} 2\gamma^2 (E_i - E_f) |\langle \psi_f | \frac{d}{dx} | \psi_i \rangle|^2 P_i(z) \quad (1)$$

where α denotes the fine structure constant, λ_c is the Compton wavelength, γ means the Lorentz factor, ψ_i and ψ_f are the eigenfunctions of the electron in the initial and final state, respectively. The photon energy at zero degree in the lab system is $2\gamma^2(E_i - E_f)$. The function $P_i(z)$ denotes the population of the i -th channeling state in dependence on the crystal thickness z . Since in our measurements we used a 200 μm thick quartz crystal, we temporarily assumed an equilibrium initial population.

Equation (1) has been applied for the $(20\bar{2}3)$ plane of quartz at the electron energies of our measurements. As can be seen in Fig. 1, at the electron energy of 34 MeV, there are only three bound states affording the transitions 1-0, 2-1 and 3-0. Measured spectra of CR corrected for detector efficiency, self absorption in the crystal, attenuation in other window materials and bremsstrahlung background are shown in Figs. 2 and 3 where the calculated CR energies and relative intensities for the transitions 1-0 and 2-1 are indicated by vertical lines of heights proportional to the values determined by means of Eq. (1) at equilibrium initial population.

Compared with diamond [4] the intrinsic CR line widths for quartz are substantially larger.

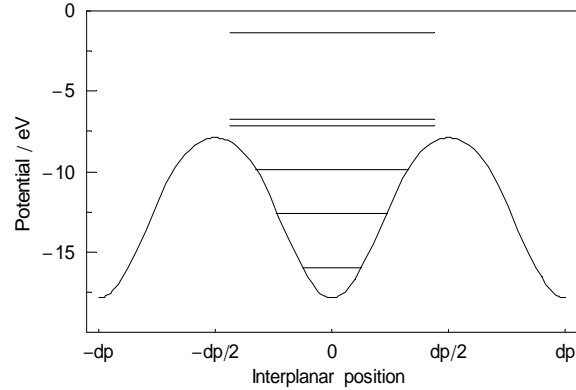


Fig. 1 Potential of the $(20\bar{2}3)$ plane of quartz and eigenvalues calculated for 34 MeV electron energy. dp means the interplanar distance.

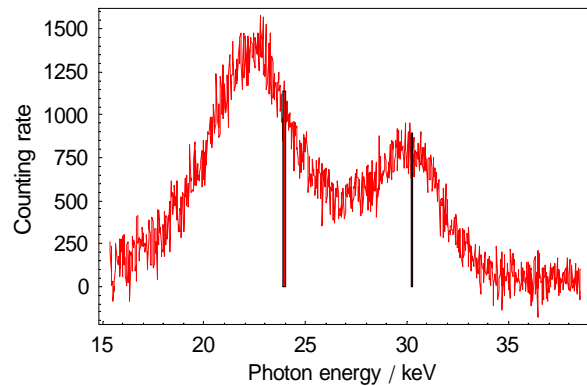


Fig. 2 Measured planar CR from 34 MeV electrons in quartz. Calculated photon energies are indicated by vertical lines.

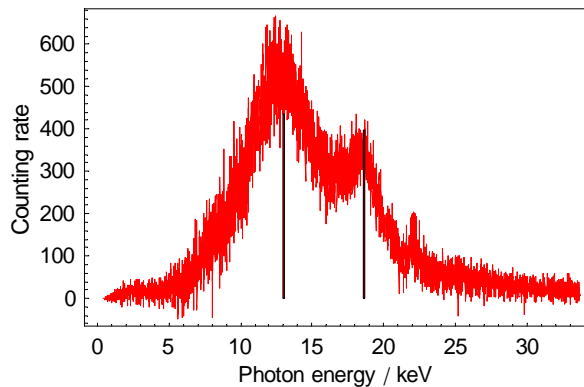


Fig. 3 Analogous to Fig. 2 but at 25 MeV electron energy.

- [1] J.U. Andersen, E. Bonderup et al., Phys. Scr. 28 (1983) 308
- [2] B. Azadegan, L.Sh. Grigoryan et al., IKH Annual Report 2004, FZR-423 (2005) 68
- [3] J.U. Andersen, K.R. Eriksen, E. Lægsgaard, Phys. Scr. 24 (1981) 588
- [4] B. Azadegan, J. Pawelke, W. Wagner, this report, p. 65

¹IAPP NAS, Yerevan, Armenia

Radiation Background Measurement at the ELBE Channeling X-Ray Beam Line

J. PAWELKE, B. NAUMANN¹, W. WAGNER

Reliable studies of radiobiological effects on living cells need a maximum irradiation dose rate of about 1 Gy/min and a sufficiently low level of radiation background at the irradiation site. The production of channeling radiation (CR) at ELBE as a source of quasi-monochromatic soft X-rays with the necessary high intensity requires an electron beam of about 100 μ A current. Five air-filled ionisation chambers (IC) were placed around the CR beam line (Fig. 1) and the photon background dose rate \dot{D}_γ has been measured by two Farmer IC (position I and II), two rigid stem IC (position III and IV) and an LB6701 IC (position V) [1]. In addition, the neutron background dose rate \dot{D}_n was measured with a BF₃ counter (2202-D, Alnor, Turku, Finland) at position VI.

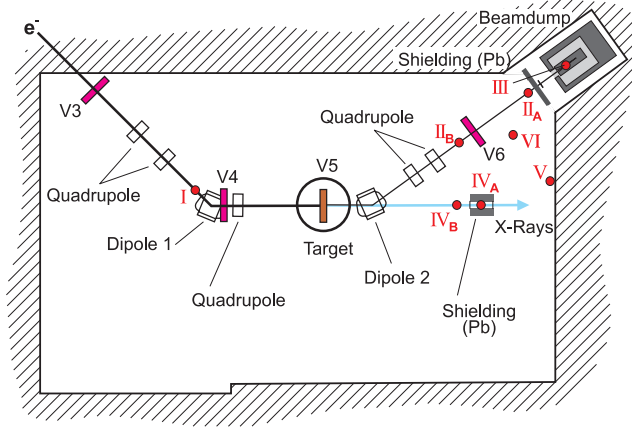


Fig. 1 Position of the ionisation chambers in the radiation physics cave. The electron beam comes from the accelerator (left) and is stopped in the dump (right).

After tuning the electron beam of 14.6, 22.5 and 30.0 MeV, respectively, up to 200 μ A current, dose rates were measured without any target in the beam (#1). The measurement was repeated after an 18 μ m thick Al foil was inserted into the beam at target position V5 in order to study the influence of electron scattering in the target on the beam loss, and corresponding generation of radiation background. The Al foil has been chosen for practical reasons and results in a roughly comparable electron scattering as the thicker

diamond crystals used for CR generation. Upon entering the cave and moving IC II and IV from position A to B the dose rates were measured again (#2) for both cases (with and without target in the beam).

Without passing a target the electron beam can be transported to the dump without loss (see Table 1) which results in a very low level of radiation background at the cell irradiation site (cf. position II_B, IV_A and V). In contrast, the electron scattering in the target results in a considerable beam loss and a corresponding overall rise of the radiation background level. However, the commissioning of the second LINAC section at ELBE not only allowed to increase the electron energy up to 35 MeV but also to reduce the radiation background level by more than one order of magnitude at low electron energy (cf. Table 1 with the dose rates reported in [1] for 17.0 MeV). Also, the high photon radiation intensity at the cell irradiation site is mainly caused by bremsstrahlung generated in the target and emitted in forward direction of the electron beam. Only a small bremsstrahlung contribution of about 5% generated at the beam line reaches the irradiation site (Fig. 2) and the neutron dose contribution is even smaller. Therefore, in a next step the irradiation of cells is prepared.

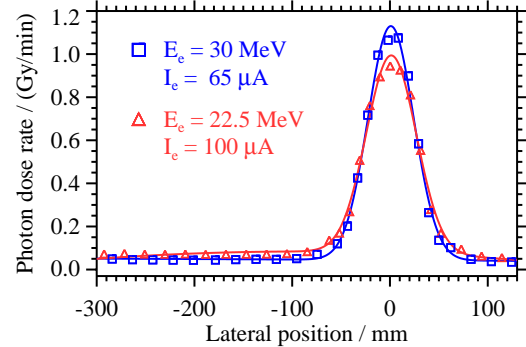


Fig. 2 Horizontal dose profile measured at position IV_B for the 18 μ m thick Al target.

[1] J. Pawelke, U. Lehnert et al., IKH Annual Report 2004, FZR-423 (2005) 71

Tab. 1 Comparison of dose rates at different positions measured for an electron beam current of 100 μ A.

E_e / MeV	Target	Photon dose rate \dot{D}_γ / (mGy/min)										\dot{D}_n / (mSv/h)			
		I		II _A		II _B		III		IV _A		V		VI	
		# 1	# 2	# 1	# 2	# 1	# 2	# 1	# 2	# 1	# 2	# 1	# 2	# 1	# 2
14.6	no	<0.6	<0.6	990	<0.6	17.1	17.4	<1.3		2.1	2.2	3.2	3.3		
	18 μ m Al	<0.6	<0.6	11900	630	20.8	24.1	363		32.3	34.3	7.3	7.0		
22.5	no	<0.6	2.6	685	<0.6	33.6	33.1	<1.3		0.9	0.9	23.3	21.7		
	18 μ m Al	<0.6	3.2	8710	2020	42.0	47.5	961		108.4	81.4	63.3	80.0		
30.0	no	1.8	6.5	556	<0.6	37.6	37.2	<1.3		0.7	0.7	96.6	104.3		
	18 μ m Al	2.3	2.8	3382	3281	47.8	63.1	2040		20.5	132.1	200.0	208.1		

¹FZR, Department of Safety and Radiation Protection

Optimization of FISH for the Determination of RBE of Soft X-Rays for the Human Mammary Epithelial Cell Line 184A1

A. LEHNERT, E. LESSMANN, J. OSWALD,¹ J. PAWELKE

The application of low-energy X-rays in medicine gains in importance in Germany due to the recent introduction of mammography screening. Mammography is nowadays the most important method for detection of breast cancer at an early stage. Dedicated mammography X-ray tubes are operated usually at 25-30 kV, therefore it is particularly important to precisely determine the relative biological effectiveness (RBE) of low-energy X-rays. With outlook to the potential of low-energy X-rays to induce neoplastic transformation, a relevant biological object has to be used for this purpose. Our cell line in choice is the human mammary epithelial cell line 184A1 (purchased from ATCC, USA). It was derived from reduction mammaplasty tissue with no detectable cell pathology. Transformation to immortality was achieved by exposure to the environmental carcinogen benzo[a]pyrene [1]. These cells are not malignant, and, although immortal, are only minimally deviant from normal human mammary epithelial cells.

The method of fluorescence in situ hybridization (FISH) allows to evaluate the stable translocations in the chromosomes, therefore revealing the hereditary damage to the genetic material. The cells were cultivated in MEBM medium, supplemented with 52 µg/ml bovine pituitary extract (BPE), 5 ng/ml epidermal growth factor, 0.5 µg/ml hydrocortisone, 5 µg/ml bovine insulin, 5 µg/ml human apo-transferrin, gentamicin sulfate and amphotericin-B (reagents from Cambrex, USA) and 2.5×10^{-8} M prostaglandin E1 (Sigma, USA). The cells were cultured at 37°C in humidified atmosphere containing 5% CO₂ in 25 cm² culture flasks. In order to synchronize the cells for the planned experiment, the cells were left for several days after achieving confluence with medium change every third day. The proportions of cells in the different cell cycle stages were determined by fluorescent activated cell sorting (FACS). For this purpose, fixed cells were stained with the fluorescence dye propidium iodide, afterwards the forward and the orthogonal scattering of a laser light were measured. These parameters were used to determine the DNA content of the cells. From the flow cytometric histogram shown in Fig. 1, the fraction of cells in the G₀/G₁ phase of the cell cycle was determined to be about 97%, showing the good applicability of the synchronization method to this cell line.

After irradiation, cells were reseeded at low density and incubated for 45 h, whereas colcemide at a concentration of 0.8 µg/ml was added for the last two hours of incubation. The metaphase suspension was obtained by scraping the cells from the flask sur-

face. After a hypotonic treatment, the cells were fixed in a methanol/acetic acid fixative and dropped onto grease-free, cold, wet slides. Whole-chromosome staining of the chromosomes 1, 8 and 17 was chosen (probes from Metasystems, Germany). An appropriate mixture of the probes was denatured at 75°C and applied onto the slides, separately denatured with NaOH. Afterwards, the mixture was dispensed onto each slide, coverslipped and incubated at 37°C in a dark humidified chamber overnight. After the hybridization, the slides were washed and stained with DAPI/Antifade-Vectashield (Vector Laboratories, USA). The slides were examined on a microscope Axiovert S100 with a fluorescent lamp HBO100 and the images were obtained with a CCD camera Axiocam MRc5. For visualization and processing of the images, Axiovision software 4.4 (all equipment from Carl Zeiss, Germany) was used. As an example, an irradiated metaphase of 184A1 cells is shown in Fig. 2.

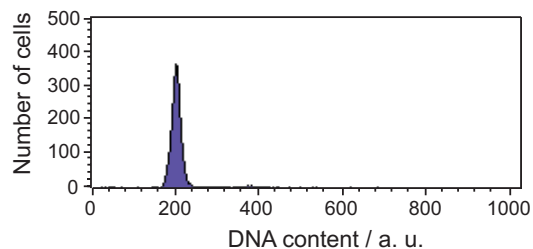


Fig. 1 Flow cytometric histogram of the 184A1 cells synchronized in the G₀/G₁ stage of the cell cycle. One single peak indicates that almost all cells are in G₀/G₁ phase.

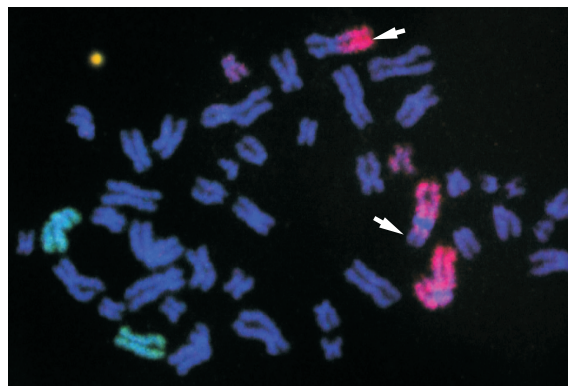


Fig. 2 A metaphase of the 184A1 mammary epithelial cells, irradiated with 3 Gy of 10 kV X-rays. Chromosomes 1, 8 and 17 are painted red, green and orange, respectively. All other chromosomes are stained with DAPI. A reciprocal translocation involving chromosome 1 is shown by arrow.

[1] M.R. Stampfer, J.C. Bartley, Proc. Natl. Acad. Sci. USA. 82 (1985) 2394

¹FZ Rossendorf, FWR

Dosimetric Validation of the Electron Photon Transport Code AMOS

U. REICHEL, J. HENNIGER,¹ W. ENGHARDT²

At many different applications of ionizing radiation in radiobiology, medicine and radiopharmacology an accurate dosimetry is necessary. Since in several cases, especially at internal exposures, this cannot be done by measurements a validated radiation transport simulation system comes to use, the Monte Carlo (MC) program AMOS [1]. It is a non analogue MC algorithm for coupled electron photon transport. Therein a single scattering model handles the propagation of electrons in matter.

Here two different validation examples specialized to determine internal dose distributions are presented. Further parameters are calculated by AMOS and are compared with published data reviewed and recommended by the Medical Internal Radiation Committee (MIRD) of the Society of Nuclear Medicine.

The first comparison bases on the dose point kernel method [2]. It is a fast way to estimate the dose distribution at internal irradiations. The dose point kernel K is defined as the deposited dose per unit activity in dependence on the distance to a point source of a specific isotope. The dose distribution is calculated from convolving the activity distribution and the dose point kernel.

Reference data was published by Cross et al. [3]. Therein amongst others they provide the dose point kernel of the β^- component of several radioactive isotopes used in nuclear medicine. For the presented comparison data for an ^{131}I point source were recalculated. The results are shown in Fig.1. At distances below 1.5mm a very good agreement can be found. The discrepancy occurring above originates from the consideration of γ - and X-ray emissions of ^{131}I in AMOS. Hence in a second calculation this primary photon emissions were neglected. The related graph in Fig. 1 shows better agreement. Cross' data is zero above 0.2 cm. The still remaining photon component results from produced bremsstrahlung photons.

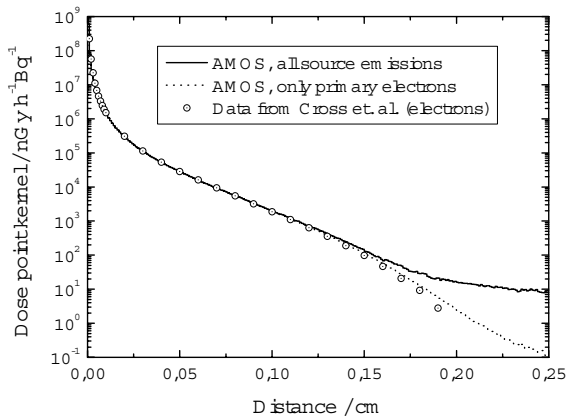


Fig. 1 Comparison of dose point kernel calculations by AMOS and from Cross et al.

¹TU Dresden, Institut für Kern- und Teilchenphysik

²also TU Dresden

As second example a method used in voxel defined irradiation environments was chosen. Therein so-called S-values S are used to determine the contribution of activity of a single source voxel to its direct and more distant neighbors. The calculation of the S-values is not only dependent on the isotope but also on the exact geometric conditions. The activity of the source isotope is treated as homogeneously distributed in the voxel volume. So the mean dose in any voxel with index (i, j, k) can be determined from

$$\bar{D}(i, j, k) = \sum_{\forall i_s} \sum_{\forall j_s} \sum_{\forall k_s} A(i_s, j_s, k_s) \cdot S((i - i_s), (j - j_s), (k - k_s)) \quad (1)$$

with the voxel based activity distribution $A(i_s, j_s, k_s)$. Bolch et al. published data for $3 \times 3 \times 3 \text{ mm}^3$ cubic voxels filled with water [4]. For their calculations the well established Monte Carlo Code EGS4 was used. In Fig. 2 a set of here determined S-values for ^{131}I is shown as an example. For reasons of clearness only single values by Bolch et al. are dotted, but they evidence well for the match of all data.

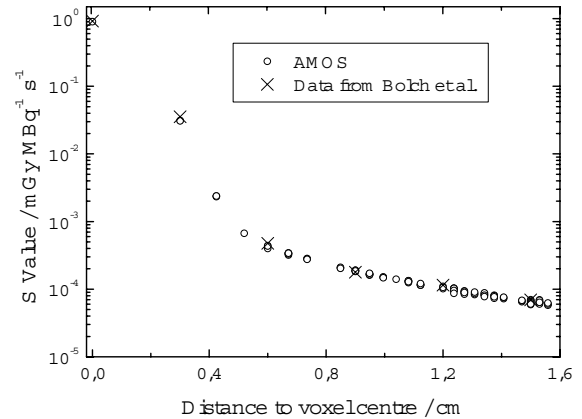


Fig. 2 Set of S-values calculated by means of AMOS compared with results of Bolch et al.

Both chosen dosimetric methods lead to very good agreement. The first proved the correct treatment of electron transport - a new developed extension of AMOS. The photon component and the coupling of electron to photon transport dominates the secondly presented example.

- [1] U. Reichelt, J. Henniger, Proc. of 14th Intl. Conf. of Solid State Dosimetry, Radiat. Protect. Dosim. (2006) in press
- [2] P.K. Lechner, J. Nucl. Med. 35 (1994) 1721
- [3] W.G. Cross, N. O. Freedman et al., Health Phys. 62(2) (1992) 160
- [4] Bolch et al., MIRD Pamphlet No. 17, J. Nucl. Med. 40 (1999) 11S

Basic Evaluation of the Influence of Tungsten in Cells at Photon Irradiation

U. REICHELT, W. ENGHARDT,¹ J. PAWELKE

A new approach in cancer therapy is to combine pharmaceutical targeting agents with external photon irradiation - the photon activation therapy (PAT) [1]. Chemical elements of large atomic number are bound to the agent. The photon absorption cross section of these atoms exceeds that of tissue by about two orders of magnitude. At energies above binding energy the ionization of the K shell dominates. The emerging vacancy is filled with outer atomic and free electrons by radiative and non radiative transitions. Beside the X-rays low energy Auger- and Coster-Kronig electrons with small ranges are emitted that are leading to localized secondary ionizations. If this takes place very close to the DNA, double-strand breaks are supposed to be significantly increased.

One applicable element is tungsten. It can be attached e. g. onto amino sugar molecules which are transported through the cell membrane into the cell plasma and also into the nucleus. The interest was pointed to the distance dependence of the damage production by low energetic secondary radiation. Therefore, the photon electron transport was studied by means of AMOS [2]. The differential energy loss in human tissue (ICRU 44 - mean male soft tissue [3]) with 0.57 at. % tungsten added was determined. Fig.1 shows the results for primary vacancy in the K shell (69.7 keV binding energy) and in the L1 shell (12.1 keV binding energy).

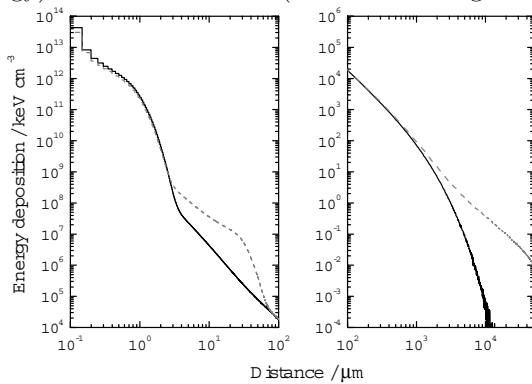


Fig. 1 Distance dependent energy deposition from initial vacancies: grey dashed - K shell, black solid - L1 shell

Comparing the graphs concerning the dimensions of the nucleus ($\approx 5 \mu\text{m}$) and the cell (a few tens of micrometer), L1 shell ionizations seem to be preferable because the energy loss for very small distances is increased and more localized to the point of the source. The absence of K_{α} X-rays decreases the radiation exposure of surrounding healthy tissue. However the external photons have to penetrate to the target volume without too much absorption. Hence an energy below the K shell binding energy is not always reasonable.

The influence of the distribution of the tungsten inside the cell was topic of further studies. The tar-

geting agent should be selective to the tumor cells (preferable directly to the DNA). This can be achieved by using e.g. antibodies or substances taking part at the often increased cell metabolism. Therefore, a simple homogeneous cell model plotted in Fig. 2 was used. The small buildup layers in front and in back of the cell monolayer represent the culture medium and cell substrate. The simplification was chosen because of the high variability of the cell anatomy depending on cell cycle, cell species and environmental conditions. An irradiation of this sample with 75 keV photons was simulated. The total energy deposition in the nucleus and its distribution in the cell volume with $(0.1 \times 0.1 \times 0.1 \mu\text{m}^3)$ sized voxels were determined. Fig.2 shows an example of the deposited energy distribution in the middle plane of a cell. Therein only the cell plasma contains tungsten.

Three different cases of tungsten distribution were chosen. Reference was the irradiation without tungsten. The deposited energy in the nucleus was found to be 0.08 eV per photon. The homogeneous distribution of 0.57 at. % tungsten in the cell results in the highest value with 0.48 keV. If the agent cannot cross the pores of the nucleus membrane ($\varnothing < 100 \text{ nm}$) the deposited energy decreases only moderately to 0.38 keV.

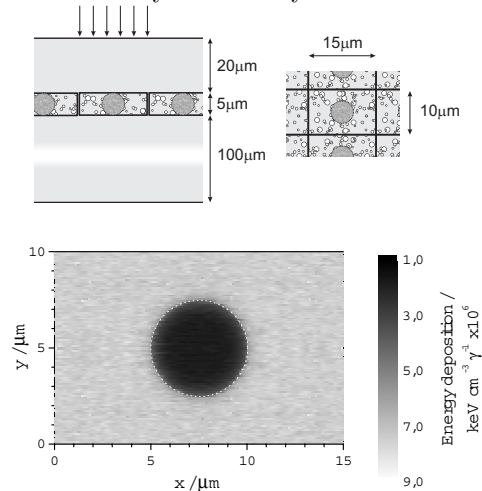


Fig. 2 Cell irradiation model and energy deposition in middle cell plane, dotted line - nucleus dimension

The presented results show a significant increase in damage production at external radiation therapy but the relatively high concentration of tungsten has to be considered. Furthermore a problematic issue is to find an appropriate target agent which can carry the heavy metal atoms while keeping them strongly bound to reduce their toxicity.

- [1] S. Corde, A. Joubert et al., Br. J. Cancer 91 (2004) 544
- [2] U. Reichelt, J. Henniger, W. Enghardt, this report, p. 69
- [3] International Commission on Radiation Units and Measurements, ICRU Report 44, Bethesda (1989)

¹also TU Dresden

Index

- Abolmaali, N. 63
Altstadt, E. 38
ANKE Collab. 48
Azadegan, B. 64–66
- Barnaföldi, G. 37
Barz, H.W. 19, 27
Beckert, C. 38
Benouaret, N. 13
Bergmann, R. 63
Bernhard, G. 53
Beyer, R. 7, 38, 40
Bluhm, M. 5, 30, 31
Brentano, P. von 10
Brinkmann, K.T. 33
- Claußner, J. 42
Cleymans, J. 29
Crespo, P. 58, 62, 63
Csernai, L. 35
- Dönau, F. 10
Date, S. 28
Dohrmann, F. 18, 24–26, 45, 46
- Enghardt, W. 58–63, 69, 70
Erhard, M. 8–11, 41, 42
Esser, N. 55
- Fahmy, K. 51, 52
Fiedler, F. 61, 62
Foerstendorf, H. 53
FOPI Collab. 32
Frauendorf, S. 9–11
Freiesleben, H. 38
Friebel, S. 54
Friedrich, M. 14–17
Furlinski, G. 51, 52
- Gensch, U. 55
Greschner, M. 38
Grigoryan, L.Sh. 66
Grosse, E. 7–14, 16, 18, 24–26, 38, 40–42, 45
- HADES Collab. 18
Hartmann, A. 14–17, 40, 42
Heidel, K. 14, 16, 40
Heim, K. 53
Heinrich, L. 40
Helm, M. 54
Henniger, J. 69
Herrmannsdörfer, T. 56
Hutsch, J. 40
- Jäkel, R. 33
Jolie, J. 10
Junghans, A.R. 7–17, 38, 40–42
- Kämpfer, B. 5, 6, 18–26, 28–31, 34, 36, 37
Käubler, L. 10
Kanaki, K. 18, 24, 25
Kaneta, M. 29
KaoS Collab. 26
Kaptari, L.P. 20, 21, 23
Kliemt, R. 33
Klug, J. 7, 8, 13, 38, 40
Kneissl, U. 10
Kohstall, C. 10
Kosev, K. 8–11, 14–17
Kostov, L.K. 10
Kotte, R. 18, 24, 25, 32, 46
Kreutz, M. 10
- Légrády, D. 38
Langer, M. 42
Lees, J.S. 55
Lehnert, A. 68
Lessmann, E. 68
Linnemann, A. 10
- Möckel, D. 59
Müller, H. 33
Mallion, S. 10
Manninen, J. 35
Marzec, J. 47
Molnar, E. 35
- Nair, C. 8, 13, 41, 42
Nankov, N. 8, 9, 14–17
Naumann, B. 38, 67
Naumann, L. 18, 24–26, 46, 47
Noack, K. 38
Nyiri, A. 35
- Ohashi, Y. 28
Oswald, J. 68
- Pawelke, J. 59, 62, 64–68, 70
Peshekhonov, V. 47
Pietralla, N. 10
Pitz, H.H. 10
Plunien, G. 34
- Reichert, U. 69, 70
Rusev, G. 7–13
- Saaydi, A. 42
Sadovsky, A. 18, 24, 25
Schade, H. 37
Schade, U. 55
Scheck, M. 10
Scheinast, W. 26
Schilling, K.D. 8–11, 13–17, 41, 42
Schleichert, R. 48
Schneider, H. 54

Schneider, S.....	38
Schulze, R.....	31
Schulze, W.....	40
Schwengner, R.....	7–13, 41, 42
Sczepan, M.....	51
Seidel, K.....	38
Seidel, W.....	51, 53–55
Seifert, A.....	42
Seliverstov, D.....	47
Sellesk, M.....	61
Shakirin, G.....	58, 62
Sineej, S.....	52
Sobiella, M.....	14, 16, 40, 42
Sommer, M.....	59
Stach, D.....	46
Stedile, F.....	10
Steiner, J.....	42, 43
Sytcheva, A.....	45
Thomas, R.....	22, 36, 37
Tikhomirov, V.....	47
Titov, A.I.....	28
Trousov, S.....	48
van der Geer, C.A.J.....	57
von Garrel, H.....	10
Wünsch, R.....	56, 57
Würschig, T.....	60
Wüstenfeld, J.....	18, 44
Wagner, A.....	7–17, 38, 40–43
Wagner, W.....	64–67
Weiss, F.-P.....	38
Werner, V.....	10
Wheaton, S.M.....	29
Will, E.....	59, 63
Winnerl, S.....	54
Wintz, P.....	47
Wohlfarth, D.....	51
Wolf, Gy.....	19
Wolf, U.....	43
Wustmann, W.....	6
Xu, N.....	29
Zétényi, M.....	19, 27
Zaremba, K.....	47
Zschocke, S.....	22, 34–36

Publications, Proceedings, Poster and Talks
Teaching Activities, Awards, Calls and Theses,
Patents and Workshops

Central depression in nuclear density and its consequences for the shell structure of superheavy nuclei

Phys. Rev. C 71 (2005) 024308

Afanasjev A.V., **S. Frauendorf**

Abstract: The influence of the central depression in the density distribution of spherical superheavy nuclei on the shell structure is studied within the relativistic mean-field theory. A large depression leads to the shell gaps at the proton $Z=120$ and neutron $N=172$ numbers, whereas a flatter density distribution favors $N=184$ and leads to the appearance of a $Z=126$ shell gap and to the decrease of the size of the $Z=120$ shell gap. The correlations between the magic shell gaps and the magnitude of the central depression are discussed for relativistic and nonrelativistic mean field theories.

Description of rotating $N = Z$ nuclei in terms of isovector pairing

Phys. Rev. C 71 (2005) 064318

Afanasjev, A.V., **S. Frauendorf**

Abstract: A systematic investigation of the rotating $N=Z$ even-even nuclei in the mass $A=68-80$ region has been performed within the frameworks of the cranked relativistic mean field, cranked relativistic Hartree-Bogoliubov theories, and cranked Nilsson-Strutinsky approach. Most of the experimental data are well accounted for in the calculations. The present study suggests the presence of strong isovector np pair field at low spin, whose strength is defined by the isospin symmetry. At high spin, the isovector pair field is destroyed and the data are well described by the calculations assuming zero pairing. No clear evidence for the existence of the isoscalar $t=0np$ pairing has been obtained in the present investigation performed at the mean field level.

Superdeformation and hyperdeformation in the ^{108}Cd nucleus

Phys. Rev. C 72 (2005) 031301

Afanasjev, A.V., **S. Frauendorf**

Abstract: Superdeformation and hyperdeformation in ^{108}Cd have been studied for the first time within the framework of the fully self-consistent cranked mean-field theory, namely, cranked relativistic mean-field theory. The structure of observed superdeformed bands 1 and 2 have been analyzed in detail. The bumps seen in their dynamic moments of inertia are explained as arising from unpaired band crossings. This is contrary to an explanation given earlier within the framework of the projected shell model. It was also concluded that this nucleus is not a doubly magic superdeformed nucleus.

The FLUKA code: New developments and application to 1 GeV/n iron beams

Adv. Space Res. 35 (2005) 214

Aiginger, H., V. Andersen, F. Ballarini, G. Battistoni, M. Campanella, M. Carboni, F. Cerutti, A. Empl, **W. Enghardt**, A. Fassò, A. Ferrari, E. Gadioli, M.V. Garzelli, d, K. Lee, A. Ottolenghi, **K. Parodi**, M. Pelliccioni, L. Pinsky, J. Ranft, S. Roesler, P.R. Sala, D. Scannicchio, G. Smirnov, F. Sommerer, T. Wilson, N. Zapp

Abstract: The modeling of ion transport and interactions in matter is a subject of growing interest, driven by the continuous increase of possible application fields. These include hadron therapy, dosimetry, and space missions, but there are also several issues involving fundamental research, accelerator physics, and cosmic ray physics, where a reliable description of heavy ion induced cascades is important. In the present work, the capabilities of the FLUKA code for ion beams will be briefly recalled and some recent developments presented. Applications of the code to the simulation of therapeutic carbon, nitrogen and oxygen ion beams, and of iron

¹From the authors printed in **bold** further information can be obtained

beams, which are of direct interest for space mission related experiments, will be also presented together with interesting consideration relative to the evaluation of dosimetric quantities. Both applications involve ion beams in the A GeV range.

Excitation function of elliptic flow in Au + Au collisions and the nuclear matter equation of state

Phys. Lett. B 612 (2005) 173

Andronic, A., V. Barret, Z. Basrak, N. Bastid, L. Benabderrahmane, G. Berek, R. Caplar, P. Crochet, P. Dupieux, M. Dzelalija, Z. Fodor, I. Gasparic, Yu. Grishkin, O.N. Hartmann, N. Herrmann, K.D. Hildenbrand, B. Hong, J. Kecskemeti, Y.J. Kim, M. Kirejczyk, P. Koczon, M. Korolija, **R. Kotte**, T. Kress, A. Lebedev, Y. Leifels, X. Lopez, M. Merschmeyer, **W. Neubert**, D. Pelte, M. Petrovici, F. Rami, W. Reisdorf, B. de Schauenburg, A. Schüttauf, Z. Seres, B. Sikora, K.S. Sim, V. Simion, K. Siwek-Wilczynska, V. Smolyankin, M.R. Stockmeier, G. Stoicea, Z. Tyminski, P. Wagner, K. Wisniewski, **D. Wohlfarth**, Z.-G. Xiao, I. Yushmanov, A. Zhilin

Abstract: We present measurements of the excitation function of elliptic flow at midrapidity in Au + Au collisions at beam energies from 0.09 to 1.49 GeV per nucleon. For the integral flow, we discuss the interplay between collective expansion and spectator shadowing for three centrality classes. A complete excitation function of transverse momentum dependence of elliptic flow is presented for the first time in this energy range, revealing a rapid change with incident energy below $0.4 A$ GeV, followed by an almost perfect scaling at the higher energies. The equation of state of compressed nuclear matter is addressed through comparisons to microscopic transport model calculations.

Calculations of K^+ , K^- and ϕ production in near-threshold proton-nucleus collisions

Acta Phys. Hung. A 22 (2005) 231

Barz, H.-W., B. Kämpfer, L. Naumann, G. Wolf, M. Zetenyi

Abstract: K^+ , K^- and ϕ meson production in proton-nucleus (pA) collisions has been calculated within a BUU transport model. It is shown that the nucleon-hyperon strangeness transfer channel is essential. The role of three-body reactions has been investigated within the medium. The mass dependence of ϕ production is predicted to give important information on the in-medium properties of all three mesons.

Angular distribution and azimuthal asymmetry for pentaquark production in proton-proton collisions

Phys. Rev. C 71 (2005) 065207

Barz, H.-W., M. Zetenyi

Abstract: Angular distributions for production of the Θ^+ pentaquark are calculated for the collisions of polarized protons with polarized target protons. We compare calculations based on different assumptions concerning spin and parity ($J = 1/2^\pm, 3/2^\pm$) of the Θ^+ state. For a wide class of interactions the spin correlation parameters describing the asymmetric angular distributions are calculated up to 250 MeV above production threshold. The deviations from the near threshold behavior are investigated.

First analysis of anisotropic flow with Lee-Yang zeroes

Phys. Rev. C 72 (2005) 011901

Bastid, N., A. Andronic, V. Barret, Z. Basrak, M.L. Benabderrahmane, R. Caplar, E. Cordier, P. Crochet, P. Dupieux, M. Dzelalija, Z. Fodor, I. Gasparic, A. Gobbi, Y. Grishkin, O.N. Hartmann, N. Herrmann, K.D. Hildenbrand, B. Hong, J. Kecskemeti, Y.J. Kim, M. Kirejczyk, P. Koczon, M. Korolija, **R. Kotte**, T. Kress, A. Lebedev, Y. Leifels, X. Lopez, A. Mangiarotti, M. Manko, M. Merschmeyer, D. Moisa, **W. Neubert**, D. Pelte, M. Petrovici, F. Rami, W. Reisdorf, A. Schüttauf, Z. Seres, B. Sikora, K.S. Sim, V. Simion, K. Siwek-Wilczynska, M.M. Smolarkiewicz, V. Smolyankin, I.J. Soliwoda, M.R. Stockmeier, G. Stoicea, Z. Tyminski, P. Wagner, K. Wisniewski, **D. Wohlfarth**, Z. Xiao, I. Yushmanov, A. Zhilin

Abstract: We report on the first analysis of directed and elliptic flow with the new method of Lee-Yang zeroes. Experimental data are presented for Ru+Ru reactions at 1.69 A GeV measured with the FOPI detector at

SIS/GSI. The results obtained with several methods, based on the event-plane reconstruction, on Lee-Yang zeros, and on multi-particle cumulants (up to 5th order) applied for the first time at SIS energies, are compared. They show conclusive evidence that azimuthal correlations between nucleons and composite particles at this energy are largely dominated by anisotropic flow.

Dilepton analysis in the HADES spectrometer for C + C at 2 A GeV

J. Phys. G 31 (2005) S231

Bielcik, J., G. Agakichiev, C. Agodi, H. Alvarez-Pol, A. Balanda, G. Bellia, M. Böhmer, J. Boyard, P. Braun-Munzinger, S. Chernenko, T. Christ, R. Coniglione, R. Djeridi, **F. Dohrmann**, I. Duran, T. Eberl, L. Fabbietti, O. Fateev, P. Finocchiaro, J. Friese, I. Fröhlich, J. Garzon, R. Gernhäuser, M. Golubeva, D. Gonzalez-Diaz, **E. Grosse**, F. Guber, T. Hennino, S. Hlavac, R. Holzmann, A. Ierusalimov, I. Iori, M. Jaskula, M. Jurkovic, **B. Kämpfer**, **K. Kanaki**, T. Karavicheva, I. Koenig, W. Koenig, B. Kolb, **R. Kotte**, J. Kotulic-Bunta, R. Krücken, A. Kugler, W. Kühn, R. Kulesa, A. Kurepin, S. Lang, J. Lehnert, C. Maiolino, J. Markert, V. Metag, J. Mousa, M. Münch, C. Müntz, **L. Naumann**, R. Novotny, J. Novotny, J. Otwinowski, Y. Pachmayer, L.M. Pant, V. Pechenov, T. Perez, J. Pietraszko, R. Pleskac, V. Pospisil, W. Pwrzygoda, N. Rabin, B. Ramstein, A. Reshetin, J. Ritman, M. Roy-Stephan, A. Rustamov, **A. Sadovsky**, B. Sailer, P. Salabura, M. Sanchez, P. Sapienza, A. Schmah, R. Simon, V. Smolyankin, L. Smykov, S. Spataro, B. Spruck, H. Stroebele, J. Stroth, C. Sturm, M. Sudol, P. Tlusty, A. Toia, M. Traxler, H. Tsertos, V. Wagner, M. Wisniowski, T. Wojcik, J. Wüstenfeld, Y. Zanevsky, D. Zovinec, P. Zumbruch (HADES collaboration)

Abstract: The high-acceptance dielectron spectrometer (HADES) has become operational at GSI Darmstadt. The primary physics programme is to study in-medium changes of light vector mesons via their e^+e^- decays. The methods of dilepton signal reconstruction in the HADES spectrometer and preliminary dilepton spectra for C + C reactions at 2 A GeV are presented. In the signal reconstruction, particularly important is the reduction of the huge combinatorial background arising from e^+e^- combinations of leptons from gamma conversion in materials with other leptons in the collision. The purity of the dilepton signal is determined by using GEANT simulations with the full HADES geometry and a realistic detector response.

Quasi-particle model of strongly interacting matter

J. Phys. G 31 (2005) S1151

Bluhm, M., B. Kämpfer, G. Soff

Abstract: The successful quasi-particle model is compared with recent lattice data of the coefficients in the Taylor series expansion of the excess pressure at finite temperature and baryon density. A chain of approximations, starting from QCD to arrive at the model expressions for the entropy density, is presented.

The QCD equation of state near T_c within a quasi-particle model

Phys. Lett. B 620 (2005) 131

Bluhm, M., B. Kämpfer, G. Soff

Abstract: We present a description of the equation of state of strongly interacting matter within a quasi-particle model. The model is adjusted to lattice QCD data near the deconfinement temperature T_c . We compare in detail the excess pressure at non-vanishing chemical potential and its Taylor expansion coefficients with two-flavor lattice QCD calculations and outline prospects of the extrapolation to large baryon density.

Vector meson production in collisions of nucleons

Int. J. Mod. Phys. A 20 (2005) 427

Brinkmann, K, M. Abdel-Bary, S. Abdel-Samad, H. Clement, E. Doroshkevich, S. Dshemuchadse, H. Dutz, K. Ehrhardt, W. Eyrich, A. Filippi, H. Freiesleben, M. Fritsch, J. Georgi, A. Gillitzer, P. Gonser, R. Jäkel, L. Karsch, K. Kilian, H. Koch, J. Kress, E. Kuhlmann, S. Marcello, W. Meyer, P. Michel, H.P. Morsch, **K. Möller**, H. Mörtel, **L. Naumann**, L. Pinna, L. Pizzolotto, E. Roderburg, A. Schamlott, P. Schönmeier, W. Schroeder, M. Schulte-Wissermann, T. Sefzick, M. Steinke, F. Stinzinger, G.Y. Sun, A. Ucar, W. Ullrich, G.J. Wagner, M. Wagner, A. Wilms, P. Wintz, S. Wirth, P. Wüstner, P. Zupranski, (COSY-TOF collaboration)

Abstract: The production of vector mesons in collisions between nucleons is studied in order to address a variety of issues concerning nucleon-nucleon interaction, reaction mechanism and properties of baryons. These studies are summarized with emphasis on the most recent experiments at the Time-of-Flight spectrometer TOF and results obtained at the COoler SYnchrotron COSY in Jülich. While currently the open questions regarding the so-called OZI violation, its relation to the meson exchange picture and the relative importance of contributions to the production mechanism from various channels within this formalism are still unresolved, the present-day experiments hold the potential to clarify the situation greatly. Possible extensions of the experimental program on vector mesons using 4π detection techniques for charged as well as neutral particles, in particular π^0 , are discussed.

Centrality dependence of thermal parameters deduced from hadron multiplicities in Au + Au collisions at $\sqrt{s_{NN}} = 130$ GeV

Phys. Rev. C 71 (2005) 054901

Cleymans, J., **B. Kämpfer**, M. Kaneta, S. Wheaton, N. Xu

Abstract: We analyse the centrality dependence of thermal parameters deduced from hadron multiplicities in Au + Au collisions at $\sqrt{s_{NN}} = 130$ GeV. While the chemical freeze-out temperature and chemical potentials are found to be roughly centrality-independent, the strangeness saturation factor γ_S increases with participant number towards unity, supporting the assumption of equilibrium freeze-out conditions in central collisions.

Suppression of random coincidences during in-beam PET measurements at ion beam radiotherapy facilities

IEEE Trans. Nucl. Sci. 52 (2005) 980

Crespo, P., T. Barthel, H. Fraiss-Koelbl, E. Griesmayer, **K. Heide**, K. Parodi, **J. Pawelke**, **W. Enghardt**

Abstract: In-beam positron emission tomography (PET) is currently the only method for an in-situ monitoring of charged hadron therapy. However, in-beam PET data, measured at beams with a sub-microsecond-microstructure due to the accelerator radiofrequency (RF), are highly corrupted by random coincidences arising from prompt γ -rays following nuclear reactions as the projectiles penetrate the tissue. Since random-correction techniques from conventional PET cannot be applied, the clinical in-beam PET at the therapy facility at the Gesellschaft fuer Schwerionenforschung (GSI) Darmstadt merely reconstructs events registered in the pauses ($\sim 2-4$ s) between the beam macropulses (< 2 s). We have successfully tested at GSI two methods for suppressing the micropulse-induced random coincidences during beam extraction. Image statistics increased by about 90%. Both methods rely on the synchronization of the γ - γ -coincidences measured by the positron camera with the time microstructure of the beam, either by using the RF-signal from the accelerator or the signal of a thin diamond detector placed in the beam path in front of the target. Energy and triple-coincidence time correlated spectra first-measured during beam extraction, combined with the corresponding tomographic images of the beta+ activity induced by the beam in a plastic phantom, clearly confirm the feasibility of the proposed random suppression methods. These methods provide the solution for applying in-beam PET at synchrotron and cyclotron radiotherapy facilities with optimal utilization of the annihilation photon flux.

Nuclear-tidal waves in the osmium nuclei

J. Phys. G 31 (2005) S1709

Cullen, D.M., R. Glover, L.K. Pattison, P.M. Walker, **S. Frauendorf**, D. Almeded

Abstract: Structures have been identified built upon the $K^\pi = 43/2^{(-)}$ and $K^\pi = 43/2^{+}$ isomeric states in ^{183}Os . Although these sequences appear quite irregular, their properties can be understood if the angular momentum is built up, to a large degree, from multiple phonons. These vibrations are found to compete with rotations in generating angular momentum.

Suppression of modes in the random phase approximation

Phys. Rev. Lett. 94 (2005) 092503

Dönau, F.

Abstract: A general but simple method is proposed to eliminate the quantum fluctuations generated by selected one-body operators in the excitation spectrum of a discrete random phase approximation (RPA) Hamiltonian. This method provides an outstanding tool for the removal of the contaminating spurious effects originated from symmetry violations. It can be also applied as a mode filter for analyzing RPA response functions.

Di-electron measurements in C + C reactions at 2 GeV*A with HADES

Nucl. Phys. A 752 (2005) 433c

Eberl, T., G. Agakichiev, C. Agodi, H. Alvarez-Pol, A. Balanda, G. Bellia, J. Bielcik, M. Böhmer, J. Boyard, P. Braun-Munzinger, S. Chernenko, T. Christ, R. Coniglione, R. Djeridi, **F. Dohrmann**, I. Duran, L. Fabbietti, O. Fateev, P. Finocchiaro, J. Friese, I. Fröhlich, J. Garzon, R. Gernhäuser, M. Golubeva, D. Gonzalez-Diaz, **E. Grosse**, F. Guber, T. Hennino, S. Hlavac, R. Holzmann, A. Ierusalimov, I. Iori, M. Jaskula, M. Jurkovic, **B. Kämpfer**, **K. Kanaki**, T. Karavicheva, I. Koenig, W. Koenig, B. Kolb, **R. Kotte**, J. Kotulic-Bunta, R. Krücken, A. Kugler, W. Kühn, R. Kulesa, A. Kurepin, S. Lang, J. Lehnert, C. Maiolino, J. Markert, V. Metag, J. Mousa, M. Münch, C. Müntz, **L. Naumann**, R. Novotny, J. Novotny, J. Otwinowski, W. Ott, Y. Pachmayer, L.M. Pant, V. Pechenov, T. Perez, J. Pietraszko, R. Pleskac, V. Pospisil, W. Pwrzygoda, N. Rabin, B. Ramstein, A. Reshetin, J. Ritman, M. Roy-Stephan, A. Rustamov, **A. Sadovsky**, B. Sailer, P. Salabura, M. Sanchez, P. Sapienza, A. Schmah, R. Simon, V. Smolyankin, L. Smykov, S. Spataro, B. Spruck, H. Stroebele, J. Stroth, C. Sturm, M. Sudol, P. Tlusty, A. Toia, M. Traxler, H. Tsertos, V. Wagner, M. Wisniowski, T. Wojcik, J. Wüstenfeld, Y. Zanevsky, D. Zovinec, P. Zumbach

Abstract: The High Acceptance DiElectron Spectrometer HADES has been recently commissioned at GSI, Darmstadt. It has been designed for systematic studies of hadron properties inside nuclear matter. We report first preliminary results on invariant masses of e^+e^- -pairs which were measured in $^{12}\text{C} + ^{12}\text{C}$ collisions at $E_{kin} = 2 \text{ GeV} \cdot A$. The analysis methods are briefly outlined and a comparison with detailed Monte-Carlo simulations is shown.

Review of the results of the KaoS collaboration

J. Phys. G: Nucl. Part. Phys. 31 (2005) S693

Förster, A., I. Böttcher, **F. Dohrmann**, **E. Grosse**, P. Koczon, B. Kohlmeyer, S. Lang, F. Laue, M. Menzel, **L. Naumann**, H. Oeschler, M. Ploskon, F. Pühlhofer, W. Scheinast, A. Schmah, T. Schuck, E. Schwab, P. Senger, Y. Shin, H. Ströbele, C. Sturm, F. Uhlig, W. Walus, **A. Wagner**

Abstract: The production of K^+ and of K^- mesons in heavy-ion collisions at beam energies of 1 to 2 A GeV has systematically been investigated with the kaon spectrometer KaoS. The ratio of the K^+ production excitation function for Au + Au and for C + C reactions increases with decreasing beam energy, which is expected for a soft nuclear equation-of-state. A comprehensive study of the K^+ and of the K^- emission as a function of the size of the collision system, of the collision centrality, of the kaon energy, and of the polar emission angle has been performed. The K^-/K^+ ratio is found to be nearly constant as a function of the collision centrality and can be explained by the dominance of strangeness exchange. On the other hand, the spectral slopes and the polar emission patterns are different for K^- and for K^+ . Furthermore the azimuthal distribution of the particle emission has been investigated. K^+ mesons and pions are emitted preferentially perpendicular to the reaction plane as well in Au + Au as in Ni + Ni collisions. In contrast for K^- mesons in Ni + Ni reactions an in-plane flow was observed for the first time at these incident energies.

Symmetries in nuclear structure

Nucl. Phys. A 752 (2005) 203c

Frauendorf, S.

Abstract: Collective rotation of tetrahedral nuclei is analyzed within a three-dimensional cranking model. The favored orientation of the rotational frequency vector with respect to the turning nucleus as function of angular momentum is obtained from the total energy calculations. A new quantum number, resulting from

the particular symmetry of the cranking Hamiltonian of the nuclei with tetrahedral nuclei is discussed. Some consequences for the structure of the rotational bands are presented.

Hindered E4 decay of the 12^+ yrast trap in ^{52}Fe

Phys. Lett. B 619 (2005) 88

Gadea, A., S.M. Lenzi, D.R. Napoli, M. Axiotis, C.A. Ur, G. Martinez-Pinedo, M. Gorska, E. Roeckl, E. Caurier, F. Nowacki, G. de Angelis, L. Batist, R. Borcea, F. Brandolini, D. Cano-Ott, J. Döring, C. Fahlander, E. Farnea, H. Gawe, M. Hellström, Z. Janas, R. Kirchner, M. La Commara, C. Mazzocchi, E. Nacher, C. Plettner, A. Plochocki, B. Rubio, K. Schmidt, **R. Schwengner**, J.L. Tain, J. Zylicz

Abstract: The γ decay of the 12^+ yrast trap in ^{52}Fe has been measured for the first time. The two E4 γ -branches to the 8^+ states are hindered with respect to other $B(E4)$ reduced transition probabilities measured in the $f_{7/2}$ shell. The interpretation of the data is given in the full pf shell model framework, comparing the results obtained with different residual interactions. It is shown that measurements of hexadecapole transition probabilities constitute a powerful tool in discriminating the correct configuration of the involved wavefunctions.

β decay of ^{95}Ag

Phys. Rev. C 72 (2005) 024303

Harissopoulos, S., J. Döring, M. La Commara, K. Schmidt, C. Mazzocchi, R. Borcea, S. Galanopoulos, M. Gońska, H. Grawe, M. Hellström, Z. Janas, R. Kirchner, E. Roeckl, I.P. Johnstone, **R. Schwengner**, L.D. Skouras

Abstract: We studied the β -decay properties of the $N = Z + 1$ nucleus ^{95}Ag by measuring β -delayed γ -rays and $\beta - \gamma - \gamma$ coincidences with a plastic scintillator as β detector and a Ge-detector array. The ^{95}Ag nuclei were produced by means of the $^{58}\text{Ni}(^{40}\text{Ca}, p2n)$ reaction and separated with the GSI online mass separator. The previously reported level scheme of the ^{95}Pd daughter nucleus was extended considerably. The deduced level scheme is compared with different shell-model calculations with or without breaking the ^{100}Sn core.

Isotopically resolved residues from the fragmentation of projectiles with largely different N/Z - the isospin-thermometer method

Nucl. Phys. A 749 (2005) 110

Henzlova, D., L. Audouin, J. Benlliure, A. Botvina, A. Boudard, E. Casarejos, J. Ducret, T. Enqvist, L. Got, A. Heinz, V. Henzl, **A. Junghans**, B. Jurado, A. Kelic, A. Krasa, T. Kurtukian, S. Leray, P. Napolitani, M. Ordonez, J. Pereira, R. Pleskac, F. Rejmund, M. Ricciardi, K. Schmidt, C. Schmitt, C. Stephan, C. Villagrasa, C. Volant, **A. Wagner**, O. Yordanov

Abstract: The mean N-over-Z (N/Z) ratio of residues produced in the fragmentation of ^{136}Xe ($N/Z = 1.519$), ^{124}Xe ($N/Z = 1.296$) in comparison with ^{56}Fe ($N/Z = 1.154$) is investigated over the full range of Z. The final residues from the ^{136}Xe projectile keep a memory on the initial N/Z . The idea to trace back the excitation energy of the fragment entering evaporation via direct exploration of the N/Z evolution in the evaporation process is investigated and applied to the data. The freeze-out temperature is deduced, which is consistent with the investigations of light and intermediate-mass fragments (IMF) in other experiments.

Charged pion production in $^{96}_{44}\text{Ru} + ^{96}_{44}\text{Ru}$ collisions at 400 A and 1528 A MeV

Phys. Rev. C 71 (2005) 034902

Hong, B., Y.J. Kim, N. Herrmann, M.R. Stockmeier, J.P. Alard, A. Andronic, V. Barret, Z. Basrak, N. Bastid, L. Benabderrahmane, R. Caplar, P. Crochet, P. Dupieux, M. Dzelalija, Z. Fodor, A. Gobbi, Y. Grishkin, O.N. Hartmann, K.D. Hildenbrand, J. Kecskemeti, M. Kirejczyk, P. Koczon, M. Korolija, **R. Kotte**, T. Kress, A. Lebedev, Y. Leifels, X. Lopez, A. Mangiarotti, M. Merschmeyer, **W. Neubert**, D. Pelte, M. Petrovici, F. Rami, W. Reisdorf, A. Schüttauf, Z. Seres, B. Sikora, K.S. Sim, V. Simion, K. Siwek-Wilczynska, V. Smolyankin, G. Stoicea, Z. Tyminski, P. Wagner, K. Wisniewski, **W. Wohlfarth**, Z.G. Xiao, I. Yushmanov, A. Zhilin (FOPI-Collab.)

Abstract: We present the transverse momentum and rapidity spectra of charged pions in central Ru+Ru collisions at 400 and 1528 A MeV. The data exhibit enhanced productions at low transverse momenta compared to the expectations from the thermal model that includes the decay of $\Delta(1232)$ -resonances and thermal pions. Modification of the Δ -spectral function and the Coulomb interaction are necessary to describe the detailed shape of the transverse momentum spectra. Within the framework of the thermal model, the freeze-out radii of pions are similar at both beam energies. The IQMD model also reproduces the shapes of the transverse momentum and rapidity spectra of pions, but the predicted absolute yields are larger than in the measurements, especially at lower beam energy.

The new Seattle-TRIUMF ${}^7\text{Be}(p, \gamma){}^8\text{B}$ S-factor determination

Nucl. Phys. B 138 (2005) 112

Junghans, A.R., E.C. Mohrmann, K.A. Snover, T.D. Steiger, E.G. Adelberger, J.M. Casandjian, H.E. Swanson, L.R. Buchmann, A. Laird, S. Parkc, A.Y. Zyuzinc

Abstract: We present new measurements of the ${}^7\text{Be}(p, \gamma){}^8\text{B}$ cross section from $\overline{E}_{\text{cm}} = 116$ to 2460 keV. Our new measurements lead to $S_{17}(0) = 22.1 \pm 0.6$ (expt) ± 0.6 (theor) eV b, where the central value is based on the theory of Descouvemont and Baye. We recommend a "best" value, $S_{17}(0) = 21.4 \pm 0.5$ (expt) ± 0.6 (theor) eV b, based on the mean of all modern direct measurements below the 1^+ resonance.

A critical analysis of the modelling of dissipation in fission

Nucl. Phys. A 747 (2005) 14

Jurado, B., C. Schmitt, K.-H. Schmidt, J. Benlliure, **A.R. Junghans**

Abstract: The time-dependent flux over the fission barrier of an excited nucleus under the influence of dissipation is investigated. Characteristic features of the evolution of the amplitude of the probability distribution and the velocity profile at the fission barrier are derived. Analytical results are compared to numerical Langevin calculations and used to develop a new analytical approximation to the solution of the Fokker-Planck equation for the time-dependent fission-decay width. This approximation is shown to be more realistic than previously proposed descriptions, which were widely used in the past.

Conditions for the manifestation of transient effects in fission

Nucl. Phys. A 757 (2005) 329

Jurado, B., C. Schmitt, K.-H. Schmidt, J. Benlliure, **A.R. Junghans**

Abstract The conditions for the manifestation of transient effects in fission are carefully examined by analysing experimental data where fission is induced by peripheral heavy-ion collisions at relativistic energies. Experimental total nuclear fission cross sections of ${}^{238}\text{U}$ at 1 A GeV on gold and uranium targets are compared with the predictions of a nuclear-reaction code, where transient effects in fission are modeled using different approximations to the numerical time-dependent fission-decay width: a new analytical description based on the solution of the Fokker-Planck equation and two widely used but less realistic descriptions, a step function and an exponential-like function. The experimental data are only reproduced when dissipation is considered. The influence of transient effects on the fission process, as well as the deduced value of the dissipation strength β , depends strongly on the approximation applied for the time-dependent fission-decay width. In particular, a meticulous analysis sheds severe doubts on the use of the exponential-like in-growth function. Finally, we investigate which should be the characteristics of experimental observables to be most sensitive to transient effects in fission. The pertinence of observables related to the excitation energy at saddle is discussed.

Strangeness and charm in QCD matter

J. Phys. G 31 (2005) S1141

B. Kämpfer, M. Bluhm

Abstract: Strangeness and charm degrees of freedom in strongly interacting matter are discussed within a quasi-particle model adjusted to lattice QCD data. While strangeness is found to appear as copious as the other light quark and gluon excitations, the charm quarks are thermally suppressed. The model allows to

extrapolate lattice QCD data to large baryo-chemical potential. We outline the thermal evolution of matter in the early universe at and slightly after confinement and comment briefly on charm dynamics in relativistic heavy-ion collisions.

Combined analysis of threshold-near production of ω and ϕ mesons in nucleon-nucleon collisions within an effective meson-nucleon model

Eur. Phys. J. A 23 (2005) 291

Kaptari, L.P., **B. Kämpfer**

Abstract: Vector meson ($V = \omega, \phi$) production in threshold-near elementary nucleon-nucleon collisions $pp \rightarrow ppV$, $pn \rightarrow pnV$ and $pn \rightarrow dV$ is studied within an effective meson-nucleon theory. It is shown that a set of effective parameters can be established to explain fairly well the available experimental data on angular distributions and the energy dependence of the total cross sections without explicit implementation of the Okubo-Zweig-Iisuka rule violation. Isospin effects are considered in details and compared with experimental data whenever available.

Beta decay of ^{103}Sn

Eur. Phys. J. A 25 (2005) 211

Kavatsyuk, O., M. Kavatsyuk, L. Batist, A. Banu, F. Becker, A. Blazhev, W. Brüche, J. Döring, T. Faestermann, M. Go'rska, H. Grawe, Z. Janas, A. Jungclaus, M. Karny, R. Kirchner, M. La Commara, S. Mandal, C. Mazzocchi, I. Mukha, S. Muralithar, C. Plettner, A. Płochocki, E. Roeckl, M. Romoli, M. Schädel, **R. Schwengner**, J. Żylicz

Abstract: The β decay of ^{103}Sn , a three-neutron-particle nucleus with respect to the ^{100}Sn core, was investigated at the GSI on-line mass separator using an array of 17 germanium crystals and a total absorption spectrometer. A total of 31 β -delayed γ -rays (29 new) of the $^{103}\text{Sn} \rightarrow ^{103}\text{In}$ decay were observed and, on the basis of $\beta - \gamma - \gamma$ coincidences, the ^{103}Sn decay scheme was established for the first time. By means of total absorption spectroscopy, β intensities, the Gamow-Teller strength distribution and the summed Gamow-Teller strength value of 3.5 ± 0.5 were determined for this decay. Its half-life and Q_{EC} value were found to be 7.0 ± 0.2 s and 7.64 ± 0.7 MeV, respectively. The β -delayed proton branching ratio was measured to be $1.2 \pm 0.1\%$. The results are discussed in comparison with shell-model predictions based on realistic and empirical interactions.

Transport theories for heavy-ion collisions in the 1 A GeV regime

J. Phys. G 31 (2005) 741

Kolomeitsev, E.E., C. Hartnack, **H.W. Barz**, M. Bleicher, E. Bratkovskaya, W. Cassing, L.W. Chen, P. Danielewicz, C. Fuchs, T. Gaitanos, C.M. Ko, A. Larionov, M. Reiter, Gy. Wolf, J. Aichelin

Abstract: We compare multiplicities as well as rapidity and transverse momentum distributions of protons, pions and kaons calculated within presently available transport approaches for heavy ion collisions around 1 A GeV. For this purpose, three reactions have been selected: Au + Au at 1 and 1.48 A GeV and Ni + Ni at 1.93 A GeV.

Two-proton small-angle correlations in central heavy-ion collisions: a beam-energy- and system-size-dependent study

Eur. J. Phys. A 23 (2005) 271

Kotte, R., J.P. Alard, A. Andronic, V. Barret, Z. Basrak, N. Bastid, M.L. Benabderrahmane, R. Caplar, E. Cordier, P. Crochet, P. Dupieux, M. Dzelalija, Z. Fodor, I. Gasparic, A. Gobbi, Y. Grishkin, O.N. Hartmann, N. Herrmann, Hildenbrand, K. D.; Hong, B.; Kecskemeti, J.; Kim, Y. J.; Kirejczyk, M.; Koczon, P.; Korolija, M.; Kress, T.; Lebedev, A.; Y. Leifels, X. Lopez, M. Merschmeyer, **J. Mösner**, **W. Neubert**, D. Pelte, M. Petrovici, F. Rami, W. Reisdorf, B. de Schauenburg, A. Schüttauf, Z. Seres, B. Sikora, K.S. Sim, V. Simion, K. Siwek-Wilczynska, G. Stoicea, Z. Tymiński, P. Wagner, K. Wiśniewski, **D. Wohlfarth**, Z.G. Xiao, Y. Yushmanov, A. Zhilin

Abstract: Small-angle correlations of pairs of protons emitted in central collisions of Ca + Ca, Ru + Ru

and Au + Au at beam energies from 400 to 1500 MeV per nucleon are investigated with the FOPI detector system at SIS/GSI Darmstadt. Dependences on system size and beam energy are presented which extend the experimental data basis of pp correlations in the SIS energy range substantially. The size of the proton-emitting source is estimated by comparing the experimental data with the output of a final-state interaction model which is processing either static Gaussian sources or the one-body phase-space distribution of protons provided by the BUU transport approach. The trends in the experimental data, *i.e.* system-size and beam energy dependences, are well reproduced by this hybrid model. However, the pp correlation function is found rather insensitive to the stiffness of the equation of state entering the transport model calculations.

Isotopic scaling and the symmetry energy in spectator fragmentation

Phys. Rev. Lett. 94 (2005) 162701

Le Fèvre, A., G. Auger, M.L. Begemann-Blaich, N. Bellaïze, R. Bittiger, F. Bocage, B. Borderie, R. Bougault, B. Bouriquet, J.L. Charvet, A. Chbihi, R. Dayras, D. Durand, J.D. Frankland, E. Galichet, D. Gourio, D. Guinet, S. Hudan, G. Immé, P. Lantesse, F. Lavaud, R. Legrain, O. Lopez, J. Tukasik, U. Lynen, W.F.J. Müller, L. Nalpas, H. Orth, E. Plagnol, G. Raciti, E. Rosato, A. Saija, C. Schwarz, **W. Seidel**, C. Sfienti, B. Tamain, W. Trautmann, A. Trzciski, K. Turzó, E. Vient, M. Vigilante, C. Volant, B. Zwiegliski, A.S. Botvina

Abstract: Isotopic effects in the fragmentation of excited target residues following collisions of ^{12}C on $^{112,124}\text{Sn}$ at incident energies of 300 and 600 MeV per nucleon were studied with the INDRA 4π detector. The measured yield ratios for light particles and fragments with atomic number $Z \leq 5$ obey the exponential law of isotopic scaling. The deduced scaling parameters decrease strongly with increasing centrality to values smaller than 50% of those obtained for the peripheral event groups. Symmetry-term coefficients, deduced from these data within the statistical description of isotopic scaling, are near $\gamma = 25$ MeV for peripheral and $\beta < 15$ MeV for central collisions.

Target mass number dependence of subthreshold antiproton production in proton-, deuteron- and alpha-particle-induced reactions

J. Phys. G 31 (2005) 285

Müller, H., V.I. Komarov

Abstract. Data from KEK on subthreshold \bar{p} as well as on π^+ and K^\pm production in proton-, deuteron- and α -induced reactions at energies between 2.0 and 12.0 A GeV for C, Cu and Pb targets are described within a unified approach. We use a model which considers a nuclear reaction as an incoherent sum over collisions of varying numbers of projectile and target nucleons. It samples complete events and thus allows for the simultaneous consideration of all final particles including the decay products of the nuclear residues. The enormous enhancement of the \bar{p} cross section, as well as the moderate increase of meson production in deuteron and α induced compared to proton-induced reactions, is well reproduced for all target nuclei. In our approach, the observed enhancement near the production threshold is mainly due to the contributions from the interactions of few-nucleon clusters by simultaneously considering fragmentation processes of the nuclear residues. The ability of the model to reproduce the target mass dependence may be considered as a further proof of the validity of the cluster concept.

Dilepton analysis in the HADES spectrometer for $^{12}\text{C} + ^{12}\text{C}$ at 2 A GeV

Int. J. Mod. Phys. A 20 (2005) 602

Otwinowski, J., G. Agakichiev, C. Agodi, H. Alvarez-Pol, A. Balanda, G. Bellia, D. Belver, J. Bielcik, M. Böhmer, H. Bokemeyer, J. Boyard, P. Braun-Munzinger, V. Chepurinov, S. Chernenko, T. Christ, R. Coniglione, H. Daues, J. Diaz, R. Djeridi, **F. Dohrmann**, I. Duran, T. Eberl, V. Emelianov, L. Fabbietti, O. Fateev, C. Fernandez, P. Finocchiaro, J. Friese, I. Fröhlich, B. Fuentes, J. Garzon, R. Gernhäuser, M. Golubeva, D. Gonzalez-Diaz, **E. Grosse**, F. Guber, J. Hehner, T. Heinz, T. Hennino, S. Hlavac, J. Hoffmann, R. Holzmann, A. Ierusalimov, I. Iori, M. Jaskula, M. Jurkovic, **B. Kämpfer**, **K. Kanaki**, T. Karavicheva, I. Koenig, W. Koenig, B. Kolb, U. Kopf, **R. Kotte**, J. Kotulic-Bunta, R. Krücken, A. Kugler, W. Kühn, R. Kulesa, A. Kurepin, T. Kutukian-Nieto, S. Lang, J. Lehnert, C. Maiolino, J. Marin, J. Markert, Y. Mishin, N. Montes, J. Mousa, M. Münch, C. Müntz, **L. Naumann**, J. Novotny, W. Ott, Y. Pachmayer, Y. Panebrasev, V. Pechenov, T. Perez, J. Pietraszko, R. Pleskac, V. Pospisil, W. Pwrzygoda, N. Rabin, B. Ramstein, A. Reshetin, J. Ritman, G. Rodriguez Pioto, M. Roy-Stephan, A. Rustamov, J. Sabin-Fernandez, **A. Sadovsky**, B. Sailer, P. Salabura, M. Sanchez, P. Sapienza, A. Schmah, C. Schroeder, E. Schwab, P. Senger, R. Simon, V. Smolyankin, L. Smykov, S. Spataro, H. Stelzer, H. Stroebele, J. Stroth, C. Sturm, M. Sudol, A. Titov, P. Tlusty, A. Toia, M. Traxler, H. Tsertos, A. Vazquez, Y. Volkov, V. Wagner, W. Walus, Y. Wang, S. Winkler, M. Wisniowski, T. Wojcik, **J. Wüstenfeld**, Y. Zanevsky, D. Zovinec, P. Zumbruch

Abstract: The identification of light mesons in the HADES spectrometer is based on an invariant mass reconstruction of their decay into e^+e^- pairs. In the dilepton (e^+e^-) signal reconstruction particularly important is the reduction of a combinatorial background arising from wrong combinations of e^+ and e^- to unlike sign pairs. The purity of the dilepton signal is determined by using GEANT simulations. The analysis methods of the dilepton signal and combinatorial background reconstruction will be presented.

Experimental study on the feasibility of in-beam PET for accurate monitoring of proton therapy

IEEE Trans. Nucl. Sci. 52 (2005) 778

Parodi, K., F. Pönisch, **W. Enghardt**

Abstract: Positron emission tomography is currently the only feasible method for in-situ and non-invasive 3D monitoring of the precision of the treatment in highly conformal ion therapy. Its positive clinical impact has been proven for fractionated carbon ion therapy of head and neck tumours at the experimental facility at the Gesellschaft für Schwerionenforschung Darmstadt, Germany. Following previous promising experiments, the possible extension of the method to the monitoring of proton therapy has been investigated further in extensive in-beam measurements at GSI. Millimetre accuracy for verification of the lateral field position and for the most challenging issue of range monitoring has been demonstrated in mono-energetic and spread-out Bragg-peak proton irradiation of PMMA targets. The irradiation of an inhomogeneous phantom with tissue equivalent inserts in combination with further dynamic analysis has supported the extension of such millimetre precision to real clinical cases, at least in regions of interest for low perfused tissues. All the experimental investigations have been reproduced by the developed modeling rather well. This indicates the possible extraction of valuable clinical information as particle range in-vivo, irradiation field position and even local deviations from the dose prescription on the basis of the comparison between measured and predicted activity distributions. Hence, the clinical feasibility of in-beam PET for proton therapy monitoring is strongly supported.

Random coincidences during in-beam PET measurements at microbunched therapeutic ion beams

Nucl. Inst. Meth., Phys. Res. A 545 (2005) 446

Parodi, K., P. Crespo, H. Eickhoff, T. Haberer, **J. Pawelke**, D. Schardt, **W. Enghardt**

Abstract: At the experimental carbon ion tumour therapy facility at GSI Darmstadt, in-beam positron emissions tomography (PET) is used to monitor the dose delivery precision. A dual head positron camera has been assembled from commercial detector components in order to measure the β^+ -activity, induced by the irradiation, simultaneously to the dose application. Despite the positive clinical impact, the image quality is limited by the low counting statistics, orders of magnitude below that in standard PET applications to nuclear medicine. This paper investigates the origin for the noisy acquisition during particle extraction from the synchrotron of GSI. The results demonstrate the failure of standard random correction techniques due to a γ -ray background correlated in time with the carbon ion beam microstructure. This prevents the use of data

acquired during beam extraction for imaging. The loss of counting statistics is expected to rise further at the future hospital-based facility at Heidelberg, due to a more efficient utilisation of the accelerator resulting in shorter beam pauses and a reduced treatment time. In respect, this paper provides the basis for a new data acquisition concept tailored to the unconventional application of in-beam PET imaging to therapy monitoring at radiofrequency pulsed radiation sources.

Metal binding by bacteria from uranium mining waste piles and its technological applications

Biotechnol. Adv. 24 (2005) 58

Pollmann, K., J. Raff, M. Merroun, **K. Fahmy**, S. Selenska-Pobell

Abstract: Uranium mining waste piles, heavily polluted with radionuclides and other toxic metals, are a reservoir for bacteria that have evolved special strategies to survive in these extreme environments. Understanding the mechanisms of bacterial adaptation may enable the development of novel bioremediation strategies and other technological applications. Cell isolates of *Bacillus sphaericus* JG-A12 from a uranium mining waste pile in Germany are able to accumulate high amounts of toxic metals such as U, Cu, Pb, Al, and Cd as well as precious metals. Some of these metals, *i.e.* U, Cu, Pd(II), Pt(II) and Au(III), are also bound by the highly ordered paracrystalline proteinaceous surface layer (S-layer) that envelopes the cells of this strain. These special capabilities of the cells and the S-layer proteins of *B. sphaericus* JG-A12 are highly interesting for the clean-up of uranium contaminated waste waters, for the recovery of precious metals from electronic wastes, and for the production of metal nanoclusters. The fabricated nanoparticles are promising for the development of novel catalysts. This work reviews the molecular biology of the S-layer of the strain JG-A12 and the S-layer dependent interactions of the bacterial cells with metals. It presents future perspectives for their application in bioremediation and nanotechnology.

Decay of 1^+ states as a new probe of the structure of 0^+ shape isomers

Phys. Rev. Lett. 95 (2005) 062501

Rusev, G., R. Schwengner, F. Dönau, S. Frauendorf, L. Käubler, L.K. Kostov, S. Mallion, **K.D. Schilling, A. Wagner**, H. von Garrel, U. Kneissl, C. Kohstall, M. Kreutz, H.H. Pitz, M. Scheck, F. Stedile, P. von Brentano, J. Jolie, A. Linnemann, N. Pietralla, V. Werner

Abstract: The nuclides ^{98}Mo and ^{100}Mo have been studied in photon-scattering experiments by using bremsstrahlung produced from electron beams with energies from 3.2 to 3.8 MeV. Six dipole transitions in ^{98}Mo and 19 in ^{100}Mo were observed for the first time in the energy range from 2 to 4 MeV. A specific feature in both nuclides is the deexcitation of one state with spin $J = 1$ to the 0^+ ground state as well as to the first excited 0^+ state, which cannot be explained in standard models. We present a model based on one-particle-one-hole excitations, which allows us to deduce the mixing amplitudes for the two 0^+ shape-isomeric states from the experimental ratio of the transition strengths from the $J = 1$ state to the 0^+ ground state and to the 0^+ excited state.

Probing of in-medium hadron structure with HADES

Nucl. Phys. A 749 (2005) 150

Salabura, P., G. Agakichiev, C. Agodi, H. Alvarez-Pol, A. Balanda, G. Bellia, J. Bielcik, M. Böhmer, J. Boyard, P. Braun-Munzinger, S. Chernenko, T. Christ, R. Coniglione, R. Djeridi, **F. Dohrmann**, I. Duran, T. Eberl, L. Fabbietti, O. Fateev, P. Finocchiaro, J. Friese, I. Fröhlich, J. Garzon, R. Gernhäuser, M. Golubeva, D. Gonzalez-Diaz, **E. Grosse**, F. Guber, T. Hennino, S. Hlavac, R. Holzmann, A. Ierusalimov, I. Iori, M. Jaskula, M. Jurkovic, **B. Kämpfer, K. Kanaki**, T. Karavicheva, I. Koenig, W. Koenig, B. Kolb, **R. Kotte**, J. Kotulic-Bunta, R. Krücken, A. Kugler, W. Kühn, R. Kulesa, A. Kurepin, S. Lang, J. Lehnert, C. Maiolino, J. Markert, V. Metag, J. Mousa, M. Münch, C. Müntz, **L. Naumann**, J. Novotny, R. Novotny, J. Otwinowski, Y. Pachmayer, V. Pechenov, T. Perez, J. Pietraszko, R. Pleskac, V. Pospisil, W. Pwrzygoda, N. Rabin, B. Ramstein, A. Reshetin, J. Ritman, M. Roy-Stephan, A. Rustamov, **A. Sadovsky**, B. Sailer, M. Sanchez, P. Sapienza, A. Schmah, V. Smolyankin, L. Smykov, S. Spataro, B. Spruck, H. Stroebele, J. Stroth, C. Sturm, M. Sudol, P. Tlusty, A. Toia, M. Traxler, H. Tsertos, V. Wagner, M. Wisniowski, T. Wojcik, **J. Wüstenfeld**, Y. Zanevsky, D. Zovinec, P. Zumbach

Abstract: The High Acceptance DiElectron Spectrometer (HADES) has been recently commissioned at GSI

Darmstadt. It has been designed to study hadron properties inside nuclear matter via measurements of dielectron decays in proton, pion and heavy ion induced reactions in 1-2 A GeV energy range. We report first preliminary results on invariant masses of e^+e^- pairs measured in $^{12}\text{C} + ^{12}\text{C}$ collisions at $E = 2$ A GeV and compare them to simulations based on UrQMD transport model. In summary we present and discuss planned experiments.

Kaon and pion emission in asymmetric C + Au and Au + C collisions at 1.0 A GeV and 1.8 A GeV

Phys. Rev. C 71 (2005) 064907

Schmah, A., S. Lang, I. Böttcher, **F. Dohrmann**, A. Förster, **E. Grosse**, P. Koczon, B. Kohlmeyer, F. Laue, M. Menzel, **L. Naumann**, H. Oeschler, W. Scheinast, T. Schuck, E. Schwab, P. Senger, Y. Shin, H. Ströbele, C. Sturm, G. Surowska, F. Uhlig, **A. Wagner**, W. Walus

Abstract: The emission of K^+ and π^\pm mesons has been studied in the asymmetric collision system Au + C and in the inverse reaction C + Au at 1.0 A GeV (and at 1.8 A GeV for C + Au only) in order to extract the effective source rapidities based on their distribution in the $p_t - \gamma$ plane. The extracted source rapidity of K^+ mesons is about $y_s/y_{\text{beam}} = 0.25$ at both incident energies [$y(\text{Au}) = 0, y(\text{C}) = y_{\text{beam}}$]. This corresponds to a reaction volume consisting of the C nucleus and a tube cut out of the Au nucleus. In clear contrast, the source rapidities of π^{pm} mesons vary from $y_s/y_{\text{beam}} = 0.5$ in peripheral collisions (corresponding to NN interactions) to about $y_s/y_{\text{beam}} < 0.33$ in central reactions. The multiplicities of K^+ and π are compared to symmetric collision systems and, together with detailed transport model calculations, are used to study the sensitivity to the nuclear equation of state.

Collective rotation of nuclei with tetrahedral symmetry

Acta Phys. Pol. B 36 (2005) 1071

Schunck, N., J. Dudek, **S. Frauendorf**

Abstract: Collective rotation of tetrahedral nuclei is analyzed within a three-dimensional cranking model. The favored orientation of the rotational frequency vector with respect to the turning nucleus as function of angular momentum is obtained from the total energy calculations. A new quantum number, resulting from the particular symmetry of the cranking Hamiltonian of the nuclei with tetrahedral nuclei is discussed. Some consequences for the structure of the rotational bands are presented.

The photon-scattering facility at the superconducting electron accelerator ELBE

Nucl. Instr. Meth., Phys. Res. A 555 (2005) 211

Schwengner, R., R. Beyer, F. Döna, **E. Grosse**, **A. Hartmann**, **A.R. Junghans**, S. Mallion, **G. Rusev**, **K.D. Schilling**, **W. Schulze**, **A. Wagner**

Abstract: A new facility for the production of polarised bremsstrahlung has been built at the superconducting electron accelerator ELBE of the Forschungszentrum Rossendorf. The bremsstrahlung facility and the setup for photon-scattering experiments are designed such that the background radiation due to scattering of photons and production of neutrons is minimised. The sensitive setup in connection with electron energies up to 20 MeV and average currents up to 1 mA delivered by the ELBE accelerator enables novel experiments using photon-induced reactions. First results of photon-scattering experiments are presented.

Reappearance of the pairing correlations at finite temperature

Phys. Rev. C 72 (2005) 041301

Sheikh, J.A, R. Palit, **S. Frauendorf**

Abstract: Rotational and deformation dependence of isovector and isoscalar pairing correlations at finite temperature are studied in an exactly solvable cranked deformed shell model Hamiltonian. It is shown that isovector pairing correlations, as expected, decrease with increasing deformation and the isoscalar pairing correlations remain constant at temperature, $T = 0$. However, it is observed that at finite temperature both isovector and isoscalar pairing correlations are enhanced with increasing deformation. It is also demonstrated

that the pair correlations, which are quenched at $T=0$ and high rotational frequency reappear at finite temperature. The changes in the individual multipole pairing fields as a function of rotation and deformation are analyzed in detail.

Investigation of antimagnetic rotation in light Cadmium nuclei: ^{106}Cd , ^{108}Cd

Phys. Rev. C 72 (2005) 024318

Simons A.J., R. Wadsworth, D.G. Jenkins, R.M. Clark, M. Cromaz, M.A. Deleplanque, R.M. Diamond, P. Fallon, G.J. Lane, I.Y. Lee, A.O. Macchiavelli, F.S. Stephens, C.E. Svensson, K. Vetter, D. Ward, **S. Frauendorf**, Y. Gu

Abstract: The lifetimes of excited states belonging to the lowest lying positive-parity bands in Cd-106, Cd-108 have been measured using the Doppler-shift attenuation method. The resulting B(E2) transition rates show a significant decrease with increasing spin in ^{106}Cd , whereas in ^{108}Cd there is tentative evidence for a similar effect. The results are compared with cranking and semiclassical model calculations, which indicate that the structures have the properties expected from an "antimagnetic" rotational band resulting from the coupling of $g_{(9/2)}$ proton holes to aligned pairs of $h_{(11/2)}$ and $g_{(7/2)}$ neutron particles.

Observation of negative-parity high-spin states of ^{68}As

Eur. Phys. J. A 24 (2005) 012301

Stefanova, E.A., K.P. Lieb, I. Stefanescu, G. de Angelis, D. Curien, J. Eberth, E. Farnea, A. Gadea, G. Gersch, A. Jungclaus, T. Martinez, **R. Schwengner**, T. Steinhardt, N. Warr, D. Weisshaar, R. Wyss

Abstract: The neutron-deficient nucleus ^{68}As was populated at high spin in two experiments using the reaction $^{40}\text{Ca}(^{32}\text{S}, 3pn)$ at beam energies of 105 and 95 MeV. A self-supporting and a gold backed, highly enriched ^{40}Ca target were used. Gamma rays were detected with the EUROBALL array, combined with the charged-particle detector array EUCLIDES and the Neutron Wall. The ^{68}As level scheme was considerably extended, especially at negative parity and many previous spin-parity assignments were confirmed or rejected. The total-Routhian-surface (TRS) calculation find shape coexistence and γ softness for the negative- and positive-parity states, respectively.

Gluon emission of heavy quarks: Dead cone effect

Acta Phys. Hung. A 22 (2005) 83

Thomas, R., B. Kämpfer, G. Soff

Abstract: The lowest-order induced soft gluon radiation processes of heavy quarks are considered with the aim to quantify the dead cone effect. The dead cone effect is expected to suppress significantly the energy loss of charm quarks passing an amorphous colour-neutral deconfined medium, as anticipated in recent experiments at RHIC.

Evidence for in-medium changes of four-quark condensates

Phys. Rev. Lett. 95 (2005) 232301

Thomas, R., S. Zschocke, B. Kämpfer

Abstract: Utilizing the QCD sum rule approach to the behavior of the ω meson in nuclear matter we derive evidence for in-medium changes of particular four-quark condensates from the recent CB-TAPS experiment for the reaction $\gamma + A \rightarrow A' + \omega (\rightarrow \pi^0 \gamma)$ with $A = \text{Nb}$ and LH2.

Spin correlations in the reaction $\pi^\pm \vec{D} \rightarrow \vec{\Sigma} \Theta^+$ and the parity of Θ^+

Phys. Rev. C 71 (2005) 062201(R)

Titov, A.I., **B. Kämpfer**

Abstract: We analyze two types of spin observables in the reaction $\pi \vec{D} \rightarrow \vec{\Sigma} \Theta^+$ near the threshold. One concerns the spin-transfer coefficients K_x^x and K_z^z . The second is the deuteron spin anisotropy. These

observables are sensitive to the Θ^+ parity and can be used as a tool for the Θ^+ parity determination.

Coherent Θ^+ and $\Lambda(1520)$ photoproduction off the deuteron

Phys. Rev. C 72 (2005) 035206

Titov, A.I., **B. Kämpfer**, S. Date, Y. Ohashi

Abstract: We analyze an effect of the coherent $\Theta^+\Lambda(1520)$ photoproduction in γD interaction near the threshold. We demonstrate that the coherence effect becomes manifest in a comparison of the nK^+ invariant mass distribution when the pK^- invariant equals the $\Lambda(1520)$ mass. Our model calculations indicate a sizeable contribution of resonant and non-resonant background processes in the $\gamma D \rightarrow npK^+K^-$ reaction which generally exceed the contribution of the coherent resonant channel. However, we find that the coherent $\Theta^+\Lambda(1520)$ photoproduction is enhanced relative to the background processes in the forward hemisphere of the pK^- pair photoproduction. Moreover, the coherence effect does not depend on the Θ^+ photoproduction amplitude and is defined by the probabilities of the $\Lambda(1520)$ photoproduction and the $\Theta^+ \rightarrow NK$ transition. Therefore, this coherence effect may be used as an independent method for studying the mechanism of Θ^+ production and Θ^+ properties.

Observation of different azimuthal emission patterns for K^+ and of K^- mesons in Heavy Ion Collisions at 1-2 A GeV

Phys. Rev. Lett. 95 (2005) 012301

Uhlig, F., A. Foerster, I. Boettcher, M. Debowski, **F. Dohrmann**, **E. Grosse**, P. Koczon, B. Kohlmeyer, F. Laue, M. Menzel, **L. Naumann**, H. Oeschler, W. Scheinast, E. Schwab, P. Senger, Y. Shin, H. Stroebele, C. Sturm, G. Surowka, **A. Wagner**, W. Walus

Abstract: Azimuthal distributions of π^+ , K^+ and K^- mesons have been measured in Au+Au reactions at 1.5 A GeV and Ni+Ni reactions at 1.93 A GeV. In semi-central collisions at midrapidity, π^+ and K^+ mesons are emitted preferentially perpendicular to the reaction plane in both collision systems. In contrast for K^- mesons in Ni+Ni reactions an in-plane elliptic flow was observed for the first time at these incident energies.

Evidence for non-termination of rotational bands in ^{74}Kr

Phys. Rev. Lett. 95 (2005) 232501

Valiente-Dobón, J.J., T. Steinhardt, C.E. Svensson, A.V. Afanasjev, I. Ragnarsson, C. Andreoiu, R.A.E. Austin, M.P. Carpenter, D. Dashdorj, G. de Angelis, **F. Dönau**, J. Eberth, E. Farnea, S.J. Freeman, A. Gadea, P.E. Garrett, A. Görge, G.F. Grinyer, B. Hyland, D. Jenkins, F. Johnston-Theasby, P. Joshi, A. Jungclaus, K.P. Lieb, A.O. Macchiavelli, E.F. Moore, G. Mukherjee, D.R. Napoli, A.A. Phillips, C. Plettner, W. Reviol, D. Sarantites, H. Schnare, M.A. Schumaker, **R. Schwengner**, D. Seweryniak, M.B. Smith, I. Stefanescu, O. Thelen, R. Wadsworth

Abstract: Three rotational bands in ^{74}Kr were studied up to (in one case one transition short of) the maximum spin I_{max} of their respective single-particle configurations. Their lifetimes have been determined using the Doppler-shift attenuation method. The deduced transition quadrupole moments reveal a modest decrease, but far from a complete loss of collectivity at the maximum spin I_{max} . This feature, together with the results of mean field calculations, indicates that the observed bands do not terminate at $I = I_{max}$.

Suppression of band crossing in the neutron-rich nuclei $^{172,173}\text{Yb}$ due to the absence of a static pairfield

Eur. Phys. J. A 26 (2005) 19

Venkova, Ts., W. Gast, R.M. Lieder, D. Bazzacco, G. de Angelis, E.O. Lieder, A.A. Pasternak, R. Menegazzo, S. Lunardi, C. Rossi Alvarez, C. Ur, T. Martinez, M. Axiotis, D. Napoli, W. Urban, T. Rzaca-Urban, **S. Frauendorf**

Abstract: High-spin states in the neutron-rich nuclei $^{172,173}\text{Yb}$ have been populated in a $^{170}\text{Er}(^7\text{Li},(p,d,t)\chi n)$ incomplete-fusion reaction and the emitted γ -radiation was detected with the GASP array. The signature partners of the $7/2^+[633]$ rotational band of the odd- $N^{173}\text{Yb}$ isotope have been newly established and were

observed up to spin values of $(45/2^+)$ and $(43/2^+)$, respectively. The ground-state band of the even-even nucleus ^{172}Yb has been observed up to a spin value of (22^+) . No band crossings were found in these bands. To explain this observation, it is proposed that the static pair field is absent, considering that the neutron odd-even mass differences reach for these nuclei very small values and that the band crossing is absent in cranked shell model calculations without pairing. The results indicate, however, that strong dynamic correlations are still present.

The new bremsstrahlung facility at the superconducting electron accelerator ELBE

J. Phys. G 31 (2005) S1969

Wagner, A., R. Beyer, M. Erhard, F. Dönau, E. Grosse, A. Hartmann, A.R. Junghans, L. Käubler, K. Kosev, S. Mallion, C. Nair, N. Nankov, G. Rusev, K.D. Schilling, W. Schulze, R. Schwengner

Abstract: A new facility for the production of polarized bremsstrahlung has been built at the superconducting electron accelerator ELBE of the Forschungszentrum Rossendorf. The bremsstrahlung facility and the detector setup are designed such that the background radiation due to scattering of photons and production of neutrons is minimized allowing for experiments close to and above particle separation energies in nuclei. First results of photon-scattering and photo-dissociation experiments on $^{92,98,100}\text{Mo}$ are presented. The results are compared to recent cross-section calculations for astrophysical networks.

Medium effects on ϕ -meson production in near threshold proton-nucleus collisions

Nucl. Phys. A 749 (2005) 174

Zetenyi, M., **H.-W. Barz**

Abstract: We study the cross section of phi-meson production in proton-nucleus collisions. The decay width of the phi-meson is affected by the change of the masses of the ϕ , K^+ , K^- mesons in medium. A strong attractive K^- potential leads to a broadening of the phi-meson, which results in a measurable change of the behavior of the cross section as a function of the target mass.

Soft chiral vibrations in ^{106}Mo

Eur. Phys. J. A 25 (2005) 459

Zhu, S.J., J.H. Hamilton, A.V. Ramayya, P.M. Gore, J.O. Rasmussen, V. Dimitrov, **S. Frauendorf**, R.Q. Xu, J.K. Hwang, D. Fong, L.M. Yang, K. Li, Y.J. Chen, X.Q. Zhang, E.F. Jones, Y.X. Luo, I.Y. Lee, W.C. Ma, J.D. Cole, M.W. Drigert, M. Stoyer, G.M. Ter-Akopian, A.V. Daniel

Abstract: High-spin states in neutron-rich ^{106}Mo were investigated by detecting the prompt γ -rays in the spontaneous fission of ^{252}Cf with Gammasphere. Several new bands are observed. Two sets of $\Delta I = 1$ bands in ^{106}Mo are found to have all the characteristics of a new class of chiral vibrational doublets. Tilted axis cranking calculations support the chiral assignment and indicate that the chirality is generated by neutron $h(11/2)$ particle and mixed $d(5/2)$, $g(7/2)$ hole coupled to the short and long axis, respectively.

Algebraic approach to bare nucleon matrix elements of quark operators

Phys. Rev. D 72 (2005) 014005

Zschocke, S., B. Kämpfer, G. Plunien

Abstract: An algebraic method for evaluating bare nucleon matrix elements of quark operators is proposed. Thereby, bare nucleon matrix elements are traced back to vacuum matrix elements. The method is similar to the soft pion theorem. Matrix elements of two-quark, four-quark and six-quark operators inside the bare nucleon are considered.

Impact of nucleon mass shift on the freeze out process

Phys. Rev. C 72 (2005) 064909

Zschocke, S., L. P. Csernai, E. Molnar, J. Manninen, A. Nyiri

Abstract: The freeze out of a massive nucleon gas through a finite layer with time-like normal is studied. The impact of in-medium nucleon mass shift on the freeze out process is investigated. A considerable modification of the thermodynamical variables temperature, flow-velocity, energy density and particle density has been found. Due to the nucleon mass shift the freeze out particle distribution functions are changed noticeably in comparison with evaluations, which use vacuum nucleon mass.

Accepted Papers

Relativistic approaches to investigations of few-nucleon systems

Phys. Part. Nucl. (2006) in print

Dorkin, S.M., L.P. Kaptari, **B. Kämpfer**, S.S. Semikh

Abstract: Theoretical approaches to investigations of relativistic effects in processes of high energy lepton and hadron scattering off few-nucleon systems are considered. The Bethe-Salpeter formalism for describing interacting two-nucleon systems both in bound and scattering states are presented in detail. In particular, special attention is paid to the partial expansions, analytic properties of the Bethe-Salpeter amplitudes and unitary transformations, connecting different sets of partial amplitudes. Various methods of numerically solving the Bethe-Salpeter equations are considered. Calculations of relativistic corrections and final state interaction effects are presented for numerous processes on the deuteron like backward pD scattering and different types of proton-deuteron break-up with formation of correlated pair in the final state.

Photodissociation of p-process nuclei studied by bremsstrahlung induced activation

Eur. Phys. J. A (2006) in print

Erhard, M., **A.R. Junghans**, **R. Beyer**, **E. Grosse**, **J. Klug**, **K. Kosev**, **C. Nair**, **N. Nankov**, **G. Rusev**, **K.D. Schilling**, **R. Schwengner**, **A. Wagner**

Abstract: A research program has been started to study experimentally the near-threshold photodissociation of nuclides in the chain of cosmic heavy element production with bremsstrahlung from the ELBE accelerator. An important prerequisite for such studies is good knowledge of the bremsstrahlung distribution which was determined by measuring the photodissociation of the deuteron and by comparison with model calculations. First data were obtained for the astrophysically important target nucleus ^{92}Mo by observing the radioactive decay of the nuclides produced by bremsstrahlung irradiation at end-point energies between 11.8 and 14.0 MeV. The results are compared to recent statistical model calculations.

QCD matter within a quasi-particle model and the critical end point

Nucl. Phys. A (2006) in print

Kämpfer, B., M. Bluhm, R. Schulze, D. Seipt, U. Heinz

Abstract: We compare our quasi-particle model with recent lattice QCD results for the equation of state at finite temperature and baryo-chemical potential. The inclusion of the QCD critical end point into models is discussed. We propose a family of equations of state to be employed in hydrodynamical calculations of particle spectra at RHIC energies and compare with the differential azimuthal anisotropy of strange and charm hadrons.

Di-electron bremsstrahlung in intermediate-energy pn and Dp collisions

Nucl. Phys. A (2006) in print

Kaptari, L.P., **B. Kämpfer**

Abstract: Invariant mass spectra of di-electrons stemming from bremsstrahlung processes are calculated in a covariant diagrammatical approach for the exclusive reaction $Dp \rightarrow p_{sp}np e^+e^-$ with detection of a forward spectator proton, psp . We employ an effective nucleon-meson theory for parameterizing the subreaction $np \rightarrow npe^+e^-$ and, within the Bethe-Salpeter formalism, derive a factorization of the cross section in the form $d\sigma_{Dp \rightarrow p_{sp}np e^+e^-}/dM = d\sigma_{np \rightarrow npe^+e^-}/dM \times$ kinematical factor related solely to the deuteron (M is the e^+e^- invariant mass). The effective nucleon-meson interactions, including the exchange mesons π, σ, ω and ρ as well as excitation and radiative decay of $\Delta(1232)$, have been adjusted to the process $pp \rightarrow ppe^+e^-$ at energies below the vector meson production threshold. At higher energies, contributions from ω and ρ meson excitations are analyzed in both, NN and Dp collisions. A relation to two-step models is discussed. Subthreshold di-electron production in Dp collisions at low spectator momenta is investigated as well. Calculations have been performed for kinematical conditions envisaged for forthcoming experiments at HADES.

In-beam PET at high-energy photon beams: a feasibility study

Phys. Med. Biol. (2006) in print

Müller, H., **W. Enghardt**

Abstract: For radiation therapy with carbon ion beams, either of the stable isotope ^{12}C or of the radioactive one ^{11}C , it has been demonstrated that the β^+ -activity distribution created or deposited, respectively, within the irradiated volume can be visualised by means of positron emission tomography (PET). Those PET images provide valuable information for quality assurance and precision improvement of ion therapy. Dedicated PET scanners have been integrated into treatment sites at HIMAC (Japan) and GSI (Germany) to make PET imaging feasible during therapeutic irradiation (in-beam PET). A similar technique may be worthwhile for radiotherapy with high-energy bremsstrahlung. In addition to monitoring the dose delivery process which in-beam PET has been primarily developed for, it may be expected that radiation response of tissue can be detected by means of in-beam PET. We investigate the applicability of PET for treatment control in case of using bremsstrahlung spectra produced by 15-50 MeV electrons. Target volume activation due to (γ, n) reactions at energies above 20 MeV yields moderate β^+ -activity levels, which can be employed for imaging. The radiation from positrons produced by pair production is not presently usable because the detectors are overloaded due to the low duty factor of medical electron linear accelerators. However the degradation of images caused by positron motion between creation and annihilation seems to be tolerable.

Application of advanced Monte Carlo methods in numerical dosimetry

Rad. Prot. Dos. (2006) in print

Reichelt, U., J. Henniger,

Abstract: Many tasks in different sectors of dosimetry are very complex and highly sensitive to changes of the radiation field, e. g. dose estimations in microdosimetry. Often experimental measurements are only available for particular conditions or at single target points. Thus only the simulation of radiation transport is capable of describing the radiation field completely. Different approaches for solving the radiation transport problem as e.g. FEM can be used. In particular the Monte Carlo (MC) method is very useful for high-dimensional problems, and it is accepted as a standard method for this purpose. Down to sub cellular dimensions the energy deposition by cascades of secondary electrons is the main pathway for damage induction in matter. A high number of interactions is taking place until such an electron is slowed down to thermal energies. For this reason the non-analog Monte Carlo program AMOS has been developed for photon and electron transport. The advanced MC algorithms implemented are able to handle a large number of histories at reasonable performance even for time consuming single scattering models. They facilitate the calculation of photon dose distributions at up to 10^6 points. Modeling the dose distribution of a ^{125}I brachytherapy source has proven the high efficiency of this MC approach. Further on results achieved by AMOS for the transport of electrons with low energies ($E < 100 \text{ keV}$) in matter with low atomic numbers were compared to measured data from the literature. It has been proven that the program code produces results in rather well agreement to the experiments also for small target structures of about one micrometre. This is especially important for the application to cell irradiation experiments as they are carried out at the FZ Rossendorf. As another example of application a simulation of the whole spectral detector response of an HPGe detector will be presented.

Pygmy dipole strength close to particle-separation energies - the case of the Mo isotopes

Eur. Phys. A (2006) in print

Rusev, G., E. Grosse, M. Erhard, A.R. Junghans, K. Kosev, K.D. Schilling, R. Schwengner, A. Wagner

Abstract: The distribution of electromagnetic dipole strength in $^{92,98,100}\text{Mo}$ has been investigated by photon scattering using bremsstrahlung from the new ELBE facility. The experimental data for well separated nuclear resonances indicate a transition from a regular to a chaotic behaviour above 4 MeV of excitation energy. As the strength distributions follow a Porter-Thomas distribution much of the dipole strength is found in weak and in unresolved resonances appearing as fluctuating cross section. An analysis of this quasi-continuum - here applied to nuclear resonance fluorescence in a novel way - delivers dipole strength functions, which are combining smoothly to those obtained from (γ, n) -data. Enhancements at 6.5 MeV and at ca. 9 MeV are linked to the pygmy dipole resonances postulated to occur in heavy nuclei.

Systematics of magnetic dipole strength in the stable even-mass Mo isotopes

Phys. Rev. C (2006) in print

Rusev, g., R. Schwengner, F. Dönau, M. Erhard, S. Frauendorf, E. Grosse, A.R. Junghans, L. Käubler, K. Kosev, L.K. Kostov, S. Mallion, K.D. Schilling, A. Wagner, H. von Garrel, U. Kneissl, C. Kohstall, M. Kreutz, H.H. Pitz, M. Scheck, F. Stedile, P. von Brentano, J. Jolie, A. Linnemann, N. Pietralla, V. Werner,

Abstract: The nuclides ^{92}Mo , ^{98}Mo and ^{100}Mo have been studied in photon-scattering experiments by using bremsstrahlung produced at an electron energy of 6 MeV at the ELBE accelerator of the Forschungszentrum Rossendorf and at electron energies from 3.2 to 3.8 MeV at the Dynamitron accelerator of the Stuttgart University. Six dipole transitions in ^{98}Mo and 19 in ^{100}Mo were observed for the first time in the energy range from 2 to 4 MeV. The experimental results are compared with predictions of the shell model and with predictions of the quasiparticle-random-phase approximation in a deformed basis. The latter show significant contributions of isovector-orbital and isovector-spin vibrations. The change of the magnetic dipole strength in the isotopic chain of the even-mass isotopes from ^{92}Mo to ^{100}Mo is discussed. The calculations within the quasiparticle-random-phase approximation are extrapolated to the particle-separation energies to estimate the possible influence of $M1$ strength on the stability of the nuclides against photodissociation in cosmic scenarios.

In-Medium Effects on Phase Space Distributions of Antikaons Measured in Proton-Nucleus Collisions

Phys. Rev. Lett. (2006) in print

Scheinast, W., I. Böttcher, M. Debowski, F. Dohrmann, A. Förster, E. Grosse, P. Koczoń, B. Kohlmeyer, F. Laue, M. Menzel, L. Naumann, E. Schwab, P. Senger, Y. Shin, H. Ströbele, C. Sturm, G. Surówka, F. Uhlig, A. Wagner, W. Waluś, B. Kämpfer, H.W. Barz

Abstract: Differential production cross sections of K^\pm mesons have been measured in $p+C$ and $p+Au$ collisions at 1.6, 2.5 and 3.5 GeV proton beam energy. At beam energies close to the production threshold, the K^- multiplicity is strongly enhanced with respect to proton-proton collisions. According to microscopic transport calculations, this enhancement is caused by two effects: the strangeness exchange reaction $NY \rightarrow K^- NN$ and an attractive in-medium K^-N potential at saturation density.

Low-energy cross section of the $^7\text{Be}(p,\gamma)^8\text{B}$ solar fusion reaction from Coulomb dissociation of ^8B

Schümann, F., S. Typel, F. Hammache, K. Sümmerer, F. Uhlig, I. Böttcher, D. Cortina, A. Förster, M. Gai, H. Geissel, U. Greife, E. Grosse, N. Iwasa, P. Koczoń, B. Kohlmeyer, R. Kulesa, H. Kumagai, N. Kurz, M. Menzel, T. Motobayashi, H. Oeschler, A. Ozawa, M. Płoskoń, W. Prokopowicz, E. Schwab, P. Senger, F. Strieder, C. Sturm, Zhi-Yu Sun, G. Surówka, A. Wagner, W. Waluś

Phys. Rev. C (2006) in print

Abstract: An exclusive measurement of the Coulomb breakup of ^8B into $^7\text{Be} + p$ at 254 A MeV was used to infer

the low-energy ${}^7\text{Be}(p,\gamma){}^8\text{B}$ cross section. The radioactive ${}^8\text{B}$ beam was produced by projectile fragmentation of 350 A MeV ${}^{12}\text{C}$ and separated with the fragment separator FRS at GSI in Darmstadt, Germany. The Coulomb-breakup products were momentum-analyzed in the KaoS magnetic spectrometer; particular emphasis was placed on the angular correlations of the breakup particles. These correlations demonstrate clearly that E1 multipolarity dominates within the angular cuts selected for the analysis. The deduced astrophysical S_{17} factors exhibit good agreement with the most recent direct ${}^7\text{Be}(p,\gamma){}^8\text{B}$ measurements. By using the energy dependence of S_{17} according to the recently refined cluster model for ${}^8\text{B}$ of Descouvemont, we extract a zero-energy S factor of $S_{17}(0) = 20.6 \pm 0.8 (stat) \pm 1.2 (syst)$ eV b. These errors do not include the uncertainty of the theoretical model to extrapolate to zero relative energy, estimated to be about 5% by Descouvemont.

Light-ion production in the interaction of 96 MeV neutrons with oxygen

Phys. Rev. C (2006) in print

Tippawan, U., S. Pomp, A. Atac, B. Bergenwall, J. Blomgren, S. Dangtip, A. Hildebrand, C. Johansson, **J. Klug**, P. Mermod, L. Nilsson, M. Österlund, N. Olsson, A. Prokofiev, P. Nadel-Turonski, V. Corcalciuc, A. Koning

Abstract: Double-differential cross sections for light-ion ($p, d, t, {}^3\text{H}$ and α) production in oxygen, induced by 96 MeV neutrons are reported. Energy spectra are measured at eight laboratory angles from 20 to 160 degrees in steps of 20 degrees. Procedures for data taking and data reduction are presented. Deduced energy-differential and production cross sections are reported. Experimental cross sections are compared to theoretical reaction model calculations and experimental data at lower neutron energies in the literature.

Electromagnetic probes of strongly interacting matter: probes of chiral symmetry restoration?

Heavy Ion Physics (2006) in print

Thomas, R., K. Gallmeister, **S. Zschocke**, **B. Kämpfer**

Abstract: The QCD sum rule approach to in-medium modifications of the ω meson in nuclear matter is reviewed with emphasis of its relation to 4-quark condensates and chiral symmetry restoration. Possible implications of the CB-TAPS experiment for the reaction $\gamma A \rightarrow A'\omega (\rightarrow \pi^0\gamma)$ are sketched and the particularly important role of di-electron probes, accessible with HADES, is highlighted. A brief update of a parametrization of the previous dilepton and photon probes from CERES and WA98 of heavy-ion collisions at CERN-SPS energies is presented.

Proceedings and Reports

Altstadt, E., C. Beckert, **R. Beyer**, H. Freiesleben, V. Galindo, M. Greschner, **E. Grosse**, **A. Junghans**, **J. Klug**, B. Naumann, S. Schneider, K. Seidel, **A. Wagner**, F.-P. Weiß

Energiedispersive Untersuchung der Wechselwirkung schneller Neutronen mit Materie - gemeinsamer Abschlussbericht der DFG Projekte GR 1674/2 und FR 575/5

Wissenschaftlich-Technische Berichte FZR-426 (2005)

Dohrmann, F., A. Ahmidouch, C.S. Armstrong, J. Arrington, R. Asaturyan, S. Avery, K. Bailey, O.K. Baker, H. Bitao, H. Breuer, D.S. Brown, R. Carlini, J. Cha, N. Chant, E. Christy, A. Cochran, L. Cole, J. Crowder, S. Danagoulian, M. Elaasar, R. Ent, H. Fenker, Y. Fujii, L. Gan, K. Garrow, D.F. Geesaman, P. Gueye, K. Hafidi, W. Hinton, H. Juengst, C. Keppel, Y. Liang, J.H. Liu, A. Lung, D. Mack, P. Markowitz, J. Mitchell, T. Miyoshi, H. Mkrtchyan, S.K. Mtingwa, B. Mueller, G. Niculescu, I. Niculescu, D.H. Potterveld, B.A. Raue, P.E. Reimer, J. Reinhold, J. Roche, M. Sarsour, Y. Sato, R.E. Segel, A.Yu. Semenov, S. Stepanyan, V. Tadevosian, S. Tajima, L. Tang, A. Uzzle, S. Wood, H. Yamaguchi, C. Yan, L. Yuan, M. Zeier, B. Zeidman, B. Zihlmann

Electroproduction of strangeness on ${}_{\Lambda}^{3,4}\text{H}$ bound states on Helium

Proc. of the 19th European Conference on Few-Body Problems in Physics, AIP Conf. Proc. 768 (2005) 294

Fiedler, F., P. Crespo, K. Parodi, M. Sellesk, W. Enhardt

The feasibility of in-beam PET for therapeutic beams of He-3

Proc. of Heavy Charged Particles in Biology and Medicine - ENLIGHT meeting, 15.-19.09.2005, Oropa, Italien, p. 192

Förstendorf, H., **W. Seidel**, G. Bernhard

FELBE - a new facility providing coherent radiation for infrared spectroscopic investigations in actinide research

Migration 2005, 10th International Conference on Chemistry and Migration Behaviour of Actinides and Fission Products, 18.-23.09.2005, Avignon, France

Grosse, E., U. Lehnert, P. Michel, R. Schlenk, W. Seidel, A. Wolf, U. Willkommen, Wohlfarth, R. Wunsch

A far-infrared FEL for the radiation source ELBE

27th Int. Free Electron Laser Conference, Stanford Univ., 21.-26.08.2005, Palo Alto, USA

www.JACoW.org/ FEL05, Proceedings, p. 290

Karny, M., L. Batist, A. Banu, F. Becker, A. Blazhev, K. Burkard, W. Brüche, J. Döring, T. Faestermann, M. Górska, H. Grawe, Z. Janas, A. Jungclaus, M. Kavatsyuk, O. Kavatsyuk, R. Kirchner, M. La Commara, S. Mandal, C. Mazzocchi, K. Miernik, I. Mukha, S. Muralithar, C. Plettner, A. Płochocki, E. Roeckl, M. Romoli, K. Rykaczewski, M. Schädel, K. Schmidt, **R. Schwengner**, J. Zylicz

Beta-decay studies near ^{100}Sn

ENAM 2004, 12.-16.9.2004, Pine Mountain, GA, USA

Eur. Phys. J. A 25 (2005) 135

Kavatsyuk, M., O. Kavatsyuk, L. Batist, A. Banu, F. Becker, A. Blazhev, W. Brüche, K. Burkard, J. Döring, T. Faestermann, M. Górska, H. Grawe, Z. Janas, A. Jungclaus, M. Karny, R. Kirchner, M. La Commara, S. Mandal, C. Mazzocchi, I. Mukha, S. Muralithar, C. Plettner, Płochocki, E. Roeckl, M. Romoli, M. Schädel, **R. Schwengner**, J. Zylicz

Beta-decay spectroscopy of $^{103,105}\text{Sn}$

ENAM 2004, 12.-16.9.2004, Pine Mountain, GA, USA

Eur. Phys. J. A 25 (2005) 139

Lehnert, U., P. Evtushenko, P. Michel, Ch. Schneider, R. Schurig, **W. Seidel**, J. Teichert, **D. Wohlfarth**

Diagnostic tools for operation and optimization of the ELBE-FEL

27th Int. Conf on Free Electron Lasers, Stanford, USA, Sep. 2005

www.JACoW.org/ FEL05, Proceedings, p. 102

Lehnert, U., P. Michel, **W. Seidel**, D. Stehr, J. Teichert, **D. Wohlfarth, R. Wunsch**

Optical beam properties and performance of the mid-IR FEL at ELBE

27th Int. Conf on Free Electron Lasers, Stanford, USA, Sep. 2005

www.JACoW.org/ FEL05, Proceedings, p. 286

Nankov, N., E. Grosse, A. Hartmann, A. R. Junghans, K. Kosev, K. D. Schilling, M. Sobiella, A. Wagner

A novel high-resolution time-of-flight spectrometer with tracking capabilities for photo-fission fragments and beams of exotic nuclei

Proc. 3rd Int. Conf. on Nucl. Fission and Fiss. Prod. Spect., Cadarache, France, Nov. 2005

AIP Conference Proceedings 798 (2005) 357

Andronenko, M. N., L.N. Andronenko, **W. Neubert**
Mass dependence of nuclear isotopic temperature for binary and ternary fission
Preprint St. Petersburg Nucl. Phys. Inst., Gatschina, Russia, PN PI - 2643 (2005)

Parodi, K., T. Haberer, **F. Pönisch, W. Enghardt**
Pet online for protons and ions
Proc. of Heavy Charged Particles in Biology and Medicine - ENLIGHT meeting, 15.-19.09.2005, Oropa, Italien, 119

Pollmann, K., J. Raff, M. Merroun, **K. Fahmy**, I. Mikechenko, N. Creamer, L. Macaskie, S. Selenska-Pobell
Analysis and engineering of the S-layer protein of Bacillus sphaericus JG-A12 and potential technological applications
Biotechnology 2004, 17.-22.10.2004, Santiago de Chile, Chile

Thusty, P. G. Agakichiev, C. Agodi, H. Alvarez-Pol, E. Atkin, A. Balanda, G. Bellia, D. Berver, J. Bielcik, M. Böhmer, H. Bokemeyer, J. Boyard, P. Braun-Munzinger, V. Chepurinov, S. Chernenko, T. Christ, R. Coniglione, H. Daues, J. Diaz, R. Djeridi, **F. Dohrmann**, I. Duran, T. Eberl, V. Emeljanov, L. Fabbietti, O. Fateev, C. Fernandez, P. Finocchiaro, J. Friese, I. Fröhlich, B. Fuentes, J. Garzon, R. Gernhäuser, M. Golubeva, D. Gonzalez, **E. Grosse**, F. Guber, J. Hehner, T. Heinz, T. Hennino, S. Hlavàè, J. Hoffmann, R. Holzmann, A. Ierusalimov, I. Iori, M. Jaskula, M. Jurkoviè, **B. Kämpfer, K. Kanaki**, T. Karavicheva, I. Koenig, W. Koenig, B. Kolb, U. Kopf, **R. Kotte**, J. Kotuliè-Bunta, R. Krücken, A. Kugler, W. Kühn, R. Kulessa, A. Kurepin, T. Kurtukian-Nieto, S. Lang, J. Lehnert, M. Maiolino, C. Marín, J. Markert, Y. Mishin, N. Montes, J. Mousa, M. Münch, C. Müntz, **L. Naumann**, J. Novotný, W. Ott, J. Otwinowski, Y. Pachmayer, Y. Panebratsev, V. Pechenov, T. Perez, J. Pietraszko, R. Pleskaè, V. Pospisíl, W. Przygoda, N. Rabin, B. Ramstein, A. Reshetin, J. Ritman, G. Rodriguez Prieto, M. Roy-Stephan, A. Rustamov, J. Sabin Fernandez, **A. Sadvovsky**, B. Sailer, P. Salabura, M. Sanchez, P. Sapienza, A. Schmäh, C. Schroeder, E. Schwab, P. Senger, R. Simon, V. Smolyankin, L. Smykov, S. Spataro, H. Stelzer, H. Stroebele, J. Stroth, C. Sturm, M. Sudol, A. Titov, A. Toia, M. Traxler, H. Tsertos, A. Vazquez, Y. Volkov, V. Wagner, W. Walus, Y. Wang, S. Winkler, M. Wisniowski, T. Wojcik, **J. Wüstenfeld**, Y. Zanevsky, D. Zovinec, P. Zumberg
Hadron production in C + C at 2 AGeV measured by the HADES spectrometer
Proc. Bormio 2004 Int. Conf., Vo. 120 (2005) p. 171

Wagner, A., R. Beyer, M. Erhard, F. Döna, E. Grosse, A. Hartmann, A.R. Junghans, L. Käubler, K. Kosev, S. Mallion, C. Nair, N. Nankov, G. Rusev, K.D. Schilling, W. Schulze, R. Schwengner
The new bremsstrahlung facility at the superconducting electron accelerator ELBE
NUSTAR 2005, P. Regan, 05.-08.01.2005, Guildford, UK, NUClear STructure, Astrophysics and Reactions, Bristol, UK: IOP, 0954-3899

Wagner, W., B. Azadegan, A. Panteleeva, J. Pawelke, W. Enghardt
Channeling X-rays at the ELBE radiation source
International Conference on Charged and Neutral Particles Channeling Phenomena, The International Society for Optical Engineering, 02.-06.11.2004, Rome, Italy
Bellingham, WA: Proc. of SPIE (2005) p. 59740B-1

Posters at Conferences

Foerstendorf, H., **W. Seidel**, F. Glotin, R. Prazeres, J.M. Ortega
Photothermal beam deflection (PTBD) spectroscopy using an FEL as a pump source
WIRMS 2005 Int. Workshop on Infrared Microscopy and Spectroscopy with Accelerator Based Sources,
26.-30.06.2005, Rathen, Deutschland

Lehmann, N., U. Alexiev, **K. Fahmy**
Steric coupling of helix 8 of rhodopsin to the Schiff base environment
European Conference on the Spectroscopy of Biological Molecules Sep. 2005, Aschaffenburg, Germany

Madathil, S., K. Fahmy
Structure and pH-Sensitivity of the Transmembrane Segment 3 of Rhodopsin
European Conference on the Spectroscopy of Biological Molecules Sep. 2005, Aschaffenburg, Germany

Michel, P., P. Evtushenko, U. Lehnert, C. Schneider, R. Schurig, J. Teichert, **W. Seidel., D. Wohlfarth**
Diagnostic Tools for Operation and Optimization of the ELBE-FEL
27th International Free Electron Laser Conference 2005, 21.-26.08.2005, Stanford, California, USA

Preusche, S., F. Wüst, **K.D. Schilling**, H. Roß, N. Dohn
Production of ^{89}Y and ^{56}Co at the Rossendorf CYCLOTRONE 18/9
CYCLONE 18/9 & 10/5 User Community, 5. Workshop, May 1-4, 2005, Montreal, Canada

Savchuk, O., H. Kezle, **K. Fahmy**
UV-flash-induced BI to BII conformational transition in DNA studied by UV-FTIR cross-correlation difference spectroscopy
European Conference on the Spectroscopy of Biological Molecules Sep. 2005, Aschaffenburg, Germany

Sczegan, M., G. Furlinski, D. Wohlfarth, W. Seidel, K. Fahmy
FEL-light-induced changes in thin organic films observed by dynamic Brewster angle microscopy
WIRMS 2005 Int. Workshop on Infrared Microscopy and Spectroscopy with Accelerator Based Sources,
26.-30.06.2005, Rathen, Deutschland

Seidel, W. for the ELBE team
The radiation source ELBE at Dresden-Rossendorf - a new FEL user facility for the infrared
WIRMS 2005 Int. Workshop on Infrared Microscopy and Spectroscopy with Accelerator Based Sources,
26.-30.06.2005, Rathen, Deutschland

Talks at Conferences and other Institutes

Bluhm, M.

Equation of state strongly interacting matter
DPG Tagung, Berlin, March 8, 2005

Bluhm, M.

Possible Critical End Point Effects on the QCD Equation of State
ITP, TU Dresden, May 27, 2005

Bluhm, M.

Strongly Interaction Matter within a Quasiparticle Perspective with Critical End Point Effects
Extreme QCD, Univ. of Wales, Swansea, England, Aug. 4, 2005

Bluhm, M.

Quasiparticle Model of QCD Matter and the QCD Critical End Point
Univ. Bielefeld, Sept. 20, 2005

Bluhm, M.

Quasiparticle Model of QCD Matter and the QCD Critical End Point
VI Workshop, Prerow, Oct. 7, 2005

Crespo, P

Optimization of in-beam positron emission tomography for monitoring heavy ion tumor therapy
Zentrum für Innovationskompetenz Oncoray, TU Dresden, Dec. 12, 2005

Dohrmann, F.

Tests of RPC detectors at ELBE: Status report
CBM Collab. Meeting, GSI Darmstadt, March 10, 2005

Dohrmann, F.

Testing RPC detectors at ELBE
HADES Collab. Meeting, JINR Dubna, Russia, June 10, 2005

Dohrmann, F.

RPC detectors at ELBE
CBM Collab. Meeting, Piaski, Poland, Sept. 10, 2005

Enhardt, W.

PET-geführte Strahlentherapie - Vision oder Realität
Med. Fakultät, TU Dresden, Jan. 17, 2005

Enhardt, W.

In-beam PET bei der Krebstherapie mit Ionenstrahlen
Atominst. der Österreichischen Uni., TU Wien, Austria, April 13, 2005

Enhardt, W.

Zentrum für Innovationskompetenz für Medizinischen Strahlenforschung in der Onkologie Dresden
Berufsakademie Riesa, May 31, 2005

Enhardt, W.

Data Processing for In-Beam Position Emission Tomography
Introductory talk, Real Time Conf. 2005, Stockholm, Sweden, June 08, 2005

Enhardt, W.

Heavy Ion Tumour Therapy and In-Beam Position Emission Tomography
TU Dresden, June 06, 2005

Enhardt, W. PET-geführte Strahlentherapie - Vision oder Realität

GDC Jahrestagung 2005, Fachgruppe Nuklearchemie, Düsseldorf, Sept. 12, 2005

Enhardt, W.

PET-guided Radiotherapy - Fact or Fiction

Workshop of the Belgian Foundation against Cancer

Emerging Hadron Therapy Projects in Europe, Brussels, Belgium, Nov. 13, 2005

Fahmy, K.

Molecular switching by GPCRs

Univ. Strasbourg, Febr. 21, 2005

Fahmy, K.

Infrared and fluorescence spectroscopic studies on molecular switching by G protein-coupled receptors

Deutsche Univ. in Kairo, March 22, 2005

Fahmy, K.

Molecular switching by GPCRs

Univ. Osnabrück, April 19, 2005

Fahmy, K.

Coupling of helix 8 of rhodopsin to the retinal Schiff base studied by infrared and fluorescence cross-correlation spectroscopy

Sektionstagung Deutsche Gesellschaft für Biophysik, May 5, 2005

Fahmy, K.

Structure and pH sensitivity of transmembrane helix 3 of rhodopsin

Eur. Conf. on the Spectroscopy of Biological Molecules, Aschaffenburg, Sept. 6, 2005

Fahmy, K.

Infrarotspektroskopie an Proteinen: Fluoreszenz-IR-Kreuzkorrelation

Anwendertreffen Bruker Ettlingen, Nov. 28, 2005

Fiedler, F.

In-beam PET für ^3He -Strahlen

DPG Tagung, Berlin, March 9, 2005

Fiedler, F., W. Enhardt

In-situ monitoring with PET

ENLIGHT-Meeting, Oropa, Italien, June 18, 2005

Fiedler, F.

The Feasibility of In-Beam PET for Therapeutic Beams of ^3He

IEEE Nuclear Science Symposium & Medical Imaging Conference, Fajardo, Puerto Rico, Oct. 23, 2005

Fiedler, F.

The feasibility of in-beam PET for therapeutic beams of ^3He

PTCOG 43, München, Dec. 11, 2005

Frauendorf, S.

New Symmetries of rotating nuclei

Colloquium, Phys. Div., Argonne Nat. Lab., Jan. 14, 2005

Frauendorf, S.

Orbitals, Shapes, and Currents
Int. Conf. on Finite Fermionic Systems, Nilsson Model 50 Years
Lund, Sweden, June 14, 2005

Frauendorf, S.

Left-handed Nuclei
Colloquium, Dep. Phys. and Astronomy, Vanderbilt Univ., Nashville, USA, Oct. 27, 2004

Frauendorf, S.

Isovector Proton-Neutron Pairing
INT Program 05-3: Nuclear Structure Near the Limits of Stability
Inst. Nucl. Theory, Univ. Washington, Seattle, USA, Nov. 14, 2005

Grosse, E.

Energie aus der Kernfusion und aus der Kernspaltung
Jugendzentrum Pi, Freiberg, March 3, 2005

Grosse, E.

Sterne und Kerne - Die Entstehung der chemischen Elemente durch nukleare Prozesse in Urknall, Sternen und Supernovae
Tag der offenen Tür, TU Dresden, April 30, 2005

Grosse, E

Search for pygmy strength in Molybdenum isotopes close to particle separation energies
Nuclear Physics in Astrophysics-II, Debrecen, Hungary, May 16-20, 2005

Junghans, A.R.

Photodissociation of p-process nuclei studied by bremsstrahlung induced activation
Nuclear Physics in Astrophysics-II, Debrecen, Hungary, May 16-20, 2005

Junghans, A.R.

Nuclear astrophysics measurements with photo-neutrons and bremsstrahlung at ELBE
Phys.-Techn. Bundesanstalt Dep. 6.4, Braunschweig, Sept. 1, 2005

Junghans, A.R.

Kerne und Sterne
Lange Nacht der Wissenschaften, TU Dresden, July 1, 2005

Kämpfer, B.

Quasi-particle description of QCD matter
Probing QCD with High Energy Nuclear Collisions, Hirschegg, Austria, Jan. 16, 2005

Kämpfer, B.

Open charm and leptons at RHIC
ECT* - Electromagnetic probes of hot and dense matter, Trento, Italy, June 3 - 11, 2005

Kämpfer, B.

QCD matter within quasi-particle model and the critical end point
Quark Matter 2005, Budapest, Hungary, Aug. 4 - 9, 2005

Kämpfer, B.

Primordiale Nukleosynthese
IKTP, TU Dresden, Nov. 10, 2005

Kämpfer, B.

Chiral Condensate and Open Charm
CBM-Meeting, GSI Darmstadt, Dec. 15-16, 2005

Klug, J.

Development of a Neutron Time-of-Flight Source at ELBE Accelerator
Int. Conf. on New Trends in Physics Applications and Technology, Pavia, Italy, Sept. 9, 2005

Kotte, R.

Seeking sub-100ps timing without fast reference detector at the Rossendorf Electron Linac ELBE
FOPI collaboration meeting, Split, Croatia, May 26-28, 2005

Kotte, R.

RPC timing tests at ELBE
FOPI collaboration meeting, GSI Darmstadt, Dec 12-13, 2005

Kotte, R.

FOPI plastic wall status (S279, S297)
FOPI collaboration meeting, GSI Darmstadt, Dec 12-13, 2005

Kotte, R.

Testing RPC timing at the Rossendorf electron Linac ELBE
CBM-RPC-Hadron-ID workshop, GSI Darmstadt, Dec 14, 2005

Möckel, D., W. Enghardt

Activity of the Rossendorf group concerning WP1 of BioCare
BioCare Meeting, Manchester, UK, Oct. 12-13, 2005

Naumann, L.

Design and construction of a prototype TRD for the CBM experiment at GSI
GSI Darmstadt, Dec. 8-9, 2005

Pawelke, J.

Mensch und Strahlung
Lange Nacht der Wissenschaften, TU Dresden, July 1, 2005

Sadovski, A.

High resolution Runge-Kutta tracking for kaon reconstruction
DPG Tagung, Berlin, March 4, 2005

Sadovski, A.

K^+ production in the reaction $C + C$ at 2 AGeV
HADES Collab. Meeting XV, Dubna, Russia, June 7-12, 2005

Sadovski, A.

K^+ production in Carbon-Carbon collisions at 2 GeV per nucleon measured with HADES experiment
IKTP, TU Dresden, June 23, 2005

Sadovski, A.

An estimate of the K^+ cross section in the reaction $C + C$ at 2 AGeV
HADES PID Meeting, Rez Czech., Dec. 12-14, 2005

Schwengner, R.

The decay of 1^+ states as a new probe of the structure of 0^+ shape isomers
DPG Tagung, Berlin, March 4-9, 2005

Schwengner, R.

Nuclear-structure and nuclear-astrophysics experiments at the superconducting electron accelerator ELBE
Invited Lecture at the XVI International School on Nuclear Physics, Neutron Physics and Nuclear Energy,
Varna, Bulgaria, Sep. 19-26, 2005

Seidel, W. & R. Wünsch

Der Rossendorfer Freie-Elektronen Laser
IKTP, TU Dresden, Jan. 27, 2005

Shakirin, G.

A method of proceeding the elements of the system matrix for iterative reconstruction of PET data
IBT, TU Dresden, Dec. 15, 2005

Thomas, R.

Gluon Radiation of Heavy Quarks in Deconfined Matter
Arbeitstreffen Kernphysik, Schleching, Febr. 2, 2005

Thomas, R.

Four-Quark condensates in QCD Sum Rules for Nucleons and Mesons
DPG Tagung, Berlin, March 4, 2005

Thomas, R.

Four-Quark condensates in QCD Sum Rules for Nucleons and Mesons
ITP, TU Dresden, June 6, 2005

Thomas, R. In-Medium Hadronic Observables: Impact of Four-Quark Condensates

Univ. Bielefeld, Sept. 29, 2005

Thomas, R.

In-Medium Hadronic Observables: Impact of Four-Quark Condensates
VI Workshop, Prerow, Oct. 8, 2005

Wagner, A.

Kernphysikalische Experimente an ELBE
Kernphysik Kolloquium, Univ. Köln, Jan. 26, 2005

Wagner, A.

Kerne und Sterne
Lange Nacht der Wissenschaften, TU Dresden, July 1, 2005

Wagner, A.

Activation of p-process nuclei by photodissociation
Int. Conf. on Frontiers in Nucl. Struc., Astrophysics and Reactions, Kos, Greece, Sept. 12, 2005

Wagner, A.

Vom Mikrokosmos zum Makrokosmos
Tag des offenen Labors, FZR, Sept. 24, 2005

Wünsch, R.

Der Rossendorfer Freie-Elektronen Laser
ILT Aachen, Nov. 17, 2005

Zschocke, S.

Renormalisation - from classical theory to quantum electrodynamics
Univ. Bergen, Norway, June 3, 2005

Talks of Visitors

Barnaföldi, G., KFKI Budapest, Hungary:
Jet-Quenching in a Medium, Nov. 4, 2005

Bečvar, F., Charles Univ. Prag, Czech Rep.:
Photon Strength Functions of Medium-Weight and Heavy Nuclei-Studied from Neutron Radiative Capture,
Apr. 29, 2005

Bemmerer, D., INFN Padova, Italy:
Nuclear Astrophysics with the LUNA 400 kV accelerator deep underground, Dec. 12, 2005

Böhl, M., TU Dresden:
Approaches to study the interaction of flavonoids with their cellular targets, Oct. 27, 2005

Cardaci, M., Univ. Neapel, Italy:
Charm semileptonic decays at BaBar, July 26, 2005

Crevenna, A., MPI of Molecular Cell Biology and Genetics Dresden:
Kinesin: a story of states, flexibility and cooperation, March 8, 2005

Deveaux M., GSI Darmstadt & IReS Strasbourg, France:
Monolithic Active Pixel Sensor for charged particle tracking, a new technology for advanced vertex detectors,
Jan. 28, 2005

Erdmenger, J., Werner-Heisenberg-Institut München:
How to calculate meson spectra from string theory, Nov. 11, 2005

Grieshammer, H., TU München:
An Effective Tale of a Few Nucleons and Photons, Nov. 21, 2005

Heil, M., FZ Karlsruhe:
Neutron Capture Reactions in Nuclear Astrophysics, June 24, 2005

Henzl, V., GSI Darmstadt:
Nuclear Equation of State studies by Multifragmentation reactions, May 13, 2005

Ignatyuk, A., Inst. of Phys. and Power Eng. Obninsk, Russia:
Nuclear Level Density, Apr. 1, 2005

Kampert, K.-H., Univ. Wuppertal:
Die höchstenergetischen Teilchen im Universum, July 22, 2005

Käppeler, F., FZ Karlsruhe:

Neutronenexperimente zur Elementsynthese in Roten Riesen, Febr. 4, 2005

Katsoulidou, V., TU Dresden:

Microtubules structure and function, Oct. 28, 2005

Kostov, L., Inst. for Nucl. Res. and Nucl. Energy, Sofia, Bulgaria:

Photon-induced fission on environmental issues, Oct. 10, 2005

Krticka, M., Charles Univ. Prague, Czech Rep.:

Gamma-decay experiments at the accelerators in Los Alamos and Karlsruhe and at the reactor in Rez - processed with help of the DICEBOX algorithm, Oct. 5, 2005

Krücken, R., TU München:

Structure of Exotic studied with REX/Isolde, Apr. 22, 2005

Kuhnhenh, J., Univ. Köln:

Erste Ergebnisse faseoptischer Dosimetrie an ELBE, Apr. 5, 2005

Lange, C., TU Dresden:

Transportrechnungen für Photonen- und Elektronenstrahlung, May 31, 2005

Pyatkov, Yu, MEPHI Moscow, Russia:

New approach to the analysis of two-dimensional data from the binary decays of heavy nuclei, Febr. 11, 2005

Ploszajczak, M., GANIL Caen, France:

Shell model for weakly bound and unbound nuclei, March 15, 2005

Salvatores, M., CEA Cadarache, France:

State of the art perspectives in radioactive waste transmutation, Dec. 7, 2005

Scheit, H., MPI for Nuclear Physics Heidelberg:

First Experiments with REX-ISOLDE an MINIBALL, Jan. 21, 2005

Sellesk, M., TU Bergakademie Freiberg:

Bestimmung der effektiven Halbwertszeit der bei der ^{12}C -Schwerionentherapie erzeugten Positronenemitter, Nov. 25, 2005

Senger, P., GSI Darmstadt:

Future Experiments on Hadron Physics and Dense Baryonic Matter at FAIR, Nov. 14, 2005

Schuettauf, A., GSI Darmstadt:

The Time of Flight Upgrade of FOPI with Multistrip RPCs, Dec. 5, 2005

Titov, A., Bogoljubov Lab. of Theor. Phys., JINR Dubna, Russia:
Parity violation in deuteron photodisintegration, May 11, 2005

Typel, S., GSI Darmstadt:
Indirekte Methoden für nukleare Astrophysik, Jan. 7, 2005

Varela, J., CERN Geneva, Switzerland:
ClearPem, a dedicated PET camera for mammography
Molecular Life Science and Imaging, March 21, 2005

Wüstenfeld, J., GSI Darmstadt:
Auslese und Qualitätskontrolle der HADES-Driftkammern, Apr. 15, 2005

Zschocke, S., Univ. Bergen, Norway:
Renormalisation: From classical theory to Quantum Electrodynamics, Aug. 24, 2005

Zilges, A., TU Darmstadt:
Nukleare Astrophysik mit Photonen, Jan. 14, 2005

Lecture Courses

Brinkmann, B., **F. Dohrmann**
Schlüsselexperimente der Kern- und Teilchenphysik
TU Dresden, SS 2005

Fahmy, K.
Struktur und Funktion in Biomolekülen
TU Dresden, SS 2005

Frauendorf, S.
Electromagnetic Waves
Undergraduate course, Univ. Notre Dame, Indiana, USA, spring 2005

Frauendorf, S.
Electricity and Magnetism
Undergraduate course, Univ. Notre Dame, Indiana, USA, fall 2005

Grosse, E.
Experimentelle Methoden der Kern- und Teilchenphysik - Beschleuniger und Detektoren
TU Dresden, SS 2005

Grosse, E., H. Freiesleben
Institutsseminare Inst. für Kern- und Teilchenphysik
TU Dresden, SS 2005,
TU Dresden, WS 2005/2006

Kämpfer, B.
Allgemeine Relativitätstheorie
TU Dresden, WS 2004/2005

Kämpfer, B., E. Grosse, A. Wagner
Kerne und Sterne
TU Dresden, WS 2004/2005

Kämpfer, B., G. Plunien
Hadronen und Kerne
TU Dresden, SS 2005

Kämpfer, B.
Standardmodell der Teilchenphysik
TU Dresden, SS 2005

Kämpfer, B., Krauss, F., Schützhold, R.
Theoretische Physik: Symmetrien
TU Dresden, SS 2005

Kämpfer, B.
Theoretische Mechanik
TU Dresden, WS 2005/2006

Wagner, A.
Nukleare Astrophysik
TU Dresden, WS 2005/2006

Lectures

Enhardt, W.

Neuere apparative Entwicklungen in der Krebstherapie mit Strahlung
Med. Fakultät u. Uni.-Klinikum C.G. Carus, OncoRay, TU Dresden, Dec. 08, 2005

Fahmy, K.

Investigation of Biological Mechanism by Spectroscopic Methods
Biozentrum Basel, Switzerland, 2005

Frauendorf, S.

Symmetries in Nuclear Physics
4 lectures, 6th Nordic Summer School in Nuclear Physics, Hillerod, Denmark, Aug. 8-19, 2005

Grosse, E.

Entstehung der chemischen Elemente im Universum
Vortragsreihe Naturwissenschaften Aktuell der Fakultät Mathematik und Naturwissenschaften, TU Dresden,
Oct. 20, 2005

Calls

Prof. Wolfgang Enhardt

Medizinische Fakultät Carl Gustav Carus Dresden, Medizinische Strahlenphysik, Nov. 2005

Awards

Dr. Katia Parodi

Christoph-Schmelzer-Preis, GSI Darmstadt, Nov. 2005

Habilitation Theses

Wolfgang Enhardt

Positronen-Emissions-Tomographie für die Qualitätssicherung der Ionenstrahl-Therapie von Tumoren
IKH, FZR Rossendorf, Nov. 2005

Frank Dohrmann

Production of strangeness in hot and cold nuclear matter induced by both leptonic and hadronic projectiles
IKH, FZR Rossendorf, submitted May 2005

Ph.D. Theses

Anna Lehnert

Establishment of the Physical and Technical Prerequisites for the Determination of the Relative Biological Effectiveness of Low-energy Monochromatic X-rays
TU Dresden, Fakultät für Mathematik und Naturwissenschaften, Oct. 24, 2005

Paulo Crespo

Optimization of in-beam position emission tomography for monitoring heavy ion tumor therapy
TU Darmstadt, Fachbereich Physik, Dec. 21, 2005

Diploma Theses

Thomas Würschig

Aufbau eines Versuchsplatzes für die Positronen-Emissions-Therapie
TU Dresden, Sept. 2005

Kerstin Mäser

Monochromatisierung von Röntgenstrahlung
Hochschule Mittweida (FH), Nov. 2005

Roland Beyer

Aufbau und Entwicklung von Neutronen-Flugzeit-Detektoren für die Untersuchung astrophysikalisch relevanter (γ, n) -Reaktionen
Friedrich-Schiller-Universität Jena, Physikalisch-Astronomische Fakultät, Dec. 2005

Patents

Enhardt, W., J. Pawelke, K. Parodi, P. Crespo

Patent: DE 10 2004 009 784 A1

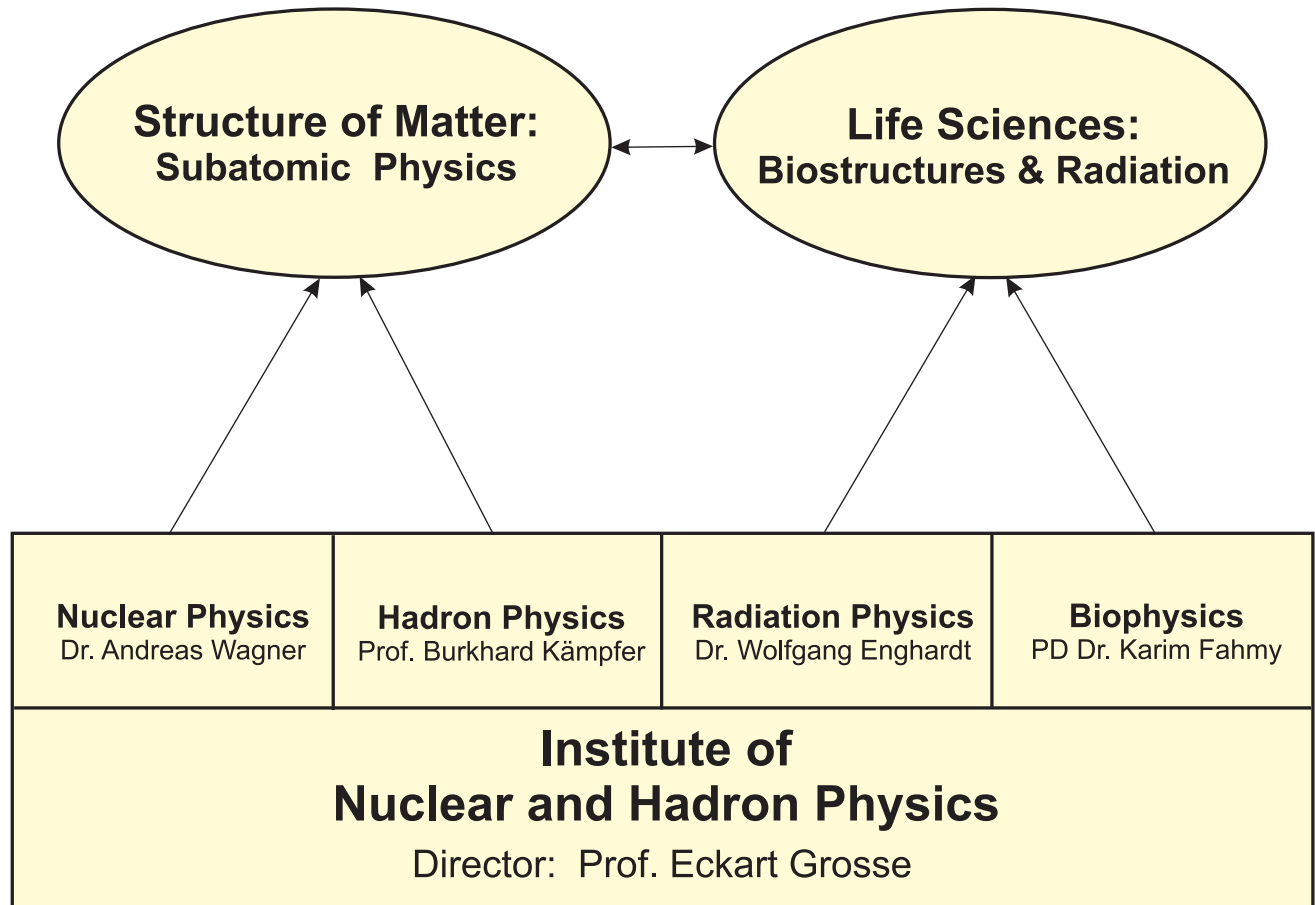
Verfahren zur Korrektur der beim Monitoring der strahlentherapeutischen Behandlung mittels in-beam Positronen-Emissions-Tomographie erhaltenen Messwerte

Meeting organized by the IKH

Topic	Period	Number of Participants
WIRMS 2005 at Rathen / Dresden "International Workshop on Infrared Microscopy and Spectroscopy with Accelerator based Sources" Workshop at Rathen / Dresden	June 26-30, 2005	102

Personnel

Departments of the IKH



Personnel of the Institute for Nuclear and Hadron Physics

Director: Prof. Dr. E. Grosse¹

Scientific Personnel

PD Dr. H.W. Barz	Dr. R. Kotte	Dr. M. Sczegan
Dr. F. Dönau	Dr. H. Müller	Dr. W. Seidel
Dr. F. Dohrmann	Dr. N. Nankov	Dr. A. Sytcheva
Prof. Dr. W. Enghardt	Dr. L. Naumann	Dr. A. Wagner
PD Dr. K. Fahmy	Dr. W. Neubert	Dr. W. Wagner
Prof. Dr. S. Frauendorf ²	Dr. K. Parodi	Dipl. Phys. D. Wohlfarth
Dr. A. Junghans	Dr. J. Pawelke	Dr. R. Wünsch
Prof. Dr. B. Kämpfer	Dr. O. Savchuk	Dr. J. Wüstenfeld
Dr. J. Klug	Dr. K.D. Schilling	Dr. S. Zschocke
Prof. H. Kötzle	Dr. R. Schwengner	

PhD Students

B. Azadegan	H. Keshbak	G. Rusev
E. Beyreuther	K. Kosev	A. Sadovsky
M. Bluhm	A. Lehnert	G. Shakirin
P. Crespo	S. Madathil	R. Thomas
M. Erhard	D. Möckel	P. Zhou
F. Fiedler	C. Nair	
K. Kanaki	U. Reichelt	

Students

B. Bannier ³	T. Kluge	M. Sellesk
R. Beyer ³	K. Mäser ³	D. Stach
M. Fauth	C. Richter	T. Würschig ³
V. Katsoulidou	H. Schade ³	K. Zeil

Technical Personnel

J.U. Berlin	J. Hutsch	S. Schaller
M. Boeck	K. Krüger	C. Schneidereit
M. Böse	E. Leßmann	W. Schulze
A. Hartmann	M. Langer	A. Seifert
K. Heidel	M. Paul	M. Sobiella
L. Heinrich	J. Philipp	J. Steiner
R.R. Hensel	B. Rimarzig	U. Wolf

¹ also TU Dresden

² also University of Notre-Dame, Indiana, USA

³ Diploma Student

Guest Scientists

Barnaföldi, G.	KFKI Budapest, Hungary
Dr. Bećvar, F.	Karls Univ. Prag, Czech. Rep.
Benouret, N.	Univ. Algier, Algerien
Bentley, I.	Notre Dame Univ., USA
Deveaux, M.	GSI Darmstadt, IReS Strاسبorg
Furlinski, G.	BAS Sofia, Bulgaria
Dr. Kamanin, D.	VIK Dubna , Russia
Dr. Kaptari, L.P.	JINR Dubna, Russia
Dr. Kapusta, M.	Soltan Institute for Nuclear Studies, Department of Electronics, Otwock-Swierk, Poland
Khesbak, H.	—, Bahrain
Dr Klug, J.	Uppsalla University, Sweden
Dr. Kostov, L.K.	Institute for Nuclear Research and Nuclear Energy, Sofia, Bulgaria
Krticka, M.	Karls Univ. Prag, Czech. Rep.
Khudyakov, A.	IHED Obninsk, Russia
Lantukh, J.	Universität Orenburg, Russia
Nassalski, A.	Soltan Institute for Nuclear Studies, Department of Electronics, Otwock-Swierk, Poland
Dr. Ortega, J.-M.	LURE, France
Pyatkov, Y.V.	MEPhI Moscow, Russia
Dr. Wolf, G.	KFKI, RMKI, Budapest, Hungary
Dr. Zschocke, S.	BCPL Bergen, Norway
Zetenyi, M.	KFKI Budapest, Hungary